Memory effects in soft matter

im Fachbereich Physik der Freien Universität Berlin eingereichte
Dissertation

zur Erlangung des akademischen Grades eines Doktors der
Naturwissenschaften (Dr. rer. nat.)

vorgelegt von
Julian Kappler

Berlin, 2018

Erster Gutachter:	Prof. Dr. Roland R. Netz Freie Universität Berlin
Zweiter Gutachter:	Prof. Dr. Petra Imhof Freie Universität Berlin
Tag der Disputation:	13.07.2018

Contents

Chapter 1

Introduction

1.1 Scale separation and effective models

At its core, statistical physics is the pursuit of effective descriptions of systems that are comprised of many degrees of freedom [1–3]. A prototypical example for this is a dilute gas, where one is typically not interested in the detailed motion of each individual particle, but rather in macroscopic properties like the pressure the gas exerts on a bounding wall. Indeed, one of the early successes of equilibrium statistical physics was the derivation of the heuristically known ideal gas law starting from atomistic detail [1–3]. The reason that simple macroscopic equations can describe properties of complicated many-body systems is separation of scales. In the above example of a gas, both length and time scales associated with the intermolecular interactions are typically much smaller than those of the macroscopic observable one is interested in. This scale separation, together with the fact that there are many particles involved, leads to the emergence of the macroscopic law [1–3].

In non-equilibrium statistical physics, a similar prototypical example is the Langevin equation [4–9]. In 1827, the botanist Robert Brown observed that a pollen grain, when suspended on water, performs a seemingly random jittery motion [10]. Since a similar motion is present for a variety of materials, for example pulverized volcanic ashes, he could exclude the possibility that living pollen is actively moving. If not life, then what was causing those particles to move? The origin of the "Brownian motion" was only fully understood at the beginning of the 20th century, independently by Albert Einstein [11] and Marian Smoluchowski [12]. They presumed that the motion of the suspended particle is caused by ongoing collisions with the surrounding water molecules, and derived a probability distribution for the particle position, which obeys the diffusion equation. That this equation indeed describes how a pollen grain on water moves was subsequently verified experimentally by Jean-Baptiste Perrin [13], who would receive the Nobel Prize in Physics for this work in 1926.

While Einstein and Smoluchowski considered the probability distribution of the suspended particle, Paul Langevin took a different, yet equivalent, perspective. In 1908, he postulated an equation of motion for the position of the particle by adding a stochastic term to Newton's equation of motion, thus obtaining [4, 5]

$$m\ddot{x}(t) = -\gamma\dot{x}(t) + F(x(t)) + F_R(t). \tag{1.1}$$

In this equation, which today is called the Langevin equation [6–9], m and x are mass and position of the particle, time derivatives are denoted by dots, γ is a friction coefficient, $F(x)$ is a deterministic external force (which in the case of Brownian motion vanishes) and $F_R(t)$ is a stochastic force, modeled as a Gaussian stochastic process with zero mean. The interaction between system (the pollen grain) and environment (the water molecules) is described by both the frictional and the stochastic force, and their common origin manifests itself in a relation called the fluctuation-dissipation theorem [6–8]. Due to the stochastic nature of F_R, solutions of the Langevin equation Eq. (1.1) are themselves stochastic, and upon averaging it can be shown that the Langevin equation is indeed equivalent to the diffusion equation originally used to model Brownian motion [6–8].

A key concept in the models of Einstein, Smoluchowski and Langevin is separation of scales. The Langevin equation is formulated for the typical time scales on which the suspended particle moves. On these time scales, which are much larger than the typical time scales of the smaller and lighter solvent molecules, the bombardment of the suspended particle by the solvent molecules seems random and uncorrelated in time. This is reflected in the properties of the stochastic force F_R and allows for formulating the relatively simple effective equation (1.1) for the interaction of the particle with its environment [7–9].

But what happens if we consider the motion of the suspended particle for very short times, comparable to the solvent time scales? Or if we consider a system with characteristic time scales comparable to those of its environment? And is there a systematic way of deriving the Langevin equation from the Newtonian equations of motion of all the particles involved? Pioneering work in this direction was done by Hazime Mori [14] and Robert Zwanzig [15, 16] in the 1960s. They considered a dynamical system with many degrees of freedom, comprised of a reaction coordinate x which is linearly coupled to an environment, also called "heat bath". The reaction coordinate is not necessarily the position of a particle but can be something more abstract, for example a particle density in a volume, or a vector connecting two particles. By eliminating the heat bath variables from the equation of motion of the reaction coordinate, Mori and Zwanzig derived what is today called the generalized Langevin equation (GLE),

$$m\ddot{x}(t) = -\int_0^t \mathrm{d}t'\, \Gamma(t')\dot{x}(t-t') + F(x(t)) + F_R(t). \tag{1.2}$$

The effect of the environment on the reaction coordinate is twofold. First, there is a frictional force modeled by a function $\Gamma(t)$, called the memory kernel. Second there is a stochastic force $F_R(t)$, where stochasticity enters by assuming appropriate random initial conditions for the environment [8]. As in the Langevin equation, the common origin of memory kernel and random force leads to a generalized fluctuation-dissipation theorem. Because of the integral in Eq. (1.2), the evolution of the reaction coordinate at a given time does not only depend on its state at that time, but also on its states at previous times. This is called memory, or the GLE is said to exhibit "non-Markovian dynamics". In contrast, the Langevin equation Eq. (1.1), where the acceleration at a given time only depends on the state at the same time, is a "Markovian" equation. If there is separation of time scales, i.e., if the time scale on which $\Gamma(t)$ decays is much smaller than the time scale on which $\dot{x}(t)$ varies, the history-dependence in Eq. (1.2) can be neglected, and the

original Langevin equation be recovered via

$$\Gamma(t) \longrightarrow 2\gamma\delta(t), \tag{1.3}$$

$$\int_0^t \mathrm{d}t'\Gamma(t')\dot{x}(t-t') \longrightarrow \gamma\dot{x}(t), \tag{1.4}$$

where $\gamma = \int_0^\infty \mathrm{d}t\,\Gamma(t)$ [8]. If there is no separation of time scales between Γ and $\dot{x}$, memory effects can influence the dynamics of x on time scales much larger than the decay time of Γ.

The works of Mori and Zwanzig reveal a very general principle, namely that eliminating degrees of freedom in a dynamical system can lead to memory effects in the effective equations for the remaining degrees of freedom [7, 8, 14–16]. As a matter of fact, the converse is also true. Typically, reaction coordinates which display memory effects can be described by a set of Markovian equations via introducing additional degrees of freedom, i.e., by adding an explicit model for the environment [7, 8]. The Mori-Zwanzig derivation furthermore illustrates that whether dynamics is Markovian or exhibits memory effects depends on what is considered "reaction coordinate" and what is considered "environment".

Since the Markovian Eq. (1.1) is easier to analyze than the non-Markovian Eq. (1.2), much effort is put into identifying relevant reaction coordinates that are (approximately) Markovian [17–26]. However, for a given physical question such reaction coordinates might not exist, so that including memory effects becomes indispensible [7, 27–34]. As we further outline in the next section, many systems encountered in biological physics are of the latter type.

1.2 Biological systems are never isolated

Cells are often referred to as the units of living matter [35–37]. Indeed, each living organism originates from the division of a single cell, and apart from having the ability to divide, cells store information, react to external stimuli, move, and can even destroy themselves [35–37]. Each cell is bounded by a biomembrane, and densely packed on the inside. An important class of biomolecules populating the cell are proteins, which together with water make up most of the mass of a cell [36]. To enable the cell to function, proteins perform a multitude of tasks including catalyzing reactions, processing information, building and transporting other molecules, and regulating in- and outfluxes through the cell membrane [27, 35–40]. Throughout, they interact with their heterogeneous environment so that, much like a pollen grain on water, no protein is ever isolated. In fact, the interaction of a protein with its surroundings is typically even necessary for proper function. For example, many proteins have to reach and maintain a folded state to be functional, and this is assisted by interactions with both surrounding molecules, and interactions among different parts of the protein itself [38, 41–46].

A quantitative model for a single reaction coordinate of a single protein would require including all the degrees of freedom that couple to the reaction coordinate, which can be computationally prohibitive or impossible due to the lack of detailed knowledge about the environment. It is therefore not surprising that one resorts to effective descriptions, and that both the Langevin equation and the generalized Langevin equation are cornerstones of biological and soft-matter physics [7, 9, 27].

The Langevin equation has successfully been applied to model, for example, both translational and rotational diffusion of bacteria [39, 40], diffusion through membranes [35, 47–49], and chemical reactions [50–52]. With advances in experimental techniques, such as Förster resonance energy transfer (FRET) or single-molecule spectroscopy, ever smaller scales can be probed directly [53–56]. In parallel, increasing computing power allows for simulation of larger systems, so that many-body dynamics can also be probed computationally [57–60]. These developments led to the observation of memory effects in many biologically relevant reaction coordinates. For example, memory effects were observed in conformational transitions in small molecules [28,29], lateral diffusion of particles in biomembranes [30,31], the dynamics of an individual monomer in large polymers [32–34], the motion of colloidal particles in actin networks [61] and other crowded environments [27], and the folding kinetics of polymers and peptides [62–65]. In these systems, there is typically no strict separation of time scales between the dynamics of what is considered "reaction coordinate" and "environment", so that memory effects cannot be neglected. We thus see that the models introduced by Einstein, Smoluchowski, Langevin, Mori, and Zwanzig continue to be of great importance, and in particular are indispensable for understanding biological and soft-matter systems on a microscopic scale.

1.3 Outline of this work

In the present work, we consider three systems in the realm of biological soft-matter physics where memory effects are relevant. In short, the first part is devoted to effectively modeling the large scale behavior of polymers using the generalized Langevin equation. In the second part, we consider a model system to study how memory effects influence processes such as chemical reactions or conformational transitions of molecules. In the third part we consider surface waves, a phenomenon usually not associated with memory, but in which such effects emerge as a consequence of dimensional reduction.

Cyclization dynamics of polymers. The kinetics of loop formation of polymers is of biophysical interest for protein folding [65–67] or regulation of gene expression [68–71]. Simply speaking, one wants to know the time needed until two residues of a polymer find each other, called the cyclization time. Figure 1.1 (a) illustrates a polymer backbone model (with the terminal residues enlarged) and highlights the appropriate reaction coordinate for studying cyclization of the polymer endpoints, the end-to-end distance of the chain. Memory effects arise because the typical time scales of the end-to-end distance motion are comparable to those of other internal degrees of freedom of the molecule, and in Chapter 2 we investigate the cyclization time by analyzing the non-Markovian dynamics of the end-to-end distance. We run Langevin simulations for several polymer backbone models, including the case where the chain can intersect itself (phantom chains) and where the chain is self-avoiding and collapses to form a globule. We numerically extract memory kernels and find that for phantom chains, the end-to-end distance dynamics is described by a memory kernel with intermediate scaling

$$\Gamma(t) \sim t^{-1/2}, \tag{1.5}$$

independent of the precise nature of the bonded interactions. On the other hand, for a self-avoiding

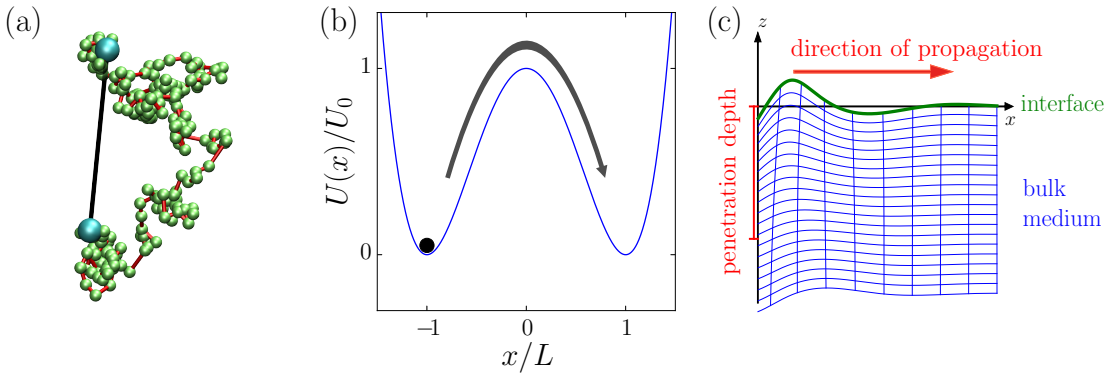

Figure 1.1: Illustrations of the systems considered in this dissertation. (a) In a polymer, the coupling of the end-to-end distance (indicated as a black line) to the internal degrees of freedom leads to memory effects. This affects folding kinetics, see Chapter 2 for details. (b) Memory effects change the barrier crossing time as compared to the Markovian (short memory) limit. This can lead to both acceleration and slowdown of barrier crossing. See Chapters 3 and 4 for details. (c) Pressure waves in a compressible interface on a viscous fluid are described by a fractional wave equation. Memory effects arise because the dynamics of the bulk medium (shown in blue) is eliminated from the dynamical equations of the interface (shown in green), and the time scales of bulk- and surface dynamics are comparable. See Chapter 6 for details. The figures shown here are based on (a) Fig. 2.3, (b) Fig. 3.1, and (c) Fig. 6.1.

collapsed chain, we find

$$\Gamma(t) \sim t^{-6/11}. \tag{1.6}$$

For both phantom and self-avoiding collapsed chains, we numerically calculate the cyclization time τ_c and observe that the phantom chain reproduces the known scalings $\tau_c \sim N^2$ [72, 73], $\tau_c \sim N^{3/2}$ [74], where N is the number of monomers. For the self-avoiding collapsed polymer we find the scaling $\tau_c \sim N^{5/3}$, and using Flory theory relate this scaling to the non-Markovian dynamics of the end-to-end distance.

Barrier crossing in systems with memory. The rate-determining step of chemical and conformational molecular reactions is typically modeled as the crossing over a single barrier in an effective one-dimensional energy landscape [75–85], see Fig. 1.1 (b) for an illustration. The one-dimensional reaction coordinate x is coupled to both solvent and intra- or intermolecular degrees of freedom, and if there is no separation of time scales between x and the orthogonal degrees of freedom, then memory effects are present [25, 29, 86]. In Chapters 3 and 4, we consider the GLE Eq. (1.2) as a model system for dynamics with memory effects, and address the question how the mean first-passage time for barrier crossing τ_{MFP} depends on the time scales of the system.

In Chapter 3 we consider a single-exponential memory kernel

$$\Gamma(t) = \frac{\gamma}{\tau_\Gamma} e^{-t/\tau_\Gamma}. \tag{1.7}$$

We simulate the corresponding GLE in the complete parameter space that encompasses both low and high friction γ as well as short and long memory times τ_Γ, compare our numerical data for τ_{MFP} to predictions of well-known non-Markovian rate theories by Grote-Hynes (GH) [87] and Pollak-Grabert-Hänggi (PGH) [88], and present a simple heuristic formula for τ_{MFP} that holds globally as a function of all parameters. We find that there is an intermediate regime where memory effects accelerate barrier crossing as compared to the Markovian case, and use our heuristic formula to establish a scaling diagram that contains all asymptotic regimes, as well as the intermediate memory acceleration regime.

In Chapter 4 we then consider a bi-exponential memory kernel

$$\Gamma(t) = \frac{\gamma}{2\tau_1} e^{-t/\tau_1} + \frac{\gamma}{2\tau_2} e^{-t/\tau_2}. \tag{1.8}$$

We simulate the corresponding GLE to obtain the barrier crossing time τ_{MFP} as a function of γ, τ_1, τ_2. We find that τ_{MFP} is dominated by the shorter of the two memory times τ_1, τ_2, and extend the heuristic formula from Chapter 3 to also include the bi-exponential scenario.

Surface waves. Recently, surface waves have received focal attention in the context of nerve pulse propagation. It was found experimentally that nerve pulses are accompanied by mechanical displacements in the nerve cell membrane [89, 90]. To address the question whether these pressure pulses are of functional relevance, extensive experimental studies of pressure pulses in membranes have been carried out on a simple model system comprised of a lipid monolayer spread at the air-water interface [91–94]. While the exact relevance of pressure pulses for nerve pulse propagation is still a matter of debate, it was found that the pressure waves which propagate in such a system share many interesting properties with nerve pulses; in particular, they show a nonlinear all-or-nothing response when excited by different driving amplitudes [93, 94]. The aim of Chapters 5 and 6 is to first understand linear surface waves, and then to derive a comprehensive theory of nonlinear pressure waves at interfaces.

In Chapter 5, we discuss the linear theory of surface waves on a semi-infinite viscoelastic medium bounded by a 2D viscoelastic interface, see Fig. 1.1 (c) for an illustration. We derive the generic dispersion relation describing the surface waves that can exist in such a system, which contains the known Rayleigh, capillary-gravity and Lucassen wave solutions as limiting cases. We furthermore identify an additional solution that differs from all previously described waves in that gravitation, surface tension and bulk shear viscosity must simultaneously be nonzero for it to exist, and which can in principle be excited on a pure air-water interface. Finally, we discuss the existence regions of the various surface waves and find that for a surfactant monolayer on water, the number of coexisting wave solutions switches between one and three, depending on interfacial compressibility and frequency.

In Chapter 6, we focus on the Lucassen wave, which is the 2D pressure wave observed in the above-mentioned experiments [93, 94]. We first derive the fractional surface wave equation that governs the linear Lucassen wave discussed in Chapter 5. The fractional character of the surface wave equation characterizes memory effects, which appear because the degrees of freedom of the bulk medium below the interface are eliminated. This results in memory effects that couple to the interface acceleration and, in the notation of Section 1.1, scale as

$$\Gamma(t) \sim t^{-1/2}. \tag{1.9}$$

Having established the linear fractional wave equation, we include nonlinear effects arising from the dependence of the interface compressibility on the local compression. This reflects a phase transition at the interface, and the precise form of our nonlinearity is based on experimental measurements by our collaborators Matthias Schneider (TU Dortmund) and Shamit Shrivastava. Numerical solutions of our nonlinear fractional theory reproduce several experimental key features of surface waves in phospholipid monolayers at the air-water interface without freely adjustable fitting parameters. In particular, the propagation distance of the surface wave abruptly increases at a threshold excitation amplitude. Similar to experimental results, we find a wave velocity of the order of 40 cm/s, which slightly increases as a function of the excitation amplitude.

Chapter 2

Cyclization dynamics of ideal and self-avoiding collapsed polymers

Bibliographic information: The content of this chapter and of Appendix A is in preparation to be submitted to a peer-reviewed journal (Ref. [i]).

2.1 Introduction

The kinetics of loop formation of polymers is of biophysical interest for protein folding [65–67] or regulation of gene expression [68–71]. Consequently, this topic has been studied extensively both experimentally [65–67, 95, 96], and theoretically [62, 68, 72, 74, 97–99]. For loop formation of polymers the observable of interest is the cyclization time τ_{c}, which is the mean time needed for the two ends of a polymer to fall below a threshold distance R_c, called the capture radius, after starting from a distance $R_s > R_c$. Pioneering theoretical works predicted the cyclization time for a Gaussian chain undergoing Rouse dynamics to scale with the number of monomers N as

$$\tau_{\mathrm{c}} \sim N^{\alpha} \tag{2.1}$$

with $\alpha = 2$ for R_c not too small, known as the Wilemski-Fixman (WF) scaling [72, 73], and $\alpha = 3/2$ for small capture radii, known as the Szabo-Schulten-Schulten (SSS) scaling [74]. Since the end-to-end distance R_{ete} is a collective variable involving all internal degrees of freedom of the chain, analytical treatments typically include the whole conformational space of the polymer to obtain the dynamics of R_{ete} [62,68,97]. Only recently effective descriptions of polymer dynamics in terms of the generalized Langevin equation (GLE) have been developed [32–34, 100, 101] to tackle the complex relaxation kinetics observed in experiments [64, 102, 103]. For realistic self-avoiding chain models approximate analytical results are sparse [100] so that numerical simulations have to be used [104, 105] to probe the dynamics of chains of short and intermediate length.

In the present chapter we investigate whether cyclization dynamics depend on the polymer model or on the presence of non-ideal effects. To this end we consider the end-to-end dynamics of three phantom polymer models, namely a Gaussian chain, a freely jointed (FJ) chain, and a freely

rotating (FR) chain. Furthermore we consider a non-ideal Gaussian chain with Lennard-Jones interactions (GLJ), see Fig. 2.1 for illustrations. We run explicit Langevin simulations of the

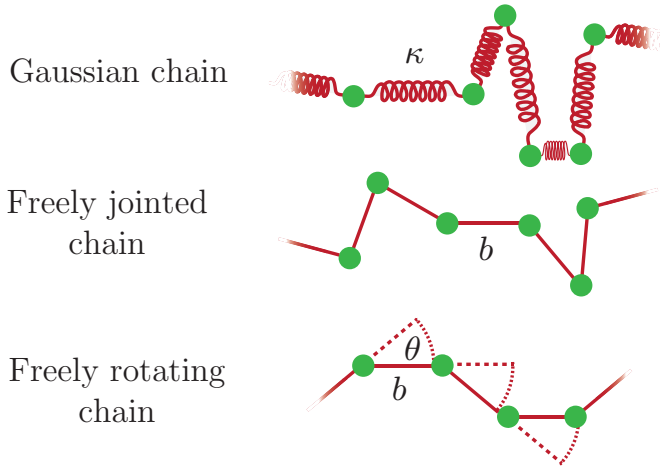

Figure 2.1: Illustration of models considered in this chapter. In the Gaussian chain model, the interaction potential between two consecutive monomers is harmonic with strength κ. In the freely jointed (FJ) chain, the bond length b between two consecutive monomers is constraint, in the freely rotating (FR) chain both bond length b and bond angle θ are constraint.

models and map the end-to-end distance R_{ete} onto a GLE, where non-Markovian friction effects are characterized by a memory kernel Γ. We find that the memory kernels of the phantom chains (Gaussian, FJ, FR) agree perfectly on time scales where details of the bond interactions are irrelevant, and in particular all show a $\Gamma \sim t^{-1/2}$ scaling behavior for intermediate times t. The GLJ model yields a memory kernel with a steeper power law decay which, for longer chains $N \gtrsim 200$ when the GLJ chain is in a collapsed globular state, is consistent with $\Gamma \sim t^{-6/11}$, as obtained from a scaling model. We then calculate cyclization times τ_{c} from simulations. Depending on the capture radius R_c, the phantom chains yield the WF and SSS scalings. For the GLJ model we find an asymptotic scaling $\tau_{\mathrm{c}} \sim N^{5/3}$ for long chains. This scaling can be derived from a scaling analysis based on Flory theory in poor solvent [105]. Thus, both memory kernel and cyclization time are insensitive to the detailed nature of bonded interactions, but substantially influenced by non-bonded interactions that lead to chain collapse.

2.2 Methods

We simulate four different models via Langevin dynamics at temperature $T = 300$ K using the GROMACS 2016.3 simulation package [57], see Fig. 2.1 for illustrations and Appendix A.1 for more details. Our parameters are based on alkane chains in water as modeled in the gromos53a6 forcefield [106].

i) Gaussian chain. The monomers of a chain of length N have masses m_i, $i = 0, ..., N-1$, where $m_0 = m_{N-1} = 15$ amu, $m_1 = ... = m_{N-2} = 14$ amu. We denote the position of the i-th

monomer by $\vec{R}_i(t)$. Each monomer is subject to friction with friction coefficient $\gamma = 110$ amu/ps. The strength of the nearest-neighbor harmonic potential is $\kappa = k_\mathrm{B}T/b^2 = 319.8$ amu/ps^2, which leads to a mean squared distance between neighboring monomers $\langle(\vec{R}_i - \vec{R}_{i+1})^2\rangle = b^2$ with $b = 0.153$ nm. A snapshot from simulations of the Gaussian chain model is shown in Fig. 2.3 (a).

ii) Freely jointed (FJ) and iii) freely rotating (FR) chain. The simulations of the FJ and FR chains are based on the Gaussian chain model, but with the distance between neighboring monomers constrained to $b = 0.153$ nm (both FJ and FR chain) and bond angles constrained to $\theta = 111^\circ$ (FR chain).

iv) Gaussian chain with Lennard-Jones interactions (GLJ). The GLJ chain is based on the Gaussian chain model, but additionally includes the standard gromos53a6 non-bonded Lennard-Jones (LJ) interactions for alkane chains [106], see Appendix A.1 for details. Figure 2.3 (a) shows a snapshot from simulations of the GLJ model and illustrates that for large N, the chain collapses to a globular state. This is expected since our parameters model a weakly hydrophobic chain. In Appendix A.2 we show that, due to the repulsive part of the LJ interactions, chain segments cannot cross, so that the chain is self-avoiding.

Employing our Langevin trajectories we parametrize a GLE

$$\mu\,\ddot{R}_\mathrm{ete}(t) = -\int_0^t \mathrm{d}t'\,\Gamma(t-t')\dot{R}_\mathrm{ete}(t') - \nabla U(R_\mathrm{ete}(t)) + F_R(t), \tag{2.2}$$

where $R_\mathrm{ete} = \sqrt{(\vec{R}_{N-1} - \vec{R}_0)^2}$ is the scalar end-to-end distance of the chain, μ is an effective mass, ∇U is the derivative of the potential of mean force (pmf) $U(R_\mathrm{ete})$, $\Gamma(t)$ is a memory kernel modeling non-Markovian friction effects, and the random force $F_R(t)$ is a Gaussian stochastic process with zero mean, and which obeys the generalized fluctuation-dissipation theorem (FDT) $\langle F_R(t)F_R(t')\rangle = k_\mathrm{B}T\,\Gamma(|t-t'|)$, where $k_\mathrm{B} \approx 1.38 \cdot 10^{-23}\,\mathrm{J/K}$ is the Boltzmann constant. To calculate Γ, we use a recent extension of the Berne method [107] developed by Daldrop et al. [108], which allows to obtain memory kernels for any given reaction coordinate from numerical data, see Appendix A.3 for details.

Before discussing the scalar end-to-end distance R_ete, we validate our numerical methods. In Fig. 2.2 we compare numerically extracted memory kernels to analytical predictions for the end-to-end distance vector $\vec{R}_\mathrm{ete} = \vec{R}_{N-1} - \vec{R}_0$, see Appendix A.4 for details. The agreement is perfect without any fitting parameters, which impressively validates our method for extracting $\Gamma(t)$. We find that for $N \gtrsim 100$, the corresponding memory kernel shows a transient $\Gamma \sim t^{-1/2}$ scaling regime. Note that the same scaling was recently derived for the memory kernel of the middle monomer of a Gaussian chain [32, 34].

2.3 End-to-end distance dynamics

Figure 2.3 (b) shows U as a function of the end-to-end distance rescaled by the Kuhn length a_i, which is defined by $\langle R_\mathrm{ete}^2\rangle \equiv a_i L$, where $i =$ G, FJ, FR, GLJ indicates the respective chain model and L is the length of the fully extended chain, $L = (N-1)b$. The pmfs of the phantom

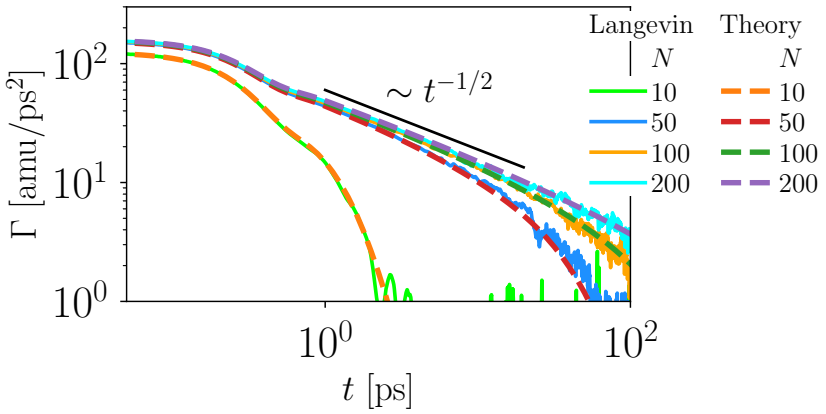

Figure 2.2: Analytical and numerical memory kernels for the end-to-end distance vector $\vec{R}_{\mathrm{ete}}$ of a Gaussian chain. Analytical memory kernels are calculated using the Mori-Zwanzig projection formalism [14, 15], see Appendix A.4 for details. Numerical memory kernels are extracted directly from Langevin simulations [108], as explained in Appendix A.3.

chains are very similar; for the GLJ chain a plateau at short end-to-end distances $R_{\mathrm{ete}}/a \approx 5$, caused by the LJ interactions, can be discerned. For $N \gtrsim 200$ the GLJ chain is more compact than the other models, as can be seen in Fig. 2.3 (c), where the mean squared end-to-end distance $\langle R_{\mathrm{ete}}^2 \rangle$ is plotted. The phantom chains all yield a linear scaling $\langle R_{\mathrm{ete}}^2 \rangle = a_i b(N-1)$ with $a_{\mathrm{G}} = a_{\mathrm{FJ}} = b$, $a_{\mathrm{FR}} = b\sqrt{(1+\cos\theta)/(1-\cos\theta)}$ [109]. For the GLJ chain we observe a length-dependent crossover between different scaling regimes, from a swollen chain for $N \lesssim 30$ to a collapsed chain for $N \gtrsim 100$ [110]. The asymptotic scaling is consistent with the Flory-theory prediction [109, 110]

$$\langle R_{\mathrm{ete}}^2 \rangle \sim N^{2\nu_{\mathrm{st}}}, \tag{2.3}$$

where ν_{st} is the Flory exponent characterizing the solvent quality in the context of the equilibrium (static) end-to-end distance. For negligible nonbonded interactions $\nu_{\mathrm{st}} = 1/2$, for a poor solvent $\nu_{\mathrm{st}} = 1/3$, and for a good solvent $\nu_{\mathrm{st}} \approx 3/5$. Our LJ parameters model a hydrophobic chain, and asymptotically $\langle R_{\mathrm{ete}}^2 \rangle$ scales with the corresponding Flory exponent $\nu_{\mathrm{st}} = 1/3$.

Moving on to the dynamics of R_{ete}, in Fig. 2.3 (d) we show mean squared displacements (MSDs) $\langle \Delta R_{\mathrm{ete}}^2(t) \rangle = \langle (R_{\mathrm{ete}}(t) - R_{\mathrm{ete}}(0))^2 \rangle$ as calculated from simulations. For Gaussian and FJ chain models we see a power law

$$\langle \Delta R_{\mathrm{ete}}^2(t) \rangle \sim t^{\beta} \tag{2.4}$$

with $\beta = 1/2$, which for the Gaussian chain can be derived analytically [109, 111]. For the FR chain model no clear power law can be observed before the MSD saturates, see Appendix A.5 for a possible explanation. For the GLJ chain, we observe a power-law scaling $\beta = 6/11$ [112, 113] extending over almost two decades in time. As we show in Appendix A.7 the observed MSD scalings can be obtained from a scaling analysis based on Flory theory, which

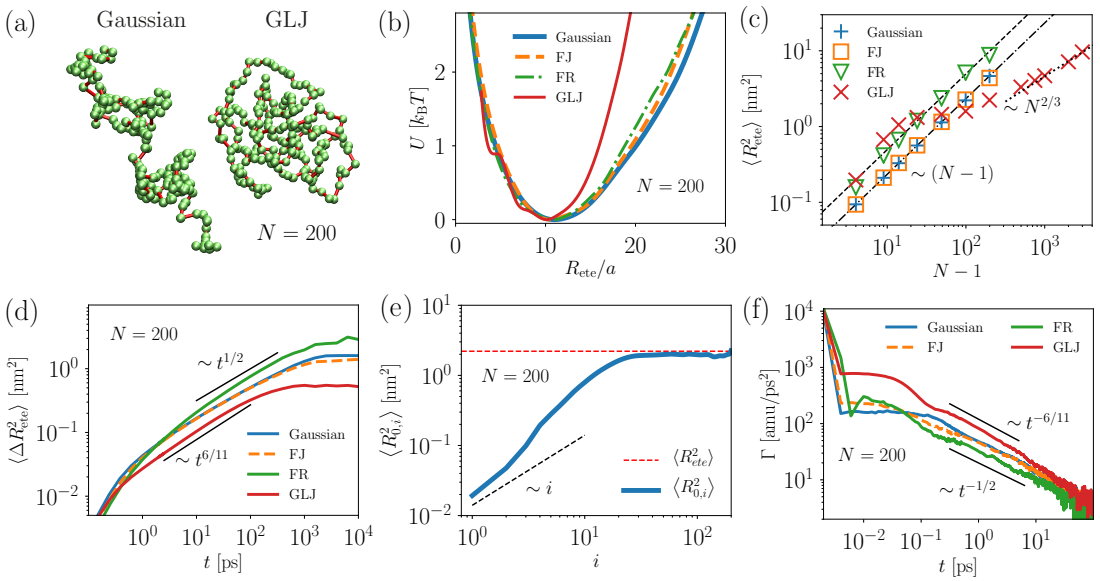

Figure 2.3: Numerical results for end-to-end distance R_{ete}. (a) Simulation snapshots of Gaussian and GLJ chains. (b) Pmfs for the end-to-end distance R_{ete} for $N = 200$. (c) Mean squared end-to-end distance as function of chain length N. Dashed lines and dashed-dotted lines show $\langle R^2_{\mathrm{ete}}\rangle = a_i L$ with $L = (N-1)b$ and Kuhn lengths $a_i = b\sqrt{(1+\cos\theta)/(1-\cos\theta)}$ (dashed line), $a_i = b$ (dashed-dotted line). The dotted line indicates the power law $\langle R^2_{\mathrm{ete}}\rangle \sim N^{2/3}$. (d) MSDs calculated from simulation trajectories. Transient power law scaling is indicated by black bars. (e) Mean squared distance $\langle R^2_{0,i}\rangle = \langle(\vec{R}_0 - \vec{R}_i)^2\rangle$ of the terminal monomer to the i-th monomer of a GLJ chain. The red dashed line represents the mean end-to-end distance $\langle R^2_{0,200}\rangle \equiv \langle R^2_{\mathrm{ete}}\rangle$. (f) Memory kernels extracted from simulations [108] for chain lengths $N = 200$. Transient power-law scaling is indicated by black bars.

predicts $\beta = 2\nu_{\mathrm{dyn}}/(1+2\nu_{\mathrm{dyn}})$ with ν_{dyn} the Flory exponent characterizing the end-to-end dynamics [112, 113]. While for $\nu_{\mathrm{dyn}} = 1/2$ one recovers $\beta = 1/2$ as observed for the Gaussian and FJ chain, for a good solvent, where $\nu_{\mathrm{dyn}} = 3/5$, we obtain $\beta = 6/11$. Remarkably we observe good-solvent scaling $\nu_{\mathrm{dyn}} = 3/5$ in the MSD, even though our LJ parameters model a hydrophobic chain and we observe poor-solvent scaling $\nu_{\mathrm{st}} = 1/3$ in the equilibrium end-to-end distance. While in the true asymptotic limit we expect that both equilibrium and dynamical properties are characterized by the same Flory exponent, $\nu_{\mathrm{st}} = \nu_{\mathrm{dyn}}$, for the finite values of N we consider, we find mixed intermediate scaling regimes where $\nu_{\mathrm{st}} \neq \nu_{\mathrm{dyn}}$. Indeed, the mean monomer distance $\langle(\vec{R}_0 - \vec{R}_i)^2\rangle$ along the chain shown in Fig. 2.3 (e) exhibits good-solvent condition up to the experimentally relevant nanometer scale.

In Fig. 2.3 (f), we show memory kernels for $N = 200$. The kernel Γ_{G} of the Gaussian chain scales as $\Gamma_{\mathrm{G}} \sim t^{-1/2}$, and except for short times agrees very well with the kernel Γ_{FJ} of the FJ chain, demonstrating that the end-to-end dynamics are insensitive to the detailed form of the bond-potentials. Note that this scaling, which we also find for $\vec{R}_{\mathrm{ete}}$ in Fig. 2.2, reflects the

Rouse spectrum [32, 34]. The kernel Γ_{FR} of the FR chain model also scales as $\Gamma_{\mathrm{FR}} \sim t^{-1/2}$, but rescaled in time as compared to Γ_{G}. As we detail in Appendix A.6, this is due to the different Kuhn lengths of the models, and after an appropriate rescaling the memory kernels Γ_{G} and Γ_{FR} agree perfectly in the power-law regime. The memory kernel Γ_{GLJ} exhibits a different power law, consistent with $\Gamma_{\mathrm{GLJ}} \sim t^{-6/11}$. The inverse relationship $\langle \Delta R_{\mathrm{ete}}^2 \rangle \sim t^{\beta}$, $\Gamma \sim t^{-\beta}$ between MSD and memory kernel is expected [114], in Appendix A.5 we give a short derivation of this relation and briefly discuss its range of validity.

As a final remark in this section, we point out that the the dynamics of the radius of gyration R_g, which is another experimentally relevant collective variable reflecting the large-scale motion of the chain, can be very different from that of the end-to-end distance. As we show in Appendix A.8, for long self-avoiding collapsed chains the MSD of R_g displays a scaling behavior $\langle \Delta R_g^2 \rangle \sim t^{1/4}$, which is different from all the scalings observed in the present section for R_{ete}.

2.4 Cyclization time

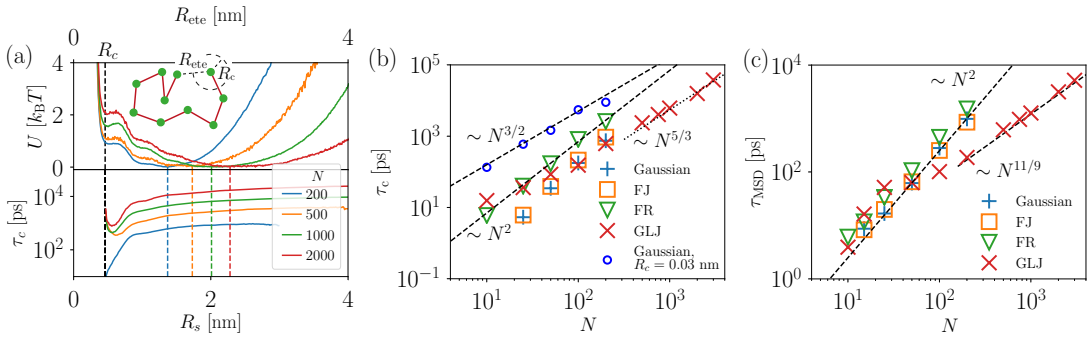

Figure 2.4: (a) Pmf for the end-to-end distance of a GLJ chain as a function of R_{ete} (upper plot) and corresponding cyclization time τ_{c} (lower plot) as a function of R_s. τ_{c} is obtained via averaging over first-passage times obtained from equilibrium simulations. $R_c = 3a_{\mathrm{G}} \approx 0.46$ nm is shown as a black vertical dashed line, each colored vertical dashed line denotes the position of the minimum of the pmf with corresponding color. The inset gives an illustration of the end-to-end distance R_{ete} and the capture radius R_c. (b) Cyclization time as a function of chain length N, together with scaling behaviors indicated by dashed and dotted black lines. Except for the blue empty circles, where $R_c = 0.03$ nm, the cyclization radius $R_c = 3a \approx 0.46$ nm is used for calculating cyclization times from simulations. For R_s, the minimum of the respective pmf is used. (c) Numerically obtained MSD saturation time τ_{MSD} as function of N. The definition of τ_{MSD} is illustrated in Fig. 2.5.

We now consider the cyclization time τ_{c}, defined as the average time for R_{ete} to reach a capture radius R_c for the first time, starting from an end-to-end distance R_s, see the inset in Fig. 2.4 (a) for an illustration. The figure furthermore shows pmfs for the end-to-end distance of the GLJ model, and τ_{c} as a function of R_s for fixed $R_c = 3a_{\mathrm{G}} \approx 0.46$ nm. The capture radius

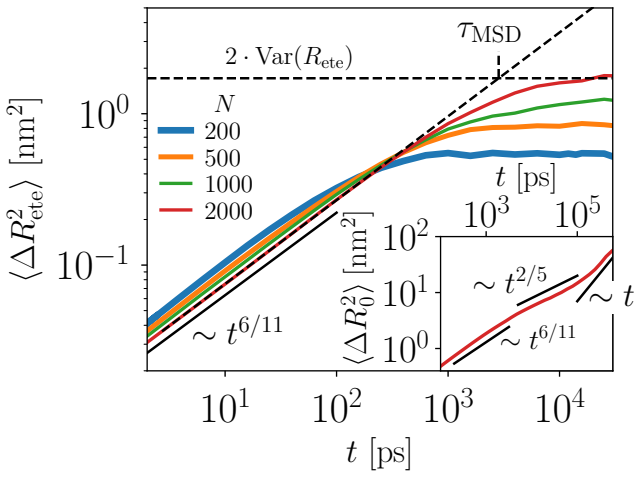

Figure 2.5: The MSD saturation time τ_{MSD} is defined as the time where the intermediate power law in the MSD intersects the limiting value $\lim_{t\to\infty} \langle \Delta R^2_{\mathrm{ete}}(t) \rangle = 2\,\mathrm{Var}(R_{\mathrm{ete}})$. The dashed black lines illustrate this for $N = 2000$. The inset shows the MSD of a terminal monomer, $\langle \Delta R^2_0(t) \rangle = \langle (\vec{R}_0(t) - \vec{R}_0(0))^2 \rangle$, for $N = 2000$. Power-law scaling regimes are denoted by black bars.

R_c is shown as black vertical dashed line, for each N the respective minimum of the pmf is indicated as colored vertical dashed line. For R_s not too close to R_c, τ_{c} is almost independent of the starting radius R_c, so that our definition of τ_{c} should lead to the same scaling behavior as a definition based on an equilibrium average over starting radii.

In Fig. 2.4 (b) we plot the cyclization time τ_{c} as a function of N for all chain models, using for R_s the minimum of the respective pmf. Phantom chains yield the WF scaling, $\tau_{\mathrm{c}} \sim N^2$ [73], which can be obtained by assuming that for R_c not too small, τ_{c} scales like the MSD saturation time τ_{MSD} [105] (see Fig. 2.5 for a graphical definition). If the MSD scales as $\langle \Delta R^2_{\mathrm{ete}}(t) \rangle \sim t^{\beta}$, c.f. Eq. (2.4), and the variance of R_{ete} scales as $\mathrm{Var}(R_{\mathrm{ete}}) \sim N^{2\nu_{\mathrm{st}}}$, c.f. Eq. (2.3), then τ_{MSD} scales as

$$\tau_{\mathrm{MSD}} \sim N^{\lambda} \tag{2.5}$$

with $\lambda = 2\nu_{\mathrm{st}}/\beta = \nu_{\mathrm{st}}(2\nu_{\mathrm{dyn}} + 1)/\nu_{\mathrm{dyn}}$, where for the MSD scaling we use the Flory-theory prediction $\beta = 2\nu_{\mathrm{dyn}}/(2\nu_{\mathrm{dyn}} + 1)$. For $\nu_{\mathrm{st}} = \nu_{\mathrm{dyn}} \equiv \nu$, this reduces to the well-known relation $\tau_{\mathrm{MSD}} \sim N^{2\nu+1}$ [115, 116]. For a Gaussian chain ($\nu = 1/2$) we obtain the WF scaling $\tau_{\mathrm{MSD}} \sim N^2$ [73] observed in Fig. 2.4 (f), so that Eq. (2.5) can be seen as a generalization of the WF scaling.

For small capture radius, $R_c/(\sqrt{N}b) \ll 1$, the cyclization time exceeds the time scale on which the internal degrees of freedom of the chain relax and the SSS scaling should be recovered, which can also be derived from a simple scaling argument. Using Eq. (2.3) and a Gaussian approximation for the distribution of R_{ete}, the probability density ρ for the two terminal residues

of the chain to be within a small capture radius scales as $\rho \sim 1/\langle R_{\rm ete}\rangle^3 \sim N^{-3\nu_{\rm st}}$, so that from transition state theory it follows that

$$\tau_{\rm c} \sim 1/\rho \sim N^{3\nu_{\rm st}}. \tag{2.6}$$

For a Gaussian chain, $\nu_{\rm st} = 1/2$, we recover the SSS scaling $\tau_{\rm c} \sim N^{3/2}$ [74], which is illustrated in Fig. 2.4 (b) for $R_c = 0.03$ nm $\approx a/15$.

For the self-avoiding collapsed chain, neither the classical WF scaling $\tau_{\rm c} \sim N^2$ nor the excluded-volume generalization of the SSS scaling, which follows from Eq. (2.6) with $\nu_{\rm st} = 1/3$ as $\tau_{\rm c} \sim N$, are observed. For long chains, we rather observe the asymptotic scaling $\tau_{\rm c} \sim N^{5/3}$, see Fig. 2.4 (b). This scaling, which is close to the results of a recent extension of the WF theory to include nonbonded interactions [100], follows directly from Eq. (2.5) for a poor solvent, $\nu_{\rm st} = \nu_{\rm dyn} = 1/3$. However, for $\nu_{\rm dyn} = 1/3$ one expects $\beta = 2/5$, in contrast to $\beta = 6/11$ as seen in Figs. 2.3 (d), 2.5. Using Eq. (2.5) with $\nu_{\rm st} = 1/3$, $\nu_{\rm dyn} = 3/5$, we rather obtain $\tau_{\rm MSD} \sim N^{11/9}$, which is consistent with the numerical results for the MSD saturation time shown in Fig. 2.4 (c). The difference $\alpha \neq \lambda$ between the two scalings Eqs. (2.1), (2.5) has an intuitive explanation in terms of the multiscale relaxation processes determining $R_{\rm ete}$. In fact, the MSD for a terminal monomer of a $N = 2000$ GLJ chain, shown in the inset of Fig. 2.5, shows three distinct scaling regimes. While for times $t \lesssim 10^3$ ps, the MSD displays good-solvent scaling $\beta = 6/11$, for intermediate times 10^3 ps $\lesssim t \lesssim 10^5$ ps we observe poor-solvent scaling $\beta = 2/5$, until for longer times diffusive behavior $\beta = 1$ is found. We thus expect poor-solvent scaling to only become relevant on time scales $t \gtrsim 10^3$ ps, and indeed the cyclization times of the GLJ chains shown in Fig. 2.4 (b) are of that order. The corresponding $\tau_{\rm MSD}$ shown in Fig. 2.4 (c) on the other hand is of the order $\tau_{\rm MSD} \lesssim 10^3$ ps, and thus still dominated by good-solvent dynamics, leading to the scaling $\tau_{\rm MSD} \sim N^{11/9}$.

2.5 Conclusions

In summary, from Langevin simulations of various polymer backbone models we calculate memory kernels for the end-to-end distance. We find that the memory kernels for all phantom chains display identical intermediate $\Gamma \sim t^{-1/2}$ scaling regimes, showing that the details of the bond-interactions are not relevant for the large scale end-to-end dynamics. For collapsed self-avoiding chains we find $\Gamma \sim t^{-6/11}$, which can be explained by Flory theory. We calculate the cyclization time $\tau_{\rm c}$ from our simulations, and while for phantom chains we observe the classical WF and SSS scalings, for the GLJ model we find the generalization of the WF scaling for a collapsed chain $\tau_{\rm c} \sim N^{5/3}$. This scaling follows from Flory theory [105], and is different from the scaling of the MSD saturation time $\tau_{\rm MSD}$. The reason for this difference is that the end-to-end relaxation of a collapsed self-avoiding polymer is a complex multiscale process, and the observed $\tau_{\rm MSD}$, $\tau_{\rm c}$ are dominated by different scaling regimes of the internal chain relaxation dynamics. In the present chapter this is expressed as $\nu_{\rm st} \neq \nu_{\rm dyn}$, and the difference between $\nu_{\rm st}$ and $\nu_{\rm dyn}$ is expected to disappear in the asymptotic limit.

Based on Flory theory, we provide the asymptotic scaling behavior for the end-to-end distance memory kernel, the end-to-end distance MSD, and the cyclization time, and show how these

quantities are interrelated. We thus provide a comprehensive picture of the relations between interactions on the molecular scale and non-Markovian effects in the large-scale end-to-end dynamics, which will be helpful in interpreting experimentally observed scaling behavior of intrachain distance dynamics [64, 117].

Chapter 3

Memory-induced acceleration and slowdown of barrier crossing

Bibliographic information: Parts of this chapter and of Appendix B have previously been published. Reprinted with permission from Ref. [ii].

3.1 Introduction

The rate-determining step of chemical and conformational molecular reactions is typically modeled as the crossing over a single barrier in an effective one-dimensional energy landscape [75–85]. Solvent reorganization and intra- or intermolecular degrees of freedom that are orthogonal to the reaction coordinate give rise to non-Markovian or memory effects. Many recipes for choosing a good reaction coordinate, i.e., a coordinate for which memory effects are minimal or even absent, have been suggested [17–26]. The existence of a good coordinate depends on a separation of time scales between orthogonal degrees of freedom and reaction coordinate. Only if orthogonal degrees of freedom relax relatively quickly (corresponding to the adiabatic approximation) is a Markovian description possible [28, 29, 118–121]. In this case, the system kinetics and the transition rate can be characterized by instantaneous friction. In this chapter, we consider the general situation where the memory time can be smaller or larger than the other intrinsic time scales of the system, and address the question how the barrier crossing time depends on the diffusive, the inertial and the memory time scales. This encompasses macromolecular reactions when there is no clear time-scale separation between the reaction coordinate and the environment, but also the case of ill-conditioned reaction coordinates that are coupled to very slow orthogonal degrees of freedom. We are particularly interested in the intermediate scenario when the diffusive, the inertial and the memory time scales are of the same order, which is relevant for dihedral barrier crossing reactions in peptides and alkanes [29], as well as for ion-pairing kinetics [25, 86].

Our general viewpoint follows from the fact that the dynamics of a complex multi-dimensional

system can be described by the one-dimensional generalized Langevin equation (GLE) [14, 15]

$$m\,\ddot{x}(t) = -U'\left(x(t)\right) - \int_0^t \Gamma(t')\dot{x}(t-t')\,\mathrm{d}t' + \eta(t), \tag{3.1}$$

where m is the effective mass of the reaction coordinate x, $U'(x)$ is the derivative of the potential $U(x)$, and $\Gamma(t)$ is the memory kernel that results from integrating out all orthogonal degrees of freedom, which is assumed to couple linearly to the velocity $\dot{x}$. The Gaussian random force $\eta(t)$ has zero mean and in equilibrium obeys the fluctuation-dissipation theorem (FDT)

$$\langle \eta(t)\eta(t')\rangle = k_{\mathrm{B}}T\,\Gamma(t-t'), \tag{3.2}$$

where $k_{\mathrm{B}}T$ is the thermal energy. If the memory kernel $\Gamma(t)$ decays fast compared to the time scale on which $\dot{x}(t)$ varies, one reaches the Markovian limit and Eq. (3.1) reduces to the ordinary memoryless Langevin equation characterized by the friction coefficient $\gamma = \int_0^\infty \Gamma(t)\,\mathrm{d}t$. In this chapter we consider a single-exponential memory kernel [122],

$$\Gamma(t) = \frac{\gamma}{\tau_\Gamma}\exp\left(-\frac{|t|}{\tau_\Gamma}\right), \tag{3.3}$$

that in addition to γ is characterized by the memory time τ_Γ. This specific form of the memory kernel allows us to vary the friction coefficient γ and the memory time τ_Γ independently from each other.

We are interested in the mean first-passage time (MFPT) τ_{MFP} needed to cross a barrier of height U_0 in the quartic double-well potential defined by

$$U(x) = U_0\left[\left(\frac{x}{L}\right)^2 - 1\right]^2, \tag{3.4}$$

see Fig. 3.1 (a) for an illustration. This problem has a long and active history. Early on it was shown that τ_{MFP}, which equals the barrier escape time in certain limits [123], as will be discussed later, is given by the Arrhenius law $\tau_{\mathrm{MFP}} \sim \exp(U_0/(k_{\mathrm{B}}T))$ [124], but the pre-exponential factor remained unclear. The transition state theory (TST) of Eyring [125] predicts τ_{MFP} in the framework of equilibrium statistical mechanics but does not include the friction coupling to the environment. This gap was filled by Kramers, who for Markovian dynamics, i.e., $\tau_\Gamma = 0$, derived τ_{MFP} for asymptotically small as well as high friction γ [50]. He found that for fixed mass m, τ_{MFP} is minimal for intermediate γ. Four decades later the Markovian theory including also the regime for intermediate γ, known as Kramers turnover, was established by Mel'nikov and Meshkov (MM) [126]. For short memory time τ_Γ, Grote and Hynes (GH) derived a self-consistent equation for τ_{MFP} in the medium-to-high friction regime [87], while Carmeli, Nitzan provided a formula for low friction [127]. These limiting cases were bridged by empirical expressions [122, 128, 129]. Finally, Pollak, Grabert and Hänggi (PGH) worked out a theory for τ_{MFP} for arbitrary memory time τ_Γ and arbitrary friction γ [88].

GH and PGH theory can be derived using the equivalence of the GLE Eq. (3.1) to a Hamiltonian system where the one-dimensional coordinate x is coupled to harmonic oscillators [16]. Using a

normal-mode approach, the particle barrier escape time can be related to the dynamic energy partitioning between the modes [88]. In contrast to GH theory, PGH theory accounts for the particle history stemming from unsuccessful barrier crossing attempts [88]. PGH theory has recently been extended to account for low barriers [130,131] and has successfully been compared with Langevin simulations in a restricted parameter range [131, 132]. Excellent accounts of the historical development of rate theories [51,52] and pedagogical introductions to PGH theory [133] exist. However, due to the complex mathematical structure of PGH theory, it is mostly GH theory that is currently used for the interpretation of molecular dynamics (MD) simulations [29,134–138]. The precise limits of accuracy of the various theories and formulations have remained unclear.

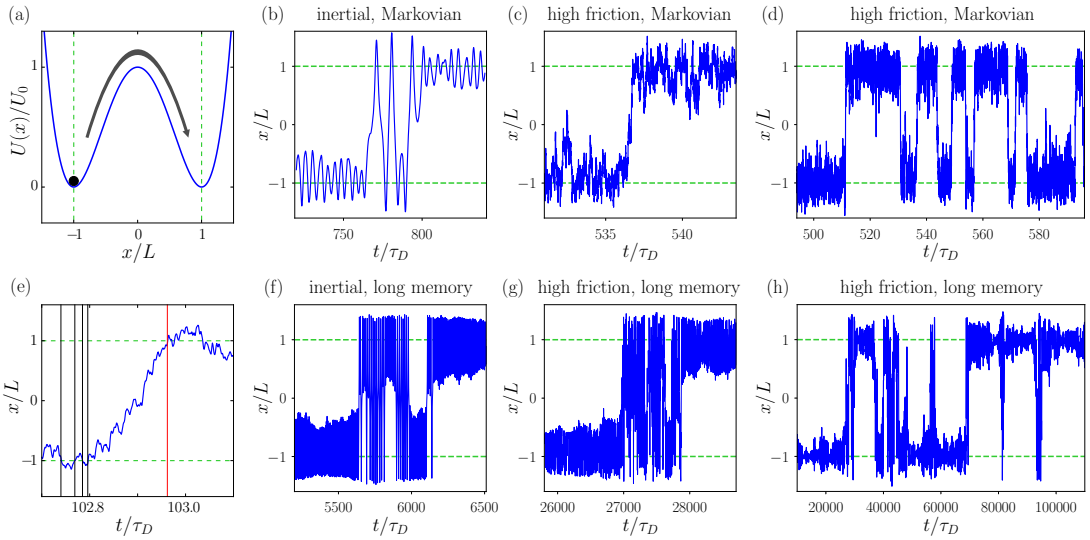

Figure 3.1: (a) Illustration of the barrier crossing of a massive particle in the double-well potential $U(x)$ defined in Eq. (3.4). The mean first-passage time τ_{MFP} is defined as the mean time difference between crossing the minimum at $x = -L$ (left vertical dashed line) and reaching the other minimum at $x = L$ (right vertical dashed line) for the first time. (b), (c), (d), (f), (g), (h) Typical simulation trajectories that display barrier crossing events for barrier height $U_0 = 3\,k_{\mathrm{B}}T$ and (b) low friction $\tau_m/\tau_D = 10$ and short memory $\tau_\Gamma/\tau_D = 0.001$, (c), (d) high friction $\tau_m/\tau_D = 0.001$ and short memory $\tau_\Gamma/\tau_D = 0.001$, (f) low friction $\tau_m/\tau_D = 10$ and long memory $\tau_\Gamma/\tau_D = 10$, (g), (h) high friction $\tau_m/\tau_D = 0.001$ and long memory $\tau_\Gamma/\tau_D = 10$. The horizontal green dashed lines indicate the potential minima. (e) Illustration of how first-passage times (FPTs) are obtained from Langevin simulation. The vertical black lines mark crossings of the trajectory with the minimum $x = -L$ (lower green dashed line), the vertical red line marks the first crossing of the trajectory with the minimum $x = L$ (upper green dashed line). Each vertical black line constitutes a sample for the FPT, obtained via calculating the time difference to the red line, and the MFPT τ_{MFP} is obtained by averaging over all FPTs. For the trajectory shown, the parameters $\tau_m/\tau_D = \tau_\Gamma/\tau_D = 0.001$ and barrier height $U_0 = 3\,k_{\mathrm{B}}T$ are used.

In this chapter we study the barrier crossing by numerical simulation of the GLE Eq. (3.1) in

the complete parameter space that encompasses both low and high friction γ as well as short and long memory times τ_Γ. By comparison of our numerical data with existing theories, we confirm that GH theory has a very limited range of applicability [122], while PGH theory is virtually exact for all parameters. We find a regime at intermediate memory time where memory accelerates barrier crossing. At long memory time the MFPT scales as $\tau_{\rm MFP} \sim \tau_\Gamma^2 e^{U_0/(k_{\rm B}T)}/\gamma$ and thus increases with τ_Γ as a power law [122], which shows that memory can modify the barrier crossing behavior at time scales that are much longer than the memory time itself. By an asymptotic dynamic propagator analysis, the barrier crossing acceleration at intermediate τ_Γ is explained by effective mass reduction due to unsuccessful barrier crossing attempts, the barrier crossing slowdown at large τ_Γ by slow energy diffusion effects. We provide a simple heuristic formula for $\tau_{\rm MFP}$ that holds globally as a function of all parameters, and use it to predict the crossover between the Markovian overdamped and inertial regimes and the two non-Markovian regimes where memory effects are relevant and either accelerate or slow down the barrier crossing rate.

3.2 Setup

To reformulate the problem defined by Eqs. (3.1)-(3.4) with a minimal set of parameters, we introduce the time scales

$$\tau_D = \frac{L^2\gamma}{k_{\rm B}T}, \qquad\qquad \tau_m = \frac{m}{\gamma}, \tag{3.5}$$

where τ_D is the diffusion time linked with the barrier separation L and friction coefficient γ, and τ_m is the inertial time that characterizes viscous dissipation of particle momentum. With this, we can rewrite the GLE Eq. (3.1) as

$$\frac{\tau_m}{\tau_D}\ddot{\tilde{x}}(\tilde{t}\,) = \frac{4U_0}{k_{\rm B}T}\tilde{x}(1-\tilde{x}^2) - \frac{\tau_D}{\tau_\Gamma}\int_0^{\tilde{t}} \exp\left(-\frac{\tau_D}{\tau_\Gamma}\tilde{t}'\right)\dot{\tilde{x}}(\tilde{t}-\tilde{t}')\mathrm{d}\tilde{t}' + \tilde{\eta}(\tilde{t}), \tag{3.6}$$

where $\tilde{t} = t/\tau_D$ is the time in units of τ_D, $\tilde{x}(\tilde{t}) = x(\tau_D\tilde{t})/L$ the dimensionless particle position, and $\tilde{\eta}(\tilde{t}) = L\eta(\tau_D\tilde{t})/(k_{\rm B}T)$ is the dimensionless random force which is characterized by the correlator $\langle\tilde{\eta}(\tilde{t})\tilde{\eta}(\tilde{t}')\rangle = \exp(-\left|\tilde{t}-\tilde{t}'\right|\tau_D/\tau_\Gamma)\tau_D/\tau_\Gamma$. It now transpires that the problem is fully specified by the rescaled potential barrier height $U_0/(k_{\rm B}T)$ and two dimensionless ratios formed by the characteristic time scales τ_m, τ_D, and τ_Γ.

For numerical simulations of Eq. (3.6) we eliminate the memory kernel by coupling to an additional fluctuating degree of freedom [122]. More explicitly, Eq. (3.6) is equivalent to the coupled system of equations

$$\frac{\tau_m}{\tau_D}\ddot{\tilde{x}}(\tilde{t}) = \frac{4U_0}{k_{\rm B}T}\tilde{x}(1-\tilde{x}^2) + R(\tilde{t}), \tag{3.7}$$

$$-\frac{\tau_\Gamma}{\tau_D}\dot{R}(\tilde{t}) = R(\tilde{t}) + \dot{\tilde{x}}(\tilde{t}) + \xi(\tilde{t}), \tag{3.8}$$

where ξ is white noise with $\langle \xi(\tilde{t}) \rangle = 0$ and variance $\langle \xi(\tilde{t}) \xi(\tilde{t}') \rangle = 2\delta(\tilde{t} - \tilde{t}')$. The solution to Eq. (3.8) with initial condition $R(0) = R_0$ is

$$R(\tilde{t}) = R_0 \exp\left(-\frac{\tau_D}{\tau_\Gamma}\tilde{t}\right) - \frac{\tau_D}{\tau_\Gamma}\int_0^{\tilde{t}} \exp\left(-\frac{\tau_D}{\tau_\Gamma}\tilde{t}'\right)\left[\dot{\tilde{x}}(\tilde{t} - \tilde{t}') + \xi(\tilde{t} - \tilde{t}')\right] \mathrm{d}\tilde{t}'. \qquad (3.9)$$

Substituting this into Eq. (3.7) one recovers Eq. (3.6) with an effective random force given by $\tilde{\eta}(\tilde{t}) = R_0 \exp(-\tilde{t}\tau_D/\tau_\Gamma) - \int_0^{\tilde{t}} \exp(-\tilde{t}'\tau_D/\tau_\Gamma)\xi(\tilde{t} - \tilde{t}')\mathrm{d}\tilde{t}'$. The FDT is fulfilled if R_0 is drawn from a Gaussian distribution with zero mean and variance $\langle R_0^2 \rangle = \tau_D/\tau_\Gamma$. In our simulations, we sample the initial position $\tilde{x}(0)$ from the equilibrium distribution within the potential well centered around $\tilde{x} = -1$, using a Gaussian approximation so that $\langle \tilde{x}(0) \rangle = -1$ and $\langle (\tilde{x}(0) + 1)^2 \rangle = k_\mathrm{B}T/(U''(-L)L^2) = k_\mathrm{B}T/(8U_0)$. The initial velocity $\dot{\tilde{x}}(0)$ is sampled from a Gaussian distribution with zero mean and variance $\langle \dot{\tilde{x}}(0)^2 \rangle = k_\mathrm{B}T\tau_D^2/(L^2 m) = \tau_D/\tau_m$, in accordance with the equipartition theorem. Equations (3.7), (3.8) are integrated numerically using a standard fourth-order Runge-Kutta scheme.

Particle trajectories for overdamped and inertial dynamics with short and long memory time, respectively, are shown in Fig. 3.1. In Figs. 3.1 (g) and (h) it is seen that even in the high friction case, for long memory time we obtain bursts of quickly repeating barrier recrossing events, similar to the inertial Markovian case shown in Fig. 3.1 (b); this hints already at a close analogy between the long-memory and the inertial limits, which we will come back to further below [122,127,139]. Most of the results for the MFPT τ_MFP shown in this chapter are extracted from a single long trajectory that in the presence of memory crosses the barrier many times and thus includes the effects of multiple recrossing events. In Appendix B.1 we discuss alternative estimates of the barrier crossing time based on first-passage events as well as based on the relaxation dynamics of the particle probability distribution. To obtain τ_MFP we average over all first-passage times, defined as the difference between the time a trajectory crosses the potential minimum at $x = -L$ and the time it reaches the other minimum at $x = L$ for the first time, as illustrated in Fig. 3.1 (e) (to increase sampling efficiency we also consider the reverse first passage events from $x = L$ to $x = -L$). Each of our trajectories includes at least thousand barrier crossing events.

Rate theories typically yield the escape time τ_esc, which is defined as the inverse of the escape rate at which the fraction of particles initially localized on one side of the barrier decays towards equilibrium. If trajectories cannot recross the barrier once they have reached their target position, corresponding to a single-well scenario which is effected by a suitably positioned absorbing boundary condition, there is no difference between the MFPT τ_MFP obtained in simulations and τ_esc. If one allows for the recrossing of trajectories, corresponding to the double-well scenario, τ_MFP and τ_esc only agree in the high-friction and Markovian limit. For MM and PGH theory formulas for the escape time in the single-well as well as in the double-well scenarios exist [88, 126, 133]. In this chapter we compare our numerically determined MFPTs in the double-well scenario (including barrier recrossing) with the escape times from single-well rate theories (which neglect barrier recrossing).

In Appendix B.1 we present explicit simulation results for double-well MFPTs and single-well escape times and demonstrate that they are numerically identical. This shows that recrossing events (which are absent in single-well rate theories) contribute negligibly to τ_MFP and therefore

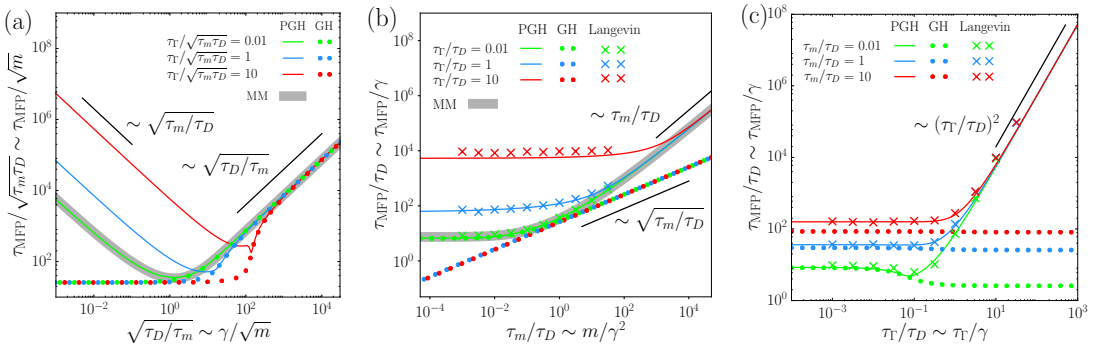

Figure 3.2: Simulation results for the mean first-passage time τ_{MFP} (crosses) are compared with predictions from the memoryless Mel'nikov-Meshkov theory (MM) [126] (thick gray line), Grote-Hynes theory (GH) [87] (dotted lines) and Pollak-Grabert-Hänggi theory (PGH) [88] (solid colored lines) for fixed barrier height $U_0 = 3\ k_{\mathrm{B}}T$. (a) The rescaled MFPT $\tau_{\mathrm{MFP}}/\sqrt{\tau_m\tau_D} \sim \tau_{\mathrm{MFP}}/\sqrt{m}$ plotted as a function of $\sqrt{\tau_D/\tau_m} \sim \gamma/\sqrt{m}$ shows the classical Kramers turnover with a minimum in τ_{MFP} at an intermediate value of $\gamma/\sqrt{m}$ between the low-friction (to the left) and the high-friction regimes (to the right). PGH theory converges to MM theory for short memory, GH theory is only valid for high friction. (b) Plot of $\tau_{\mathrm{MFP}}/\tau_D$ as a function of τ_m/τ_D for several values of the rescaled memory time τ_Γ/τ_D. Simulation results agree accurately with PGH theory. (c) Plot of $\tau_{\mathrm{MFP}}/\tau_D$ as a function of τ_Γ/τ_D for several values of τ_m/τ_D, for long memory the MFPT scales as $\tau_{\mathrm{MFP}} \sim \tau_\Gamma^2$. For intermediate values of the rescaled memory time τ_Γ/τ_D, memory effects in fact accelerate barrier crossing as compared to the Markovian (memoryless) case.

validates our comparison of numerically determined MFPTs in the double-well scenario with escape times from single-well rate theories.

While the results in this chapter are based on the quartic potential defined in Eq. (3.4), in Appendix B.2 we compare results for quartic and cubic potentials and demonstrate that the differences are insignificant if suitable rescaled variables are used.

3.3 Comparison of rate theory results to Langevin simulations

Before we display numerical results, we compare in Fig. 3.2 (a) different theoretical predictions for the rescaled MFPT $\tau_{\mathrm{MFP}}/\sqrt{\tau_D\tau_m}$ for a few different fixed memory times τ_Γ and fixed barrier height $U_0 = 3\,k_{\mathrm{B}}T$ as a function of the rescaled friction coefficient $\sqrt{\tau_D/\tau_m} \sim \gamma/\sqrt{m}$. This is the standard way of illustrating the friction-dependent Kramers turnover [88, 126] since the rescaled MFPT $\tau_{\mathrm{MFP}}/\sqrt{\tau_D\tau_m} \sim \tau_{\mathrm{MFP}}/\sqrt{m}$ does not explicitly depend on γ. For short memory time $\tau_\Gamma/\sqrt{\tau_D\tau_m} = 0.01$ the MM theory (thick gray line) agrees perfectly with the full PGH theory (green line), which is expected since MM theory is valid in the Markovian limit $\tau_\Gamma = 0$. For intermediate and long memory times $\tau_\Gamma/\sqrt{\tau_D\tau_m} = 1, 10$ the PGH theory predicts the MFPT to increase, compared to the Markovian limit $\tau_\Gamma = 0$, in the inertial low-friction limit (to the

left), while for high friction the increase in memory time has no influence on the barrier-crossing time. The power law behavior is independent of the memory time and (for fixed $U_0/k_{\mathrm{B}}T$) given by $\tau_{\mathrm{MFP}} \sim m/\gamma$ for low friction and $\tau_{\mathrm{MFP}} \sim \gamma$ for high friction, the standard Kramers scaling [50, 126]. The minimum in the MFPT at intermediate friction is shifted upwards and to larger friction as the memory time increases. The GH theory (dotted lines) clearly breaks down in the inertial regime, which is expected and has been noted before [129].

To reveal the global scaling structure of the barrier crossing time, it is useful to slightly change the rescaling and to express all times in units of τ_D. Figure 3.2 (b) shows $\tau_{\mathrm{MFP}}/\tau_D$ as a function of τ_m/τ_D for a few fixed values of the rescaled memory time τ_Γ/τ_D, crosses denote simulation results, which quantitatively agree with the PGH theory (solid colored lines). The small deviations between simulations and PGH theory for long memory time are discussed in Appendix B.1 The high-friction regime (to the left) is characterized by a constant rescaled MFPT $\tau_{\mathrm{MFP}}/\tau_D \sim \mathrm{const.}$, and thus $\tau_{\mathrm{MFP}} \sim \gamma$, while the low-friction regime (to the right) displays a linear scaling $\tau_{\mathrm{MFP}}/\tau_D \sim \tau_m/\tau_D$ and thus $\tau_{\mathrm{MFP}} \sim m/\gamma$ (as indicated by a black bar). Notably, in this presentation it is seen that GH theory not only fails in the inertial regime (to the right), it also fails in the diffusive regime for elevated memory times $\tau_\Gamma/\tau_D = 1$, 10, and reduces to the transition-state theory scaling $\tau_{\mathrm{MFP}} \sim \sqrt{m}$ as indicated by a black bar.

In Fig. 3.2 (c) we present the scaling behavior of the MFPT as a function of the memory time τ_Γ, for this we plot $\tau_{\mathrm{MFP}}/\tau_D$ versus τ_Γ/τ_D for a few different fixed values of τ_m/τ_D. Again, simulations (crosses) agree quantitatively with PGH theory (solid lines) for all parameter values, which demonstrates that PGH theory is virtually exact both for long and short memory times as well as for low and high friction. The power-law behavior $\tau_{\mathrm{MFP}} \sim \tau_\Gamma^2$ for long memory times $\tau_\Gamma/\tau_D \gg 1$, which has been demonstrated before [122], is clearly seen both for low and high friction, i.e., for all values of τ_m/τ_D. Note that this power-law scaling is not captured by GH theory (dotted lines), but rather by the Carmeli-Nitzan energy diffusion formula [122, 139]. Unfortunately, the Carmeli-Nitzan theory is rarely used when applying rate theories to MD data. In between the asymptotic short- and long-memory regimes the MFPT shows a minimum, which is most visible for small mass $\tau_m/\tau_D = 0.01$ (shown in green). For the other two friction values shown ($\tau_m/\tau_D = 1$, 10), a minimum cannot be discerned in the log-log representation, but is still present. This is more clearly seen in Fig. 3.3, where we replot the simulation data and the PGH prediction in a semi-logarithmic presentation and obtain quite good agreement between the two. As we will discuss in more detail in Sections 3.4, 3.5, intermediate memory time speeds up barrier crossing, while a long memory time invariably slows down reaction rates and in fact gives rise to a power-law dependence of τ_{MFP} on τ_Γ.

The three different ways of representing the data in Fig. 3.2 bring out the three fundamental scaling properties of the MFPT, namely the scaling $\tau_{\mathrm{MFP}} \sim \gamma$ for high friction, seen in Fig. 3.2 (a) to the right, the scaling $\tau_{\mathrm{MFP}} \sim m/\gamma$ for large mass, seen in Fig. 3.2 (b) to the right, and the scaling $\tau_{\mathrm{MFP}} \sim \tau_\Gamma^2$ for large memory time, seen in Fig. 3.2 (c) to the right.

To present this scaling behavior of the MFPT in one graph, we show the PGH predictions for $\tau_{\mathrm{MFP}}/\tau_D$ in Fig. 3.4 (a) in a triple-logarithmic plot as a function of τ_m/τ_D and τ_Γ/τ_D for fixed $U_0 = 3\ k_{\mathrm{B}}T$. $\tau_{\mathrm{MFP}}/\tau_D$ shows a plateau in the short-memory high-friction regime for $\tau_m/\tau_D \ll 1$ and $\tau_\Gamma/\tau_D \ll 1$. The comparison with Figs. 3.2 (b) and 3.4 (c), where the GH prediction is shown, demonstrates that this is the only regime where GH theory is reliable; this was

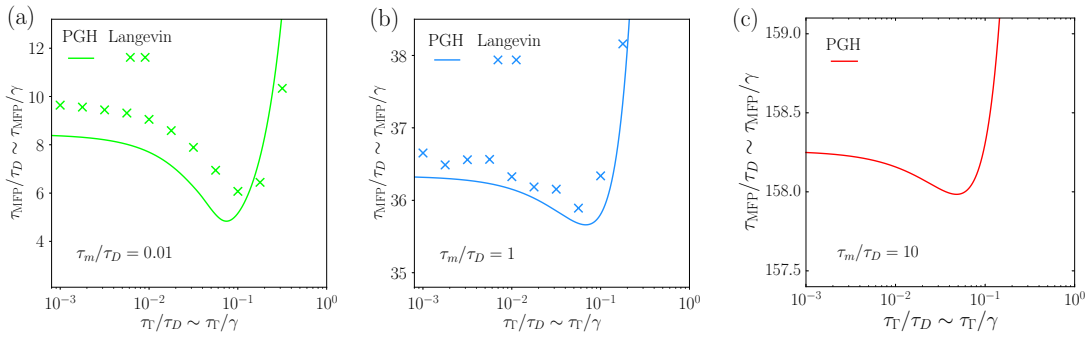

Figure 3.3: Simulation data and PGH predictions for the MFPT $\tau_{\rm MFP}$. Same data as shown in Fig. 3.2 (c), in semi-logarithmic representation, in order to illustrate the minimum in $\tau_{\rm MFP}$ at intermediate memory times τ_Γ. The numerical results shown in subplots (a), (b) illustrate that the speedup in barrier crossing is also observed in the Langevin simulations. For subplot (c), no numerical data is shown because a speedup could not be observed within statistical error.

clear when GH theory was devised [87]. For long memory $\tau_\Gamma/\tau_D \gg \sqrt{\tau_m/\tau_D}$ (for $\tau_m/\tau_D > 1$) or $\tau_\Gamma/\tau_D \gg 1$ (for $\tau_m/\tau_D < 1$) the power law $\tau_{\rm MFP}/\tau_D \sim (\tau_\Gamma/\tau_D)^2$ emerges in PGH theory as shown in Fig. 3.4 (a), while the low-friction short-memory scaling $\tau_{\rm MFP}/\tau_D \sim \tau_m/\tau_D$ is seen for $\tau_m/\tau_D \gg 1$ and $\tau_m/\tau_D \gg (\tau_\Gamma/\tau_D)^2$.

3.4 A simple heuristic formula for the mean first-passage time

Based on the scaling behavior of $\tau_{\rm MFP}$ exhibited in Fig. 3.4 (a), we construct the heuristic crossover function

$$\tau_{\rm MFP}/\tau_D = e^{U_0/(k_{\rm B}T)} \left[\frac{(U_0/(k_{\rm B}T))^{-1}}{1 + 10\, U_0/(k_{\rm B}T)\, \tau_\Gamma/\tau_D} + \left(\frac{U_0}{k_{\rm B}T}\right)^{-1} \frac{\tau_m}{\tau_D} + 2\sqrt{\left(\frac{U_0}{k_{\rm B}T}\right)^{-1} \frac{\tau_m}{\tau_D} + e \left(\frac{\tau_\Gamma}{\tau_D}\right)^2} \right], \tag{3.10}$$

where $e \approx 2.72$ is Euler's number. Equation (3.10) is plotted in Fig. 3.4 (a), (d) as a red thick line at the boundaries and reproduces PGH theory very accurately.

In Fig. 3.5 we compare simulation results for $\tau_{\rm MFP}$ (crosses) with PGH theory (solid lines) and our heuristic formula Eq. (3.10) (dotted lines) as a function of the barrier height U_0. We compare two representative scenarios, one for high friction $\tau_m/\tau_D = 0.1$ and long memory $\tau_\Gamma/\tau_D = 10$ (in green), and the other for low friction $\tau_m/\tau_D = 10$ and short memory $\tau_\Gamma/\tau_D = 0.1$ (in blue). The heuristic formula Eq. (3.10) and PGH theory agree closely with each other and also with the simulation results for not too low barrier heights. It transpires that low-barrier corrections to PGH theory [130–132] are not significant for barrier heights $U_0 \gtrsim 3\, k_{\rm B}T$. In Appendix B.3, we present a quantitative comparison of Eq. (3.10) to PGH theory predictions and find that

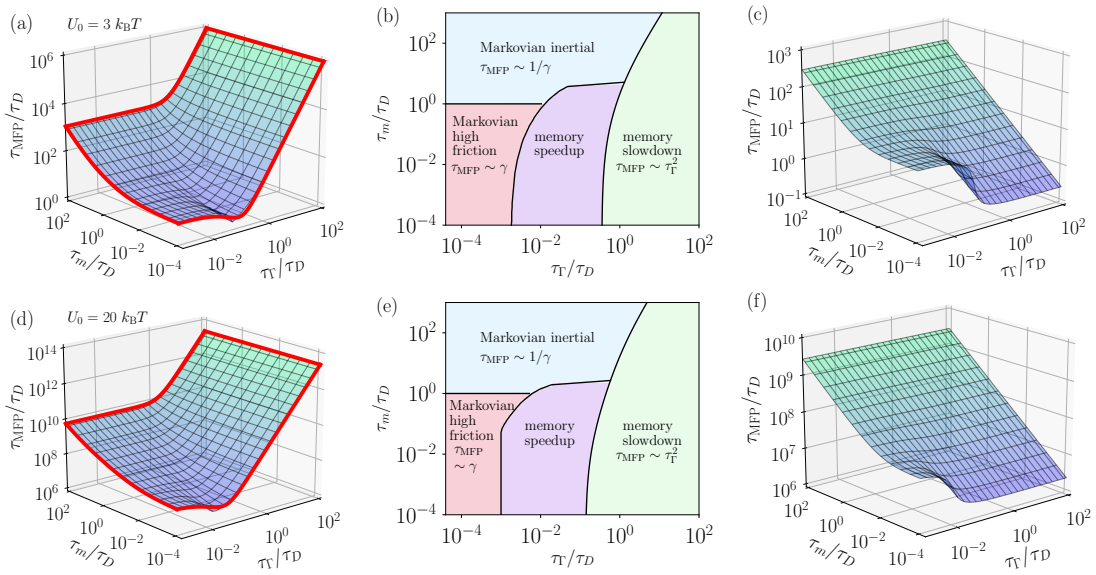

Figure 3.4: (a), (d) Global plots of the mean first-passage time $\tau_{\mathrm{MFP}}/\tau_D$ as function of τ_m/τ_D and τ_Γ/τ_D according to PGH theory for barrier heights (a) $U_0 = 3\,k_\mathrm{B}T$ and (d) $U_0 = 20\,k_\mathrm{B}T$. The red lines at the boundaries represent the heuristic formula Eq. (3.10). (b), (e) Scaling diagrams showing the different scaling regimes for τ_{MFP} for barrier heights (b) $U_0 = 3\,k_\mathrm{B}T$ and (e) $U_0 = 20\,k_\mathrm{B}T$, respectively. The phase boundaries are determined by estimating the crossovers between the different scaling forms Eqs. (3.11), (3.12), (3.13), (3.14) of the heuristic formula Eq. (3.10). The memory speedup regime is defined by the parameter range where the heuristic formula (3.10) yields a value for $\tau_{\mathrm{MFP}}/\tau_D$ less than 95% of the Markovian limit (3.12). (c), (f) Global plots of the mean first-passage time $\tau_{\mathrm{MFP}}/\tau_D$ as function of τ_m/τ_D and τ_Γ/τ_D according to GH theory for barrier heights (c) $U_0 = 3\,k_\mathrm{B}T$ and (f) $U_0 = 20\,k_\mathrm{B}T$, which agrees with the PGH theory only in the short-memory high-friction regime, defined by $\tau_\Gamma/\tau_D \ll 1$ and $\tau_m/\tau_D \ll 1$.

throughout the parameter range considered, in which τ_{MFP} varies over 27 orders of magnitude, relative deviations between our heuristic formula and the full PGH theory are small. Thus, over many orders of magnitude in the parameters τ_m/τ_D, τ_Γ/τ_D, U_0 and especially in the asymptotic regimes, our formula (3.10) is a simple and accurate means for calculating τ_{MFP}.

Equation (3.10) allows us to establish a global scaling diagram. While in the long memory limit $\tau_\Gamma/\tau_D \gg 1$, Eq. (3.10) reduces to

$$\tau_{\mathrm{MFP}}/\tau_D \approx e^{U_0/(k_\mathrm{B}T)+1} \left(\frac{\tau_\Gamma}{\tau_D}\right)^2, \tag{3.11}$$

in the Markovian limit $\tau_\Gamma/\tau_D \ll 1$, one obtains

$$\tau_{\mathrm{MFP}}/\tau_D \approx e^{U_0/(k_\mathrm{B}T)} \left(\frac{U_0}{k_\mathrm{B}T}\right)^{-1} \left[1 + \frac{\tau_m}{\tau_D} + 2 \cdot \sqrt{\frac{U_0}{k_\mathrm{B}T}\frac{\tau_m}{\tau_D}}\right]. \tag{3.12}$$

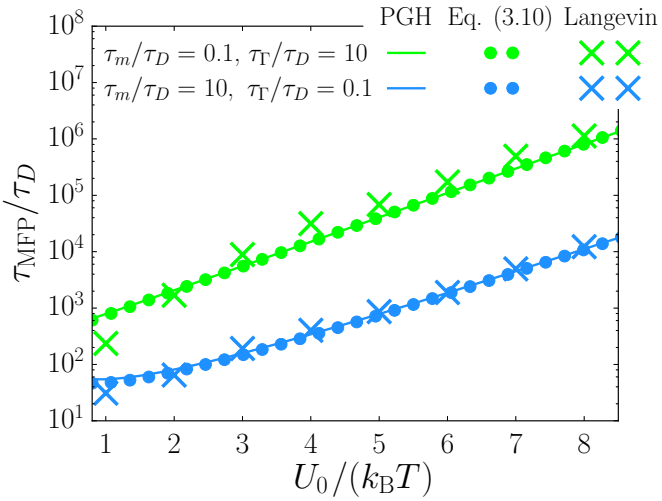

Figure 3.5: Mean first-passage time $\tau_{\mathrm{MFP}}/\tau_D$ as a function of barrier height U_0 for two different parameter combinations of τ_m/τ_D and τ_Γ/τ_D. Crosses denote simulation results, solid lines predictions from PGH theory, and dotted lines represent the heuristic formula Eq. (3.10).

The boundary between the Markovian and the non-Markovian regimes follows by equating Eqs. (3.11) and (3.12), and constitutes the left boundary of the memory slowdown regime, shown in green in the scaling diagram for barrier height $U_0 = 3\,k_{\mathrm{B}}T$ in Fig. 3.4 (b). The asymptotic boundaries are given by $(\tau_\Gamma/\tau_D)^2 = k_{\mathrm{B}}T/U_0$ for high friction $\tau_m/\tau_D \ll 1$ and $(\tau_\Gamma/\tau_D)^2 = k_{\mathrm{B}}T/U_0 \cdot \tau_m/\tau_D$ for low friction $\tau_m/\tau_D \gg 1$. Similarly, the crossover from the high-friction Markovian limit ($\tau_m/\tau_D \ll 1$) of Eq. (3.12),

$$\tau_{\mathrm{MFP}}/\tau_D \approx e^{U_0/(k_{\mathrm{B}}T)} \left(\frac{U_0}{k_{\mathrm{B}}T}\right)^{-1}, \tag{3.13}$$

to the low-friction Markovian limit ($\tau_m/\tau_D \gg 1$)

$$\tau_{\mathrm{MFP}}/\tau_D \approx e^{U_0/(k_{\mathrm{B}}T)} \left(\frac{U_0}{k_{\mathrm{B}}T}\right)^{-1} \frac{\tau_m}{\tau_D}, \tag{3.14}$$

occurs at $\tau_m/\tau_D = 1$, and separates the Markovian low-friction (inertial) from the Markovian high-friction (overdamped) regimes in Fig. 3.4 (b). We define the regime within which memory accelerates barrier crossing as the parameter range where $\tau_{\mathrm{MFP}}/\tau_D$ according to the heuristic formula Eq. (3.10) is smaller by 5% compared to the Markovian limit (3.12). This defines the memory speedup regime, which in Fig. 3.4 (b) is shown in purple and is obtained for intermediate memory time and not too large mass. Note that while a slight speedup is obtained even for large mass τ_m/τ_D, the relative speedup goes to zero as $\tau_m/\tau_D \gg 1$, as is clearly seen in Fig. 3.3.

In Fig. 3.4 (e) we show the scaling diagram for $U_0 = 20\,k_{\mathrm{B}}T$. Compared to the result for $U_0 = 3\,k_{\mathrm{B}}T$ in (b), the boundary of the memory slowdown regime (shown in green) shifts to slightly smaller values of τ_Γ/τ_D. Otherwise, the scaling diagrams for $U_0 = 3\,k_{\mathrm{B}}T$ and

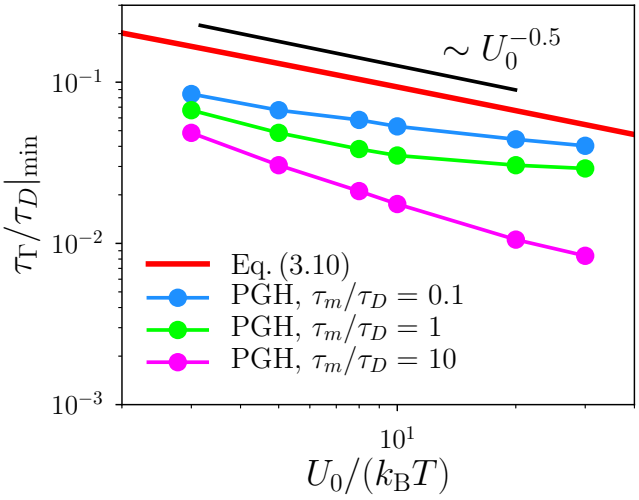

Figure 3.6: Memory time which minimizes $\tau_{\mathrm{MFP}}/\tau_D$ for given τ_m/τ_D, as predicted by Eq. (3.10) (red solid line) and PGH theory (data points), as function of U_0. Note that according to Eq. (3.10), $\tau_\Gamma/\tau_D|_{\min}$ does not depend on τ_m/τ_D. The power law $\tau_\Gamma/\tau_D|_{\min} \sim 1/\sqrt{U_0}$, denoted by a black bar, approximates well the result from Eq. (3.10).

$U_0 = 20\,k_\mathrm{B}T$ are very similar, which shows that the general scaling structure of the MFPT is robust with respect to variations of the barrier energy U_0. The comparison of PGH theory and our heuristic formula for $U_0 = 20\,k_\mathrm{B}T$ in Fig. 3.4 (d) shows that the heuristic formula also works well for high barriers.

In Fig. 3.6 we show the memory time $\tau_\Gamma/\tau_D|_{\min}$ at which, for given inertial time scale τ_m/τ_D and barrier height U_0, the MFPT $\tau_{\mathrm{MFP}}/\tau_D$ is minimal. We compare results from the heuristic formula Eq. (3.10) with predictions of PGH theory. According to Eq. (3.10), $\tau_\Gamma/\tau_D|_{\min}$ is independent of τ_m/τ_D and decays as a power law $\tau_\Gamma/\tau_D|_{\min} \sim 1/\sqrt{U_0}$ with U_0. While $\tau_\Gamma/\tau_D|_{\min}$ as predicted by PGH theory does slightly depend on τ_m/τ_D and is smaller than the value obtained from the heuristic formula, the general agreement is quite good.

3.5 Propagator analysis

The scaling $\tau_{\mathrm{MFP}} \sim \tau_\Gamma^2$ for long memory time has been observed before and can be derived from the energy diffusion limit of the barrier crossing rate [122]. Alternatively, it can be obtained by an asymptotic analysis of the propagator $C(t) \equiv \langle x(t)x(0)\rangle$ that describes the particle motion within the potential well. This approach has the advantage that one can also derive the barrier-crossing speedup at intermediate memory time in a straightforward fashion.

We consider the GLE (3.1) in a harmonic potential $U(x) \simeq Kx^2/2$ and for times $t \gg \tau_\Gamma$, so that we can replace the upper limit in the memory integral by infinity. Fourier transforming

Eq. (3.1) and solving for $\tilde{x}(\omega)$ yields

$$\tilde{x}(\omega) = \frac{\tilde{\eta}(\omega)}{K - m\omega^2 + i\omega\tilde{\Gamma}_+(\omega)} \equiv \tilde{Q}(\omega)\tilde{\eta}(\omega), \tag{3.15}$$

where the half-sided Fourier transform $\tilde{\Gamma}_+$ of the memory kernel $\Gamma(t)$ is given by

$$\tilde{\Gamma}_+(\omega) = \int_0^\infty \mathrm{d}t\, e^{-i\omega t}\Gamma(t) = \frac{\gamma}{1 + i\omega\tau_\Gamma}, \tag{3.16}$$

while the Fourier transform of the full memory kernel is

$$\tilde{\Gamma}(\omega) = \tilde{\Gamma}_+(\omega) + \tilde{\Gamma}_+(-\omega) = \frac{2\gamma}{1 + \omega^2\tau_\Gamma^2}. \tag{3.17}$$

Using Eq. (3.15), we calculate $\langle x(t)x(0)\rangle$ as

$$C(t) \equiv \langle x(t)x(0)\rangle = \int \frac{\mathrm{d}\omega}{2\pi} e^{i\omega t} \int \frac{\mathrm{d}\omega'}{2\pi}\, \langle \tilde{x}(\omega)\tilde{x}(\omega')\rangle \tag{3.18}$$

$$= \int \frac{\mathrm{d}\omega}{2\pi} e^{i\omega t} \int \frac{\mathrm{d}\omega'}{2\pi}\, \tilde{Q}(\omega)\tilde{Q}(\omega')\langle\tilde{\eta}(\omega)\tilde{\eta}(\omega')\rangle \tag{3.19}$$

$$= k_\mathrm{B}T \int \frac{\mathrm{d}\omega}{2\pi} e^{i\omega t} \int \frac{\mathrm{d}\omega'}{2\pi}\, 2\pi\delta(\omega + \omega')\tilde{\Gamma}(\omega)\tilde{Q}(\omega)\tilde{Q}(\omega') \tag{3.20}$$

$$= k_\mathrm{B}T \int \frac{\mathrm{d}\omega}{2\pi} e^{i\omega t}\, \tilde{\Gamma}(\omega)\tilde{Q}(\omega)\tilde{Q}(-\omega), \tag{3.21}$$

where we used that the Fourier transform of the generalized FDT Eq. (3.2) is $\langle\tilde{\eta}(\omega)\tilde{\eta}(\omega')\rangle = k_\mathrm{B}T\, 2\pi\delta(\omega + \omega')\, \tilde{\Gamma}(\omega)$. Thus the propagator, i.e., the Fourier transform of $C(t)$, is finally given by

$$\tilde{C}(\omega)/(k_\mathrm{B}T) = \tilde{\Gamma}(\omega)\tilde{Q}(\omega)\tilde{Q}(-\omega) \tag{3.22}$$

$$= \frac{2\gamma}{1 + \omega^2\tau_\Gamma^2} \frac{1}{K - m\omega^2 + i\omega\tilde{\Gamma}_+(\omega)} \frac{1}{K - m\omega^2 - i\omega\tilde{\Gamma}_+(-\omega)} \tag{3.23}$$

$$= 2\gamma \left[(K - m\omega^2)^2 + \omega^2\gamma^2 + 2\omega^2\gamma\tau_\Gamma(K - m\omega^2) + \omega^2\tau_\Gamma^2(K - m\omega^2)^2\right]^{-1}. \tag{3.24}$$

For vanishing memory time, $\tau_\Gamma = 0$, we obtain the standard damped harmonic oscillator result

$$\tilde{C}(\omega)/(k_\mathrm{B}T) = 2\gamma \left[(K - m\omega^2)^2 + \omega^2\gamma^2\right]^{-1}. \tag{3.25}$$

We now investigate the properties of Eq. (3.24) for small and large memory times τ_Γ.

For τ_Γ small we rewrite Eq. (3.24) as

$$\tilde{C}(\omega)/(k_\mathrm{B}T) = 2\gamma \left[(K - \omega^2 m(1 - \tau_\Gamma/\tau_m))^2 + \omega^2\gamma^2 + \omega^2\tau_\Gamma^2(K - m\omega^2 - \omega^2\gamma^2\right]^{-1} \tag{3.26}$$

$$= 2\gamma \left[(K - \omega^2 m(1 - \tau_\Gamma/\tau_m))^2 + \omega^2\gamma^2 + \mathcal{O}(\omega^2\tau_\Gamma^2)\right]^{-1}. \tag{3.27}$$

Neglecting the $\mathcal{O}(\omega^2\tau_\Gamma^2)$ terms in Eq. (3.27), we see that Eq. (3.27) reduces to the memoryless propagator Eq. (3.25) with an effective mass

$$m_{\text{eff}} = m(1 - \tau_\Gamma/\tau_m), \tag{3.28}$$

which is smaller than the bare mass m. Thus, short but finite memory effectively leads to a reduction of the mass, which according to high-friction Kramers theory is associated with a speedup of the dynamics. This is indeed what we observe in both the Langevin simulations and the PGH theory predictions, see Figs. 3.2 (c) and 3.3. Note that Eq. (3.28) was derived from the linearized GLE. To arrive at Eq. (3.28) in the general nonlinear case, one can alternatively perform a gradient expansion of the memory integral in the GLE Eq. (3.1). If the memory kernel Γ decays quickly compared to the time scale on which $\dot{x}$ varies, Taylor expansion of $\dot{x}(t-t')$ around t and using the exponential memory kernel Eq. (3.3) yields

$$\int_0^\infty \Gamma(t')\dot{x}(t-t')\,\mathrm{d}t' \approx \int_0^\infty \Gamma(t')\,\mathrm{d}t'\,\dot{x}(t) - \int_0^\infty t'\Gamma(t')\,\mathrm{d}t'\,\ddot{x}(t) \tag{3.29}$$

$$= \gamma\dot{x}(t) - m\frac{\tau_\Gamma}{\tau_m}\ddot{x}(t). \tag{3.30}$$

Replacing the memory integral in Eq. (3.1) by this expression, one obtains the ordinary Langevin equation with friction coefficient γ and the effective mass m_{eff} given by Eq. (3.28), in agreement with our propagator analysis.

For large τ_Γ, we rewrite Eq. (3.24) as

$$\tilde{C}(\omega)/(k_{\mathrm{B}}T) = 2\frac{\gamma}{\omega^2\tau_\Gamma^2}\left[(K-m\omega^2)^2 + \frac{1}{\omega^2\tau_\Gamma^2}\left((K-m\omega^2) + \omega^2\gamma^2 + 2\omega^2\gamma\tau_\Gamma(K-m\omega^2)\right)\right]^{-1} \tag{3.31}$$

$$= 2\frac{\gamma}{\omega^2\tau_\Gamma^2}\left[(K-m\omega^2)^2 + \mathcal{O}((\omega\tau_\Gamma)^{-1})\right]^{-1} \tag{3.32}$$

$$= 2\gamma_{\text{eff}}\left[(K-m\omega^2)^2 + \mathcal{O}((\omega\tau_\Gamma)^{-1})\right]^{-1}. \tag{3.33}$$

To leading order in τ_Γ^{-1}, this is the low friction limit $\tau_m\omega \gg 1$ of the memoryless propagator Eq. (3.25) with a frequency-dependent effective friction coefficient $\gamma_{\text{eff}} = \gamma/(\omega^2\tau_\Gamma^2)$. Indeed, even though the friction coefficient is very high, the long-memory trajectories shown in Fig. 3.1 (g), (h) look inertial, in the sense that once a barrier crossing event takes place, there is a cascade of recrossings, reminiscent of low-friction barrier crossing, as shown in Fig. 3.1 (b). For low effective friction, the propagator Eq. (3.25) is dominated by the pole at $\omega_*^2 = K/m$, so that the effective friction asymptotically equals $\gamma_{\text{eff}} = \gamma/(\omega_*^2\tau_\Gamma^2) = \gamma m/(K\tau_\Gamma^2)$. Using the Kramers scaling for τ_{MFP} for low friction and replacing γ by the effective friction coefficient γ_{eff}, we finally obtain

$$\tau_{\text{MFP}} \sim e^{U_0/(k_{\mathrm{B}}T)} m\,k_{\mathrm{B}}T/(\gamma_{\text{eff}}U_0) = e^{U_0/(k_{\mathrm{B}}T)}\tau_\Gamma^2 K k_{\mathrm{B}}T/(\gamma U_0) \tag{3.34}$$

$$= 8e^{U_0/(k_{\mathrm{B}}T)}\tau_\Gamma^2 k_{\mathrm{B}}T/(\gamma L^2) \sim e^{U_0/(k_{\mathrm{B}}T)}\tau_\Gamma^2/\tau_D, \tag{3.35}$$

where we used $K = 8U_0/L^2$, appropriate for the quartic potential Eq. (3.4). This is precisely the scaling behavior obtained for large memory times τ_Γ both for large and small bare friction γ in Fig. 3.2 (c), and which is also recovered by the heuristic formula Eq. (3.10).

This scaling result is noteworthy for several reasons. First, it demonstrates that the non-Markovian limit, corresponding to memory times τ_Γ much larger than the diffusion and inertial times τ_D and τ_m, is characterized by a very simple and universal scaling of the barrier crossing time τ_{MFP}. Secondly, orthogonal degrees of freedom, which are at the core of non-Markovian effects [14, 15], modify τ_{MFP} in a crucial but intuitive manner. To see this, we assume that non-Markovian effects are caused by a single orthogonal degree of freedom subject to an energy barrier of height W_0, so that the memory time can be written as $\tau_\Gamma \sim \gamma e^{W_0/(k_\mathrm{B}T)}$ to leading order. Combining this with the scaling $\tau_{\mathrm{MFP}} \sim e^{U_0/(k_\mathrm{B}T)}\tau_\Gamma^2/\gamma$, we obtain $\tau_{\mathrm{MFP}} \sim \gamma e^{(U_0+2W_0)/(k_\mathrm{B}T)}$. This shows that in the long-memory limit, the orthogonal barrier height W_0 is even more relevant than the barrier height U_0 associated with the reaction coordinate, which presumably reflects multiple recrossing events over the orthogonal barrier.

A simple picture allows to rationalize the observed acceleration of the barrier crossing at intermediate memory time in an intuitive manner. Consider a particle that has just returned from an unsuccessful barrier-crossing attempt and is located at the potential minimum. For a memory time that is of the order of the time it took the particle to move down from the barrier, the net effect of friction will be to accelerate the particle up the barrier again, so this is a simple way of understanding the effective mass reduction expressed by Eq. (3.28). For much longer memory times the memory kernel will average over many previous barrier crossing attempts, which cancel out on average and thus lead to a reduced effective friction. This explains why the particle trajectories in Fig. 3.1 (g) and (h) look inertial and why the kernel derived in the long-memory limit, Eq. (3.33), has a similar pole structure as the memoryless kernel Eq. (3.25) for vanishing friction.

3.6 Conclusions

In summary, we compare several rate theories (MM, GH, PGH) for the barrier-crossing time with explicit Langevin simulation results, and determine the range of applicability of the various theoretical predictions. We confirm that the commonly used GH theory is only applicable in the double limit of short memory and high-friction (overdamped) dynamics, and that PGH theory is very accurate in predicting MFPTs in the entire parameter space. From asymptotic analysis of the propagator, we derive that there is a regime at intermediate memory times where memory leads to a decrease of the MFPT τ_{MFP}, and a distinct regime at long memory times where memory effects slow down barrier crossing and the asymptotic power law $\tau_{\mathrm{MFP}} \sim \tau_\Gamma^2$ is obtained. As an easy-to-implement alternative to the PGH formula, we provide the heuristic formula (3.10), show that it accurately predicts the MFPT over many orders of magnitude in the parameters τ_m/τ_D, τ_Γ/τ_D, U_0, and use it to establish the scaling diagram featuring the Markovian high-friction and inertial regimes as well as the non-Markovian long memory regime. In particular, we identify a regime at intermediate memory times where finite memory reduces the barrier crossing time.

The heuristic formula we provide is a convenient tool for the calculation of rates from known

memory times, or, conversely, for the estimation of memory times from barrier crossing times measured in MD simulations or experiments. Based on the heuristic formula we estimate the memory time which maximizes the barrier crossing rate, this might be useful for the design of systems with optimal barrier flux by tuning memory time and barrier height. More generally, our analysis allows to quickly determine whether memory effects are relevant or not, as summarized in Figs. 3.4 (b) and (e). The location in the scaling diagrams where the memory time, the diffusion time and the inertial time are all of the same order, $\tau_\Gamma/\tau_D \sim \tau_m/\tau_D \sim 1$, is experimentally relevant for dihedral barrier crossing phenomena [29, 140] and ion-pair kinetics in water [25, 86], since in both cases the diffusion time, the memory time, and the inertial time are all of the order of around one picosecond. The scaling diagrams Figs. 3.4 (b) and (e) show that in this area the three scaling regimes corresponding to memory slowdown, memory speedup and the inertial regimes touch. Since in this regime neither the Markovian models nor the GH theory, which are easy to handle, are reliable, our heuristic formula will be useful as a convenient and accurate tool to estimate reaction rates for such systems.

Chapter 4

Barrier crossing in the presence of bi-exponential memory is dominated by the shorter memory time

Bibliographic information: The content of this chapter and of Appendix C is in preparation to be submitted to a peer-reviewed journal (Ref. [iii]).

4.1 Introduction

Conformational transitions are usually modeled as barrier crossing in a one-dimensional energy landscape. The corresponding reaction coordinate is coupled to both intra- and extramolecular degrees of freedom, and only if there is separation of time scales between reaction coordinate and orthogonal degrees of freedom is the dynamics of the reaction coordinate Markovian. However, the time scales of the dynamics of microscopic systems are typically comparable to those of their environment, and indeed non-Markovian dynamics, i.e., memory effects, have been observed in ion-pair kinetics [25, 86], conformational transitions in small molecules [28, 29], and protein folding [62, 98, 102, 141].

Memory effects can have substantial influence on barrier crossing times [88, 122, 127, 129, 132]. In Chapter 3 we studied barrier crossing for the case where the orthogonal degrees of freedom are characterized by a single time scale and a single long-time friction coefficient, and memory effects are described by an exponential memory kernel. Due to its simplicity, this is the most-studied scenario for non-Markovian barrier crossing in the literature [88, 122, 131, 132]. However, in many physical reaction coordinates non-exponential memory effects have been found [29, 86, 142–145], and only few systematic numerical studies of barrier crossing that go beyond the single-exponential case exist [146]. As for theoretical results, the popular Grote-Hynes (GH) theory [87] for barrier crossing in the presence of memory is easily applied to arbitrary memory kernels, but in Chapter 3 we saw that even in the single-exponential case its predictions only agree with numerical results in the double limit of high friction and short memory times. On the other hand, for the rate theory developed by Pollak, Grabert and Hänggi (PGH) [88], which in Chapter 3 is found to accurately describe the numerical data throughout the parameter

range studied, the only solution readily available in the literature is that for single-exponential memory [88].

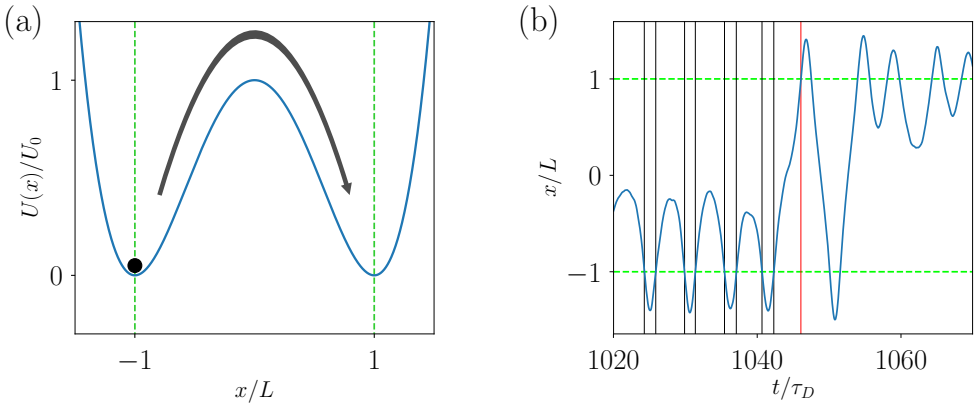

Figure 4.1: (a) Illustration of barrier crossing of a massive particle in the double-well potential $U(x)$ given by Eq. (4.3). The barrier crossing time τ_{MFP} is defined as the mean time between crossing the minimum at $x = -L$ (left green vertical dashed line) and reaching the other minimum at $x = L$ (right green vertical dashed line) for the first time. (b) Illustration of how first-passage times (FPTs) are obtained from Langevin simulation. Vertical black lines mark crossings of the trajectory with the minimum $x = -L$ (lower green dashed line), the vertical red line marks the first crossing of the trajectory with the minimum $x = L$ (upper green dashed line). Each vertical black line constitutes a sample for the FPT, obtained via calculating the time difference to the red line, and the MFPT τ_{MFP} is obtained by averaging over all FPTs. For the trajectory shown, the parameters $\tau_m/\tau_D = 10$, $\tau_1/\tau_D = \tau_2/\tau_D = 0.01$ and barrier height $U_0 = 3\,k_{\mathrm{B}}T$ are used. Both the potential and the algorithm used for calculating FPTs in this chapter are the same as in Chapter 3.

In the present chapter, we consider the situation where the orthogonal degrees of freedom are characterized by two time scales. We consider the one-dimensional generalized Langevin equation (GLE)

$$m\,\ddot{x}(t) = -\int_0^t \Gamma(t-t')\dot{x}(t')\,\mathrm{d}t' - U'(x(t)) + \eta(t), \tag{4.1}$$

where m is the effective mass of the reaction coordinate x, $\Gamma(t)$ is a memory kernel, U' denotes the derivative of a potential $U(x)$, and η is a random force. The random force η is Gaussian with zero mean, $\langle\eta(t)\rangle = 0$, and obeys the generalized fluctuation-dissipation theorem (FDT)

$$\langle\eta(t)\eta(t')\rangle = k_{\mathrm{B}}T\,\Gamma(|t-t'|). \tag{4.2}$$

As in Chapter 3, we consider a double-well potential

$$U(x) = U_0\left[\left(\frac{x}{L}\right)^2 - 1\right]^2, \tag{4.3}$$

illustrated in Fig. 4.1. We consider a bi-exponential memory kernel

$$\Gamma(t) = \sum_{i=1}^{2} \frac{\gamma}{2\tau_i} \exp\left(-|t|/\tau_i\right) = \frac{\gamma}{2\tau_1} \exp\left(-|t|/\tau_1\right) + \frac{\gamma}{2\tau_2} \exp\left(-|t|/\tau_2\right), \tag{4.4}$$

where τ_1, τ_2 are two memory time scales and $\gamma = \int_0^\infty \mathrm{d}t\, \Gamma(t)$ is the long-time friction coefficient. We here consider the special case where each of the two exponentials contributes equally to the long-time diffusion coefficient γ,

$$\int_0^\infty \mathrm{d}t \frac{\gamma}{2\tau_1} e^{-t/\tau_1} = \int_0^\infty \mathrm{d}t \frac{\gamma}{2\tau_2} e^{-t/\tau_2} = \gamma/2. \tag{4.5}$$

If both memory times are equal, i.e., if $\tau_\Gamma \equiv \tau_1 = \tau_2$, then Eq. (4.4) reduces to the single-exponential memory kernel considered in Chapter 3.

We study barrier crossing by numerical simulations of the GLE Eq. (4.1), (4.4), in the complete parameter space which includes both low- and high-friction γ, as well as short and long memory times τ_1, τ_2. For equal memory times $\tau_\Gamma \equiv \tau_1 = \tau_2$, we recover the single-exponential results discussed in Chapter 3, which we describe in the present chapter using a slight modification of the single-exponential heuristic formula Eq. (3.10). If the two memory times τ_1, τ_2 are very different, the corresponding trajectories resemble those of single-exponential dynamics, with the single-exponential memory time given by the shorter of the two memory times τ_1, τ_2. For long memory times, we analytically show that indeed the shorter memory time dominates the propagator of the GLE. We define an effective single-exponential friction coefficient γ_{eff} and an effective single-exponential memory time τ_{eff}, which interpolate between the symmetric case $\tau_\Gamma \equiv \tau_1 = \tau_2$ and the asymmetric case where $\tau_i \ll \tau_j$. Used in conjunction with the effective single-exponential parameters γ_{eff}, τ_{eff}, the single-exponential heuristic formula for barrier-crossing times describes our numerical data globally. Our results thus show that in the asymmetric case, the shorter memory time determines the barrier-crossing time.

4.2 Setup

To formulate the GLE in dimensionless form, we introduce the time scales

$$\tau_m = \frac{m}{\gamma}, \qquad \tau_D = \frac{L^2\gamma}{k_{\mathrm{B}}T}. \tag{4.6}$$

Here, τ_m is the inertial time which characterizes viscous dissipation of particle momentum, and τ_D is the diffusion time linked with the barrier separation L and long-time friction coefficient γ.

With these definitions, Eq. (4.1) can be rewritten as

$$\frac{\tau_m}{\tau_D} \ddot{\tilde{x}}(\tilde{t}) = -\frac{1}{2} \sum_{i=1}^{2} \frac{\tau_D}{\tau_i} \int_0^{\tilde{t}} \mathrm{d}\tilde{t}' \exp\left[-\frac{\tau_D}{\tau_i}\left(\tilde{t} - \tilde{t}'\right)\right] \dot{\tilde{x}}(\tilde{t}') + \tilde{F}\left(\tilde{x}(\tilde{t})\right) + \tilde{\eta}(\tilde{t}), \tag{4.7}$$

where $\tilde{t} = t/\tau_D$ is the time in units of τ_D, $\tilde{F}(\tilde{x}) = -L\,U'(L\tilde{x})/k_\mathrm{B}T$ is the dimensionless deterministic force, and $\tilde{\eta}(\tilde{t}) = L\eta(\tau_D\tilde{t})/k_\mathrm{B}T$ is the dimensionless random force. The autocorrelation function of $\tilde{\eta}$ follows from Eq. (4.2) as

$$\left\langle \tilde{\eta}(\tilde{t})\tilde{\eta}(\tilde{t}')\right\rangle = \frac{1}{2}\sum_{i=1}^{2}\frac{\tau_D}{\tau_i}\exp\left(-\frac{\tau_D}{\tau_i}|\tilde{t}-\tilde{t}'|\right). \tag{4.8}$$

To simulate the GLE Eq. (4.7) numerically, we eliminate the memory kernel by introducing two auxiliary degrees of freedom R_1, R_2. More explicitly, Eqs. (4.7), (4.8) are equivalent to the coupled system of equations

$$\frac{\tau_m}{\tau_D}\ddot{\tilde{x}}(\tilde{t}) = \tilde{F}\left(\tilde{x}(\tilde{t})\right) + R_1(\tilde{t}) + R_2(\tilde{t}), \tag{4.9}$$

$$-\frac{\tau_1}{\tau_D}\dot{R}_1(\tilde{t}) = R_1(\tilde{t}) + \frac{1}{2}\dot{\tilde{x}}(\tilde{t}) + \frac{1}{\sqrt{2}}\xi_1(\tilde{t}), \tag{4.10}$$

$$-\frac{\tau_2}{\tau_D}\dot{R}_2(\tilde{t}) = R_2(\tilde{t}) + \frac{1}{2}\dot{\tilde{x}}(\tilde{t}) + \frac{1}{\sqrt{2}}\xi_2(\tilde{t}), \tag{4.11}$$

where ξ_i are Gaussian stochastic processes with zero mean and autocorrelation given by $\langle\xi_i(t)\xi_j(t')\rangle = 2\delta_{i,j}\delta(t-t')$. As we show in Appendix C.2, solving Eqs. (4.10), (4.11) for $R_i(t)$ and substituting the result into Eq. (4.9), one obtains the GLE Eq. (4.7), with an effective random force $\tilde{\eta}_R(\tilde{t}) = \sum_{i=1}^{2}[R_i(0)\exp(-\tau_D/\tau_i\tilde{t}\,) - \tau_D/(\tau_i\sqrt{2})\int_0^{\tilde{t}}\mathrm{d}\tilde{t}'\exp(-\tau_D/\tau_i(\tilde{t}-\tilde{t}'))\xi(\tilde{t}')]$. If the initial conditions $R_i(0)$ are Gaussian random variables with zero mean and variance $\langle R_i(0)R_j(0)\rangle = \delta_{i,j}\tau_D/(2\tau_i)$, then $\tilde{\eta}_R$ fulfills the FDT Eq. (4.8), so that $\tilde{\eta}_R \equiv \tilde{\eta}$.

Using a fourth-order Runge-Kutta integration scheme, we simulate Eqs. (4.9)-(4.11) for the parameter range $\tau_m/\tau_D \in [10^{-3}, 10^3]$, $\tau_1/\tau_D, \tau_2/\tau_D \in [10^{-3}, 10^2]$. Initial positions are sampled from a Gaussian approximation of the probability distribution in the well $\tilde{x} = -1$, i.e., $\langle\tilde{x}(0)\rangle = -1$, $\langle(\tilde{x}(0)+1)^2\rangle = k_\mathrm{B}T/(U''(-L)L^2) = k_\mathrm{B}T/(8U_0)$. Initial velocities are sampled from a Gaussian distribution with zero mean and variance $\langle\dot{\tilde{x}}(0)\rangle = \tau_D/\tau_m$, in accordance with the equipartition theorem. Throughout, we use the barrier height $U_0 = 3\,k_\mathrm{B}T$.

From our simulations we obtain distributions for the first-passage time (FPT) τ_FP by collecting samples for the time needed from crossing the minimum at $x = -L$ to reaching the minimum at $x = L$ for the first time, see Fig. 4.1 (b) for an illustration. Since the potential is symmetric, we also collect FPT samples from crossings starting at $x = L$ and reaching $x = -L$ for the first time. The mean first-passage time (MFPT) τ_MFP is subsequently calculated by averaging over all samples, and we showed in Chapter 3 that this yields the same MFPT as is obtained when using absorbing boundary conditions to eliminate recrossing, or using an absorbing boundary condition and fitting an exponential decay to the time-dependent probability for a particle to remain in the well $x < 0$.

In Fig. 4.2 we plot simulation trajectories showcasing typical barrier crossing events. In Figs. 4.2 (a), (b), (d), (e) the two memory times are equal, $\tau_\Gamma \equiv \tau_1 = \tau_2$, so that in fact single-exponential memory is studied. In the energy diffusion limit, which is attained if $\tau_m/\tau_D \gg 1$ or $\tau_\Gamma/\tau_D \gg 1$, we recover bursts of recrossings similar to our results in Chapter 3. Recrossing begins when the particle has acquired enough energy to cross the barrier; it subsequently oscillates back

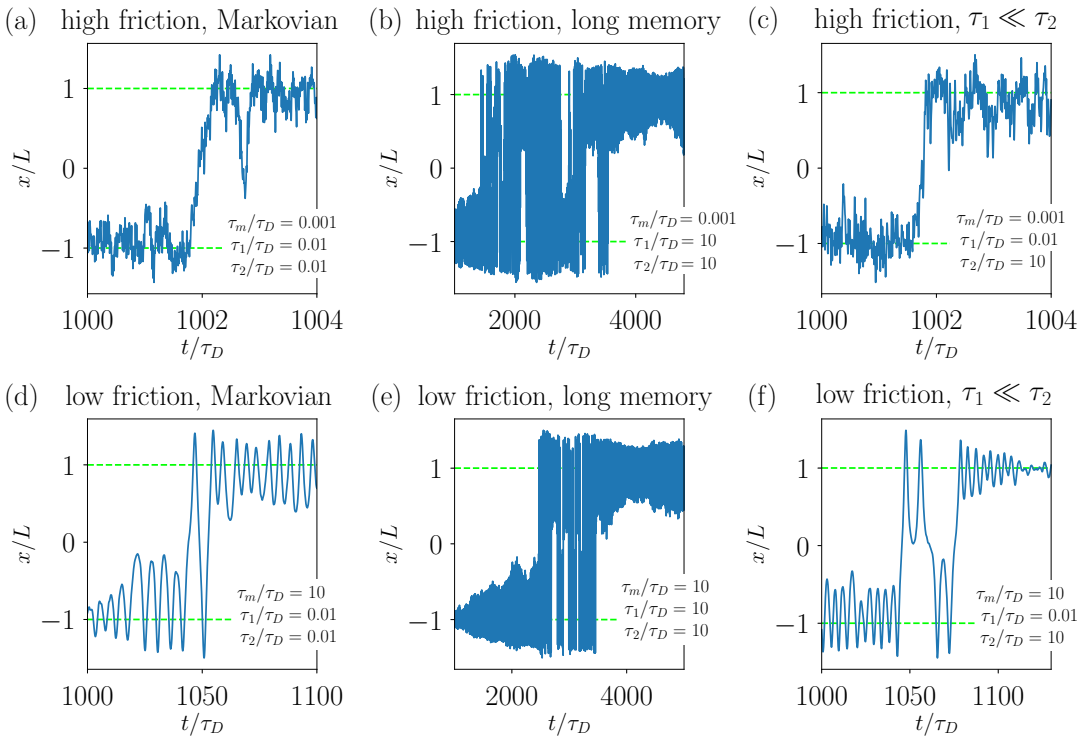

Figure 4.2: Typical sections of simulated trajectories displaying barrier crossing events for barrier height $U_0 = 3\,k_\mathrm{B}T$. Simulation parameters used are given in the legends. The horizontal green dashed lines indicate the minima of the quartic potential Eq. (4.3), which is shown in Fig. 4.1 (a).

and forth between the two wells until its energy falls below the barrier energy again [126, 147]. Figure 4.2 (c) shows a trajectory with high friction $\tau_m/\tau_D = 0.001 \ll 1$, and memory times $\tau_1/\tau_D = 0.01 \ll \tau_2/\tau_D = 10$. The trajectory is reminiscent of the high-friction short-memory dynamics shown in Fig. 4.2 (a), and markedly different from the long burst of recrossings displayed in Fig. 4.2 (b). Similarly, the trajectory for low friction $\tau_m/\tau_D = 10 \gg 1$ and $\tau_1/\tau_D = 0.01 \ll \tau_2/\tau_D = 10$ shown in Fig. 4.2 (f) resembles more the low-friction Markovian trajectory from Fig. 4.2 (d) than the low-friction long-memory trajectory shown in Fig. 4.2 (e). While these observations are a first hint that the shorter memory time determines the dynamics of the particle, we emphasize that both memory times always contributes equally to the long-time diffusive behavior, see Appendix C.3 for details.

To check whether bi-exponential memory implies bi-exponential first-passage time distribution, we in Fig. 4.3 present numerically obtained FPT distributions in a semi-logarithmic representation, calculated using the trajectories depicted in Fig. 4.2. For all parameters considered we see that

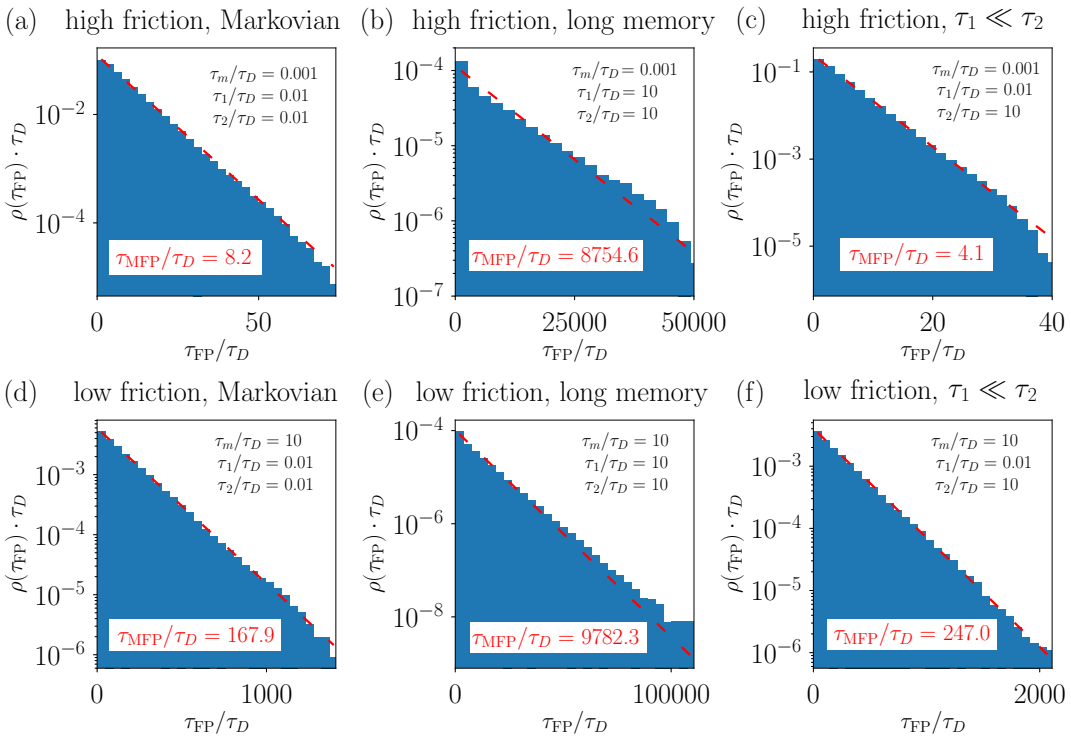

Figure 4.3: First-passage time distributions for barrier crossing. Simulation parameters are given in the legends. For each subplot, samples are obtained from numerical simulations as illustrated in Fig. 4.1 (b). The resulting normalized probability distribution $\rho(\tau_{\mathrm{FP}})$ is shown as blue histogram. The MFPT τ_{MFP} given in the plots is obtained by averaging over the samples, and used to plot an exponential distribution as defined in Eq. (4.12), and shown as red dashed line.

the observed FPTs are well-approximated by an exponential distribution

$$\rho(\tau_{\mathrm{FP}}) = \frac{1}{\tau_{\mathrm{MFP}}} \exp(-\tau_{\mathrm{FP}}/\tau_{\mathrm{MFP}}), \tag{4.12}$$

shown as red dashed lines in Fig. 4.3. Only for the long-memory regime shown in Figs. 4.3 (b), (e) we see slight deviations from the exponential distribution for short τ_{FP}, which we attribute to the recrossing events shown in Fig. 4.2 (b), (e), and which do not affect the MFPT significantly, as shown in Chapter 3. Both for high friction (upper row) and low friction (lower row), we see that if the two memory times are very different, as in Figs. 4.3 (c), (f), then the resulting FPT distribution is single-exponential; the MFPT is close to the corresponding single-exponential MFPT of the shorter memory time, shown in Figs. 4.3 (a), (d), and can differ by orders of magnitude from the single-exponential MFPT of the longer memory time, as shown in Figs. 4.3 (b), (e).

4.3 Propagator analysis

In Figs. 4.2, 4.3 we observed similarities between the dynamics in the asymmetric bi-exponential scenario and the single-exponential scenario for the corresponding smaller memory time, indicating that the smaller memory time dominates short-time dynamics and barrier crossing. For long memory times, this can be rationalized by an asymptotic analysis of the propagator $C(t) \equiv \langle x(t)x(0)\rangle$ that characterizes the particle motion within one potential well. The following calculation is a generalization of the propagator analysis carried out for the single-exponential memory kernel in Chapter 3. We consider the GLE (4.1) in a harmonic potential $U(x) \simeq Kx^2/2$ and for times $t \gg \tau_1, \tau_2$, so that we can replace the upper limit in the memory integral by infinity. Fourier transforming Eq. (4.1) and solving for $\tilde{x}(\omega)$ yields

$$\tilde{x}(\omega) = \frac{\tilde{\eta}(\omega)}{K - m\omega^2 + i\omega\tilde{\Gamma}_+(\omega)} \equiv \tilde{Q}(\omega)\tilde{\eta}(\omega), \tag{4.13}$$

where the half-sided Fourier transform $\tilde{\Gamma}_+$ of the bi-exponential memory kernel $\Gamma(t)$ is given by

$$\tilde{\Gamma}_+(\omega) = \int_0^\infty \mathrm{d}t\; e^{-i\omega t}\Gamma(t) = \frac{\gamma}{2}\sum_{j=1}^{2}\frac{1}{1+i\omega\tau_j}, \tag{4.14}$$

while the full Fourier transform is

$$\tilde{\Gamma}(\omega) = \tilde{\Gamma}_+(\omega) + \tilde{\Gamma}_+(-\omega) = \gamma\sum_{j=1}^{2}\frac{1}{1+\omega^2\tau_j^2}. \tag{4.15}$$

Using Eq. (4.13), we calculate the propagator $C(t) \equiv \langle x(t)x(0)\rangle$ as

$$C(t) \equiv \langle x(t)x(0)\rangle = \int\frac{\mathrm{d}\omega}{2\pi}e^{i\omega t}\int\frac{\mathrm{d}\omega'}{2\pi}\,\langle\tilde{x}(\omega)\tilde{x}(\omega')\rangle \tag{4.16}$$

$$= \int\frac{\mathrm{d}\omega}{2\pi}e^{i\omega t}\int\frac{\mathrm{d}\omega'}{2\pi}\,\tilde{Q}(\omega)\tilde{Q}(\omega')\langle\tilde{\eta}(\omega)\tilde{\eta}(\omega')\rangle \tag{4.17}$$

$$= k_\mathrm{B}T\int\frac{\mathrm{d}\omega}{2\pi}e^{i\omega t}\int\frac{\mathrm{d}\omega'}{2\pi}\,2\pi\delta(\omega+\omega')\tilde{\Gamma}(\omega)\tilde{Q}(\omega)\tilde{Q}(\omega') \tag{4.18}$$

$$= k_\mathrm{B}T\int\frac{\mathrm{d}\omega}{2\pi}e^{i\omega t}\,\tilde{\Gamma}(\omega)\tilde{Q}(\omega)\tilde{Q}(-\omega), \tag{4.19}$$

where we used that the Fourier transform of the generalized FDT Eq. (4.2) is $\langle\tilde{\eta}(\omega)\tilde{\eta}(\omega')\rangle = k_\mathrm{B}T\;2\pi\delta(\omega+\omega')\;\tilde{\Gamma}(\omega)$. Thus the propagator, i.e., the Fourier transform of $C(t)$, is finally given

by

$$\tilde{C}(\omega)/(k_{\mathrm{B}}T) = \tilde{\Gamma}(\omega)\tilde{Q}(\omega)\tilde{Q}(-\omega) \tag{4.20}$$

$$= \gamma \sum_{j=1}^{2} \left[\frac{1}{1+\omega^2\tau_j^2} \frac{1}{K - m\omega^2 + i\omega\gamma/2\sum_{k=1}^{2}(1+i\omega\tau_k)^{-1}} \right.$$

$$\left. \times \frac{1}{K - m\omega^2 - i\omega\gamma/2\sum_{l=1}^{2}(1-i\omega\tau_l)^{-1}} \right] \tag{4.21}$$

$$= \gamma \sum_{j=1}^{2} \left\{ (1+\omega^2\tau_j^2) \left[(K-m\omega^2)^2 - \omega\gamma \sum_{k=1}^{2} \omega\tau_k (1+\omega^2\tau_k^2)^{-1} \right. \right. \tag{4.22}$$

$$\left. \left. + \frac{\omega^2\gamma^2}{4} \sum_{k,l=1}^{2} (1+i\omega\tau_k)^{-1}(1-i\omega\tau_l)^{-1} \right] \right\}^{-1}.$$

For τ_1, τ_2 large, we rewrite this as

$$\frac{\tilde{C}(\omega)}{k_{\mathrm{B}}T} = \frac{\gamma}{\omega^2\tau_1^2} \left[(K-m\omega^2)^2 + \sum_{j=1}^{2} \mathcal{O}\left((\omega\tau_j)^{-1}\right) \right]^{-1}$$

$$+ \frac{\gamma}{\omega^2\tau_2^2} \left[(K-m\omega^2)^2 + \sum_{j=1}^{2} \mathcal{O}\left((\omega\tau_j)^{-1}\right) \right]^{-1}, \tag{4.23}$$

and for $\tau_1 \ll \tau_2$, we obtain the approximate expression

$$\frac{\tilde{C}(\omega)}{k_{\mathrm{B}}T} \approx \frac{\gamma}{\omega^2\tau_1^2} \left[(K-m\omega^2)^2 \right]^{-1}. \tag{4.24}$$

The result is independent of τ_2, showing that the dynamics is indeed dominated by τ_1 and giving an explanation for the behavior of the trajectories shown in Figs. 4.2 (c), (f).

Note that similar to the long memory time limit for the single-exponential propagator discussed in Chapter 3, Eq. (4.24) is the low-friction limit $\tau_m\omega \gg 1$ of the memoryless propagator, and using the same argument as in Section 3.5, the scaling $\tau_{\mathrm{MFP}}/\tau_D \sim (\tau_1/\tau_D)^2$ can be obtained from Eq. (4.24), which holds for intermediate times where $\tau_m \ll \tau_1 \ll \tau_2$.

4.4 Single-exponential scenario with improved heuristic formula

Before exploring the global behavior of $\tau_{\mathrm{MFP}}/\tau_D$, we consider the symmetric scenario defined by $\tau_\Gamma \equiv \tau_1 = \tau_2$, where the memory kernel Eq. (4.4) reduces to a single exponential. This situation was studied in detail in Chapter 3, and based on PGH theory [88] we obtained a heuristic formula for τ_{MFP} in the single-exponential case, given by Eq. (3.10). However, we also observed that in the long-memory regime $\tau_\Gamma/\tau_D \gg 1$, PGH theory deviates slightly from numerical MFPTs,

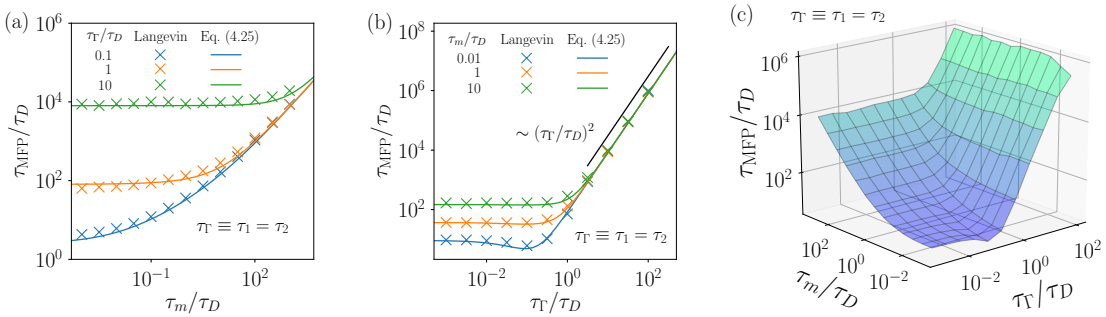

Figure 4.4: Simulation results for the MFPT for single-exponential memory, i.e., for $\tau_\Gamma \equiv \tau_1 = \tau_2$. (a) The rescaled MFPT $\tau_{\mathrm{MFP}}/\tau_D$ is shown as a function of τ_m/τ_D for several values of τ_Γ/τ_D (colored crosses). The colored lines represent the improved heuristic formula Eq. (4.25). (b) The rescaled MFPT $\tau_{\mathrm{MFP}}/\tau_D$ is shown as a function of τ_Γ/τ_D for several values of τ_m/τ_D (colored crosses). The colored lines represent the heuristic single-exponential formula Eq. (4.25), the asymptotic power law scaling $\tau_{\mathrm{MFP}}/\tau_D \sim (\tau_\Gamma/\tau_D)^2$ [122] is shown as black bar. (c) The rescaled MFPT $\tau_{\mathrm{MFP}}/\tau_D$ is shown as a function of both τ_m/τ_D, τ_Γ/τ_D. The data shown in subplot (a) corresponds to sections parallel to the τ_m/τ_D-axis, the data shown in subplot (b) corresponds to sections parallel to the τ_Γ/τ_D-axis. For all simulations $U_0 = 3\,k_{\mathrm{B}}T$ is used.

so that consequently also our heuristic formula deviates slightly from numerical MFPTs in that regime, c.f. Fig. B.2 (c). To remedy this, in the present chapter we use a modified version of the heuristic formula Eq. (3.10), given by

$$\tau_{\mathrm{MFP}}/\tau_D = e^{U_0/(k_{\mathrm{B}}T)} \left[\frac{(U_0/(k_{\mathrm{B}}T))^{-1}}{1 + 10\,U_0/(k_{\mathrm{B}}T)\,\tau_\Gamma/\tau_D} + \left(\frac{U_0}{k_{\mathrm{B}}T}\right)^{-1} \frac{\tau_m}{\tau_D} + 2\sqrt{\left(\frac{U_0}{k_{\mathrm{B}}T}\right)^{-1} \frac{\tau_m}{\tau_D} + 4\left(\frac{\tau_\Gamma}{\tau_D}\right)^2} \right]. \tag{4.25}$$

The difference between Eq. (3.10) and Eq. (4.25) is the prefactor 4 in the last term, which in the original heuristic formula Eq. (3.10) is given by Euler's number $e \approx 2.72$. In Figs. 4.4 (a), (b) we compare numerical data for the symmetric scenario $\tau_\Gamma \equiv \tau_1 = \tau_2$ to predictions of Eq. (4.25), and consistent with our results from Chapter 3 we find very good agreement. The improved heuristic formula Eq. (4.25) matches the long-memory regime $\tau_\Gamma/\tau_D \gg 1$, shown in Fig. 4.4 (b) to the right, slightly better than the original heuristic formula, compare Fig. B.2 (c). In Fig. 4.4 (c) we display the global behavior of the single-exponential MFPT in a triple-logarithmic plot, which shows $\tau_{\mathrm{MFP}}/\tau_D$ as a function of both τ_m/τ_D and τ_Γ/τ_D.

4.5 Heuristic formula for the mean first-passage time for bi-exponential memory

Both Figs. 4.2, 4.3, and the propagator analysis carried out in Section 4.3 suggest that if $\tau_i \ll \tau_j$, then the dynamics relevant for barrier crossing is dominated by the term in the memory kernel Eq. (4.4) which contains τ_i, and is rather independent of τ_j.

We now show that bi-exponential MFPTs can be described quantitatively by considering a single-exponential friction coefficient γ_{eff} and an effective single-exponential memory time τ_{eff}, which interpolate between the symmetric scenario $\tau_\Gamma \equiv \tau_1 = \tau_2$, when the GLE Eq. (4.1), (4.4) is single-exponential with friction coefficient γ and memory time τ_Γ, and the asymmetric scenario $\tau_i \ll \tau_j$, where the friction coefficient $\gamma/2$ and the memory time τ_i determine the particle dynamics. To this end, we define γ_{eff}, τ_{eff} as

$$\gamma_{\text{eff}} = \alpha\,\gamma, \tag{4.26}$$

$$\tau_{\text{eff}} = \alpha \frac{2}{\tau_1^{-1} + \tau_2^{-1}}, \tag{4.27}$$

where

$$\alpha = \frac{1}{2} + 2\frac{\tau_1 \cdot \tau_2}{(\tau_1 + \tau_2)^2}. \tag{4.28}$$

Both γ_{eff} and τ_{eff}/τ_i only depend on the ratio τ_1/τ_2, and by construction both γ_{eff} and τ_{eff} are symmetric in τ_1, τ_2. In Fig. 4.5 we plot $\gamma_{\text{eff}}/\gamma$ and τ_{eff}/τ_i as a function of τ_1/τ_2. As the figure shows, for $\tau_\Gamma \equiv \tau_1 = \tau_2$ we obtain

$$\gamma_{\text{eff}} = \gamma, \qquad \tau_{\text{eff}} = \tau_\Gamma, \tag{4.29}$$

so that the parameters of the GLE Eq. (4.1), (4.4) with $\tau_\Gamma \equiv \tau_1 = \tau_2$ are recovered. On the other hand, for $\tau_i/\tau_j \ll 1$, we obtain

$$\gamma_{\text{eff}} \approx \gamma/2, \qquad \tau_{\text{eff}} \approx \tau_i. \tag{4.30}$$

Based on γ_{eff}, τ_{eff}, we define effective time scales

$$\tau_{D,\text{eff}} = \frac{L^2\gamma_{\text{eff}}}{k_\text{B}T} = \alpha\,\tau_D, \tag{4.31}$$

$$\tau_{m,\text{eff}} = \frac{m}{\gamma_{\text{eff}}} = \frac{\tau_m}{\alpha}, \tag{4.32}$$

and use these effective values and τ_{eff} in Eq. (4.25) to obtain

$$\tau_{\text{MFP}}/\tau_{D,\text{eff}} = e^{U_0/(k_\text{B}T)} \left[\frac{(U_0/(k_\text{B}T))^{-1}}{1 + 10\,U_0/(k_\text{B}T)\,\tau_{\text{eff}}/\tau_{D,\text{eff}}} + \left(\frac{U_0}{k_\text{B}T}\right)^{-1} \frac{\tau_{m,\text{eff}}}{\tau_{D,\text{eff}}} + 2\sqrt{\left(\frac{U_0}{k_\text{B}T}\right)^{-1} \frac{\tau_{m,\text{eff}}}{\tau_{D,\text{eff}}} + 4\left(\frac{\tau_{\text{eff}}}{\tau_{D,\text{eff}}}\right)^2} \right]. \tag{4.33}$$

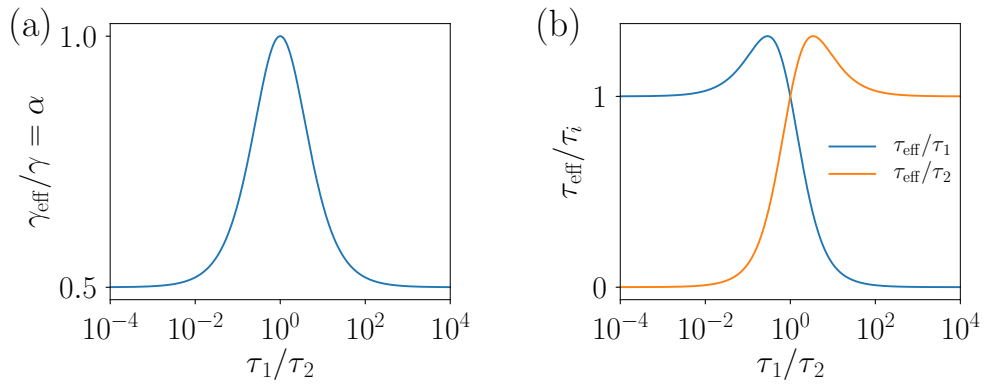

Figure 4.5: (a) Relative effective friction coefficient $\gamma_{\text{eff}}/\gamma$, as defined in Eq. (4.26), and (b) relative effective single-exponential memory time τ_{eff}/τ_i, as defined in Eq. (4.27), plotted as function of τ_1/τ_2.

Employing Eqs. (4.27), (4.31), (4.32) to explicitly express this formula in terms of the parameters of the bi-exponential system leads to

$$\tau_{\text{MFP}}/\tau_D = e^{U_0/k_{\text{B}}T}\left[\frac{\alpha(U_0/(k_{\text{B}}T))^{-1}}{1+10\,U_0/(k_{\text{B}}T)\tau_{\text{eff}}/\tau_{D,\text{eff}}} + \frac{1}{\alpha}\left(\frac{U_0}{k_{\text{B}}T}\right)^{-1}\frac{\tau_m}{\tau_D} + 2\sqrt{\left(\frac{U_0}{k_{\text{B}}T}\right)^{-1}\frac{\tau_m}{\tau_D} + \alpha\cdot 4\left(\frac{\tau_{\text{eff}}}{\tau_{D,\text{eff}}}\right)^2}\right], \tag{4.34}$$

where

$$\frac{\tau_{\text{eff}}}{\tau_{D,\text{eff}}} = \frac{2}{(\tau_1/\tau_D)^{-1} + (\tau_2/\tau_D)^{-1}}. \tag{4.35}$$

In Figs. 4.6, 4.7, 4.8 we compare predictions of the heuristic bi-exponential formula Eq. (4.34) for τ_{MFP} to numerical results. These figures, which we discuss in detail in the following paragraphs, show that Eq. (4.34) quantitively describes the bi-exponential MFPTs over the whole parameter range considered, and therefore that the numerical data is consistent with the hypothesis that the MFPT is dominated by the shorter memory time. In Appendix C.4 we show that, similar to the single-exponential scenario considered in Chapter 3, Grote-Hynes (GH) theory [87] only describes the numerical data in the triple-limit of high-friction $\tau_m/\tau_D \ll 1$ and short memory $\tau_1/\tau_D \ll 1$, $\tau_2/\tau_D \ll 1$, which is why we exclude the GH predictions from the plots in the main text.

Figure 4.6 shows τ_{MFP}/τ_D as function of τ_1/τ_D for fixed values of τ_m/τ_D, τ_2/τ_D. In Figs. 4.6 (a)-(c) we see that for $\tau_1 \ll \tau_2$, i.e., to the left of the black vertical dashed lines that denote $\tau_1 = \tau_2$, the MFPT behaves similar to the single-exponential MFPT shown in Fig. 4.4 (b). In particular, for $\tau_m/\tau_D = 0.01$ (magenta crosses) the memory acceleration regime can be seen in Figs. 4.6 (b), (c) for $\tau_1/\tau_D \approx 0.1$, followed by the power-law scaling $\tau_{\text{MFP}}/\tau_D \sim (\tau_1/\tau_D)^2$

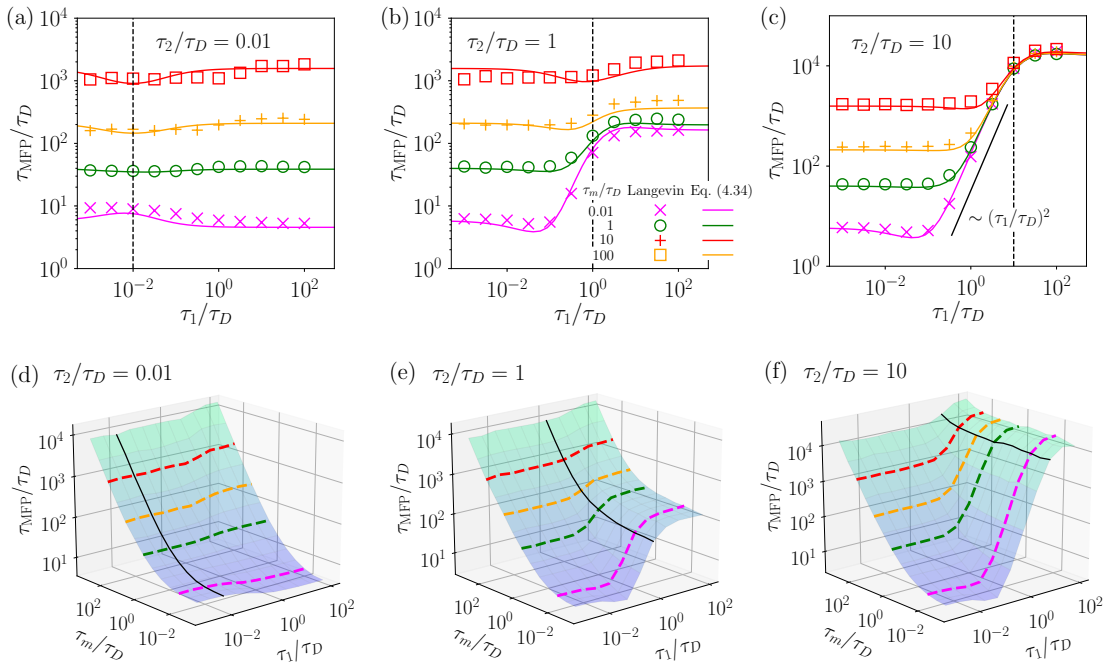

Figure 4.6: Simulation results for the MFPT at fixed τ_2/τ_D. (a)-(c) Colored symbols denote the rescaled MFPT $\tau_{\mathrm{MFP}}/\tau_D$ as function of τ_1/τ_D for several values of τ_m/τ_D and fixed values of τ_2/τ_D, given by (a) $\tau_2/\tau_D = 0.01$, (b) $\tau_2/\tau_D = 1$, (c) $\tau_2/\tau_D = 10$. The legend given in (b) also applies to subplots (a), (c). The colored lines represent the heuristic bi-exponential formula Eq. (4.34), the black bar in (c) indicates the intermediate scaling $\tau_{\mathrm{MFP}}/\tau_D \sim (\tau_1/\tau_D)^2$. (d)-(f) Global plots of the MFPT $\tau_{\mathrm{MFP}}/\tau_D$ as a function of τ_1/τ_D, τ_m/τ_D for fixed values of τ_2/τ_D, given by (a) $\tau_2/\tau_D = 0.01$, (b) $\tau_2/\tau_D = 1$, (c) $\tau_2/\tau_D = 10$. Each colored dashed line represents the respective numerical MFPTs with corresponding color from subplots (a)-(c), the black line indicates where $\tau_1 = \tau_2$ and represents the special case of single-exponential memory shown in Fig. 4.4 (a). All data is obtained using $U_0 = 3\,k_{\mathrm{B}}T$.

for $0.1 \lesssim \tau_1/\tau_D \lesssim \tau_2/\tau_D$. As $\tau_1 \gtrsim \tau_2$, i.e., to the right of the black vertical dashed lines that denote $\tau_1 = \tau_2$, the MFPT becomes independent of τ_1. This can prominently be seen in Fig. 4.6 (a), where $\tau_2/\tau_D = 0.01$ is small and $\tau_{\mathrm{MFP}}/\tau_D$ is almost constant for $\tau_1 > \tau_2$. Throughout Figs. 4.6 (a)-(c) the heuristic formula Eq. (4.34) describes the numerical results very well. For a more comprehensive illustration of the MFPTs, we show global triple-logarithmic plots of the numerical MFPTs for fixed values of τ_2/τ_D in Figs. 4.6 (d)-(f). The numerical results from the upper row of Fig. 4.6 are highlighted as dashed lines with corresponding colors, the parameter range where the single-exponential case is recovered ($\tau_1 = \tau_2$) is shown as black solid line.

Figure 4.7 shows $\tau_{\mathrm{MFP}}/\tau_D$ as function of τ_1/τ_D for fixed values of τ_2/τ_D, τ_m/τ_D. In Fig. 4.7 (a), we again see single-exponential behavior reminiscent of Fig. 4.4 (b). More explicitly, for $\tau_2/\tau_D = 1$, 10, 100, we observe a dip in $\tau_{\mathrm{MFP}}/\tau_D$ for $\tau_1/\tau_D \approx 0.1$, followed by power-law scaling $\tau_{\mathrm{MFP}}/\tau_D \sim (\tau_1/\tau_D)^2$ for $0.1 \lesssim \tau_1/\tau_D \lesssim \tau_2/\tau_D$. As $\tau_1 \gtrsim \tau_2$, $\tau_{\mathrm{MFP}}/\tau_D$ saturates to

a value determined by τ_m/τ_D, τ_2/τ_D. For $\tau_2 = 0.01$ (magenta crosses), Fig. 4.7 (a) contains no regime where $\tau_1 \ll \tau_2$, so that τ_{MFP} is almost independent of τ_1/τ_D throughout. Figs. 4.7 (b), (c) show similar behavior, and as expected from the single-exponential data for $\tau_m/\tau_D = 1$, 10 (see Fig. 4.4 (b)), a dip in the MFPT for $\tau_1/\tau_D \approx 0.1$ cannot be observed in the logarithmic representation of $\tau_{\mathrm{MFP}}/\tau_D$. Again, the heuristic formula Eq. (4.34) describes the data very accurately throughout, and we illustrate the global behavior of the numerical data at fixed τ_m/τ_D in triple-logarithmic plots in Figs. 4.7 (d)-(f).

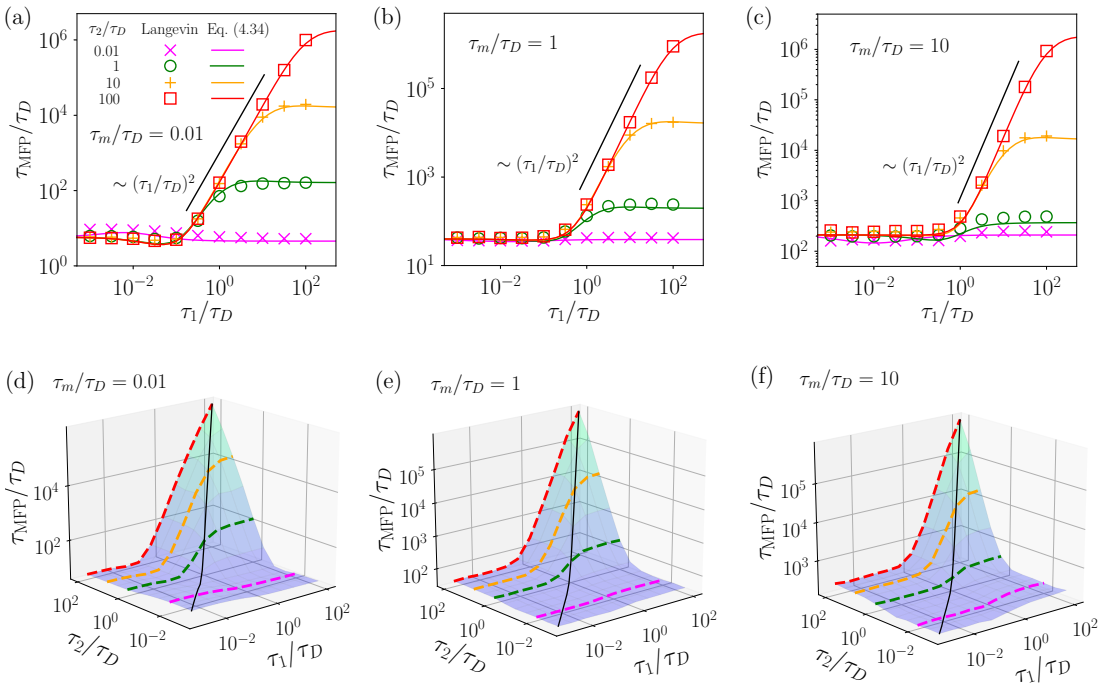

Figure 4.7: Simulation results for the MFPT at fixed τ_m/τ_D. (a)-(c) Colored symbols denote the rescaled MFPT $\tau_{\mathrm{MFP}}/\tau_D$ as function of τ_1/τ_D for several values of τ_2/τ_D and fixed τ_m/τ_D, given by (a) $\tau_m/\tau_D = 0.01$, (b) $\tau_m/\tau_D = 1$, (c) $\tau_m/\tau_D = 10$. The legend given in (a) also applies to subplots (b), (c). The colored lines represent the heuristic bi-exponential formula Eq. (4.34), the black bars indicate the intermediate scaling $\tau_{\mathrm{MFP}}/\tau_D \sim (\tau_1/\tau_D)^2$. (d)-(f) Global plots of the MFPT $\tau_{\mathrm{MFP}}/\tau_D$ as a function of τ_1/τ_D, τ_2/τ_D for fixed τ_m/τ_D, given by (a) $\tau_m/\tau_D = 0.01$, (b) $\tau_m/\tau_D = 1$, (c) $\tau_m/\tau_D = 10$. Each colored dashed line represents the respective numerical MFPTs with corresponding color from subplots (a)-(c), the black line indicates where $\tau_1 = \tau_2$ and represents the special case of single-exponential memory shown in Fig. 4.4 (b). All data is obtained using $U_0 = 3\, k_{\mathrm{B}}T$.

Figures 4.8 (a)-(c) show $\tau_{\mathrm{MFP}}/\tau_D$ as a function of τ_m/τ_D for fixed values of τ_1/τ_D, τ_2/τ_D. In all three plots, the MFPT displays a similar τ_m/τ_D-dependence as the single-exponential case shown in Fig. 4.4 (a). For $\tau_2/\tau_D = 0.01$ we see in Fig. 4.8 (a) that $\tau_{\mathrm{MFP}}/\tau_D$ is almost independent of τ_1/τ_D, consistent with the picture that $\tau_{\mathrm{MFP}}/\tau_D$ is determined by the shorter

memory time τ_2. On the other hand, for large $\tau_2/\tau_D = 10$ the MFPT shown in Fig. 4.8 (c) depends very much on τ_1/τ_D and is qualitatively identical to the single-exponential MFPT shown in Fig. 4.4 (a). Also for this case, we see that the heuristic formula Eq. (4.34) remains accurate, and provide triple-logarithmic plots of the numerical data in Figs. 4.8 (d)-(f).

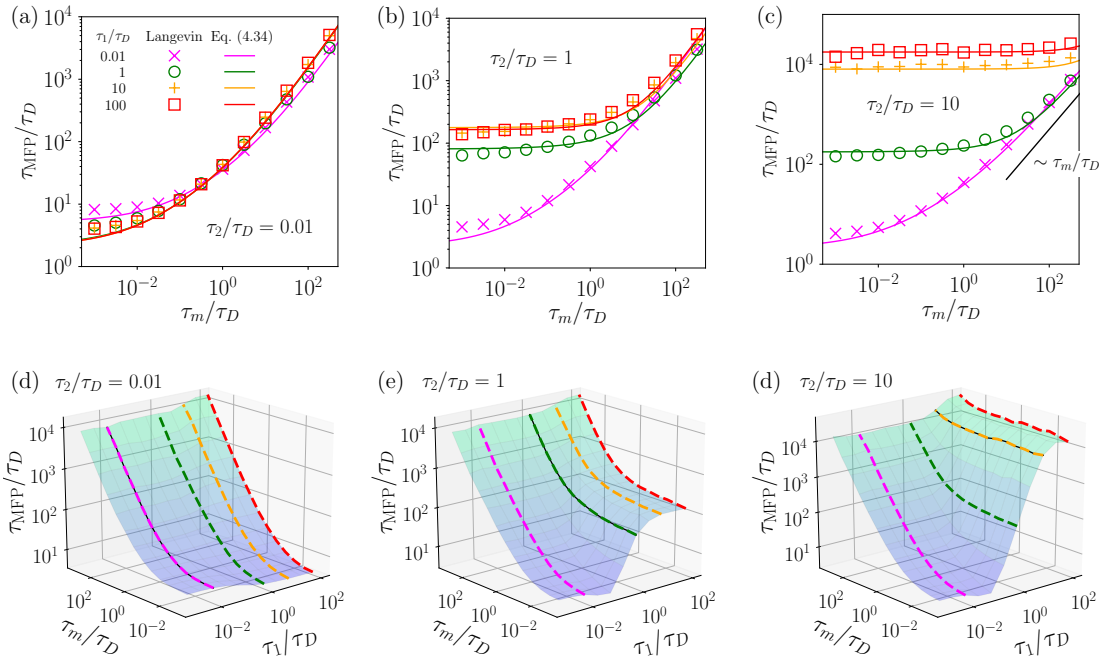

Figure 4.8: Simulation results for the MFPT at fixed τ_2/τ_D. (a)-(c) Colored crosses denote the rescaled MFPT $\tau_{\mathrm{MFP}}/\tau_D$ as function of τ_1/τ_D for several values of τ_m/τ_D and fixed τ_2/τ_D, given by (a) $\tau_2/\tau_D = 0.01$, (b) $\tau_2/\tau_D = 1$, (c) $\tau_2/\tau_D = 10$. The legend given in (a) also applies to subplots (b), (c). The colored lines represent the heuristic bi-exponential formula Eq. (4.34), the black bar in (c) indicates the asymptotic scaling $\tau_{\mathrm{MFP}} \sim \tau_m$ which corresponds to Markovian low-friction. (d)-(f) Global plots of the MFPT $\tau_{\mathrm{MFP}}/\tau_D$ as a function of τ_1/τ_D, τ_m/τ_D for fixed τ_2/τ_D, given by (a) $\tau_2/\tau_D = 0.01$, (b) $\tau_2/\tau_D = 1$, (c) $\tau_2/\tau_D = 10$. Each colored dashed line represents the respective numerical MFPTs with corresponding color from subplots (a)-(c), the black line indicates where $\tau_1 = \tau_2$ and represents the special case of single-exponential memory shown in Fig. 4.4 (a). All data is obtained using $U_0 = 3\,k_{\mathrm{B}}T$.

4.6 Conclusions

In summary, we perform explicit Langevin simulations to calculate barrier crossing times for bi-exponential memory, for the special case where both exponentials contribute equally to the long-time diffusion coefficient. Both numerical results and an asymptotic propagator analysis suggest that the smaller of the two memory times determines the barrier-crossing time τ_{MFP}.

We construct an effective friction coefficient γ_{eff} and an effective memory time τ_{eff} to reduce the bi-exponential system to an effective single-exponential system. Used in conjunction with the effective parameters, the heuristic formula for single-exponential barrier crossing times established in Chapter 3 describes the bi-exponential MFPT globally over the full parameter regime probed in our simulations.

As our numerical results demonstrate, barrier crossing times are often orders of magnitude larger than both τ_1, τ_2, which makes it surprising that τ_{MFP} is independent of the larger memory time. It is interesting that, in the context of barrier crossing, the bi-exponential system can be approximated by an effective single-exponential one. Physical reaction coordinates are typically coupled to orthogonal degrees of freedom with several intrinsic time scales [29, 86, 142–145]. Since the single-exponential system is the most studied [88, 122, 131, 132], a reliable method for reducing more complex memory kernels to an effective single-exponential memory kernel is of great practical value, in particular since no solutions to PGH theory [88] are readily available for multiexponential memory kernels. In this context, a generalization of our heuristic formula for memory kernels that are arbitrary sums of exponentials would be desirable. A step in that direction will be to find out whether a similar reduction of the bi-exponential system is also possible for arbitrary partitioning of the long-time diffusion coefficient among the two exponentials.

Chapter 5

Multiple surface wave solutions on linear viscoelastic media

Bibliographic information: Parts of this chapter and of Appendix D have previously been published. Reprinted with permission from Ref. [iv].

5.1 Introduction

Surface waves are ubiquitous phenomena with direct relevance for daily life. They are solutions of the equations of motion of a semi-infinite continuum medium that are localized at the interface. The dispersion relation for capillary-gravity waves on ideal fluids has been known for a long time [148] and explains salient effects such as the existence of a minimal nonzero phase velocity or the qualitatively different dispersion effects for small and long wave lengths. Subsequent works included the effects of a nonzero fluid viscosity [149, 150] and the bending rigidity of the surface [151, 152]. For elastic solids, the existence of Rayleigh surface waves [153] accounts for the disastrous effects of earthquakes, and it was later shown that for viscoelastic solids several distinct surface wave solutions exist [154, 155]. In the presence of an interface with viscoelastic properties, the existence of yet another surface wave was established, which we refer to as Lucassen wave [156–159].

While different surface waves have been amply studied experimentally, their interconnections are less explored [160, 161]. On the theoretical side, it seems natural to ask what a minimal framework is to derive all three distinct surface waves. Furthermore, do all three surface wave types coexist for a given frequency (possibly in a restricted range of parameters) or do they transform into each other as parameters are varied? In fact, the capillary-gravity and Lucassen waves were shown to coexist for an incompressible Newtonian bulk fluid [159, 162]. Subsequently, bulk shear viscoelasticity was taken into account [163–165], which is relevant for gels [161], but not bulk compressibility, excluding Rayleigh waves in their general form. On the other hand, theoretical approaches including bulk compressibility [166, 167] neglected surface viscoelasticity, thereby excluding Lucassen waves. In short, a unified theory including all three surface waves is missing in the literature.

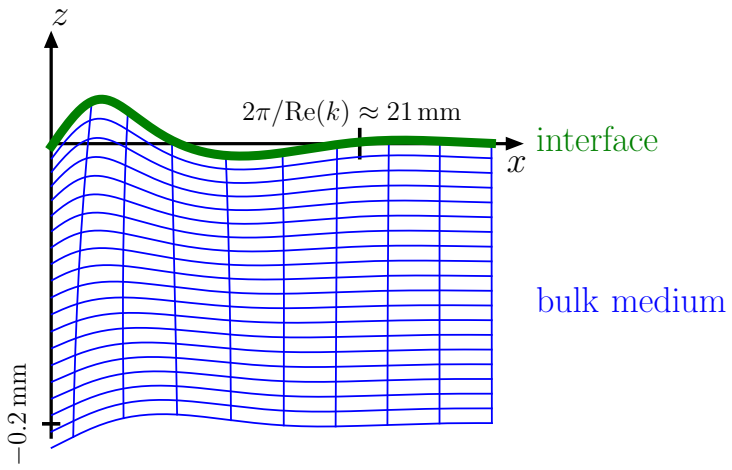

Figure 5.1: Displacement field for the Lucassen surface wave calculated from the solution $k(\omega)$ of Eq. (5.8) and the harmonic wave ansatz Eq. (5.3). The bulk medium at $z \leq 0$ is shown in blue while the interface around $z = 0$ is shown in green. The explicit parameters correspond to an air-water interface covered by an elastic surfactant layer and are $\sigma_{2D} = 72\ \mathrm{mN/m}$, $K_{2D} = 10\ \mathrm{mN/m}$, $\eta = 1\ \mathrm{mPa \cdot s}$, $\rho = 10^3\ \mathrm{kg/m^3}$, $g = 9.81\ \mathrm{m/s^2}$, with all other interface parameters set to zero. Φ and t are chosen in such a way that the displacement at the origin is approximately zero. For the used frequency $\omega = 100\ \mathrm{s^{-1}}$, the wave length is $2\pi/\mathrm{Re}(k) \approx 21\ \mathrm{mm}$.

In this chapter, we formulate the general dispersion relation for surface waves that contains capillary-gravity, Rayleigh and Lucassen waves. From that, we derive modified capillary-gravity and Lucassen dispersion relations that include viscoelasticity of both the bulk medium and the surface. Interestingly, our general framework yields a surface wave that is different from all previously studied solutions and only exists if surface tension, gravitation and bulk viscosity are all simultaneously nonzero. For a pure air-water interface this wave is predicted to coexist with the capillary-gravity wave for small frequencies and should be detectable experimentally. For the experimentally relevant case of an air-water interface with an adsorbed surfactant layer we present a phase diagram for the number of coexisting wave solutions in terms of frequency and surface compression modulus. We demonstrate that Rayleigh and Lucassen waves do not coexist but rather continuously transform into each other and that our novel capillary-gravity-viscosity wave coexists with both capillary-gravity and Lucassen waves for a small range of nonzero surface compressibilities.

5.2 General theory

We consider a linear viscoelastic medium in the half-space at $z \leq 0$, bounded at $z = 0$ by a 2D interface, as illustrated in Fig. 5.1. The linearized continuum mechanical momentum conservation equations are given as [168]

$$\rho(\vec{r},t)\partial_t^2 u_j(\vec{r},t) = \partial_k \sigma_{jk}(\vec{r},t) + F_j(\vec{r},t) \qquad j \in \{x,y,z\}, \tag{5.1}$$

where $\rho(\vec{r},t)$ is the mass density, $\vec{u}(\vec{r},t)$ is the displacement field, $\vec{F}(\vec{r},t)$ an external force, we use Cartesian coordinates $\vec{r}=(x,y,z)$ and the Einstein summation convention. Assuming the bulk medium to be linear, isotropic and homogeneous, it is characterized by the shear- and dilatational-relaxation functions $g_{\mathrm{s}}(t)$, $g_{\mathrm{d}}(t)$ [168], which relate the stress tensor σ_{jk} and the strain tensor ϵ_{jk} via

$$\sigma_{jk}(\vec{r},t)=\int_{-\infty}^{\infty} g_{\mathrm{s}}(t-t')\partial_{t'}\epsilon_{jk}(\vec{r},t')\,\mathrm{d}t'+\frac{\delta_{j,k}}{3}\int_{-\infty}^{\infty}\left[g_{\mathrm{d}}(t-t')-g_{\mathrm{s}}(t-t')\right]\partial_{t'}\epsilon_{ll}(\vec{r},t')\,\mathrm{d}t', \tag{5.2}$$

where the components of the strain tensor are given by $\epsilon_{jk}=\left(\partial_j u_k+\partial_k u_j\right)/2$. Furthermore, mass conservation allows to express $\rho(\vec{r},t)$ in terms of the equilibrium mass density ρ and the displacement field, as explained in detail in Appendix D.1. For the displacement field $\vec{u}$, we use an ansatz for harmonic waves of frequency ω and wave number k, which decay exponentially both away from the interface and in the direction of propagation [153],

$$\vec{u}=\vec{\nabla}\varphi+\vec{\nabla}\times\vec{\psi}, \tag{5.3}$$

where

$$\varphi=\Phi\exp\left(z/\lambda_l\right)\exp\left[i(kx-\omega t)\right], \tag{5.4}$$

$$\vec{\psi}=\Psi\exp\left(z/\lambda_t\right)\exp\left[i(kx-\omega t)\right]\hat{e}_y, \tag{5.5}$$

with Φ, Ψ the amplitudes of the longitudinal and transversal parts of the wave and $\hat{e}_y$ the unit vector in y-direction. As shown in Appendix D.1, the momentum conservation Eq. (5.1) determines the decay constants λ_l, λ_t of the longitudinal and transversal wave components in z-direction as

$$\lambda_l^{-2}(k,\omega)=k^2-3i\omega\rho/(2\tilde{g}_{\mathrm{s}}(\omega)+\tilde{g}_{\mathrm{d}}(\omega)), \tag{5.6}$$

$$\lambda_t^{-2}(k,\omega)=k^2-2i\omega\rho/\tilde{g}_{\mathrm{s}}(\omega), \tag{5.7}$$

where $\tilde{g}_{\mathrm{s}}(\omega)$ and $\tilde{g}_{\mathrm{d}}(\omega)$ are the temporal Fourier transforms. The stress continuity condition at the interface at $z=0$ leads to a system of linear equations for Φ and Ψ, which only has a nontrivial solution if the determinant of the coefficient matrix vanishes. As we show in detail in Appendix D.1, this leads to the general dispersion relation

$$\begin{aligned}0=&\,4\left(k^2\tilde{\Pi}_{2D}+\rho g-\omega^2\rho_{2D}\right)\left[\left(k^2\tilde{g}_{2\mathrm{D}}-i\omega\rho_{2\mathrm{D}}\right)\left(k^2-\lambda_l^{-1}\lambda_t^{-1}\right)+i\omega\rho\lambda_l^{-1}\right]\\&+4\left(k^2\tilde{g}_{2\mathrm{D}}-i\omega\rho_{2\mathrm{D}}\right)\omega^2\rho\lambda_t^{-1}+\tilde{g}_{\mathrm{s}}\left[i\omega\tilde{g}_{\mathrm{s}}\left(-4k^2\lambda_l^{-1}\lambda_t^{-1}+(k^2+\lambda_t^{-2})^2\right)\right.\\&\left.+2\rho_{2\mathrm{D}}gk^2\left(2\lambda_l^{-1}\lambda_t^{-1}-(k^2+\lambda_t^{-2})\right)\right].\end{aligned} \tag{5.8}$$

The interface is characterized by a surface tension $\sigma_{2\mathrm{D}}$ and an equilibrium excess mass density $\rho_{2\mathrm{D}}$. In plane, we assume a completely viscous shear response with viscosity $\eta_{2\mathrm{D}}$, and

a viscoelastic dilatational response with viscosity $\eta'_{2\mathrm{D}}$ and area elastic modulus $K_{2\mathrm{D}}$. For out-of-plane deformations, we assume a bending rigidity $\kappa_{2\mathrm{D}}$ and a transverse viscosity $\eta^{\perp}_{2\mathrm{D}}$ [169], leading to the 2D stress-strain relations $\tilde{g}_{2\mathrm{D}}(\omega) = \eta_{2\mathrm{D}} + \eta'_{2\mathrm{D}} + K_{2\mathrm{D}}/(-i\omega)$ and $\tilde{\Pi}_{2\mathrm{D}}(k,\omega) = \sigma_{2\mathrm{D}} - i\omega\eta^{\perp}_{2\mathrm{D}} + k^2\kappa_{2\mathrm{D}}$. Gravitational acceleration g acts on both bulk and interface and is directed in the negative z-direction.

A solution $k(\omega)$ to Eq. (5.8) yields a surface wave dispersion relation, from which the phase velocity and the propagation distance along the x-direction follow as

$$c_{\parallel}(\omega) = \frac{\omega}{\mathrm{Re}(k(\omega))}, \tag{5.9}$$

$$\lambda_{\parallel}(\omega) = \frac{1}{\mathrm{Im}(k(\omega))}. \tag{5.10}$$

5.3 Limiting cases

Although Eq. (5.8) is not analytically tractable in its full generality, the classical dispersion relations follow in different physical limits of the parameters. Removing interfacial effects ($\rho_{2\mathrm{D}} = 0$, $\tilde{g}_{2\mathrm{D}} = 0$, $\tilde{\Pi}_{2\mathrm{D}} = 0$) and gravity ($g = 0$), Eq. (5.8) simplifies to

$$4k^2\lambda_l^{-1}\lambda_t^{-1} = \left(k^2 + \lambda_t^{-2}\right)^2, \tag{5.11}$$

which is the classical Rayleigh conditional equation [153]. For an elastic bulk medium, where $\tilde{g}_{\mathrm{s}}$, $\tilde{g}_{\mathrm{d}}$ are purely imaginary, Eq. (5.11) has only one solution [153]. In the more general viscoelastic case, up to three solutions can in principle coexist [154, 155, 170].

Assuming on the other hand that

$$\frac{3\omega\rho}{|2\tilde{g}_{\mathrm{s}}(\omega) + \tilde{g}_{\mathrm{d}}(\omega)|} \ll |k(\omega)|^2 \ll \frac{2\omega\rho}{|\tilde{g}_{\mathrm{s}}(\omega)|}, \tag{5.12}$$

and furthermore neglecting gravitational coupling to the interface, $\rho_{2\mathrm{D}}g/(\omega|\tilde{g}_{\mathrm{s}}|) \ll 1$, Eq. (5.8) factorizes and yields two equations

$$0 = (k^2\tilde{\Pi}_{2\mathrm{D}} + \rho g - \omega^2\rho_{2\mathrm{D}})\lambda_l^{-1} - \omega^2\rho \tag{5.13}$$

$$0 = \lambda_t^{-1}(k^2\tilde{g}_{2\mathrm{D}} - i\omega\rho_{2\mathrm{D}}) - i\omega\rho, \tag{5.14}$$

which is a generalization of previous factorization approaches [165, 171]. Equation (5.13) is the generalized capillary-gravity-flexural surface wave dispersion relation [152] which additionally includes the effects of interfacial excess mass $\rho_{2\mathrm{D}}$, interfacial transverse shear viscosity $\eta^{\perp}_{2\mathrm{D}}$ (entering via $\tilde{\Pi}_{2\mathrm{D}}$), as well as bulk compressibility. Equation (5.14) is the generalized Lucassen wave dispersion relation [159] which additionally includes the effects of interfacial excess mass $\rho_{2\mathrm{D}}$. As can be seen, the Rayleigh solutions defined by Eq. (5.11) are not valid solutions of

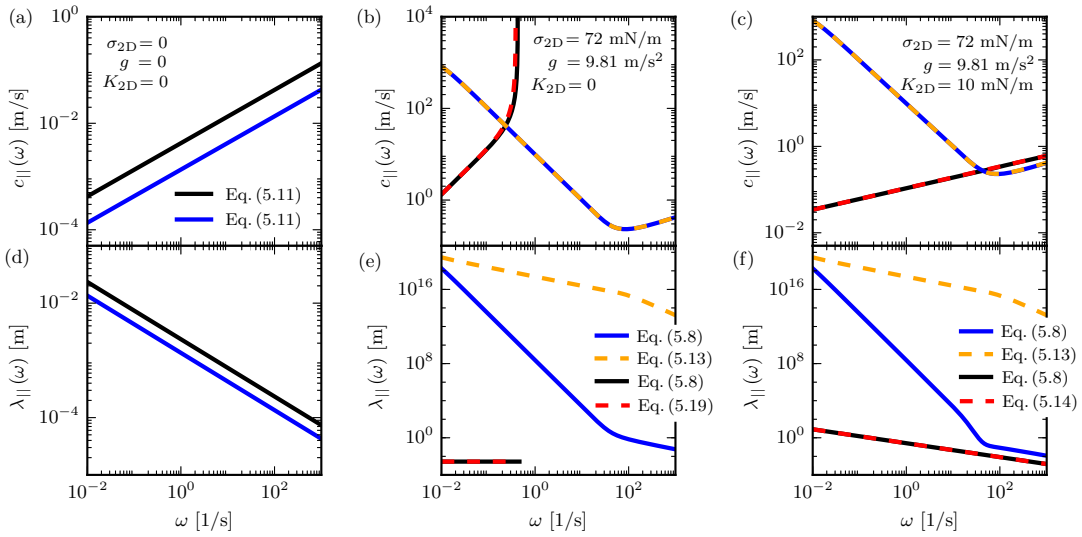

Figure 5.2: Surface wave phase velocities $c_{\parallel}(\omega)$ and propagation distances $\lambda_{\parallel}(\omega)$ on a water-like viscoelastic half-space according to Eqs. (5.9), (5.10). (a), (d) For vanishing gravitational acceleration $g = 0$, surface tension $\sigma_{2D} = 0$ and area elastic modulus $K_{2D} = 0$, two Rayleigh wave solutions exist. (b), (e) For $g = 9.81\ \mathrm{m/s^2}$, $\sigma_{2D} = 72\ \mathrm{mN/m}$ but $K_{2D} = 0$, the capillary-gravity wave and the novel CGV wave coexist. (c), (f) For $g = 9.81\ \mathrm{m/s^2}$, $\sigma_{2D} = 72\ \mathrm{mN/m}$ and $K_{2D} = 10\ \mathrm{mN/m}$, the capillary-gravity wave and the Lucassen wave coexist. Solid lines denote numerical solutions of the exact dispersion relation Eq. (5.8), dashed lines denote the various approximate asymptotic expressions. All other interfacial parameters are set to zero. Note that a two-colored line amounts to a dashed line being on top of a solid line.

Eq. (5.13) and Eq. (5.14), which shows that Rayleigh waves do not coexist with capillary-gravity and Lucassen waves if the factorization holds.

Assuming instead of the inequalities (5.12) that

$$\frac{3\omega\rho}{|2\tilde{g}_{\mathrm{s}}(\omega) + \tilde{g}_{\mathrm{d}}(\omega)|} \ll \frac{2\omega\rho}{|\tilde{g}_{\mathrm{s}}(\omega)|} \ll |k(\omega)|^2, \tag{5.15}$$

Eq. (5.8) can be approximated as

$$0 = 2\tilde{g}_{\mathrm{s}}^2 k^4 + \rho\sigma_{2D} k^3 - 3i\omega\rho\tilde{g}_{\mathrm{s}} k^2 + \rho^2 g k - \omega^2\rho^2. \tag{5.16}$$

5.4 Compressible Newtonian fluid and new wave solution

To simplify the discussion, we from now on consider a compressible Newtonian fluid, for which the Fourier transformed relaxation functions are,

$$\tilde{g}_{\mathrm{s}}(\omega) = 2\eta, \tag{5.17}$$

$$\tilde{g}_{\mathrm{d}}(\omega) = 3\eta' + \frac{3K}{-i\omega}, \tag{5.18}$$

see Appendix D.1 for details. Here η is the shear viscosity, η' is the dilatational viscosity and K is the adiabatic bulk modulus, which is related to the bulk sound velocity c_{bulk} via $K = \rho c_{bulk}^2$ [172]. For this special case, we give a physical interpretation of the approximations in Eq. (5.12), (5.15) in Appendix D.2, and furthermore show that Eq. (5.16) has, for positive real part of the wave vector k, the asymptotic solution

$$k(\omega) = \left[\frac{4\eta^2 g}{\sigma_{2\mathrm{D}}^2} - \frac{\omega^2}{2g}\right] + i\sqrt{\frac{\rho g}{\sigma_{2\mathrm{D}}}}. \tag{5.19}$$

Unlike the Rayleigh, capillary-gravity and Lucassen wave solutions, defined in Eqs. (5.11), (5.13), and (5.14), the dispersion relation Eq. (5.19) requires simultaneously nonzero shear viscosity η, gravitation g and surface tension $\sigma_{2\mathrm{D}}$. We therefore refer to this solution as the capillary-gravity-viscous (CGV) surface wave.

For the display of explicit dispersion relations, we consider water at $25\,^{\circ}\mathrm{C}$, for which the parameters are $\eta = 1\ \mathrm{mPa \cdot s}$, $\eta' = 3\ \mathrm{mPa \cdot s}$, $\rho = 10^3\ \mathrm{kg/m^3}$, $c_{bulk} = 1.5 \cdot 10^3\ \mathrm{m/s}$ [173]. In the absence of an interface ($\rho_{2\mathrm{D}} = 0$, $\tilde{g}_{2\mathrm{D}} = 0$, $\tilde{\Pi}_{2\mathrm{D}} = 0$) and without gravity ($g = 0$), Eq. (5.8) reduces to the Rayleigh dispersion relation, Eq. (5.11), and yields two distinct solutions $k(\omega)$. In Figs. 5.2 (a), (d), we show the corresponding phase velocities $c_{\parallel}(\omega)$ and propagation distances $\lambda_{\parallel}(\omega)$ which exhibit very similar behavior, namely power laws $c_{\parallel} \sim \omega^{1/2}$, $\lambda_{\parallel} \sim \omega^{-1/2}$. This is discussed in more detail in Appendix D.2.

In Figs. 5.2 (b), (e) we consider the case of nonzero gravitation $g = 9.81\ \mathrm{m/s^2}$ and an interface characterized by a nonzero surface tension $\sigma_{2\mathrm{D}} = 72\ \mathrm{mN/m}$, with all other interfacial parameters set to zero. We observe two distinct dispersion relations with behavior very different from the Rayleigh wave solutions shown in Figs. 5.2 (a), (d). By comparing the phase velocities and decay lengths from the two numerical solutions of the full Eq. (5.8) with the capillary-gravity dispersion Eq. (5.13) and the CGV dispersion Eq. (5.19) we conclude that the asymptotic expressions are very good approximations to the phase velocities of the full numerical solution. Note that for the capillary-gravity wave, the decay length is not predicted very accurately by Eq. (5.13); this reflects that Eq. (5.12) is dominated by the real part of the wave number k and thus allows for large deviations in the imaginary part, which determines the decay length according to Eq. (5.10). Most importantly, we see that the CGV wave exists in parallel to the standard capillary-gravity wave on pure water for low frequencies and thus should be detectable experimentally. Figure 5.3 illustrates the displacement field of the CGV wave for $\omega = 0.1\ \mathrm{s^{-1}}$. At the surface the displacement is almost horizontal, away from the interface it becomes more elliptical.

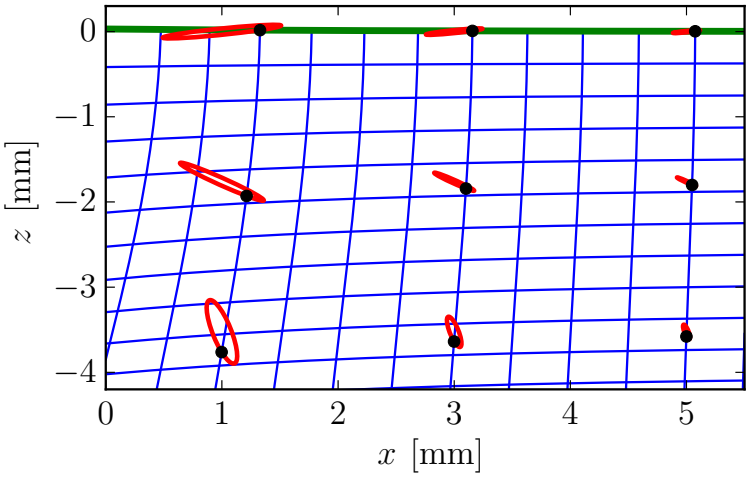

Figure 5.3: Displacement field of the novel CGV wave for $\omega = 0.1\ \mathrm{s}^{-1}$, as calculated from the harmonic wave ansatz Eq. (5.3) and the wave number $k(\omega = 0.01\ \mathrm{s}^{-1})$ obtained from solving Eq. (5.8) numerically, with interface and bulk medium as in Figs. 5.2 (b), (e). The green line shows the displacement of the surface, the blue grid illustrates the displacement below the surface. The red ellipses depict trajectories of fluid elements, the black dots denote the respective position at $t = 0$.

In Figs. 5.2 (c), (f) we assume nonzero gravitation $g = 9.81\ \mathrm{m/s^2}$, interfacial tension $\sigma_{2\mathrm{D}} = 72\ \mathrm{mN/m}$ and area elastic modulus $K_{2\mathrm{D}} = 10\ \mathrm{mN/m}$, with all other interfacial parameters set to zero. We again compare phase velocities and decay lengths calculated numerically from Eq. (5.8) with the solutions of the factorized Eqs. (5.13) and (5.14). We see that the two numerically determined dispersion relations correspond to the capillary-gravity and the Lucassen waves. It transpires that $K_{2\mathrm{D}}$ is a crucial parameter as it switches the observed surface waves from a combination of capillary-gravity and CGV wave (for $K_{2\mathrm{D}} = 0$) to capillary-gravity and Lucassen wave (for $K_{2\mathrm{D}} = 10\ \mathrm{mN/m}$).

This raises the question whether the CGV wave is the low $K_{2\mathrm{D}}$ limit of the Lucassen wave, i.e., whether the two solutions continuously transform into each other as $K_{2\mathrm{D}}$ is varied. In Fig. 5.4 (a) we show a state diagram for the existence of the distinct solutions of the general dispersion equation as function of the surface modulus $K_{2\mathrm{D}}$ and the wave frequency ω for fixed $\sigma_{2\mathrm{D}} = 72\ \mathrm{mN/m}$, $g = 9.81\ \mathrm{m/s^2}$ and all other interfacial parameters set to zero.

In the green section a wave solution exists that in the horizontally hatched region is described by the CGV wave dispersion relation Eq. (5.19). In the blue section a wave solution exists that in the low frequency range is represented by the Lucassen dispersion relation Eq. (5.14) and in the high-frequency range by the Rayleigh dispersion relation Eq. (5.11), as indicated by the differently hatched areas. Note that the capillary-gravity wave exists throughout the entire parameter range and transforms into one of the two Rayleigh solutions at frequencies $\omega \gtrsim 10^{10}$ 1/s, see Appendix D.4 for more details. From the figure we conclude that the CGV

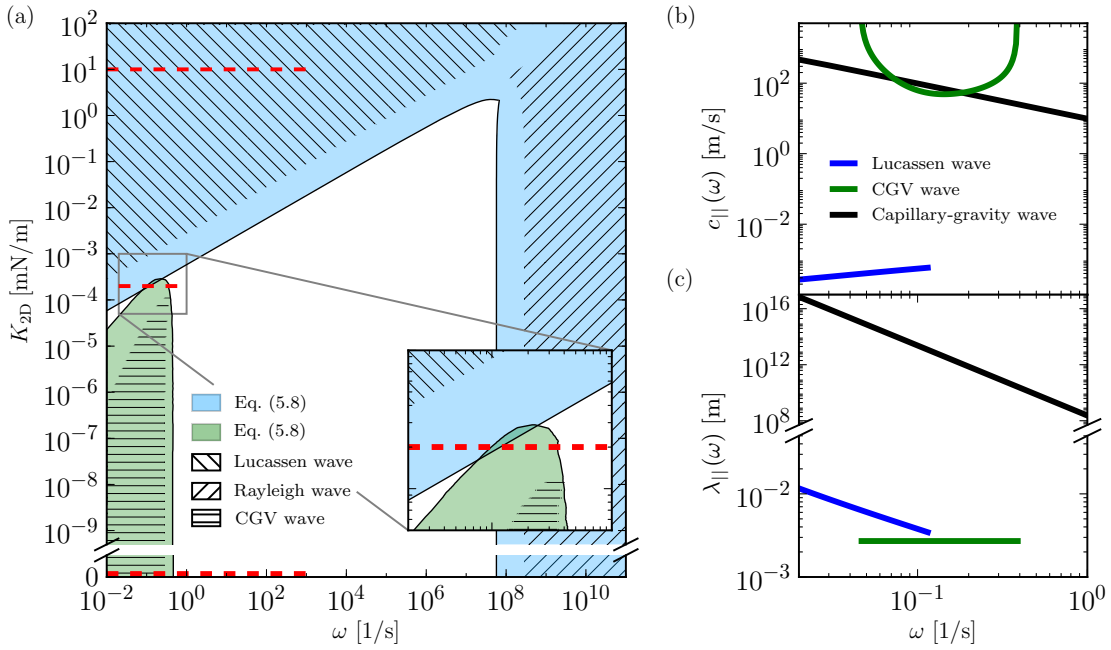

Figure 5.4: (a) Existence state diagram of surface waves for fixed $\sigma_{2D} = 72$ mN/m, $g = 9.81$ m/s^2, as a function of interface modulus K_{2D} and frequency ω, based on numerical solutions of Eq. (5.8). The capillary-gravity wave exists in the entire domain and is therefore not shown. In the green domain the novel CGV wave exists, which in the hatched region is well described by Eq. (5.19). In the blue domain a distinct wave solution exists which for low frequency corresponds to the Lucassen wave Eq. (5.14) and for high frequencies continuously transforms into one of the two Rayleigh wave solutions Eq. (5.11). The upper and lower horizontal red dashed lines denote value of K_{2D} for which dispersion relations are shown in Fig. 5.2. The inset is a detailed view of the region where all three wave solutions coexist. (b), (c) Phase velocities and propagation distances for the three wave solutions as a function of ω for $K_{2D} = 2 \cdot 10^{-4}$ mN/m, indicated by a horizontal red dashed line in (a), obtained from Eqs. (5.9), (5.10).

wave is not the low K_{2D} limit of the Lucassen wave. This is strikingly demonstrated in the the inset of Fig. 5.4 (a), since in a small parameter range all three solutions (capillary-gravity, Lucassen, and CGV waves) coexist. In contrast, there is a wide parameter range where only the capillary-gravity wave solution exists, indicated by the white region in Fig. 5.4 (a). Figures 5.4 (b), (c) show the phase velocities and decay lengths across the three-solution coexistence region at $K_{2D} = 2 \cdot 10^{-4}$ mN/m, demonstrating that the three solutions are very distinct in their physical properties. As a final remark on the CGV wave, the requirement that the real part of $k(\omega)$ be positive in Eq. (5.19) implies that the CGV wave only exists up to a frequency

$$\omega_{\max}^{\mathrm{CGV}} = \sqrt{2}\frac{2\eta g}{\sigma_{2D}}, \tag{5.20}$$

which, for the parameters considered here, evaluates to $\omega_{\max}^{\mathrm{CGV}} \approx 0.39$ s^{-1}. This is in agreement

with Fig. 5.4 (a), where it can be seen that the numerical solution disappears at around this frequency, independent of $K_{2\mathrm{D}}$. For simplicity, in Figs. 5.2, 5.3, 5.4 we chose a fixed surface tension $\sigma_{2\mathrm{D}} = 72\ \mathrm{mN/m}$, corresponding to the free air-water interface. In Appendix D.3 we demonstrate that for experimentally realistic reduced surface tension values [174, 175], very similar results are obtained.

5.5 Conclusions

In summary, we derive the general dispersion relation for surface waves at a viscoelastic interface and demonstrate that in a restricted parameter region three distinct solutions $k(\omega)$ exist. We find a new wave solution that only exists when surface tension (capillarity), gravitation and bulk viscosity are simultaneously nonzero. Although this CGV wave only exists for low frequencies and is highly damped on a pure air-water interface, it should be within reach of experiments. In a possible experimental setup one could excite waves mechanically and measure phase velocities and propagation distances using Wilhelmy plates [92] or optically [93, 176]. Alternatively, thermally excited surface wave spectra can be obtained by scattering techniques [177].

Chapter 6

Nonlinear fractional waves at elastic interfaces

Bibliographic information: Parts of this chapter and of Appendix E have previously been published. Reprinted with permission from Ref. [v]. Copyright 2017 by the American Physical Society.

6.1 Introduction

Surface waves are waves that are localized at the interface between two media and are at the core of many important everyday life phenomena [178–183]. As a consequence of energy conservation and the interfacial localization, and neglecting dissipative damping effects, the intensity of a surface wave excitation at a planar interface originating from a point source falls off with the inverse distance and not with the inverse squared distance, as for ordinary bulk waves. Consequently, in the absence of viscous effects, a surface wave emanating from a line excitation travels basically without attenuation. This demonstrates that surface waves dominate over regular bulk waves at large enough distance and thus explains why they have been amply studied experimentally and theoretically [148, 152–155, 157–159, 161, 164, 165, 171, 184–187]. As we also discuss in Chapter 5, for different systems one finds distinct surface wave types. At the interface between two fluids that have different densities, one finds capillary-gravity waves, the best-known realization of which are deep-water waves at the air-water interface [148]. Depending on the wave length, these waves are either dominated by gravity or by the interfacial tension. From measurements of the dispersion relation, the functional relationship between wave length and frequency, fluid [150] as well interfacial properties [188] can be extracted. At the surface of an elastic solid one finds Rayleigh waves, with a dispersion relation that depends on the viscoelastic modulus of the solid [153–155, 189]. Rayleigh and capillary-gravity waves are distinct surface wave types that in fact can, for suitably chosen material parameters, coexist [189], c.f. Chapter 5. Since they are linear phenomena, i.e., described by a theory that is linear in the surface wave amplitude, they are predicted to travel independently from each other even if they are excited at the same frequency or the same wave length. If the interface in addition to tension exhibits a finite compressibility, a third surface wave type exists, referred to as Lucassen wave [157–159].

A well-studied experimental realization is a monolayer of amphiphilic molecules at the air-water interface [157–159, 161, 165, 190]. At the experimentally relevant low-frequency range and for realistic values of the interfacial elastic modulus [174], Lucassen waves exhibit wave lengths in the centimeter range and are thus easily excitable and observable in typical experiments with self-assembled monolayers [157, 161].

Wave guiding phenomena in monolayers have recently received focal attention because of the possible connection to nerve-pulse propagation [92, 93, 191–194], cell-membrane mediated acoustic cell communication [91, 92, 195, 196] and pressure-pulse-induced regulation of membrane protein function [93, 197, 198]. One exciting recent finding was the discovery of nonlinear wave switching phenomena in a simple system of a Dipalmitoylphosphatidylcholine (DPPC) lipid monolayer spread on the air-water interface [93]. In the experiments, both wave propagation speed and wave attenuation were demonstrated to depend in a highly nonlinear fashion on the excitation amplitude, showing almost all-or-nothing behavior. Only above a certain threshold of the excitation amplitude does wave propagation set in, while below that threshold wave transmission is experimentally almost negligible [93]. Such a nonlinear switching phenomenon offers a multitude of exciting applications and interpretations, in particular since it has been known for a long time that nerve pulse propagation is always accompanied by a mechanical displacement traveling in the axon membrane [89, 90, 191, 199]. In that connection, it should be noted that many membrane proteins are pressure sensitive [197, 198], so the existence of nonlinear acoustic phenomena in membranes constitutes an exquisite opportunity for smart membrane-based regulation and information processing applications [196, 200, 201].

The theoretical description of such nonlinear surface wave phenomena is challenging for several reasons. First of all, the dispersion relation between wave frequency ω and wave number $k = 2\pi/\lambda$ that describes small-amplitude linear surface waves can generally be written as

$$k^2 \sim \omega^\alpha, \tag{6.1}$$

where we define the dispersion exponent α that allows to classify surface wave equations. For normal compression waves one has $\alpha = 2$ and thus the frequency is linearly related to the wave vector. However, for surface waves one typically finds $\alpha \neq 2$. For gravity waves $\alpha = 4$, for capillary waves $\alpha = 4/3$ and for Lucassen waves one has $\alpha = 3/2$ [158, 172].

Nonlinear wave effects (i.e., effects that are nonlinear in the wave amplitude) cannot be simply added on the level of a dispersion relation, since a dispersion relation is obtained by Fourier transforming a linear wave equation and by construction is restricted to the linear regime. Rather, nonlinear effects in the wave amplitude are only captured by a properly derived nonlinear differential equation in terms of the local perturbation field that describes the microscopic wave propagation. This is why in previous theoretical treatments of nonlinear surface waves, the starting point was typically the standard wave equation with $\alpha = 2$ and nonlinear effects were introduced phenomenologically [192, 195, 202]. It is altogether not clear whether this constitutes an accurate theoretical framework for the description of nonlinear surface compression waves, which Lucassen predicted to have $\alpha = 3/2$. On the other hand, hitherto no real-space differential equation for the Lucassen dispersion relation had been derived.

In this chapter we first derive the linear real-space equation that describes Lucassen surface waves from standard hydrodynamics. We show that these waves are described by a so-called

fractional wave equation, which is a differential equation with fractional, i.e., non-integer, time derivative. Although linear fractional wave equations have been amply described in the literature [203–209], until now no derivation of such an equation based on physical first principles had been available. In a second step, we also include nonlinear effects in the wave amplitude by accounting for the nonlinear interfacial compressibility. The necessary material parameters are taken from experimental measurements of the interfacial compressibility of DPPC monolayers at the air-water interface, performed by our collaborators Prof. Dr. Matthias F. Schneider and Dr. Shamit Shrivastava. We show that nonlinear effects become dominant for monolayers close to a phase transition, where the 2D elastic modulus (the inverse compressibility) becomes small or even vanishes, thus explaining previous experimental observations [93]. We solve our nonlinear fractional wave equation numerically and calculate the wave velocity and the compression amplitude as a function of the excitation amplitude. In agreement with experimental observations [93] we find an abrupt decrease of wave damping accompanied by a mild increase in wave velocity above a threshold excitation amplitude. In this comparison, no fitting parameter is used, rather, we extract the nonlinear monolayer compressibility and all other parameters from the experimental measurements.

Our results show that acoustic phenomena at self-assembled phospholipid monolayers are quantitatively described by a nonlinear fractional wave equation derived from physical first principles. Since phospholipids at typical surface pressures are quite close to a phase transition accompanied by a anomalously high interfacial compressibility [210], nonlinear effects are substantial and lead to a nonlinear dependence of the wave propagation properties on the excitation amplitude. This not only shows that phospholipid layers can guide the propagation of acoustic waves, they can also process these waves in a nonlinear fashion. In this context it is interesting to note that biological membranes are actively maintained at a state close to a membrane phase transition [196, 210, 211], so this nonlinear switching phenomenon could possibly play a crucial role in the communication between pressure-sensitive membrane proteins and other functional units situated in membranes. The resulting acoustic wave speed close to the threshold excitation amplitude is found to be about 40 cm/s both in experiments and theory. Remarkably, this speed is thus in a range comparable to the action potential speed in non-myelinated axons [212–215]. The present work should be viewed as a step in understanding the relation between the acoustic nonlinear membrane wave, treated in this article, and the electrochemically generated action potential, described by the nonlinear Hodgkin-Huxley equations [216].

The structure of this chapter is as follows. We first sketch the derivation of the dispersion relation for Lucassen waves using linearized theory. We then convert this dispersion relation into a corresponding fractional wave equation. We present a simple physical interpretation of the fractional derivative that appears in the differential equation in terms of the frequency-dependent coupling range of the surface wave to the underlying bulk fluid. It is important to note that the linear fractional wave equation is also systematically derived from interfacial momentum conservation, which is detailed in Appendix E.2. In a second step we include nonlinear effects by accounting for the change of the monolayer compressibility due to the local monolayer density change that accompanies a finite-amplitude surface wave. The resulting nonlinear fractional wave equation is numerically solved in an interfacial geometry that closely mimics the experimental setup used to study surface waves in monolayers at the air-water interface [93]. Finally, we

compare numerical predictions for the wave velocity and the wave damping with experimental results. This comparison is done without any fitting parameters, as all model parameters are extracted from experiments. The experimental wave speed of about 40 cm/s is very accurately reproduced by the theory. We also reproduce the sudden change of the surface wave propagation properties at a threshold excitation amplitude and thus explain the nonlinear surface wave behavior in terms of the compressibility nonlinearity of a lipid monolayer.

6.2 Derivation of the nonlinear fractional surface wave equation

6.2.1 Dispersion relation for Lucassen surface waves

We here recapitulate the main steps in the derivation of the Lucassen dispersion relation [158, 159, 165], complete details can be found in Appendix E.1. Note that the present derivation constitutes a special case of the more general theory presented in Chapter 5. We consider a semi-infinite incompressible Newtonian fluid in the half space $z \leq 0$ with shear viscosity η and mass density ρ, covered by an interface at $z = 0$ with two-dimensional excess mass density $\rho_{2\mathrm{D}}$, and which responds elastically under compression, with elastic modulus (inverse compressibility) $K_{2\mathrm{D}}$ [157–159, 165], see Fig. 6.1. We neglect interfacial excess viscosity [217, 218] and bending rigidity [219, 220] effects in this work, which could easily be included in the derivation [169].

We start with the linearized incompressible Navier-Stokes equation in the absence of external forces [172]

$$\rho \frac{\partial \vec{v}(\vec{r},t)}{\partial t} = -\vec{\nabla} P(\vec{r},t) + \eta \vec{\nabla}^2 \vec{v}(\vec{r},t) \tag{6.2}$$

where $\vec{v}(\vec{r},t)$ is the vectorial velocity field and $P(\vec{r},t)$ is the pressure field. The gradient operator is denoted as $\vec{\nabla} = (\partial/\partial x, \partial/\partial y, \partial/\partial z)$ where the Cartesian coordinates are defined as $\vec{r} = (x, y, z)$. Note that in the linearized Navier-Stokes equation Eq. (6.2) we have neglected the convective term nonlinear in the velocity field. This approximation is valid since, as we show in detail in Appendix E.4, the nonlinear effects due to surface compression we will consider later on are much stronger than this convective term. Relating the velocity field to the time derivative of the displacement field $\vec{u}(\vec{r},t)$ as

$$\vec{v}(\vec{r},t) = \partial \vec{u}(\vec{r},t)/\partial t, \tag{6.3}$$

and decomposing the displacement field into the longitudinal and transversal parts according to

$$\vec{u}(\vec{r},t) = \vec{\nabla}\Phi(\vec{r},t) + \vec{\nabla} \times \vec{\Psi}(\vec{r},t), \tag{6.4}$$

one finds that the incompressibility condition $\vec{\nabla} \cdot \vec{v}(\vec{r},t) = 0$ and the linearized Navier-Stokes Eq. (6.2) can be rewritten as

$$\vec{\nabla}^2 \Phi(\vec{r},t) = 0, \tag{6.5}$$

$$\eta \vec{\nabla}^2 \vec{\Psi}(\vec{r},t) = \rho \partial \vec{\Psi}(\vec{r},t)/\partial t. \tag{6.6}$$

Likewise, the pressure profile follows as

$$P(\vec{r},t) = -\rho\partial^2\Phi(\vec{r},t)/\partial t^2. \tag{6.7}$$

To solve Eqs. (6.5), (6.6) for a wave of frequency ω and wave number k that is localized in the xy-plane and travels along the x-direction, we make the harmonic wave ansatz [158]

$$\Phi(\vec{r},t) = \phi e^{z/\lambda_l} e^{i(kx-\omega t)}, \tag{6.8}$$

$$\vec{\Psi}(\vec{r},t) = \psi e^{z/\lambda_t} e^{i(kx-\omega t)} \hat{e}_y, \tag{6.9}$$

where the prefactors ϕ and ψ are the wave amplitudes and $\hat{e}_y$ is the unit vector in the y-direction. The decay lengths λ_l and λ_t describe the exponential decay of the longitudinal and transversal parts away from the interface (in the negative z-direction) and follow from Eqs. (6.5) and (6.6) as

$$\lambda_l^{-2} = k^2, \tag{6.10}$$

$$\lambda_t^{-2} = k^2 + \frac{-i\omega\rho}{\eta}. \tag{6.11}$$

The ratio of the wave amplitudes ϕ and ψ is fixed by the stress continuity boundary condition at the surface $z = 0$, which gives rise to a rather complicated dispersion relation, see Appendix E.1 for the full derivation. In the long wave length limit, defined by the condition $\rho\omega \gg \eta k^2$, this dispersion relation simplifies to

$$k^2 = \frac{\omega^2}{K_{2\mathrm{D}}} \left(\rho_{2\mathrm{D}} + \rho\lambda_t\right), \tag{6.12}$$

as derived in detail in Appendix E.1. In the same long wave length limit, $\rho\omega \gg \eta k^2$, the expression for the transversal decay length Eq. (6.11) simplifies to

$$\lambda_t = \sqrt{\frac{\eta}{-i\omega\rho}}, \tag{6.13}$$

so that we finally obtain, by combining Eqs. (6.12) and (6.13), the Lucassen dispersion relation

$$k^2 = \frac{\omega^2}{K_{2\mathrm{D}}} \left(\sqrt{\frac{i\rho\eta}{\omega}} + \rho_{2\mathrm{D}}\right). \tag{6.14}$$

This expression in fact constitutes a slight generalization of the standard Lucassen dispersion relation [158] as it additionally contains the interfacial excess mass density $\rho_{2\mathrm{D}}$ [189]. This generalized dispersion relation is very useful for our discussion, since it allows to distinguish two important physical limits. In case the coupling to the subphase vanishes, which can be achieved by either sending the bulk viscosity η or the bulk mass density ρ to zero, the first term on the right hand side of Eq. (6.14) vanishes. In this limit we are left with the standard dispersion relation for an elastic wave which involves the elasticity and excess mass density parameters $K_{2\mathrm{D}}$ and $\rho_{2\mathrm{D}}$ of the interface. On the other hand, if the interfacial excess mass is neglected, $\rho_{2\mathrm{D}} = 0$, the classical Lucassen dispersion relation is obtained from Eq. (6.14). A simple physical interpretation of Eq. (6.14) will be presented in the next section.

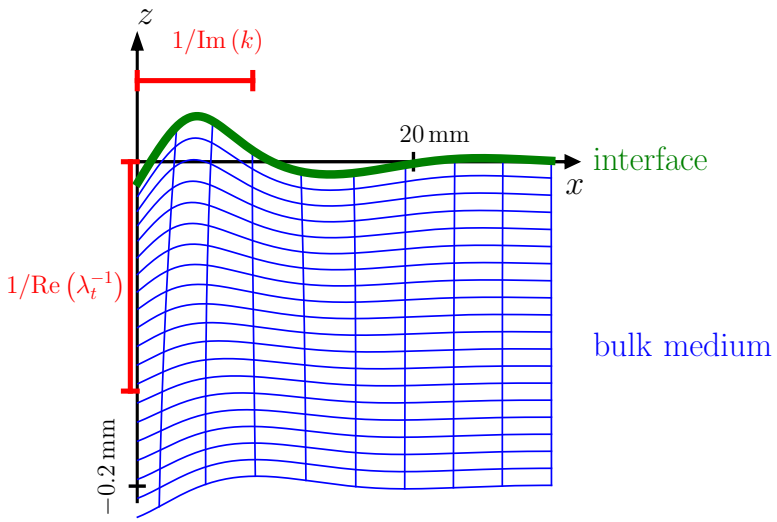

Figure 6.1: Displacement field of the Lucassen wave. The figure shows the displacement field of a Lucassen wave, given by Eqs. (6.4), (6.8), (6.9). The decay lengths in both the x- and z-directions are shown in red, with k, λ_t given by Eqs. (6.14), (6.13). For the bulk medium, water is used ($\rho = 10^3\ \mathrm{kg/m^3}$, $\eta = 10^{-3}\ \mathrm{Pa \cdot s}$); the interface parameters are chosen appropriately for a DPPC monolayer ($K_{2D} = 10\ \mathrm{mN/m}$, $\rho_{2D} = 10^{-6}\ \mathrm{kg/m^2}$). The shown solution has a frequency $\omega = 100\ \mathrm{s^{-1}}$. Note the anisotropic scaling in x- and z-direction.

6.2.2 Linear fractional differential equation for Lucassen surface waves

We now give a simple heuristic derivation of the linear fractional wave equation corresponding to the Lucassen wave. In Appendix E.2, we provide a rigorous derivation based on momentum conservation and utilizing the stress continuity boundary conditions at the interface.

The key observation for arriving at a linear fractional wave equation is that the generalized Lucassen dispersion relation Eq. (6.14) can be rewritten as

$$(ik)^2 K_{2D} = (-i\omega)^2 \rho_{2D} + (-i\omega)^{3/2} \sqrt{\rho\eta}, \tag{6.15}$$

or, using the approximate expression Eq. (6.13) for the longitudinal decay length λ_t, which characterizes the vertical decay of the surface wave, as

$$(ik)^2 K_{2D} = (-i\omega)^2 (\rho_{2D} + \lambda_t \rho). \tag{6.16}$$

The latter equation allows for a simple physical interpretation. The effective area mass density of the interface is given by the sum of the interfacial excess mass density, ρ_{2D}, and the area mass density of the bulk fluid layer that via viscosity is coupled to the interface. The area mass density of the coupled bulk fluid layer is $\lambda_t \rho$, which is the product of the surface wave decay length λ_t and the bulk mass density ρ. The fractional exponent in Eq. (6.15) emerges because the decay length λ_t in Eq. (6.13) depends as an inverse square root on the wave frequency ω, reflecting that lower frequencies reach deeper into the fluid bulk medium.

Since Eq. (6.15) is derived from the harmonic wave ansatz Eqs. (6.8), (6.9), it is not straightforward to interpret it is as the Fourier transform of a one-dimensional displacement field. However, as we detail in Appendix E.1, for the Lucassen wave the displacement in the z-direction is much smaller than the displacement in the x-direction, which allows us to interpret Eq. (6.15) as the Fourier transform of the fractional differential equation

$$K_{2\mathrm{D}}\frac{\partial^2 U(x,t)}{\partial x^2} = \rho_{2\mathrm{D}}\frac{\partial^2 U(x,t)}{\partial t^2} + \sqrt{\rho\eta}\frac{\partial^{3/2} U(x,t)}{\partial t^{3/2}}, \tag{6.17}$$

acting on the displacement of the interface in the x-direction, i.e., along the surface, which we define as $U(x,t) = u_x(x, z=0, t)$. As in the derivation of Eq. (6.15), the displacement field $U(x,t)$ is independent of y, we are thus considering a surface wave front that travels in the x-direction and that is translationally invariant in the y-direction. While we derive Eq. (6.17) based on the dispersion relation Eq. (6.15) and the properties of the Lucassen wave solution, it is also possible to derive the fractional wave equation (6.17) directly from the stress boundary condition at the interface $z = 0$, see Appendix E.2 for details. As discussed there, it is possible to recover the interfacial displacement in the z-direction from a solution of Eq. (6.17). The fractional derivative $\partial^{3/2}/\partial t^{3/2}$ on the right hand side of Eq. (6.17) is defined in Fourier space, where it amounts to multiplication by $(-i\omega)^{3/2}$ [203,204]. In real space, the fractional derivative in Eq. (6.17) can be formulated using the Caputo formula [203, 221]

$$\frac{\partial^{3/2} U(x,t)}{\partial t^{3/2}} = \frac{1}{\sqrt{\pi}}\int_0^t (t-s)^{-1/2}\frac{\partial^2 U(x,s)}{\partial s^2}\,\mathrm{d}s, \tag{6.18}$$

which holds for times $t \geq 0$ and where we assume the interface to be in equilibrium at $t = 0$ so that both $U(x,t)$ and $\partial U(x,t)/\partial t$ vanish for $t < 0$. Thus, Eq. (6.17) is actually an integro-differential equation that is non-local in time. The non-Markovian nature of Eq. (6.17) has an intuitive interpretation. It is well known that eliminating degrees of freedom from a dynamical system leads to non-Markovian equations [14, 15], the integral appearing in Eq. (6.18) can thus be thought of as a consequence of eliminating the displacement field of the bulk medium at $z < 0$ from the dynamics.

For a DPPC monolayer on water we have a typical interfacial excess mass density $\rho_{2\mathrm{D}} = 10^{-6}\,\mathrm{kg/m^2}$ [92], the bulk water mass density is $\rho = 10^3\,\mathrm{kg/m^3}$ and the viscosity of water is $\eta = 10^{-3}\,\mathrm{Pa\cdot s}$ [173]. It follows that for frequencies $\omega \lesssim 10^7\ 1/\mathrm{s}$, the effects due to the membrane mass $\rho_{2\mathrm{D}}$ in Eq. (6.15) are negligible compared to the water layer mass. Thus we will for our comparison with experimental data neglect the membrane excess mass term proportional to $\rho_{2\mathrm{D}}$ in Eq. (6.17) in the following. We note that the resulting linear fractional wave equation has been studied in detail and in fact analytical solutions are well known [203, 222, 223], which we use to test our numerical implementation. For the nonlinear fractional wave equation that we derive in the next section no analytical solutions are known, so that it must be solved numerically.

6.2.3 Nonlinear compressibility effects

The isothermal elastic modulus $K_{2\mathrm{D}}$ of a lipid monolayer at the air-water interface follows from the surface pressure isotherm $\pi(a)$ as [151]

$$K_{2\mathrm{D}} = -a \left. \frac{\partial \pi(a)}{\partial a} \right|_T , \tag{6.19}$$

where a is the area per lipid. An experimentally measured isotherm $\pi(a)$ for a DPPC monolayer at room temperature is shown in the inset of Fig. 6.2, the resulting elastic modulus $K_{2\mathrm{D}}$ according to Eq. (6.19) follows by numerical differentiation and is shown in Fig. 6.2 as a solid line. Note that lipid molecules are essentially insoluble in water, so that the number of lipid molecules in the monolayer at the air-water interface stays fixed as the surface pressure is changed, which is why a finite equilibrium compressibility is obtained; such a monolayer is called a Langmuir monolayer. In Fig. 6.2 it is seen that the modulus $K_{2\mathrm{D}}$ depends sensitively on the area per lipid molecule a and exhibits a minimum at an intermediate value of the area. This minimum signals a smeared-out surface phase transition, at which the area per lipid a changes drastically as the surface pressure π is varied, as can be clearly seen in the inset of Fig. 6.2. The overall area-dependence of the area modulus $K_{2\mathrm{D}}$ can be well represented by a second order polynomial fit to the experimental data,

$$K_{2\mathrm{D}} = K_{2\mathrm{D}}^{(0)} + K_{2\mathrm{D}}^{(2)} (a - a_0)^2 \tag{6.20}$$

which is shown as a red broken line in Fig. 6.2. The fit values we extract from our experimental data are $K_{2\mathrm{D}}^{(0)} = 2.55$ mN/m, $a_0 = 75.4\,\text{Å}^2$ and $K_{2\mathrm{D}}^{(2)} = 0.12$ mN/Å^2.

The linear wave equation (6.17) assumes that the local change of the area per lipid during wave propagation is small, so that the elastic modulus $K_{2\mathrm{D}}$ does not change appreciably. This approximation is valid for small wave amplitudes, but for large enough amplitudes the wave will cause local changes in $K_{2\mathrm{D}}$ that cannot be neglected in Eq. (6.17). For a one-dimensional surface wave characterized by the in-plane displacement field $U(x,t)$, the local time-dependent area per lipid is related to the derivative of the displacement field via [151]

$$a(x,t) = \bar{a} \left(1 + \frac{\partial U(x,t)}{\partial x} \right) , \tag{6.21}$$

where $\bar{a}$ denotes the equilibrium area per lipid in the absence of the surface wave.

Inserting the expression Eq. (6.21) for the space- and time-dependent area $a(x,t)$ into the parabolic approximation for the elastic modulus Eq. (6.20), we obtain

$$K_{2\mathrm{D}} = K_{2\mathrm{D}}^{(0)} + K_{2\mathrm{D}}^{(2)} \left(\bar{a} + \bar{a} \frac{\partial U(x,t)}{\partial x} - a_0 \right)^2 , \tag{6.22}$$

which constitutes a relation between the local elastic modulus $K_{2\mathrm{D}}$ and the interfacial displacement field $U(x,t)$. In deriving this relation, we assume that the experimental isotherm in Fig. 6.2, which is obtained from an equilibrium experiment where the entire monolayer is uniformly

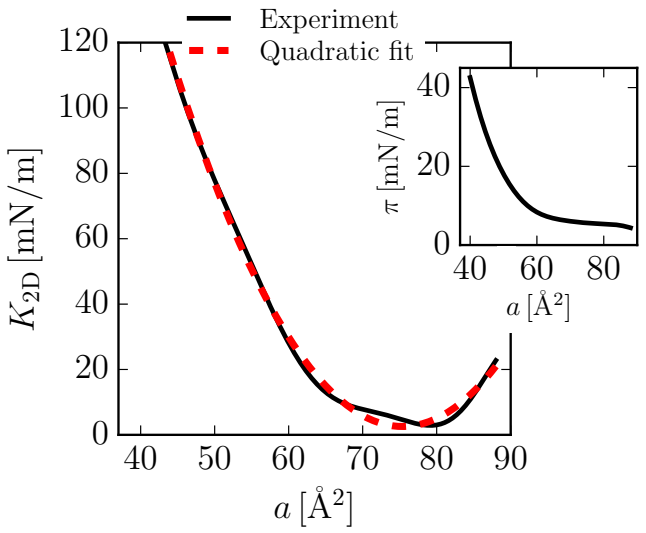

Figure 6.2: Langmuir isotherm and corresponding isothermal elastic modulus. The inset shows an experimentally measured pressure-area isotherm for a (Langmuir) DPPC monolayer [94]. The main plot shows the corresponding isothermal elastic modulus K_{2D}, as calculated from Eq. (6.19) using the isotherm from the inset. The red dashed line shows a quadratic polynomial fit to the elastic modulus.

compressed at fixed temperature, also describes the local time-dependent elastic response of the monolayer at the typical length and time scales of a propagating surface wave. The question whether the measured isotherm is appropriate for the time scales we consider will be discussed later, for now we show that it is applicable at the length scales of interest. The typical surface wave lengths $\lambda = 2\pi/k$ are, in the experimentally relevant frequency range ω from 1 to 10^6 Hz, in the range of tens of centimeters down to 0.1 mm, as follows directly from the Lucassen dispersion relation Eq. (6.15); they are therefore much larger than the lipid size $\sim \sqrt{a}$ and the locality approximation is not expected to lead to any problems. So we conclude that the expression for the local isothermal elastic modulus Eq. (6.22) is valid to leading order at the length scales of interest.

Combining the displacement-dependent expression for the elastic elastic modulus Eq. (6.22) with the fractional wave equation (6.17), we finally obtain

$$\left[K_{2D}^{(0)} + \bar{a}^2 K_{2D}^{(2)} \left(1 + \frac{\partial U(x,t)}{\partial x} - \frac{a_0}{\bar{a}}\right)^2\right] \frac{\partial^2 U(x,t)}{\partial x^2} = \sqrt{\rho\eta}\frac{\partial^{3/2} U(x,t)}{\partial t^{3/2}}, \tag{6.23}$$

where, as discussed after Eq. (6.18), we neglect the inertial term proportional to the membrane mass density ρ_{2D}.

This nonlinear fractional wave equation constitutes the central result of this chapter, and a few comments on the approximations involved and the limits of applicability are in order:

i) We emphasize in our derivation that the displacement $U(x,t)$ is so small that the linearized

Navier Stokes equation (6.2) is valid, while at the same time $U(x,t)$ is large enough so that the assumption of a constant elastic modulus $K_{2\mathrm{D}}$ breaks down. In essence, Eq. (6.23) is valid and relevant for an intermediate range of displacement amplitudes. In Appendix E.4 we show that this assumption is indeed appropriate for the experiments we are comparing with further below, and also discuss at which amplitudes nonlinear effects become relevant [224]. In short, this happens once the spatial derivative of $U(x,t)$ is so large that $K_{2\mathrm{D}}$ as defined in Eq. (6.22) can no longer be approximated as constant.

ii) Note that when the elastic modulus $K_{2\mathrm{D}}$ depends on the displacement field $U(x,t)$, as demonstrated in Eq. (6.22), it makes a difference whether $K_{2\mathrm{D}}$ appears in front, in between or after the two spatial derivatives in Eq. (6.17). In our nonlinear Eq. (6.23), $K_{2\mathrm{D}}$ is positioned in front of the spatial derivatives, so that the derivatives do not act on $K_{2\mathrm{D}}$. This structure of the equation is rigorously derived in Appendix E.2.

iii) The explicit values for the coefficients appearing in the parabolic fit of the experimental elastic modulus in Eq. (6.20) are taken from the equilibrium measurement shown in Fig. 6.2, these values thus correspond to an isothermal measurement at fixed temperature. In Appendix E.5, we show that the elastic modulus appropriate for small amplitude Lucassen waves is expected to be somewhat between isothermal and adiabatic, as the time scale of heat transport into the bulk medium is comparable to the oscillation time. For large wave amplitudes the heat produced or consumed during expansion and compression is therefore not transported into the bulk fluid quickly enough, so that the temperature locally deviates from the environment. For large wave amplitudes the interface deformation is thus expected to become rather adiabatic. The details of this depend on material parameters such as the monolayer heat conductivity and heat capacity, which are not well characterized experimentally. We thus perform our actual numerical calculations with the isothermal values extracted from Fig. 6.2, bearing in mind that this is clearly an approximation.

6.3 Numerical solution

We numerically solve Eq. (6.23) in the finite spatial domain $x \in [0, L]$ with the initial condition

$$U(x, t=0) = \frac{\partial U(x, t=0)}{\partial t} = 0 \tag{6.24}$$

for all x, corresponding to an initially relaxed and undeformed membrane, and the boundary conditions

$$U(x=0, t) = U_0(t), \tag{6.25}$$

$$U(x=L, t) = 0. \tag{6.26}$$

The function $U_0(t)$ in Eq. (6.25) models the mechanical monolayer excitation at the left boundary, $x = 0$, which experimentally is produced by a moving piezo-driven blade that is in direct contact with the monolayer at the interface (see Ref. [93] for more experimental details). The boundary condition Eq. (6.26) mimics the effects of a bounding wall with vanishing monolayer displacement at a distance L from the excitation source.

We solve the boundary value problem defined by Eqs. (6.23)-(6.26) by a modification of a general numerical scheme for nonlinear fractional wave equations [225]. In the numerics we discretize Eq. (6.23) on 300 grid points and use a system size of $L = 3$ cm, which in Appendix E.8 is demonstrated to be large enough so that finite size effects in the observables we consider can be neglected. The accuracy of our numerical scheme is demonstrated by comparison with analytical solutions that are available for the linear fractional wave equation Eq. (6.17) [203, 222, 223, 226]. Details of our numerical implementation can be found in Appendix E.7.

For the mechanical boundary excitation $U_0(t)$ we use a smoothed pulse function of the form

$$U_0(t) = U_0^{\max} \cdot \begin{cases} \exp\left[-(t-t_1)^2/\tau^2\right] & t < t_1, \\ 1 & t_1 \leq t \leq t_2, \\ \exp\left[-(t-t_2)^2/\tau^2\right] & t_2 < t, \end{cases} \tag{6.27}$$

which mimics the experimental protocol [93]. The pulse duration is set by the start and end times, which are fixed at $t_1 = 8.39\,\mathrm{ms}$ and $t_2 = 13.63\,\mathrm{ms}$, the switching time is given by $\tau = 2.2\,\mathrm{ms}$, all values are motivated by the experimental boundary conditions, see Appendix E.9 for details. The amplitude $U_0^{\max}$ is the important control parameter that is used to drive the system from the linear into the nonlinear regime. The function $U_0(t)$ is shown as dashed black curves in Figs. 6.4 (a)-(c).

For better interpretation of our results, we introduce the negative derivative of the displacement field

$$-U_x(x,t) = -\frac{\partial U(x,t)}{\partial x}, \tag{6.28}$$

which is a dimensionless quantity that is, according to Eq. (6.21), a measure of the relative local lipid area change or compression.

In Fig. 6.3 we show numerically calculated solutions of the nonlinear fractional wave equation Eq. (6.23) for three different driving amplitudes $U_0^{\max}$ as solid colored lines. The equilibrium area per lipid is taken as $\bar{a} = 88.4\ \text{Å}^2$, corresponding to a monolayer that is quite far from the minimum in the area modulus, see Fig. 6.2. The upper row of Fig. 6.3 shows the displacement $U(x,t)$ as a function of position x for a few different fixed times. The lower row shows the corresponding compression profiles $-U_x$, defined in Eq. (6.28), which are just the negative spatial derivatives of the displacement profiles in the upper row. The three driving amplitudes $U_0^{\max}$ are chosen such as to illustrate the effects of the nonlinear term in Eq. (6.23). For the smallest driving amplitude $U_0^{\max} = 10^{-3}$ mm, the numerically calculated profiles in Figs. 6.3 (a), (d) (solid colored lines) perfectly agree with the analytic solutions of the linearized fractional wave equation (6.17) (broken colored lines), see Appendix E.8 for details on this comparison. We thus not only see that the numerical algorithm works, we also find that $U_0^{\max} = 10^{-3}$ mm is in the linear regime. For the intermediate driving amplitude $U_0^{\max} = 0.54$ mm in Figs. 6.3 (b), (e) one can discern pronounced deviations between the nonlinear numerical results and the linear predictions, so a sub-millimeter driving amplitude already moves the system deep into the nonlinear regime. For the largest driving amplitude $U_0^{\max} = 1.85$ mm in Figs. 6.3 (c), (f) we see

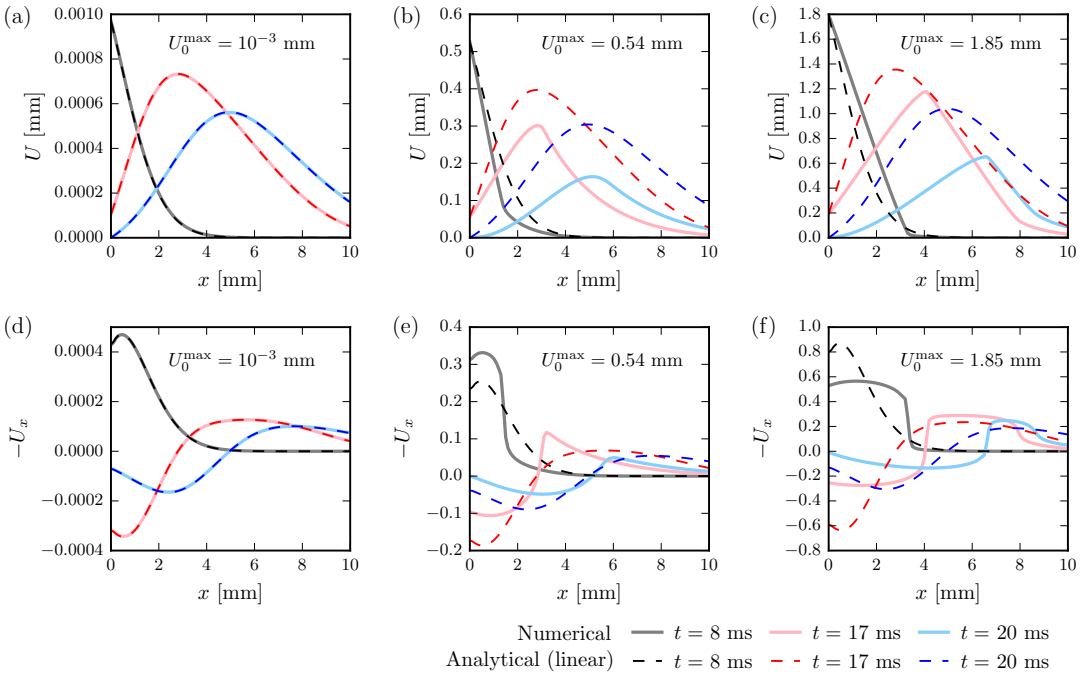

Figure 6.3: Displacement and compression profiles as a function of position x for a few different fixed times. Results are shown for three different driving amplitudes $U_0^{\max}$ as indicated in the figure legends and for a fixed equilibrium area per lipid of $\bar{a} = 88.4$ Å^2. Solid lines are obtained by numerical solution of the nonlinear fractional wave equation (6.23). Dashed lines denote analytical solutions of the linear fractional wave equation (6.17) with $\rho_{2\mathrm{D}} = 0$. Compression profiles in the lower row are calculated according to Eq. (6.28).

that the nonlinear equation predicts wave shapes that are completely different from the linear scenario, in particular, the compression profiles in Fig. 6.3 (f) exhibit rather sharp fronts.

In Fig. 6.4 we show results for the same parameters, now plotted as a function of time t and for a few different fixed separations x from the source of excitation located at $x = 0$. This way of presenting the data is in fact quite close to how nonlinear surface waves are studied experimentally [93]. The upper row of Fig. 6.4 again shows the displacement profiles $U(x,t)$, while the lower row shows the corresponding compression profiles $-U_x(x,t)$. The black curves for $x = 0$ show the excitation pulse that is applied at the boundary $x = 0$, which drives the surface wave. Again, we see that for the smallest driving amplitude $U_0^{\max} = 10^{-3}$ mm in Figs. 6.4 (a), (d) the agreement between the numerical profiles (solid colored lines) and the analytic linear solutions (broken colored lines) is perfect. The wave shape, which at the boundary $x = 0$ resembles a pulse with rather sharp flanks, changes into a much smoother function as one moves away from the driven boundary. Distinct deviations between nonlinear and linear predictions occur for larger values of $U_0^{\max}$, as shown in Figs. 6.4 (b), (e) and Figs. 6.4 (c), (f).

Based on $-U_x(x,t)$, we consider two observables that are directly measured in the experiments.

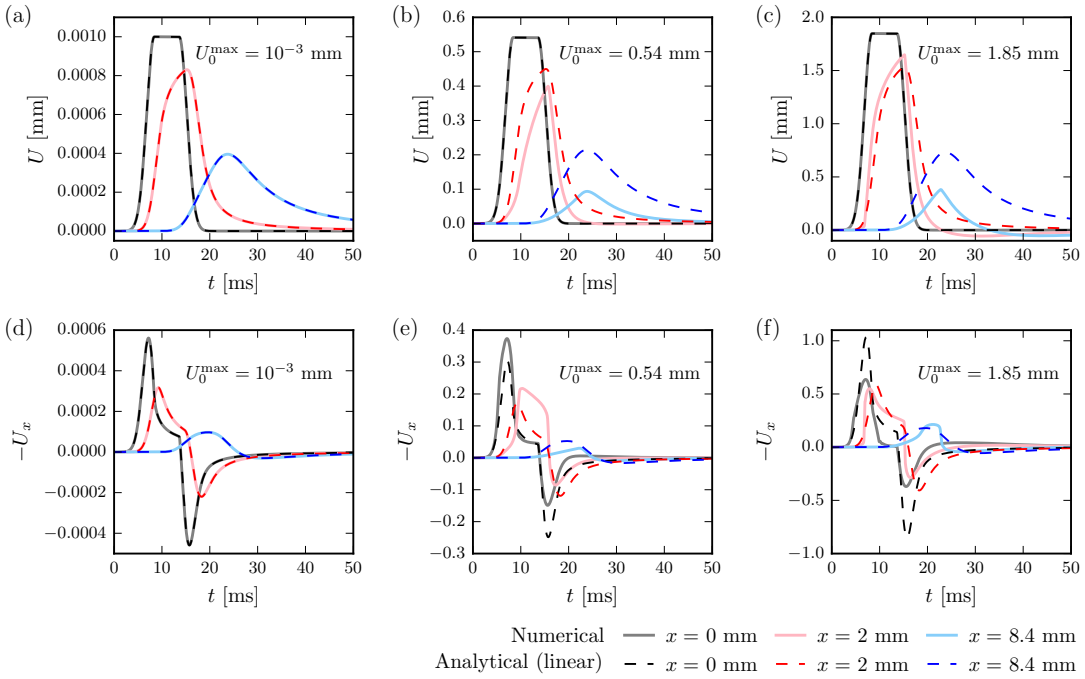

Figure 6.4: Displacement and compression profiles as a function of time t for a few different fixed separations x from the driven boundary. Results are shown for three different driving amplitudes $U_0^{\max}$ as indicated in the figure legends and for a fixed equilibrium area per lipid of $\bar{a} = 88.4$ Å^2. Solid lines are obtained by numerical solution of the nonlinear fractional wave equation (6.23). Dashed lines denote analytical solutions of the linear fractional wave equation (6.17) with $\rho_{2D} = 0$. The dashed black curves for $x = 0$ show the driving function $U_0(t)$ that is imposed as a boundary condition. Compression profiles in the lower row are calculated according to Eq. (6.28).

The first is the maximal local compression at a fixed separation x from the excitation source,

$$-\frac{\Delta a^{\min}(x)}{\bar{a}} = -\min_t \{ U_x(x,t) \} . \tag{6.29}$$

This maximal compression is in the experiments measured by the locally resolved fluorescence of pressure sensitive dyes that are incorporated into the monolayer [176], as will be further explained below.

The other important observable is the wave speed, defined by

$$c(x) = \frac{x}{t_{\min}(x) - t_1 + \tau}, \tag{6.30}$$

where $t_{\min}(x)$ is the time at which the maximal compression with a value of $-\Delta a^{\min}/\bar{a}$ arrives at position x (see Fig. 6.5 for a schematic illustration). Note that the denominator in Eq. (6.30)

is a measure of the difference of the time at which the boundary excitation $U_0(t)$ has risen to $1/e$ of its maximal value, which happens at $t = t_1 - \tau$, and the time at which the monolayer is maximally compressed at position x.

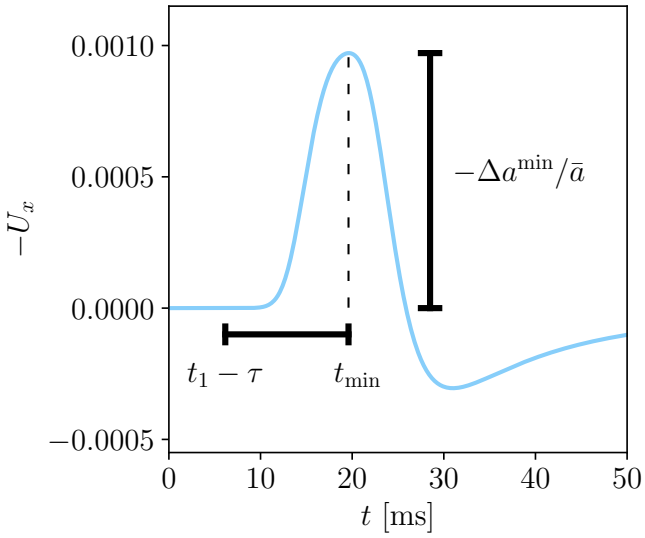

Figure 6.5: Illustration of the time it takes to observe maximal compression at a fixed position. The blue curve shows the compression field observed at $x = 8.4$ mm for a driving amplitude $U_0^{\max} = 10^{-3}$ mm. The vertical black line indicates the maximal compression $-\Delta a^{\min}/\bar{a}$ at $x = 8.4$ mm, i.e., the value of the maximum of the blue curve. The horizontal black line indicates the time difference between the boundary condition rising to $1/e$ of its maximal value, which happens at time $t_1 - \tau \approx 7$ ms, and the time when the maximal compression is observed at $x = 8.4$ mm, $t_{\min} \approx 20$ ms. The difference between these times is used to calculate the wave speed in Eq. (6.30).

In Fig. 6.6 (b) we show the maximal compression $-\Delta a^{\min}/\bar{a}$ as defined in Eq. (6.29) as a function of the driving amplitude $U_0^{\max}$ at a fixed separation $x = 8.4$ mm from the driving boundary, which is the same separation as used in the experiments [93]. Different colors correspond to different values of the equilibrium area per lipid $\bar{a}$; all employed values of $\bar{a}$ are denoted in Fig. 6.6 (a) by spheres with matching colors, superimposed with the quadratic fit for the monolayer elastic modulus K_{2D} used in the calculations. For small excitation amplitudes $U_0^{\max}$ linear behavior is obtained and the maximal compression $-\Delta a^{\min}/\bar{a}$, which in Fig. 6.6 (b) is divided by the driving amplitude $U_0^{\max}$, exhibits a plateau.

As $U_0^{\max}$ is increased, nonlinear effects are noticeable, meaning that the ratio $-\Delta a^{\min}/(\bar{a}U_0^{\max})$ depends on $U_0^{\max}$. This nonlinear behavior depends sensitively on the equilibrium area per lipid $\bar{a}$ and in particular on whether $\bar{a}$ is larger or smaller than $a_0 \approx 75\,\text{Å}^2$ for which the elastic modulus $K_{2\text{D}}$ is minimal. For $\bar{a} < a_0$ nonlinear effects lead to a monotonic increase of $-\Delta a^{\min}/(\bar{a}U_0^{\max})$ with rising $U_0^{\max}$, see the violet curve for $\bar{a} = 70\,\text{Å}^2$ in Fig. 6.6 (b). In contrast, for $\bar{a} > a_0$, $-\Delta a^{\min}/(\bar{a}U_0^{\max})$ first decreases and then shows a sudden jump as $U_0^{\max}$

increases, see the red curve for $\bar{a} = 90\,\text{Å}^2$ in Fig. 6.6 (b). The latter behavior is close to what has been seen experimentally [93].

The dependence of the wave speed c in Fig. 6.6 (c) on the excitation amplitude shows an even more pronounced nonlinear behavior. For $\bar{a} < a_0$ nonlinear effects lead to a monotonic and smooth increase of the wave speed as a function of the driving amplitude $U_0^{\max}$, while for $\bar{a} > a_0$ the speed decreases slightly and then abruptly increases at a threshold amplitude of about $U_0^{\max} = 2$ mm. These excitation amplitudes are easily reached experimentally and thus relevant to the experimentally observed nonlinear effects, as will be discussed later.

Since the nonlinear effects in our theory are introduced via taking into account local variations of the area modulus $K_{2\text{D}}$, they can be rationalized by analyzing how the linear Lucassen relation depends on $K_{2\text{D}}$. Within the linear Lucassen theory, the characteristic length that characterizes the damping along the wave propagation direction is given by

$$\lambda_{\|} = \frac{1}{\text{Im}(k)} \sim \sqrt{K_{2\text{D}}}, \tag{6.31}$$

while the phase velocity follows as

$$c_{\|} = \frac{\omega}{\text{Re}(k)} \sim \sqrt{K_{2\text{D}}}, \tag{6.32}$$

where we used the result in Eq. (6.14) for the wave number $k(\omega)$. According to Eqs. (6.31), (6.32), a larger area modulus $K_{2\text{D}}$ thus not only leads to a larger decay length $\lambda_{\|}$, but also to a larger phase velocity $c_{\|}$. For an initial area $\bar{a} = 70\text{Å}^2$, in the compressive part of the pulse, i.e., where $-U_x > 0$, the monolayer is compressed and thus characterized by a smaller local area $a < \bar{a}$. From Fig. 6.6 (a) it becomes clear that since $\bar{a}$ is located to the left of the minimum at a_0, this compression increases the local area modulus. Thus, according to Eqs. (6.31), (6.32), for $\bar{a} < a_0$, nonlinear effects are expected to increase the range and the speed of the surface waves, as indeed seen in Fig. 6.6.

For initial areas $\bar{a} > a_0$, on the other hand, a small local compression will decrease $K_{2\text{D}}$, and only beyond a certain threshold driving amplitude the regime $a < a_0$, where $K_{2\text{D}}$ increases upon further local compression, will be reached. We can thereby explain the non-monotonic behavior of the maximal compression and the wave speed seen in the numerical data in Figs. 6.6 (b), (c) in a simple manner. In physical terms, the minimum in range and velocity for $\bar{a} > a_0$ occurs when nonlinear compression effects are large enough to locally drive the membrane into the minimum in the area modulus $K_{2\text{D}}$ located at a_0.

6.4 Comparison with experimental data

Nonlinear surface waves in a DPPC monolayer have been recently discovered experimentally [93, 94, 176]. In the experimental setup of our collaborators Prof. Dr. Matthias F. Schneider and Dr. Shamit Shrivastava, a DPPC monolayer that contains a small amount of pressure-sensitive fluorophores is spread at the air-water interface. A razor blade is placed on top of the interface so that it touches the monolayer at a line, consistent with the harmonic wave ansatz Eqs. (6.8), (6.9)

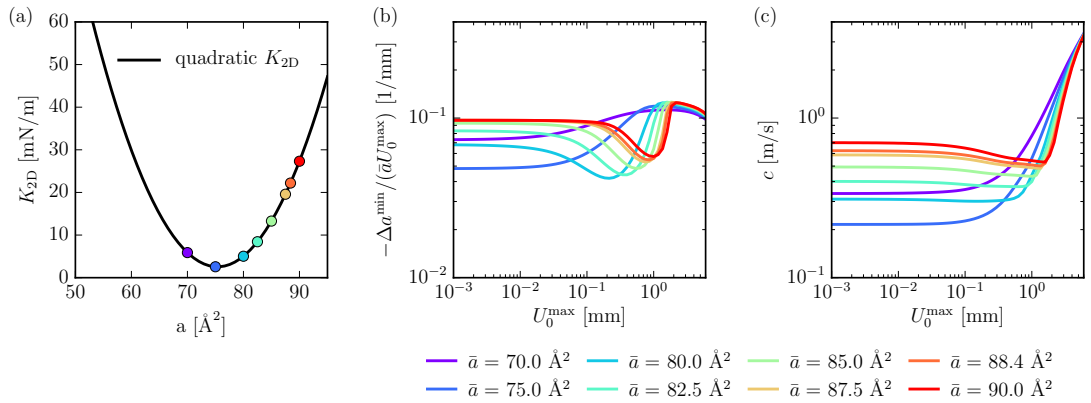

Figure 6.6: Numerical nonlinear results. (a) Black line: Quadratic fit to the elastic modulus shown in Fig. 6.2. Colored dots: The different initial areas per lipid $\bar{a}$ used for generating subplots (b), (c). (b), (c) Numerical results for the boundary value problem given by Eqs. (6.23-6.26), with the boundary condition given by Eq. (6.27) and the quadratic K_{2D} shown in subplot (a), for different initial areas per molecule $\bar{a}$. Subplot (b) shows the maximal compression $-\Delta a^{\min}/\bar{a}$ at a distance $x = 8.4$ mm from the excitation source, calculated using Eq. (6.29) and divided by $U_0^{\max}$. Subplot (c) shows the corresponding wave velocity c according to Eq. (6.30).

upon which or theory is based, which assumes that the displacement field decays exponentially for $z < 0$, i.e., away from the interface. A piezo element is used to drive the blade laterally and thereby to compress the monolayer at one end. The excitation pulse shape resembles the smoothed rectangular pulse defined in Eq. (6.27). At a fixed separation $x = 8.4\,\mathrm{mm}$ from the razor blade a fast camera records the fluorescence resonance energy transfer (FRET) efficiency of the fluorophores as a function of time. Using an independent measurement of the FRET efficiency as a function of the area per lipid for an equilibrium isothermal compression of a DPPC monolayer, the recorded time-dependent FRET efficiency is converted into the time-dependent area per lipid $a(t)$, as described in detail before [94]. Waves are excited using different driving voltage amplitudes V_0 of the piezo element, for each value of V_0 the FRET efficiency as a function of time is recorded and converted to yield the compression $\Delta a(t) = a(t) - \bar{a}$. From the maximum of $\Delta a(t)$ the maximal compression $-\Delta a^{\min}$ at a separation $x = 8.4\,\mathrm{mm}$ and the time shift $t_{\min}$ at which this maximal compression occurs are calculated [94]. Figure 6.7 (a) shows the experimental results for the relative maximal compression $-\Delta a^{\min}/\bar{a}$ (red spheres) as a function of the piezo driving potential V_0. The data show a steep increase at a threshold excitation amplitude and level off at a compression of roughly $-\Delta a^{\min}/\bar{a} \approx 0.2$. The experimental wave velocity (red spheres) in Fig. 6.7 (b) slightly increases with rising driving voltage and is in the order of $c \approx 0.35$ m/s.

To compare with our theoretical results we evaluate Eqs. (6.23)-(6.26) at an equilibrium lipid area $\bar{a} = 88.4$ Å^2, which corresponds to the experimental equilibrium surface pressure $\pi = 4.3\,\mathrm{mN/m}$, see Fig. 6.2. For different values of the excitation amplitude $U_0^{\max}$ we calculate

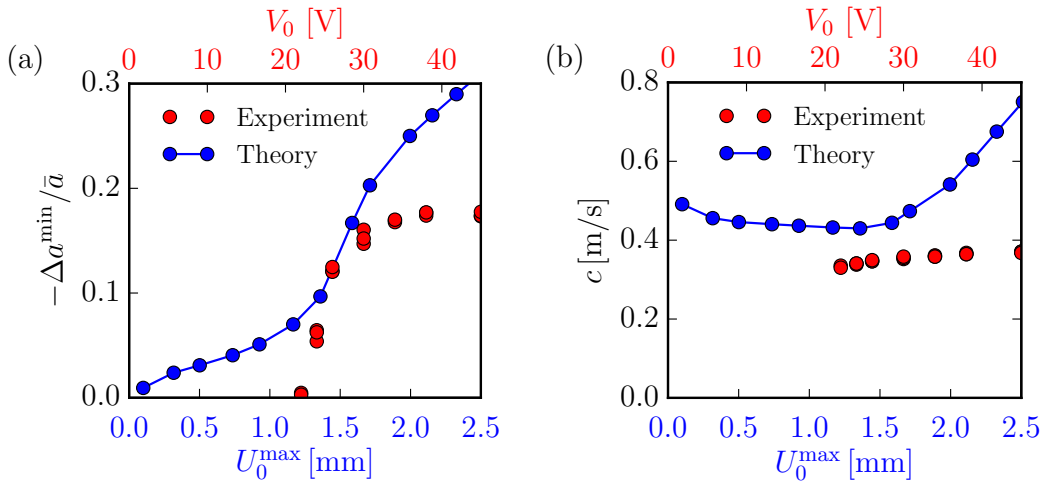

Figure 6.7: Comparison of numerical and experimental results at a distance $x = 8.4$ mm from the excitation source as a function of the excitation amplitude. The numerical data is obtained by solution of the boundary value problem given by Eqs. (6.23-6.26), with the boundary condition given by Eq. (6.27) and the quadratic elastic modulus K_{2D} shown in Fig. 6.2, and various driving amplitudes $U_0^{\max}$. The initial area per lipid $\bar{a} = 88.4\,\text{Å}^2$ corresponds to an initial pressure $\pi = 4.3\,\text{mN/m}$, c.f. Fig. 6.2. Observables are calculated using Eqs. (6.29), (6.30), with $x = 8.4$ mm. The experimental data is obtained by exciting waves in a DPPC monolayer on a Langmuir trough filled with water using various driving voltages V_0, and measuring the FRET efficiency of pressure sensitive fluorophores at distance $x = 8.4$ mm away from the excitation source [93, 94]. The equilibrium surface pressure of the DPPC monolayer is $\pi = 4.3$ mN/m.

the maximal compression and the wave velocity c at a separation $x = 8.4$ mm using Eqs. (6.29) and (6.30). Figure 6.7 shows that our theory (blue data points connected by lines) is in reasonable agreement with the experiments, the only adjustable parameter in the comparison is a rescaling of the driving amplitude $U_0^{\max}$, which is necessary since the piezo voltage can not precisely be converted to the oscillation amplitude of the razor blade. The theoretical maximal relative compression $-\Delta a^{\min}/\bar{a}$ shows a quite sharp increase of the relative compression from around $-\Delta a^{\min}/\bar{a} \approx 0.1$ to $-\Delta a^{\min}/\bar{a} \approx 0.2$, while the experimental data seem to increase from $-\Delta a^{\min}/\bar{a} \approx 0$ to $-\Delta a^{\min}/\bar{a} \approx 0.2$. In both theory and experiment, at the threshold driving amplitude a slight increase in the wave velocity is obtained, the value of the wave velocity is quite similar in experiments and theory. This is remarkable, since no freely adjustable parameter is present in the theory.

One possible reason for the deviations between theory and experiments is that our theoretical model employs the isothermal elastic modulus extracted from the equilibrium pressure isotherm shown in Fig. 6.2. This is an approximation, since the temperature is not expected to be strictly constant during the wave propagation, as mentioned before and discussed in Appendix E.5. Indeed, it is well known that isotherms obtained from compressing a monolayer depend on the compression speed used [227], that the slowest relaxation modes in a lipid monolayer are on

time scales comparable to those of the wave oscillation time [228, 229], and furthermore that the viscoelastic properties of lipid membranes close to phase transitions can show anomalous behavior like an effective negative surface viscosity [190]. Thus, the elastic modulus relevant for the non-equilibrium phenomenon of a propagating large-amplitude surface wave might differ significantly from the isothermal elastic modulus characterizing quasi-static monolayer compression. Turning this around, our theory might in fact be used to shed light on the transition of monolayer elasticity from the isothermal to the adiabatic regime, as will be explained below.

6.5 Conclusions

In the present chapter, we derive a fractional wave equation for a compressible surface wave on a viscous liquid from classical hydrodynamic equations. This fractional wave equation has a simple physical interpretation in terms of the frequency-dependent penetration depth of the surface wave into the liquid subphase. Our derivation complements previous approaches where fractional wave equations were obtained by invoking response functions with fractional exponents [205–209], and constitutes the first derivation of a fractional wave equation from first physical principles. Therefore, on a fundamental level, our theory sheds light on how fractional wave behavior emerges from the viscous coupling of an interface to the embedding bulk medium.

For the explicit system of a monolayer at the air-water interface, nonlinear behavior emerges naturally since large monolayer compression changes the local monolayer compressibility. Our theory describes the experimentally observed nonlinear acoustic wave propagation in a DPPC monolayer without adjustable fit parameters. In particular, the all-or-nothing response for the maximal compression of a monolayer as a function of the driving amplitude is reproduced and explained by the fact that the acoustic wave locally drives the monolayer through a smeared-out phase transition.

Our theory reveals the origin of nonlinear behavior of pressure waves in compressible monolayers, which are fundamentally different from the nonlinear mechanism for action potential propagation. The connection between these two phenomena, which experimentally are always measured together, have fascinated researchers from different disciplines for a long time [92, 93, 191, 192, 230].

Our theory might also be used to extract non-equilibrium mechanical properties of biomembranes: Experimental monolayer compressibilities depend on the compression speed employed in the measurement [227], consequently the elastic modulus that enters the Lucassen wave theory is neither strictly isothermal nor adiabatic. Our theory could via inversion be used to extract the elastic modulus from experimentally measured surface wave velocities and thereby help to bridge the gap from isothermal membrane properties to adiabatic membrane properties, which is relevant for membrane kinetics.

More specifically, our theory might be able to shed light on the origin of effective negative surface viscosities of lipid membranes extracted from surface wave experiments [190]. In these experiments, linear surface wave theories are employed to analyze experimental data, and a negative surface viscosity in a linear theory could be the signature of nonlinear effects that enhance wave propagation, as indeed observed in our nonlinear theory.

Chapter 7

Summary and Outlook

In this thesis we consider several biological soft-matter systems where memory effects are relevant. The first part discusses the large-scale dynamics of several polymer backbone models and how these relate to the loop-formation time. In the second part we analyze model systems to understand how non-Markovian dynamics determines reaction kinetics. The third part considers surface waves, both linear and nonlinear, and relates compression waves in interfaces to a non-Markovian generalization of the wave equation.

In Chapter 2, we investigate the loop-formation kinetics of different polymer backbone models. We consider several models with only bonded interactions (phantom chains), and a self-avoiding collapsed chain. From Langevin simulations we calculate memory kernels for the scalar end-to-end distance. For all phantom chains we find identical intermediate $\Gamma \sim t^{-1/2}$ scaling regimes; for the self-avoiding collapsed chain we find $\Gamma \sim t^{-6/11}$. Both scalings are derived using Flory theory. We calculate cyclization times τ_c from our simulations to investigate the asymptotic scaling $\tau_c \sim N^{\lambda}$ with chain length N. For the phantom chains we recover the classical results $\lambda = 2$ due to Wilemski-Fixman (WF) [72, 73], and $\lambda = 3/2$ due to Szabo-Schulten-Schulten (SSS) [74], depending on the terminal-monomer distance where one considers a loop to have formed. For the self-avoiding collapsed chain we find $\lambda = 5/3$. We use Flory theory to provide generalizations of both the WF and SSS scalings to include non-ideal conditions, and identify the observed scaling $\lambda = 5/3$ as a generalization of the WF scaling for poor solvent conditions [105].

Experiments found that both diffusion of the terminal monomer in double-stranded DNA [231] and equilibrium fluctuations of intramolecular distances in proteins display non-Markovian effects [64, 117], the latter ones being characterized by a memory kernel scaling $\Gamma \sim t^{-1/2}$. The same scaling was obtained in an effective model for the dynamics of single monomers in a Gaussian chain undergoing Rouse dynamics [32, 34]. We connect these results by demonstrating that the memory kernel for the end-to-end distance of a Gaussian chain also scales as $\Gamma \sim t^{-1/2}$, and is independent of the detailed nature of the bonded interactions. Our results for self-avoiding collapsed chains furthermore demonstrate that this scaling breaks down once self-avoidance effects become relevant. We provide a comprehensive picture of the relations between interactions on the molecular scale and non-Markovian effects in the large-scale end-to-end dynamics, which will be helpful in interpreting experimentally observed scaling behavior of intrachain distance dynamics.

In Chapter 3, we investigate barrier crossing for non-Markovian dynamics characterized by an exponential memory kernel with a single memory time scale and a single long-time friction coefficient. We simulate the corresponding generalized Langevin equation and compare the resulting barrier-crossing times to theoretical predictions. We confirm that the commonly used Grote-Hynes (GH) theory [87] is only applicable in the double limit of short memory and high-friction (overdamped) dynamics, and that the theory by Pollak-Grabert-Hänggi (PGH) [88] yields accurate predictions of the mean first-passage time (MFPT) for barrier crossing over the entire parameter space. In particular, both simulations and PGH theory recover the various known asymptotic scalings for the MFPT as well as a regime at intermediate memory times where memory leads to a decrease of the MFPT. As an easy-to-implement alternative to the PGH formula, we supply a heuristic formula, show that it accurately predicts the MFPT over many orders of magnitude in the system parameters, and use it to establish a scaling diagram featuring the Markovian high-friction and inertial regimes, the non-Markovian long-memory regime, and the regime at intermediate memory times where finite memory reduces the barrier crossing time. Our results are corroborated by an asymptotic analysis of the propagator for the generalized Langevin equation, which recovers both the long-memory regime and predicts the acceleration of barrier crossing at intermediate memory times.

The heuristic formula we provide is a convenient tool for the calculation of barrier crossing times from known memory times, or, conversely, for the estimation of memory times from barrier crossing times measured in MD simulations or experiments. Our analysis allows to quickly determine whether, for a given system, memory effects are relevant or not. Physically relevant parameters [25, 29, 86, 140] encompass the regime where neither Markovian models nor GH theory, which are easy to use, are reliable, so that our heuristic formula will be useful to simply and accurately estimate reaction rates for such systems.

In Chapter 4, we move on to a generalization of the non-Markovian system from Chapter 3 by adding a second memory time scale, i.e., we consider a memory kernel given by the sum of two exponentials. From simulations of the corresponding generalized Langevin equation we find that the shorter of the two memory times determines the barrier-crossing time; for the long-memory regime, we derive this from an analysis of the propagator of the generalized Langevin equation. Based on these observations, we reduce the bi-exponential system to an effective single-exponential system. Using the resulting effective parameters in the heuristic formula established in Chapter 3 yields a global description of our numerical results. This explicitly demonstrates that bi-exponential barrier crossing can be reduced to an effective single-exponential scenario.

Although physical reaction coordinates are typically coupled to orthogonal degrees of freedom with several intrinsic time scales [29, 86, 142–145], due to its simplicity the single-exponential system is the most studied [88, 122, 131, 132]. Thus, a reliable method for reducing more complex memory kernels to an effective single-exponential memory kernel is of great practical value. Our results constitute a first step in this direction, and it will be interesting to find out whether, for the purpose of estimating barrier-crossing times, more complex memory kernels can also be reduced to an effective single-exponential scenario. A logical next step in this direction will be to consider a memory kernel given by a sum of an instantaneous frictional force and a single exponential decay.

In Chapter 5 we derive the general dispersion relation for surface waves at a viscoelastic interface. We show that our theory contains the classical Rayleigh [153–155], capillary-gravity [148, 172] and Lucassen wave solutions [156–159] as limiting cases. We furthermore identify an additional wave solution, which is different from all previously studied solutions and requires surface tension, gravitation and bulk viscosity all to be simultaneously nonzero. For the experimentally relevant case of an air-water interface with an adsorbed surfactant layer we establish a phase diagram for the number of coexisting wave solutions in terms of frequency and surface compression modulus. In particular, we demonstrate that Rayleigh and Lucassen waves do not coexist but rather continuously transform into each other, and that our novel capillary-gravity-viscosity (CGV) wave coexists with both capillary-gravity and Lucassen waves for a small range of nonzero surface compressibilities.

Although the CGV wave only exists for low frequencies and is highly damped on a pure air-water interface, it should be within reach of experiments. Surface waves have many applications ranging from microfluidics [232] to earthquake modeling [233], so that our unifying general dispersion relation is not only of theoretical interest. In particular, our analysis allows to quickly identify which surface wave is relevant for which parameter regime and how the various surface wave solutions are related to each other.

In Chapter 6, we derive the fractional wave equation governing two-dimensional sound waves in a compressible interface on a viscous liquid. These surface waves are the Lucassen waves from Chapter 5, and their properties are different from three-dimensional sound waves because of the coupling of the interface to the bulk medium. More specifically, the frequency-dependent penetration depth of the surface wave into the liquid subphase leads to the fractional derivative in the effective equation for the surface wave; this fractional derivative constitutes a memory effect, and effectively models the effects of the liquid subphase on the interface. For the explicit system of a monolayer at the air-water interface, nonlinear behavior emerges naturally since large monolayer compression causes local changes in the monolayer compressibility. Employing isotherms measured by our experimental collaborators Matthias Schneider and Shamit Shrivastava, we include nonlinear effects into our theory, and find that numerical solutions of the resulting nonlinear fractional wave equation describe the experimentally observed nonlinear acoustic wave propagation in a DPPC monolayer without adjustable fit parameters. In particular, the all-or-nothing response for the maximal compression of a monolayer as a function of the driving amplitude is reproduced, and explained by the fact that the acoustic wave locally drives the monolayer through a smeared-out phase transition.

Our theory is interesting from a theoretical, biophysical and membrane-focused standpoint. From a theoretical perspective, we present the first derivation of a fractional wave equation from first physical principles, and thus, on a fundamental level, shed light on how fractional wave behavior emerges from the viscous coupling of an interface to the embedding bulk medium. The fractional wave equation is easily generalized to include the effects of surface viscosity or bending rigidity, which might be useful for modeling pressure waves in other systems with interfaces. Our theory reveals the origin of nonlinear behavior of pressure waves in compressible monolayers, which are fundamentally different from the nonlinear mechanism for action potential propagation. The connection between these two phenomena, which experimentally are always measured to-

gether, have fascinated researchers from different disciplines for a long time [92,93,191,192,230]. From a membrane-focused perspective, our theory might also be used to extract non-equilibrium mechanical properties of biomembranes. Experimental monolayer compressibilities depend on the compression speed employed in the measurement [227], consequently the elastic modulus that enters the Lucassen wave theory is neither strictly isothermal nor adiabatic. Via inversion, our fractional wave equation could be used to extract the elastic modulus from experimentally measured surface wave velocities and thereby help to bridge the gap from isothermal membrane properties to adiabatic membrane properties, which is relevant for membrane kinetics. More specifically, our theory might be able to explain the origin of effective negative surface viscosities of lipid membranes extracted from surface wave experiments [190]. In these experiments, linear surface wave theories are employed to analyze experimental data, and a negative surface viscosity in a linear theory could be the signature of nonlinear effects that enhances wave propagation, as indeed observed in our theory.

Appendix A

Supplemental Material for Chapter 2

A.1 Simulation details

We simulate four different polymer backbone models via Langevin dynamics at temperature $T = 300$ K using GROMACS 2016.3 [57].

i) Gaussian chain. We consider a Gaussian chain comprised of N monomers with masses m_i, governed by the equations of motion

$$m_i \ddot{\vec{R}}_i = -\gamma \dot{\vec{R}}_i + \kappa \left(\vec{R}_{i-1} - 2\vec{R}_i + \vec{R}_{i+1} \right) + \vec{F}_i, \tag{A.1}$$

where $i = 0, ..., N-1$, $\vec{R}_i$ is the position of the i-th monomer, γ is a friction coefficient, κ describes the strength of the quadratic nearest-neighbor interaction, and the random forces $\vec{F}_i$ obey the fluctuation dissipation theorem

$$\langle \vec{F}_i(t) \vec{F}_j^T(t') \rangle = 2\gamma k_\mathrm{B} T \mathbb{1} \delta_{i,j} \delta(t - t'), \tag{A.2}$$

where $k_\mathrm{B} \approx 1.38 \cdot 10^{-23}\,\mathrm{J/K}$ is the Boltzmann constant, $\mathbb{1}$ is the (3×3) unit matrix, $\delta_{i,j}$ is the Kronecker delta and $\delta(t)$ is the Dirac delta function. For ease of notation we introduced $\vec{R}_{-1} \equiv \vec{R}_0$, $\vec{R}_N \equiv \vec{R}_{N-1}$ in Eq. (A.1). Our parameters are based on the model for alkanes in the gromos53a6 forcefield [106], where an alkane containing N carbon atoms is modeled as a linear chain of monomers with masses $m_0 = m_{N-1} = 15$ amu (representing terminal CH_3 residues), $m_1 = ... = m_{N-2} = 14$ amu (representing in-chain CH_2 residues). The mean squared distance between neighboring monomers is $\langle (\vec{R}_i - \vec{R}_{i+1})^2 \rangle = b^2$ with $b = 0.153$ nm, which we reproduce in our simulation by using $\kappa = k_\mathrm{B}T/b^2 = 319.8\,\mathrm{amu/ps^2}$. We use the friction coefficient $\gamma = 110$ amu/ps, which is smaller than the expected friction coefficient in explicit water by about an order of magnitude, but allows for more efficient sampling of the polymer dynamics.

ii) Freely jointed (FJ) chain. The simulations of the FJ chain are similar to the Gaussian chain simulations, but with the distance between neighboring monomers constraint to $b = 0.153$ nm using the LINCS constraint algorithm included in the GROMACS simulation package.

iii) Freely rotating (FR) chain. The simulations of the FR chain are similar to the Gaussian chain simulations, but with distances between nearest neighbors constraint to $b = 0.153$ nm

and bond angles constraint to $\theta = 111^\circ$, which is the average bond angle for alkane chains in the standard gromos53a6 forcefield. The constraints are implemented using SHAKE algorithm included in the GROMACS simulation package.

iv) Gaussian chain with LJ interactions (GLJ). For the GLJ chain, the Gaussian chain model described in i) is extend to include the standard non-bonded LJ interactions for alkane chains as modeled in the gromos53a6 forcefield [106]. For the interaction between monomer i and monomer j (with $|i-j| > 3$), the potential is

$$U_{i,j}^{\mathrm{LJ}}(R_{i,j}) = \frac{C_{12,(i,j)}}{R_{i,j}^{12}} - \frac{C_{6,(i,j)}}{R_{i,j}^{6}}, \tag{A.3}$$

where $R_{i,j} = \sqrt{(\vec{R}_i - \vec{R}_j)^2}$, and the parameters $C_{12,(i,j)}$, $C_{6,(i,j)}$ are given as [106]

$$C_{12,(i,j)} = \begin{cases} 3.40 \cdot 10^{-5}\ \mathrm{nm}^{12} \cdot \mathrm{kJ/mol} & 1 \le i,j \le N-2, \\ 2.67 \cdot 10^{-5}\ \mathrm{nm}^{12} \cdot \mathrm{kJ/mol} & i,j \in \{0, N-1\}, \\ & i \in \{0, N-1\}, \\ 3.01 \cdot 10^{-5}\ \mathrm{nm}^{12} \cdot \mathrm{kJ/mol} & 1 \le j \le N-2, \\ & \text{or vice versa,} \end{cases} \tag{A.4}$$

and

$$C_{6,(i,j)} = \begin{cases} 7.47 \cdot 10^{-3}\ \mathrm{nm}^{6} \cdot \mathrm{kJ/mol} & 1 \le i,j \le N-2, \\ 9.61 \cdot 10^{-3}\ \mathrm{nm}^{6} \cdot \mathrm{kJ/mol} & i,j \in \{0, N-1\}, \\ & i \in \{0, N-1\}, \\ 8.47 \cdot 10^{-3}\ \mathrm{nm}^{6} \cdot \mathrm{kJ/mol} & 1 \le j \le N-2, \\ & \text{or vice versa.} \end{cases} \tag{A.5}$$

The minimum in the LJ potential Eq. (A.3) is at $R_{(i,j)}^{\min} = (2C_{12,(i,j)}/C_{6,(i,j)})^{1/6}$, so that

$$R_{(i,j)}^{\min} \approx \begin{cases} 0.46\ \mathrm{nm} & 1 \le i,j \le N-2, \\ 0.42\ \mathrm{nm} & i,j \in \{0, N-1\}, \\ & i \in \{0, N-1\}, \\ 0.44\ \mathrm{nm} & 1 \le j \le N-2, \\ & \text{or vice versa,} \end{cases} \tag{A.6}$$

and consequently $R_{(i,j)}^{\min} \approx 3b$.

A.2 Chain segments of our self-avoiding collapsed chain model do not cross

One qualitative difference between the Gaussian, FJ, FR chains and the GLJ chain is self-avoidance. This means that, depending on κ and the LJ parameters, in the GLJ model different

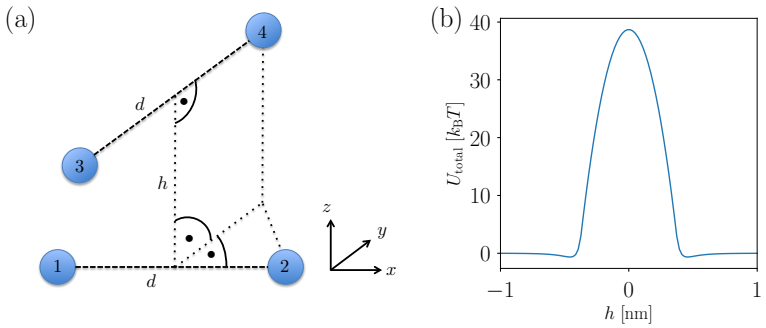

Figure A.1: (a) Setup for calculation of chain-self-crossing energy. The two pairs (1,2), (3,4) represent consecutive monomers along the chain that interact via a harmonic potential, respectively. Note that despite the numbering, here monomers 2 and 3 are not consecutive monomers in the chain. The non-bonded pairs (1,3), (1,4), (2,3), (2,4) interact via the LJ potential Eq. (A.3). (b) Total energy of the configuration defined in subplot (a). For each value of h, the total interaction energy (A.7) is minimized as a function of d.

chain segments do not cross each other anymore. To show that for our parameters this is the case, we estimate the potential barrier faced by two chain segments passing through each other. We consider two chain segments in the geometry depicted in Fig. A.1 (a). Along the chain, the monomer pairs (1,2), (3,4) interact via harmonic potentials and are a distance d apart, respectively. The non-bonded pairs (1,3), (1,4), (2,3), (2,4) interact via LJ potentials. Note that despite the numbering, here monomers 2 and 3 are not consecutive monomers in the chain. We assume that monomers (1,2) lie in the x-y-plane, and monomers (3,4) are positioned at a height h above that plane. The total interaction energy of this system is given by

$$U_{\text{total}}(d,h) = 2U^{\text{H}}(d) + 4U^{\text{LJ}}_{i,j}\left(\sqrt{h^2 + d^2/2}\right), \tag{A.7}$$

where $U^{H}(d) = \kappa/2d^2$ is the (bonded) harmonic interaction and $U^{\text{LJ}}_{i,j}$ the LJ potential defined in Eq. (A.3). Chain crossing means that h changes continuously from a (large) positive value to a (large) negative value. To estimate the potential barrier for two chain segments crossing, we vary h/nm in the range $[-1, 1]$, and for each value of h minimize $U_{\text{total}}(d,h)$ as a function of d. Employing κ and the LJ parameters for in-chain beads ($1 \leq i,j \leq N-2$) as defined Appendix A.1, the resulting total energy is shown as a function of h in Fig. A.1 (b). We see that for the two chain segments to pass through each other, an energy barrier of almost 40 $k_{\text{B}}T$ has to be crossed. We thus conclude that it is extremely unlikely that two distant chain segments cross.

A.3 Extraction of memory kernels from simulations

The goal of memory kernel extraction is to use a given numerical trajectory $x(t)$ to parametrize the generalized Langevin equation (GLE)

$$\mu\,\ddot{x}(t) = -\int_0^t \mathrm{d}t'\,\Gamma(t-t')\dot{x}(t') - \nabla U(x(t)) + F_R(t), \tag{A.8}$$

where μ is an effective mass, ∇U is the derivative of the potential of mean force (pmf) U, Γ is a memory kernel describing non-Markovian friction effects, and the random force F_R is a Gaussian stochastic process with zero mean, and which obeys the generalized fluctuation-dissipation theorem (FDT)

$$\langle F_R(t)F_R(t')\rangle = k_\mathrm{B}T\,\Gamma(|t-t'|). \tag{A.9}$$

We extract memory kernels using a recent generalization of the Berne method [107] developed by Daldrop et al. [108]. In a nutshell, to obtain the memory kernel from numerical simulations, the GLE (A.8) is multiplied by $\dot{x}(0)$ and then an ensemble average is performed. Since $\langle F_R(t)\dot{x}(0)\rangle = 0$, this leads to the equation

$$\mu\langle\dot{x}(0)\ddot{x}(t)\rangle = -\int_0^t \mathrm{d}t'\,\Gamma(t-t')\left\langle\dot{x}(0)\dot{x}(t')\right\rangle - \left\langle\dot{x}(0)\nabla U(x(t))\right\rangle. \tag{A.10}$$

Discretizing time using a timestep Δt then leads to a recurrence relation for the memory kernel, namely [108]

$$\Gamma_i = -\frac{1}{\omega_{i,i}\Delta t C_0^{\dot{x}\dot{x}}}\left(\sum_{j=0}^{i-1}\omega_{i,j}\Delta t\Gamma_i C_{i-j}^{\dot{x}\dot{x}} + \mu C_i^{\dot{x}\ddot{x}} + C_i^{\dot{x}\nabla U}\right), \tag{A.11}$$

where $\Gamma_i := \Gamma(i\cdot\Delta t)$, $\omega_{i,j} := 1-\delta_{i,0}/2-\delta_{i,j}/2$ is the integration weight for the trapezoidal rule, we define $C_i^{\dot{x}\dot{x}} := \langle\dot{x}(0)\dot{x}(i\cdot\Delta t)\rangle$ and similarly for $C_i^{\dot{x}\ddot{x}}$, $C_i^{\dot{x}\nabla U}$. After U is obtained from simulations via Boltzmann inversion and approximated by a cubic spline, all correlation functions can be evaluated directly from the numerical data. The effective mass μ can be obtained employing the equipartition theorem $\mu\langle\dot{x}(0)\dot{x}(0)\rangle = k_\mathrm{B}T$. For more details, we refer the reader to Ref. [108].

A.4 Comparison of numerical and analytical memory kernels

A.4.1 Analytical formula for the memory kernel of the end-to-end vector of a Gaussian chain

To validate the numerical algorithm Eq. (A.11), we compare numerically calculated memory kernels to analytically calculated memory kernels. For the end-to-end distance $R_\mathrm{ete} = \sqrt{(\vec{R}_{N-1}-\vec{R}_0)^2}$ considered in Chapter 2 no analytical formula for the memory kernel Γ is

available. However, as we show now, for the end-to-end distance vector $\vec{R}_{\mathrm{ete}} = \vec{R}_{N-1} - \vec{R}_0$ of a Gaussian chain an analytical formula for the memory kernel can be obtained using the Mori-Zwanzig projection operator technique [14, 15].

Since in Eq. (A.1), the x-, y- and z-components of the positions decouple and have identical equations of motion, it is sufficient to consider the x-component. The equations for the x-components of the N monomers can be rewritten as a first-order equation in $2N$ dimensions,

$$\dot{\vec{v}}(t) = \Omega \vec{v}(t) + \vec{f}(t), \tag{A.12}$$

with

$$\vec{v}(t) := \begin{pmatrix} \vec{R}(t) \\ \dot{\vec{R}}(t) \end{pmatrix} \in \mathbb{R}^{2N}, \tag{A.13}$$

$$\Omega := \begin{pmatrix} 0 & \mathbb{1} \\ M^{-1}K & -M^{-1}\gamma \end{pmatrix} \in \mathbb{R}^{(2N)\times(2N)} \tag{A.14}$$

$$\vec{f}(t) := \begin{pmatrix} \vec{0} \\ M^{-1}\vec{F}(t) \end{pmatrix} \in \mathbb{R}^{2N} \tag{A.15}$$

where $\vec{R} = (R_{0,x}, R_{1,x}, ..., R_{N-1,x})^T$ are the x-components of the monomer positions, $\mathbb{1}$ denotes the $N \times N$ unit matrix and the coupling matrix K for the nearest-neighbor interactions has components $K_{ij} = \kappa\Delta_{ij} = \kappa(-2\delta_{i,j} + \delta_{i+1,j} + \delta_{i,j+1} + \delta_{i,0}\delta_{j,0} + \delta_{i,N-1}\delta_{j,N-1})$, where $\delta_{i,j}$ denotes the Kronecker delta. Note that the following derivation generalizes to arbitrary coupling matrices K.

To derive the effective dynamics of the x-component of the end-to-end distance vector, we define $\vec{b} \in \mathbb{R}^N$ with components $b_i = -\delta_{i,0} + \delta_{i,N-1}$, and subsequently define the projection operator

$$P := B\left(B^T B\right)^{-1} B^T \in \mathbb{R}^{(2N)\times(2N)}, \tag{A.16}$$

where

$$B := \begin{pmatrix} \vec{b} & 0 \\ 0 & \vec{b} \end{pmatrix} \in \mathbb{R}^{(2N)\times 2}. \tag{A.17}$$

With these definitions, it follows that

$$B^T\vec{v} = \begin{pmatrix} R_{N-1,x} - R_{0,x} \\ \dot{R}_{N-1,x} - \dot{R}_{0,x} \end{pmatrix} \equiv \begin{pmatrix} R_{\mathrm{ete},x} \\ \dot{R}_{\mathrm{ete},x} \end{pmatrix}, \tag{A.18}$$

so that P projects onto the x-component of the end-to-end vector $\vec{R}_{\mathrm{ete}}$. Consequently, the operator $Q := \mathbb{1} - P$, projects onto the orthogonal complement. Acting with P, Q onto Eq. (A.12) and using $\mathbb{1} = P + Q$, we obtain

$$P\dot{\vec{v}} = P\Omega\left(P\vec{v}\right) + P\Omega\left(Q\vec{v}\right) + P\vec{f}, \tag{A.19}$$

$$Q\dot{\vec{v}} = Q\Omega\left(P\vec{v}\right) + Q\Omega\left(Q\vec{v}\right) + Q\vec{f}. \tag{A.20}$$

Formally solving Eq. (A.20) for $Q\vec{v}$, substituting the result into Eq. (A.19) and multiplying from the left with B^T, we get

$$\begin{aligned}\begin{pmatrix}\dot{R}_{\mathrm{ete},x}(t)\\ \ddot{R}_{\mathrm{ete},x}(t)\end{pmatrix} &= \mathcal{M}(0)\begin{pmatrix}R_{\mathrm{ete},x}(t)\\ \dot{R}_{\mathrm{ete},x}(t)\end{pmatrix} + \int_0^t \mathrm{d}t'\,\dot{\mathcal{M}}(t-t')\begin{pmatrix}R_{\mathrm{ete},x}(t')\\ \dot{R}_{\mathrm{ete},x}(t')\end{pmatrix} \\ &\quad + B^T\vec{f}(t) + \int_0^t \mathrm{d}t'\,B^T\Omega e^{Q\Omega(t-t')}Q\vec{f}(t') + B^T\Omega e^{Q\Omega t}Q\vec{v}(0),\end{aligned} \tag{A.21}$$

where we define

$$\mathcal{M}(t) := B^T\Omega e^{Q\Omega t}B(B^TB)^{-1} \in \mathbb{R}^{2\times 2}. \tag{A.22}$$

In Appendix A.4.2 we show that if the first and last monomer have identical mass, $m_0 = m_{N-1}$, then $\mathcal{M}$ is of the form

$$\mathcal{M}(t) = \begin{pmatrix}0 & 1\\ k(t)/\mu & -\gamma/(2\mu)\end{pmatrix}, \tag{A.23}$$

where $\mu = m_0/2$ is the reduced mass of the first and last monomer and $k(t)$ is defined by Eq. (A.23). Using integration by parts, Eq. (A.21) is seen to be equivalent to

$$\mu\,\ddot{R}_{\mathrm{ete},x}(t) = -\int_0^t \mathrm{d}t'\Gamma(t-t')\dot{R}_{\mathrm{ete},x}(t') - (\nabla U)(R_{\mathrm{ete},x}(t)) - \zeta(t)R_{\mathrm{ete},x}(0) + F_R(t), \tag{A.24}$$

with memory kernel

$$\Gamma(t) := \gamma\delta(t) + \zeta(t), \tag{A.25}$$

where we define $\zeta(t) := \mu\left[\lim_{t'\to\infty}k(t') - k(t)\right]$, and furthermore use the convention $\int_0^t \mathrm{d}t'\,\delta(t-t')R_{\mathrm{ete},x}(t') = R_{\mathrm{ete},x}(t)/2$ for the case when the root of the argument of the Dirac delta function coincides with one of the integration limits. The effective potential U is given by [109]

$$U(R_{\mathrm{ete},x}) = \frac{\kappa}{2(N-1)}R^2_{\mathrm{ete},x}, \tag{A.26}$$

and the random force is defined as

$$\begin{aligned}F_R(t) := \mu\begin{pmatrix}0 & 1\end{pmatrix}B^T\vec{f}(t) + \mu\int_0^t \mathrm{d}t'\,\begin{pmatrix}0 & 1\end{pmatrix}B^T\Omega e^{Q\Omega(t-t')}Q\vec{f}(t') \\ + \mu\begin{pmatrix}0 & 1\end{pmatrix}B^T\Omega e^{Q\Omega t}Q\vec{v}(0).\end{aligned} \tag{A.27}$$

Numerically it is found that the generalized FDT

$$\langle F_R(t)F_R(t')\rangle = k_{\mathrm{B}}T\,\Gamma(|t-t'|) \tag{A.28}$$

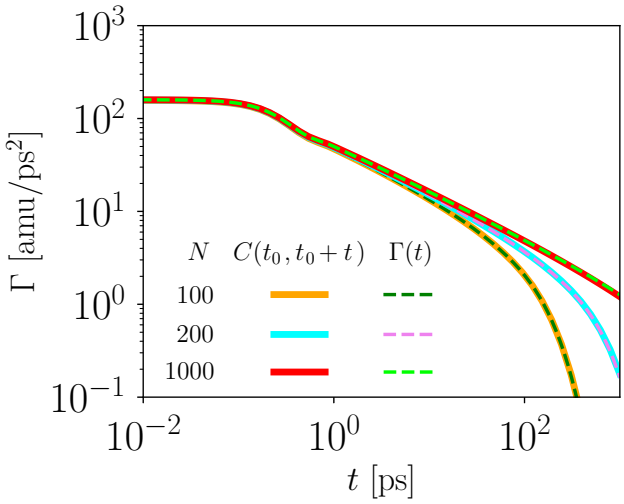

Figure A.2: Numerical verification of the generalized FDT Eq. (A.28). The correlation function C is defined as $C(t_0, t_0 + t) := \langle F_R(t_0) F_R(t_0 + t)\rangle/(k_\mathrm{B}T)$, with F_R given by Eq. (A.27). The memory kernel Γ is defined in Eq. (A.25). Both correlation function and memory kernel are calculated using $\gamma = 110$ amu/ps, $\kappa = 319.8$ amu/ps^2, $m_0 = m_{N-1} = 15$ amu, $m_1 = ... = m_{N-2} = 14$ amu, $t_0 = 2 \cdot 10^3$ ps ($N = 100$, 200), $t_0 = 6 \cdot 10^3$ ps ($N = 1000$).

holds once boundary effects are negligible, i.e., for t, t' larger than the decay time τ_Γ of Γ, see Fig. A.2. After this time, also the term $\zeta(t) R_{\mathrm{ete},x}(0)$ in Eq. (A.24) is negligible and the equation is of the form of the GLE, Eq. (A.8).

Equations (A.22), (A.23), (A.25) constitute an explicit formula for the memory kernel of the end-to-end distance vector for the Gaussian chain model undergoing Rouse dynamics.

In Fig. A.3, we compare analytical results based on Eq. (A.25) to numerical data. Figure A.3 (a) shows the potential of mean force (pmf) U, obtained from both Langevin simulations using Boltzmann inversion, and Eq. (A.26) for various chain lengths N. As can be seen the agreement is excellent, which also serves as a validation that the simulations have equilibrated. In Fig. A.3 (b), (c) we show memory kernels calculated using Eq. (A.25) for chain lengths ranging from $N = 5$ to $N = 2000$. While for the shortest chain length $N = 5$, the memory kernel changes sign (see pink curve in Fig. A.3 (b)), for longer chains it is strictly positive. Figure A.3 (c) shows that for longer chains, a $\Gamma \sim t^{-1/2}$ scaling behavior at intermediate time scales can clearly be discerned. Since the memory kernel of the center monomer of a Gaussian chain is known to scale as $\Gamma \sim t^{-1/2}$ for large N and intermediate t [32, 34], it is not surprising that the end-to-end distance shows a similar behavior. In Fig. A.3 (d), we compare the analytical memory kernels from subplots (b), (c) to memory kernels extracted from simulations. As can be seen, the agreement is excellent, and in particular the transient $\Gamma \sim t^{-1/2}$ scaling is also observed in the numerical kernels.

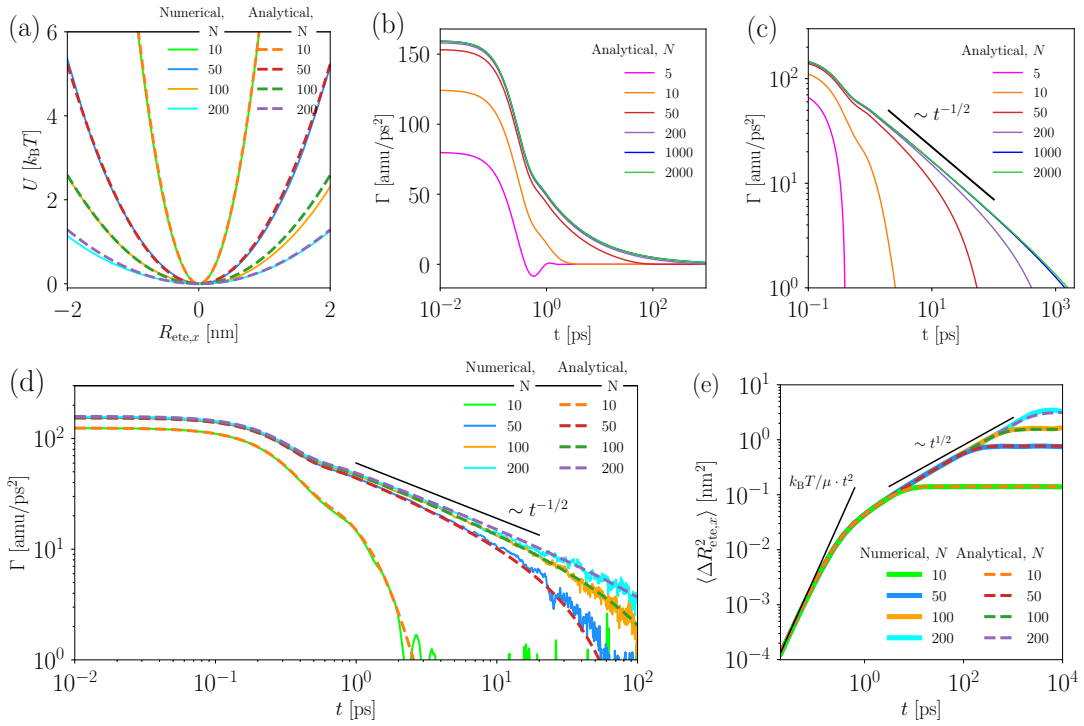

Figure A.3: Numerical and analytical results for the dynamics of $R_{\mathrm{ete},x}$, the x-component of the end-to-end distance vector $\vec{R}_{\mathrm{ete}}$ of a Gaussian chain. Parameters used for m_i, κ, γ are given in Appendix A.1. Numerical data is obtained from Langevin simulation of the Gaussian chain model Eq. (A.1) for various chain lengths N, as indicated in the legends. (a) Potential of mean force (pmf). The solid lines show pmfs obtained from numerical data via Boltzmann inversion, the dashed lines depict analytical pmfs based on Eq. (A.26). (b), (c) Analytical memory kernels shown both in semi-logarithmic and double-logarithmic representation are calculated using Eq. (A.25). (d) Numerical and analytical memory kernels. Analytical memory kernels are replots of subplots (b), (c), numerical memory kernels are calculated from simulations using the modified Berne method [107, 108], see Appendix A.3. Transient power law scaling is indicated by a black bar. (e) Mean squared displacements (MSDs) as calculated directly from Langevin simulations (solid lines) and from the memory kernel and harmonic potential using Eq. (A.65). Black bars display the expected MSD for unaccelerated motion with the thermal velocity $v = \sqrt{kT/\mu}$, and the power law $t^{1/2}$.

In Fig. A.3 (e) we furthermore compare the mean squared displacement (MSD)

$$\left\langle \Delta R^2_{\mathrm{ete},x}(t) \right\rangle := \left\langle \left[R_{\mathrm{ete},x}(t) - R_{\mathrm{ete},x}(0) \right]^2 \right\rangle \tag{A.29}$$

as calculated directly from simulations to the MSD as calculated using the quadratic potential (A.26) and the memory kernel (A.25), details of the calculation are given in Appendix A.5. Again, the agreement between analytical and numerical results is excellent, showing that MSDs

can reliably be calculated from memory kernels. For longer chains $N \gtrsim 50$, the MSDs show an intermediate scaling $\left\langle \Delta R^2_{\mathrm{ete},x}(t) \right\rangle \sim t^{1/2}$, consistent with the memory kernel scaling $\Gamma(t) \sim t^{-1/2}$ [114], c.f. Appendix A.5.

A.4.2 Proof of Eq. (A.23)

In the derivation of the GLE in Appendix A.4.1 we use that if $m_0 = m_{N-1}$ then $\mathcal{M}$, defined by Eq. (A.22), is of the form

$$\mathcal{M}(t) = \begin{pmatrix} 0 & 1 \\ k(t)/\mu & -\gamma/(2\mu) \end{pmatrix}, \tag{A.30}$$

where $\mu = m_0/2$ is the reduced mass of the first and last monomer and this equation defines $k(t)$. In the present appendix, we prove Eq. (A.30).

We consider Ω, P, B as defined in Eqs. (A.14), (A.16), (A.17), and start by noting that

$$(B^T B)^{-1} = \frac{1}{\vec{b}^2} \begin{pmatrix} 1 & 0 \\ 0 & 1 \end{pmatrix}. \tag{A.31}$$

We furthermore write

$$q := \mathbb{1} - \vec{b} \otimes \vec{b}^T \in \mathbb{R}^{N \times N}, \tag{A.32}$$

so that

$$Q = \begin{pmatrix} q & 0 \\ 0 & q \end{pmatrix}. \tag{A.33}$$

Note that for $m_0 = m_{N-1}$, it holds that

$$qM^{-1}\vec{b} = 0, \tag{A.34}$$

since for all $i \in \{0, ..., N-1\}$ we have

$$(qM^{-1}\vec{b})_i = \left(\delta_{i,j} - b_i b_j/\vec{b}^2\right) \delta_{j,k} m_j^{-1} b_k = b_i \left[m_i^{-1} - (m_0^{-1} + m_{N-1}^{-1})/2\right] = 0, \tag{A.35}$$

where we use the Einstein sum convention, and at the last equality sign we use that b_i is zero unless $i = 0, N-1$, and that for $i = 0, N-1$ the sum in the brackets vanishes.

With these preparations, we now consider the power series for $\mathcal{M}(t)$, given by

$$\mathcal{M}(t) = B^T \Omega e^{Q\Omega t} B (B^T B)^{-1} = \sum_{n=0}^{\infty} \frac{t^n}{\vec{b}^2 n!} B^T \Omega (Q\Omega)^n B. \tag{A.36}$$

The $n = 0$ term can be calculated directly to yield

$$\frac{1}{\vec{b}^2} B^T \Omega B = \begin{pmatrix} 0 & 1 \\ (\vec{b}^T M^{-1} K \vec{b})/\vec{b}^2 & -\gamma/(2\mu) \end{pmatrix}. \tag{A.37}$$

To show that for $n \geq 1$ only the lower left component of $B^T\Omega(Q\Omega)^n B$ is nonzero, we use induction to prove that $(Q\Omega)^n B$ is of the form

$$(Q\Omega)^n B = \begin{pmatrix} q\vec{\alpha}_n & 0 \\ q\vec{\beta}_n & 0 \end{pmatrix}. \tag{A.38}$$

Indeed, for $n = 1$ we obtain

$$(Q\Omega)^1 B = \begin{pmatrix} 0 & 0 \\ qM^{-1}K\vec{b} & -q\gamma M^{-1}b \end{pmatrix} \overset{\text{(A.34)}}{=} \begin{pmatrix} 0 & 0 \\ qM^{-1}K\vec{b} & 0 \end{pmatrix}, \tag{A.39}$$

so that $(Q\Omega)^1 B$ is of the form (A.38) with $\vec{\alpha}_1 = 0$, $\vec{\beta}_1 = M^{-1}K\vec{b}$. If $(Q\Omega)^n B$ is of the form (A.38), then

$$(Q\Omega)^{n+1} B = (Q\Omega)\left[(Q\Omega)^n B\right] \tag{A.40}$$

$$= \begin{pmatrix} 0 & q \\ qM^{-1}K & -q\gamma M^{-1} \end{pmatrix} \begin{pmatrix} q\vec{\alpha}_n & 0 \\ q\vec{\beta}_n & 0 \end{pmatrix} \tag{A.41}$$

$$= \begin{pmatrix} q\vec{\beta}_n & 0 \\ qM^{-1}Kq\vec{\alpha}_n - q\gamma M^{-1}q\vec{\beta}_n & 0 \end{pmatrix}, \tag{A.42}$$

so that $(Q\Omega)^{n+1} B$ is also of the form Eq. (A.38). Note that this yields a recursion relation for $\vec{\alpha}_n$, $\vec{\beta}_n$, namely

$$\begin{pmatrix} \vec{\alpha}_1 \\ \vec{\beta}_1 \end{pmatrix} = \begin{pmatrix} 0 \\ qM^{-1}K\vec{b} \end{pmatrix}, \tag{A.43}$$

$$\begin{pmatrix} \vec{\alpha}_{n+1} \\ \vec{\beta}_{n+1} \end{pmatrix} = \begin{pmatrix} \vec{\beta}_n \\ M^{-1}Kq\vec{\alpha}_n - \gamma M^{-1}q\vec{\beta}_n \end{pmatrix}. \tag{A.44}$$

Using Eq. (A.38), we then calculate

$$B^T\Omega(Q\Omega)^n B = \begin{pmatrix} \vec{b}^T & 0 \\ 0 & \vec{b}^T \end{pmatrix} \begin{pmatrix} 0 & \mathbb{1} \\ M^{-1}K & -M^{-1}\gamma \end{pmatrix} \begin{pmatrix} q\vec{\alpha}_n & 0 \\ q\vec{\beta}_n & 0 \end{pmatrix} \tag{A.45}$$

$$= \begin{pmatrix} 0 & \vec{b}^T \\ \vec{b}^T M^{-1}K & -\vec{b}^T\gamma M^{-1} \end{pmatrix} \begin{pmatrix} q\vec{\alpha}_n & 0 \\ q\vec{\beta}_n & 0 \end{pmatrix} \tag{A.46}$$

$$= \begin{pmatrix} 0 & 0 \\ \vec{b}^T M^{-1}Kq\vec{\alpha}_n - \vec{b}^T\gamma M^{-1}q\vec{\beta}_n & 0 \end{pmatrix}, \tag{A.47}$$

where we use that $\vec{b}^T q = 0$. Thus, for each term with $n \geq 1$ in the power series (A.36), only the lower left matrix component is nonzero, so that together with Eq. (A.37) we finally obtain the form Eq. (A.30) for $\mathcal{M}$.

A.4.3 Numerical evaluation of the memory kernel for large systems

The technically most challenging aspect of calculating the memory kernel Γ given by Eq. (A.25) is evaluating the matrix exponential that appears in the definition of $\mathcal{M}$, Eq. (A.22),

$$\mathcal{M}(t) := B^T \Omega e^{Q\Omega t} B (B^T B)^{-1}. \tag{A.48}$$

For large systems, $N \gtrsim 200$, standard methods for evaluating matrix exponentials like for example the python routine `scipy.linalg.expm` become numerically unfeasible.

To obtain memory kernels also for large N, we numerically integrate the linear ODE

$$\dot{x}(t) = (Q\Omega) x(t) \tag{A.49}$$

using the initial condition

$$x(0) = B \left(B^T B\right)^{-1} \in \mathbb{R}^{N \times 2}. \tag{A.50}$$

and a timestep Δt, thus obtaining

$$x_k := x(t_k) = e^{Q\Omega t_k} B \left(B^T B\right)^{-1}, \tag{A.51}$$

where $t_k := k \cdot \Delta t$. The solution x_k allows us to calculate $\mathcal{M}(t_k)$ as

$$\mathcal{M}(t_k) = B^T \Omega e^{Q\Omega t_k} B \left(B^T B\right)^{-1} = B^T \Omega x_k. \tag{A.52}$$

Note that to solve Eq. (A.49) numerically using a timestep Δt, the propagator $e^{Q\Omega\Delta t}$ needs to be calculated only once, for example using a truncated power series

$$e^{Q\Omega\Delta t} \approx \sum_{n=0}^{n_{\max}} \frac{1}{n!} (Q\Omega\Delta t)^n, \tag{A.53}$$

and can then be used to calculate x_{k+1} from x_k via matrix multiplication as

$$x_{k+1} = e^{Q\Omega\Delta t} x_k. \tag{A.54}$$

Since the 2×2 matrix $\mathcal{M}(t_k)$ can be calculated on the fly at each integration step, the large $(2N) \times (2N)$ matrix $e^{Q\Omega t_k}$ does not need to be saved or stored once $\mathcal{M}(t_k)$ and $e^{Q\Omega t_{k+1}}$ have been calculated. For large N, this can significantly improve performance as compared to first calculating the matrix exponential $e^{Q\Omega t_k}$ for all timesteps and only then calculating $\mathcal{M}(t_k)$.

Our algorithm yields the values of $\mathcal{M}(t)$ on an evenly spaced grid $t \in \Delta t \cdot \mathbb{N}$. To plot the memory kernel on a logarithmic t-axis, we optimize computational time by first solving Eq. (A.49) for times $t < 1$ ps using a timestep $\Delta t = 0.001$ ps, and then continue using a larger timestep $\Delta t = 0.1$ ps. In both cases, truncating the exponential sum in Eq. (A.53) at $n_{\max} = 50$ turns out to be sufficient.

In Fig. A.4 we show a comparison of the memory kernel as calculated using both the method described in this section and directly evaluating the matrix exponential using the python routine `scipy.linalg.expm`. The memory kernels we obtain using both methods are identical, so that we conclude that both are robust. In particular we can confidently use the method presented here to calculate memory kernels for systems with large numbers of degrees of freedom $N \gtrsim 200$.

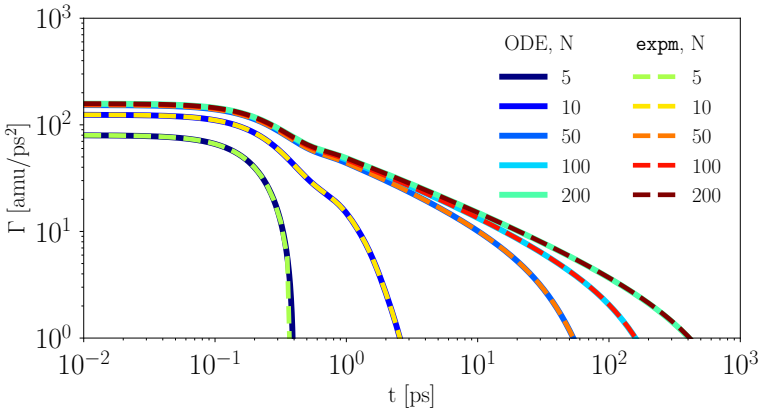

Figure A.4: Comparison of memory kernels calculated using two different numerical methods. In both cases, Eq. (A.48) is used to calculate $\mathcal{M}$, from which the memory kernel is calculated via Eq. (A.25). For the solid lines, $\mathcal{M}$ is obtained integrating the ODE Eq. (A.49) as described in Appendix A.4.3. For the dashed lines, the matrix exponential $e^{Q\Omega t}$ is calculated directly using the python routine `scipy.linalg.expm`. Parameters used are $\kappa = 319.8$ amu/ps^2, $m_0 = m_{N-1} = 15$ amu, $m_i = 14$ amu ($i = 1, ..., N-2$), and $\gamma = 110$ amu/ps.

A.5 Calculating MSDs from memory kernels

In this appendix, we derive a formula for the MSD

$$\left\langle \Delta x^2(t) \right\rangle \equiv \left\langle [x(t) - x(0)]^2 \right\rangle \tag{A.55}$$

of a particle with position x which obeys the GLE (A.8), (A.9) with a harmonic potential

$$U(x) = \frac{K}{2} x^2. \tag{A.56}$$

Fourier transforming the GLE using the convention

$$\tilde{x}(\omega) = \int_{-\infty}^{\infty} \mathrm{d}t\, e^{-i\omega t} x(t), \qquad x(t) = \int_{-\infty}^{\infty} \frac{\mathrm{d}\omega}{2\pi}\, e^{i\omega t} \tilde{x}(\omega), \tag{A.57}$$

and solving for $\tilde{x}(\omega)$, we obtain

$$\tilde{x}(\omega) = \frac{\tilde{F}_R(\omega)}{K - m\omega^2 + i\omega\tilde{\Gamma}_+(\omega)} \equiv \tilde{Q}(\omega)\tilde{F}_R(\omega), \tag{A.58}$$

where

$$\tilde{\Gamma}_+(\omega) = \int_0^{\infty} \mathrm{d}t\, e^{-i\omega t} \Gamma(t) \tag{A.59}$$

is the half-sided Fourier transform of Γ. From Eq. (A.57) it follows that

$$x(t) - x(0) = \int_{-\infty}^{\infty} \frac{\mathrm{d}t}{2\pi} \left(e^{i\omega t} - 1\right) \tilde{x}(\omega), \tag{A.60}$$

so that, using Eqs. (A.55), (A.58), we get

$$\left\langle \Delta x^2(t) \right\rangle = \int_{-\infty}^{\infty} \frac{\mathrm{d}\omega}{2\pi} \int_{-\infty}^{\infty} \frac{\mathrm{d}\omega'}{2\pi} \left(e^{i\omega t} - 1\right) \left(e^{i\omega' t} - 1\right) \tilde{Q}(\omega)\tilde{Q}(\omega')\langle \tilde{F}_R(\omega)\tilde{F}_R(\omega')\rangle. \tag{A.61}$$

Since the Fourier transform of the generalized FDT, Eq. (A.9), is given by

$$\langle \tilde{F}_R(\omega)\tilde{F}_R(\omega')\rangle = 2\pi\delta(\omega+\omega')k_\mathrm{B}T\,\tilde{\Gamma}(\omega), \tag{A.62}$$

the MSD is finally given as

$$\left\langle \Delta x^2(t) \right\rangle = k_\mathrm{B}T \int_{-\infty}^{\infty} \frac{\mathrm{d}\omega}{2\pi} \left(e^{i\omega t} - 1\right) \left(e^{-i\omega t} - 1\right) \tilde{Q}(\omega)\tilde{Q}(-\omega)\tilde{\Gamma}(\omega) \tag{A.63}$$

$$= k_\mathrm{B}T \int_{-\infty}^{\infty} \frac{\mathrm{d}\omega}{2\pi} (2 - e^{i\omega t} - e^{-i\omega t})\tilde{Q}(\omega)\tilde{Q}(-\omega)\tilde{\Gamma}(\omega) \tag{A.64}$$

$$= 2k_\mathrm{B}T \int_{-\infty}^{\infty} \frac{\mathrm{d}\omega}{2\pi} \left[1 - \cos(\omega t)\right] \tilde{Q}(\omega)\tilde{Q}(-\omega)\tilde{\Gamma}(\omega), \tag{A.65}$$

where at the last equality sign we use $2\cos(\omega t) = e^{i\omega t} + e^{-i\omega t}$.

From Eq. (A.65) it follows that if the memory kernel has a scaling regime $\Gamma \sim t^{-\beta}$, then the MSD can show a scaling regime $\left\langle \Delta x^2(t) \right\rangle \sim t^\beta$. For this, first note that power counting yields a scaling regime

$$\tilde{\Gamma}(\omega) \sim \int_{-\infty}^{\infty} \mathrm{d}t\, e^{-i\omega t} t^{-\beta} \sim \omega^{\beta-1} \tag{A.66}$$

for the Fourier transform of the memory kernel. If an intermediate regime, between short-time inertial motion and long-time saturation of the MSD due to the quadratic potential, exists where the denominator in Eq. (A.65) is dominated by the term $-i\omega\tilde{\Gamma}_+(\omega)$ and the scaling $\tilde{\Gamma} \sim \omega^{\beta-1}$ holds, we thus obtain [114]

$$\left\langle \Delta x^2(t) \right\rangle \sim \int_{-\infty}^{\infty} \mathrm{d}\omega \left[1 - \cos(\omega t)\right] \frac{\omega^{\beta-1}}{\omega^2\omega^{2(\beta-1)}} \sim t^\beta, \tag{A.67}$$

where we again use power counting.

Note that, depending on the specific values of m, K and the kernel Γ, there might not exist a frequency regime where the denominator in Eq. (A.65) is dominated by $-i\omega\tilde{\Gamma}_+(\omega)$, so that a power-law scaling in the memory kernel is not a guarantee to observe the corresponding power law in the MSD. Indeed, for the FR chain MSD shown in Fig. 2.3 (d), the power law scaling can hardly be observed between the inertial regime at small times and the long-time saturation.

A.6 Scaling relation between Gaussian chain end-to-end distance memory kernels with different Kuhn lengths

In Fig. 2.3 (f), we find that the memory kernels of Gaussian and FR chain models show a similar $\Gamma \sim t^{-1/2}$ regime, but rescaled in time. As we show now, the rescaling is due to the different Kuhn lengths of Gaussian and FR chain models and, taking this into account, the kernels agree perfectly in the power-law scaling regime.

We consider the Gaussian chain model given by Eq. (A.1). Using a scale factor χ we define $\vec{\mathcal{R}}_i(t) := \vec{R}_i(\chi \cdot t)/\chi$, so that $\dot{\vec{\mathcal{R}}}_i(t) = \dot{\vec{R}}_i(\chi \cdot t)$, $\ddot{\vec{\mathcal{R}}}_i(t)/\chi = \ddot{\vec{R}}_i(\chi \cdot t)$. Evaluating Eq. (A.1) at time t/χ and eliminating $\vec{R}_i$ in favor of $\vec{\mathcal{R}}_i$ then yields

$$\frac{m_i}{\chi}\ddot{\vec{\mathcal{R}}}_i(t) = -\gamma\dot{\vec{\mathcal{R}}}_i(t) + (\chi\kappa)\left[\vec{\mathcal{R}}_{i-1}(t) - 2\vec{\mathcal{R}}_i(t) + \vec{\mathcal{R}}_{i+1}(t)\right] + \vec{\mathcal{F}}_i(t), \tag{A.68}$$

where $\vec{\mathcal{F}}_i(t) := \vec{F}_i(t/\chi)$ obeys

$$\left\langle \vec{\mathcal{F}}_i(t)\vec{\mathcal{F}}_j^T(t)\right\rangle = 2\gamma k_\mathrm{B}T\chi\mathbb{1}\delta_{i,j}\delta(t-t'). \tag{A.69}$$

Comparing Eqs. (A.1), (A.2) to Eqs. (A.68), (A.69), we see that a Gaussian chain with parameters (m_i, γ, κ, T) is equivalent to a Gaussian chain with parameters (m_i/χ, γ, $\chi\kappa$, χT) and with time rescaled by a factor χ. In particular, since the memory kernel is independent of temperature, in a regime where inertial effects are negligible we expect the relation

$$\Gamma_{\chi\kappa}(t) = \Gamma_\kappa(t/\chi) \tag{A.70}$$

for the end-to-end-distance memory kernels of two Gaussian chains with monomer coupling strengths $\chi\kappa$, κ, as indicated by the indices.

The Gaussian and FR chains we consider in Chapter 2 have equal bond distance b, but different Kuhn lengths $a_\mathrm{G} = b$, $a_\mathrm{FR} = b\sqrt{(1+\cos\theta)/(1-\cos\theta)}$ [109]. To obtain a FR chain with Kuhn length b, the bond distance needs to be $b' = b/\sqrt{\chi}$ with $\chi = (1+\cos\theta)/(1-\cos\theta)$, and to have this bond distance in a Gaussian chain, the coupling parameter needs to be $\kappa' = k_\mathrm{B}T/b'^2 = \chi \cdot k_\mathrm{B}T/b = \chi\kappa$. If the difference between the power-law scaling regimes of the Gaussian chain and the FR chain memory kernels shown in Fig. 2.3 (f) is only due to the difference in Kuhn lengths, then the rescaled FR chain memory kernel

$$\Gamma_{\mathrm{FR},\chi\kappa}(t) = \Gamma_{\mathrm{FR},\kappa}(t/\chi) \equiv \Gamma_\mathrm{FR}(t/\chi) \tag{A.71}$$

should agree with the Gaussian chain memory kernel $\Gamma_{\mathrm{G},\kappa}(t) \equiv \Gamma_{\mathrm{G}}(t)$, where for clarity we added the coupling parameters associated with the respective models (if no index is written, the coupling parameter is understood to be κ; note that for the FR chain bond lengths are frozen, and κ denotes the coupling strength of a Gaussian chain with the same bond length). Indeed, as we show in Fig. A.5, the rescaled FR chain memory kernel agrees perfectly with the Gaussian chain memory kernel in the power-law regime. From this we conclude that the dynamical differences between the models at intermediate times are only due to the different Kuhn lengths, and not due to other details of the bonded interactions.

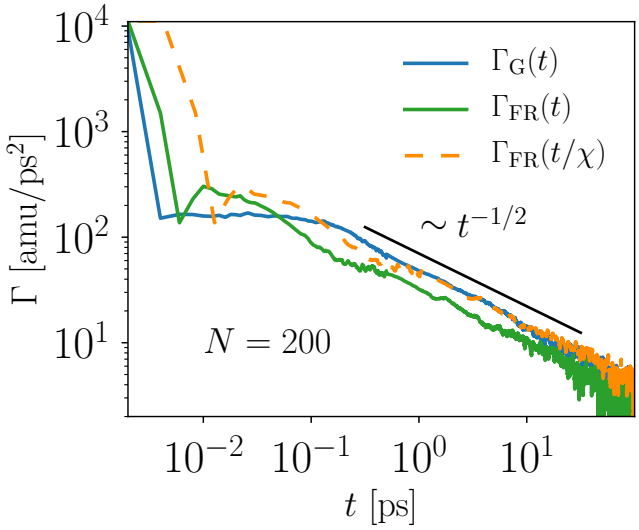

Figure A.5: Memory kernels of Gaussian and FR chain models for $N = 200$, calculated from Langevin simulations. Blue and green lines are replots of the memory kernels shown in Fig. 2.3 (f). The orange line is the memory kernel of the FR chain (green line), but with time rescaled by a factor $\chi = (1 + \cos\theta)/(1 - \cos\theta)$ according to Eq. (A.71). For our bond angle, $\theta = 111°$, we obtain $\chi \approx 2.1$.

A.7 MSD scaling for Flory chains

For a freely draining chain (no hydrodynamic interactions) comprised of N monomers, the effective diffusion coefficient of one tagged monomer scales as $D \sim 1/N$. However, on short time scales the dynamics of that monomer is not affected by the whole chain, so that

$$\langle \Delta R_i^2(t) \rangle \sim \frac{1}{N_{\mathrm{eff}}} t \tag{A.72}$$

with a time-dependent effective coupled chain length N_{eff} that for long times approaches N. How does this effective chain length the tagged monomer feels scale with t? We assume that the part of the chain that affects the tagged monomer scales with the number of monomers the

tagged monomer can reach via diffusion, $\langle \Delta R_i^2(t) \rangle \sim N_{\text{eff}}^{\nu}$, where ν is the Flory exponent. Thus, at time t we have $N_{\text{eff}}^{2\nu} \sim t/N_{\text{eff}}$, so that N_{eff} scales as $N_{\text{eff}} \sim t^{1/(2\nu+1)}$. Reinserting this into Eq. (A.72), we obtain [112, 113]

$$\langle \Delta R_i^2(t) \rangle \sim t^{2\nu/(2\nu+1)}. \tag{A.73}$$

A.8 Radius of gyration

In this appendix we show that for a self-avoiding collapsed chain, the dynamics of the end-to-end distance is very different from the dynamics of the radius of gyration.

Using GROMACS, we calculate the mass-weighted radius of gyration

$$R_g = \sqrt{\frac{\sum_i m_i (\vec{R}_i - \vec{R}_{\text{com}})^2}{\sum_i m_i}}, \tag{A.74}$$

where $\vec{R}_{\text{com}} = (\sum_i m_i \vec{R}_i)/(\sum_i m_i)$ is the center of mass of the chain. Figure A.6 (a) shows the equilibrium average of R_g, which displays the same asymptotic scaling behavior as the end-to-end distance, c.f. Fig. 2.3. However, the MSD depicted in Fig. A.6 (b) shows an intermediate power-law scaling with exponent $1/4$, which is different from both the good-solvent exponent $6/11$ and the bad-solvent exponent $2/5$ observed for the end-to-end distance and single-monomer dynamics in Fig. 2.5. Thus, we find that for a self-avoiding chain, the dynamics of the two collective variables R_g, R_{ete}, which characterize the large-scale behavior of the chain, are rather different.

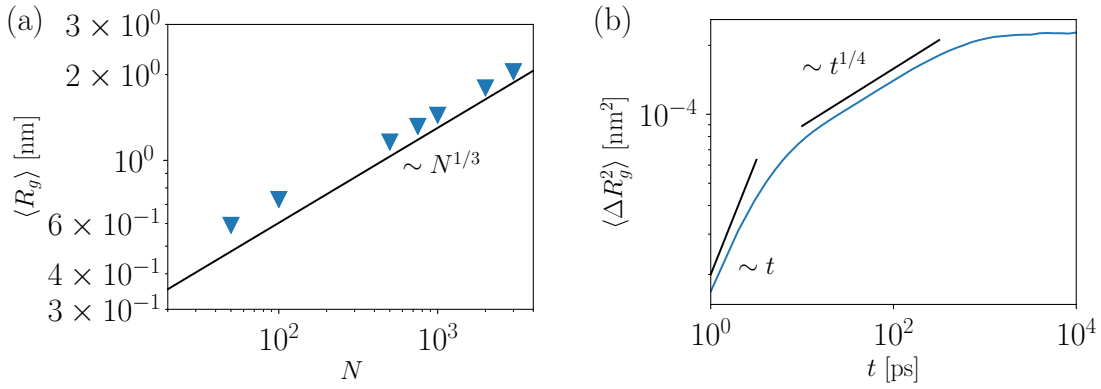

Figure A.6: (a) Mean radius of gyration $\langle R_g \rangle$ for self-avoiding collapsed chains of various lengths N, obtained from Langevin simulations as described in Appendix A.1. R_g is defined in Eq. (A.74), the black bar denotes the power-law scaling $\langle R_g \rangle \sim N^{1/3}$. (b) MSD for the radius of gyration R_g of a self-avoiding collapsed chains of length $N = 2000$, obtained from Langevin simulations. The black bars illustrate intermediate power-law scaling.

Appendix B

Supplemental Material for Chapter 3

B.1 Mean first-passage times versus escape times and double-well versus single-well scenarios

In Chapter 3, we perform Langevin simulations in a quartic double well defined in Eq. (3.4) and extract MFPTs from a single long simulation trajectory that includes multiple recrossing events. We compare these simulation results to PGH theory using an explicit formula for the escape time of particles in a single potential well, which obviously does not allow for barrier recrossing [88]. The PGH theory has been adapted to calculate the escape time also in a double well [51, 88, 133], which allows for recrossing events, using a method introduced by Mel'nikov and Meshkov [126], so the obvious question arises why we do not compare our MFPT simulation results with PGH theory for a double well.

In this appendix, we first define and discuss the differences between escape and mean first-passage times and between single-well and double-well scenarios. After that we explain why we compare our MFPTs obtained from simulations of a particle in a double-well potential, with the single-well PGH formula for the escape time. We finally compare escape time predictions of single-well and double-well PGH theory with MFPTs and escape times extracted from Langevin simulations of single and double wells.

In single-well PGH theory [88], the escape time $\tau_{\rm esc}$, defined as the inverse of the escape rate, is obtained from the probability flux out of a potential well with an absorbing boundary condition located to the right of the barrier top so that the particle has negligible probability to recross, assuming a steady-state probability distribution within the well. The escape time $\tau_{\rm esc}$ is defined by the rate equation [88, 126]

$$\tau_{\rm esc}\dot{P}(t) = -P(t) \tag{B.1}$$

for the probability $P(t)$ to find the particle in the well. Starting from the initial condition $P(0) = 1$, the solution of Eq. (B.1) is

$$P(t) = e^{-t/\tau_{\rm esc}}. \tag{B.2}$$

The extension of PGH theory to the double-well scenario only makes a difference in the limits of large mass or long memory, and includes barrier recrossing events [126]. In such recrossing

events, a particle recrosses the barrier several times after having reached its target position, which is caused by slow energy diffusion. According to our use of the term, recrossing is a characteristic property of trajectories in the inertial or long memory limits, as shown in Figs. 3.1 (b), (f), (g), (h). It should not be mixed up with Markovian barrier recrossing which occurs in the high-friction short-memory limit and consists of the trivial scenario of a particle returning to the starting well after having reached the barrier top. Recrossing events induce a probability influx from the target well, so that the escape rate from the starting well is decreased as compared to a single well. In a symmetric double well, the escape time $\tau_{\rm esc}$ follows from the coupled rate equations for the probabilities to find the particle in the starting well P_s and the target well P_t [88, 126]

$$\tau_{\rm esc}\dot{P}_s(t) = -P_s(t) + P_t(t), \tag{B.3}$$

$$\tau_{\rm esc}\dot{P}_t(t) = P_s(t) - P_t(t). \tag{B.4}$$

If the particle resides in the starting well at time $t = 0$, we have $P_s(0) = 1$ and $P_t(0) = 0$, so that the solution reads

$$P_s(t) = \frac{1}{2}\left(1 + e^{-2t/\tau_{\rm esc}}\right). \tag{B.5}$$

Probabilities to be in one well can easily be estimated numerically, so that Eqs. (B.2), (B.5) can be used to obtain the escape time $\tau_{\rm esc}$ also from simulation trajectories.

A mean first-passage time (MFPT) is defined as the mean time needed for a particle to reach, starting from a given position x_s, a target position x_t for the first time [123]. In Chapter 3 we calculate MFPTs from Langevin simulations via averaging the time a particle needs to go from one potential minimum $x_s = -L$ to the other potential minimum $x_t = L$. Each MFPT shown in Chapter 3 is obtained from one long trajectory and thus allows for multiple recrossing events. Our choice of x_t makes sure that in the high-friction short-memory limit the particle recrosses the barrier with negligible probability right after reaching the target position, and matches the above definition of the escape time.

We now compare escape times defined in Eqs. (B.2), (B.5) with MFPTs, both calculated from simulations. We perform this comparison for simulations in the single-well as well as in the double-well scenarios. The double-well scenario, employed in Chapter 3, consists of a single, long trajectory and allows for multiple recrossing events. For the single-well simulations, we use the same quartic potential Eq. (3.4) but impose an absorbing boundary at $x_t = L$, i.e., we stop the simulation once the particle reaches the minimum of the target well at $x_t = L$ for the first time. The single-well scenario thus consists of many simulation trajectories, each initialized as explained in Chapter 3. The results, together with the predictions of both single- and double-well PGH theory, are shown in Fig. B.1.

For the single-well simulation data, the escape time (squares) perfectly equals the MFPT (plus signs). This is easy to understand, since both approaches impose an absorbing boundary at the target position $x_t = L$. For the double well, simulated escape times (circles) and MFPTs (crosses) only agree in the limit of high-friction and short memory time, for $\tau_m/\tau_D \ll 1$ and $\tau_\Gamma/\tau_D \ll 1$. In the energy diffusion regime, i.e., for large mass $\tau_m/\tau_D \gg 1$ or for long memory $\tau_\Gamma/\tau_D \gg 1$, the simulated escape time is larger than the simulated MFPT by a factor of

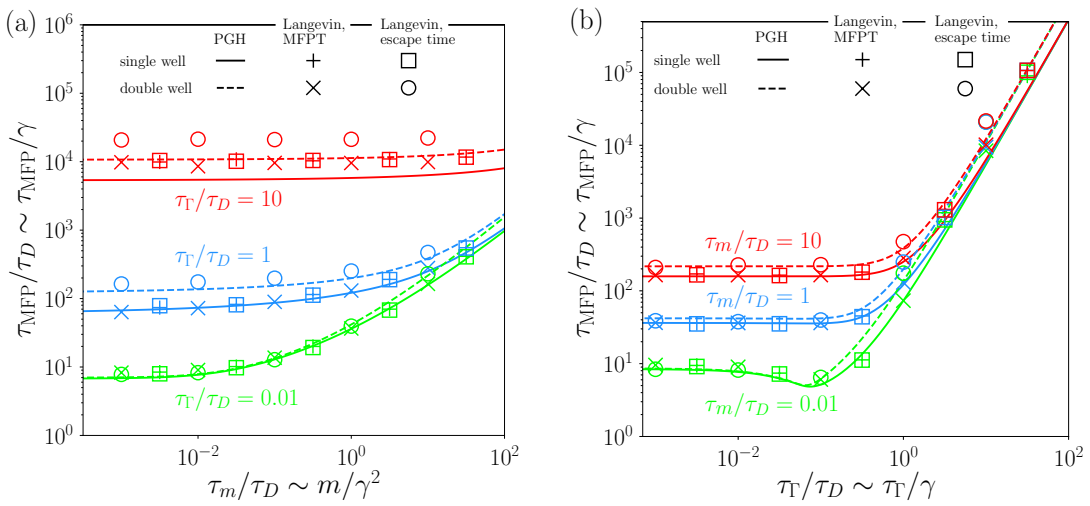

Figure B.1: Simulation results for τ_{MFP} and τ_{esc} in a single-well and double-well quartic potential together with predictions of PGH theory, using the single-well [88] (solid colored lines) and double-well [51, 126, 133] (dashed colored lines) PGH formulas. The potential used for both single- and double well is given by Eq. (3.4), with a barrier height $U_0 = 3\ k_{\mathrm{B}}T$. For the single well, an absorbing boundary is placed at $x_t = L$ so that only the region $x < L$ of the quartic potential is used. For the single well, MFPTs τ_{MFP} (plus signs) are calculated via direct sampling of first-passage times, escape times τ_{esc} (empty squares) are calculated using Eq. (B.2). For the double well, MFPTs τ_{MFP} (crosses) are calculated via direct sampling of first-passage times from a long trajectory allowing for barrier recrossing, as described in Chapter 3, escape times τ_{esc} (empty circles) are calculated using Eq. (B.5). (a) Plot of $\tau_{\mathrm{MFP}}/\tau_D$ as a function of τ_m/τ_D for several values of the rescaled memory time τ_Γ/τ_D as denoted by the colored labels in the figure. (b) Plot of $\tau_{\mathrm{MFP}}/\tau_D$ as a function of τ_Γ/τ_D for several values of τ_m/τ_D, as denoted by the colored labels in the figure.

about 2. The difference between escape times and MFPTs has been discussed before [123] and in our case has an intuitive explanation. In the energy diffusion regime, after the particle has crossed the barrier once, it has a high kinetic energy and will oscillate back and forth between the two wells multiple times, as is seen in the example trajectories in Figs. 3.1 (b), (f), (g), (h). After the particle has stopped oscillating between the wells, it will be found in the target or in the starting well with equal probability. This fundamental difference between Markovian and non-Markovian barrier crossing is clearly seen in Figs. 3.1 (d) and (h), where long trajectories in the high-friction Markovian regime (exhibiting no recrossings) and in the high-friction non-Markovian regime (with multiple recrossings) are shown. Thus, in the energy diffusion regime, encompassing both the inertial case but also the high-friction non-Markovian case, only half of the barrier-crossing events will be productive and bring the particle from the starting well to the target well. This explains why the escape time becomes twice the MFPT in the energy diffusion regime, namely because in the calculation of a MFPT each barrier crossing event is counted, regardless of whether it is productive or not.

On the other hand, the simulated single-well and double-well MFPTs agree nicely with each other and also with the single-well escape times for all parameters considered, thus only the escape time for the double-well system yields different results from the other scenarios, and becomes twice as large as the other barrier crossing times in the energy diffusion regime for $\tau_m/\tau_D \gg 1$ or $\tau_\Gamma/\tau_D \gg 1$. From the fact that double-well and single-well MFPTs agree with each other, we conclude that recrossing events, which are definitely present in the calculation of MFPTs in a double well, contribute negligibly to the statistical average in τ_{MFP}. This is a nontrivial and noteworthy finding.

The difference between escape times in the single-well and double-well scenarios in the energy diffusion regime is also obtained in PGH theories, shown as solid and dashed lines in Fig. B.1. While in the regime of high friction and short memory both lines agree, in the regime of long memory or large mass the two lines differ by a factor of about 2, similar to our simulation results. Overall, PGH theory matches the numerical escape times remarkably well for both the single-well and the double-well scenarios. Only for long memory $\tau_\Gamma/\tau_D \gg 1$ the PGH predictions are smaller than the numerical results by a factor of about 2, as can most clearly be seen in Fig. B.1 (a) by comparing the numerical escape times for $\tau_\Gamma/\tau_D = 10$ to the corresponding PGH theory predictions. Note that the small deviation between PGH predictions and simulated escape times happens to be of the same order of magnitude as the difference between the simulated MFPTs and escape times in the double-well scenario, which we believe to be purely coincidental. The difference between simulation and PGH predictions for the escape times could be caused by imperfections of PGH theory but also by numerical inaccuracies.

In conclusion, the MFPTs we calculate in Chapter 3 from simulations in a double well can rightfully be compared to escape times calculated within single-well PGH theory. The reason is that MFPTs within the double-well scenario (which is numerically the most efficient scenario to obtain barrier crossing times) agree perfectly with escape times (or MFPTs) obtained from the single-well scenario, as demonstrated by our simulations in Fig. B.1.

B.2 Comparison of quartic and cubic potentials

Based on the PGH expression for the escape time from a quartic single well, we construct the heuristic formula Eq. (3.10), which describes MFPTs calculated from Langevin simulations in a quartic potential very well. In this appendix we show that the heuristic formula Eq. (3.10) also captures the MFPTs in a cubic potential. To allow for a meaningful comparison, we consider a cubic single-well potential

$$U(x) = -2U_0 \frac{x}{L}\left[\left(\frac{x}{L}+\frac{3}{4}\right)^2 - \frac{9}{16}\right] + U_0, \tag{B.6}$$

and a quartic single-well potential

$$U(x) = \begin{cases} U_0\left[(x/L)^2 - 1\right]^2 & x \leq L, \\ -\infty & x > L. \end{cases} \tag{B.7}$$

The two potentials are shown in Fig. B.2 (a), both have a barrier height U_0 and a distance L between the potential minimum at $x = -L$ and the barrier top. For each potential we run many simulations using initial conditions as explained in Chapter 3, and absorbing boundary conditions at the target position $x_t = L$, so that a simulation is stopped once the particle reaches x_t for the first time. Resulting MFPTs are shown together with the heuristic formula Eq. (3.10) in Figs. B.2 (b), (c). We find that the two potentials (B.6), (B.7) lead to almost identical MFPTs, which are well described by the heuristic formula Eq. (3.10). Only in the long memory time regime $\tau_\Gamma/\tau_D \gtrsim 1$ the heuristic formula systematically yields MFPTs that are slightly smaller than the Langevin results for both potentials. These small discrepancies are expected, since PGH theory shows similar behavior, see Fig. 3.2, and since the heuristic formula is based on PGH theory.

We conclude that our heuristic formula Eq. (3.10), using as only input the barrier height U_0 and the distance L between the minimum at $x = -L$ and the barrier maximum at $x = 0$, accurately predicts MFPTs for different potential shapes and is not limited to the quartic double well Eq. (3.4) we consider in Chapter 3. This is expected to hold as long as the curvatures at the potential minimum and the barrier top are not very different. If in contrast one has a narrow well and a broad barrier top or vice versa, the predictions of PGH theory can be very different from the rather symmetric scenario we use to construct our heuristic formula [122], so that the full PGH theory should be employed in such situations.

B.3 Relative deviation between heuristic formula and PGH theory

To demonstrate the global validity of Eq. (3.10), we show in Fig. B.3 contour plots of the relative deviation

$$\frac{\Delta\tau_{\mathrm{MFP}}}{\tau_{\mathrm{MFP}}} \equiv \left|\frac{\tau_{\mathrm{MFP}} - \tau_{\mathrm{MFP}}^{\mathrm{PGH}}}{\tau_{\mathrm{MFP}}^{\mathrm{PGH}}}\right|, \tag{B.8}$$

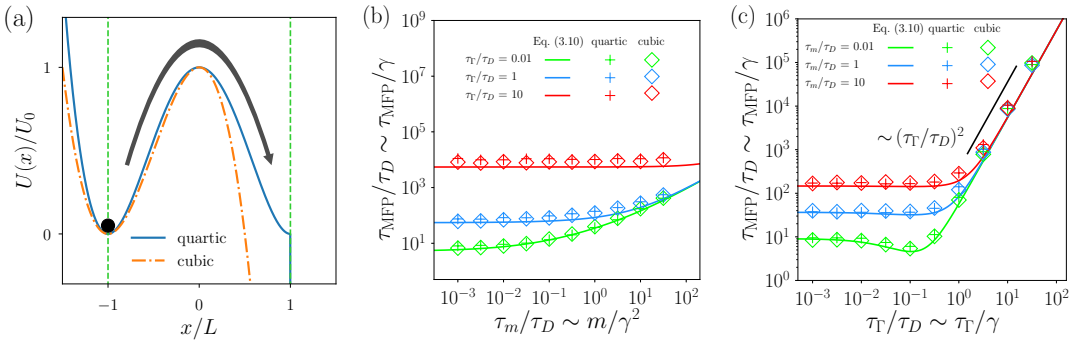

Figure B.2: (a) Illustration of the barrier crossing of a particle in the potentials $U(x)$ defined in Eqs. (B.6), (B.7). The mean first-passage time τ_{MFP} is defined as the mean time difference between crossing the minimum at the starting position $x_s = -L$ (left vertical dashed line) and reaching the target position $x_t = L$ (right vertical dashed line) for the first time. (b), (c) MFPTs obtained from Langevin simulations using the potentials shown in subplot (a) are compared to the heuristic formula Eq. (3.10). For each datapoint, thousands of simulations are run for $U_0 = 3\,k_{\mathrm{B}}T$ with stochastic initial conditions as described in Chapter 3, and using an absorbing boundary condition at $x_t = L$. While subplot (b) shows MFPTs as a function of τ_m/τ_D for various values of τ_Γ/τ_D, subplot (c) shows MFPTs as a function of τ_Γ/τ_D for various values of τ_m/τ_D.

between the MFPT as predicted by PGH theory, denoted here by $\tau_{\mathrm{MFP}}^{\mathrm{PGH}}$, and the heuristic formula (3.10), denoted here by τ_{MFP}, as a function of τ_m/τ_D, τ_Γ/τ_D. As the figure shows, the relative deviation between the heuristic formula and PGH theory, whose predictions for τ_{MFP} range over 27 orders of magnitude in the parameter range considered, is typically of the order of 10%.

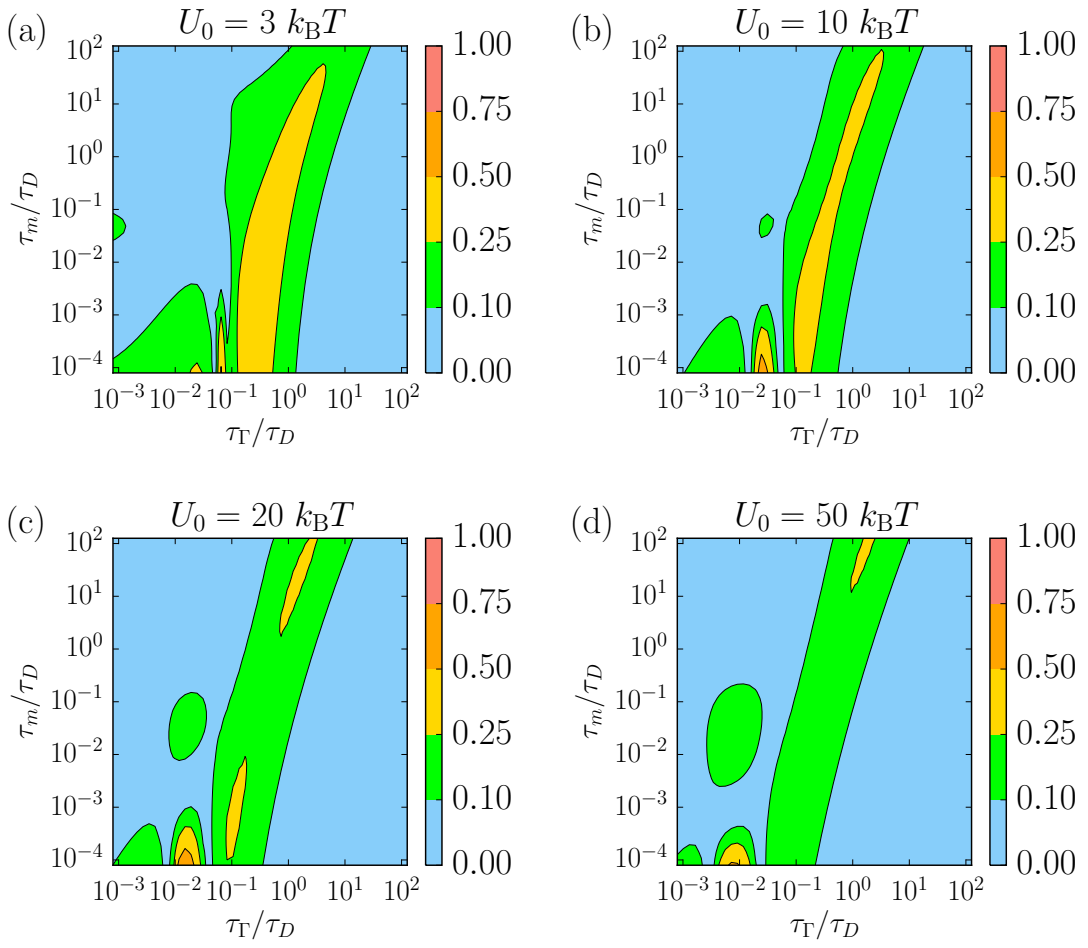

Figure B.3: The subplots show the relative deviation, as defined by Eq. (B.8), between PGH theory and the heuristic formula, Eq. (3.10), for barrier heights $U_0 = 3$, 10, 20, 50 $k_\mathrm{B}T$.

Appendix C

Supplemental Material for Chapter 4

C.1 Dimensionless form of the GLE

We consider the one-dimensional Langevin equation

$$m\,\ddot{x}(t) = -\int_0^t \Gamma(t-t')\dot{x}(t')\,\mathrm{d}t' - U'(x(t)) + \eta(t), \tag{C.1}$$

where m is the mass of the particle, x its position, Γ a memory kernel, U' denotes the derivative of an external potential U, and η is a random force. The random force η is Gaussian with zero mean, $\langle\eta(t)\rangle = 0$, and obeys the generalized fluctuation-dissipation theorem (FDT)

$$\langle\eta(t)\eta(t')\rangle = k_\mathrm{B}T\,\Gamma(|t-t'|). \tag{C.2}$$

We consider a multiexponential memory kernel with friction coefficients γ_i and memory times τ_i,

$$\Gamma(t) = \sum_{i=1}^{N} \frac{\gamma_i}{\tau_i} e^{-|t|/\tau_i}, \tag{C.3}$$

and define the total friction $\gamma := \sum_{i=1}^{N}\gamma_i$. Further defining a dimensionless position $\tilde{x}(\tilde{t}) := x(\tau_D\tilde{t})/L$, evaluating Eq. (C.1) at $t = \tilde{t}\tau_D$ and multiplying by $L/(k_\mathrm{B}T)$, we obtain

$$\frac{\tau_m}{\tau_D}\ddot{\tilde{x}}(\tilde{t}) = -\sum_{i=1}^{N}\frac{\gamma_i}{\gamma}\frac{\tau_D}{\tau_i}\int_0^{\tilde{t}} \mathrm{d}\tilde{t}'\exp\left[-\frac{\tau_D}{\tau_i}\left(\tilde{t}-\tilde{t}'\right)\right]\dot{\tilde{x}}(\tilde{t}') + \tilde{F}\left(\tilde{x}(\tilde{t})\right) + \tilde{\eta}(\tilde{t}), \tag{C.4}$$

where $\tilde{F}(\tilde{x}) := L\nabla U(L\tilde{x})/(k_\mathrm{B}T)$ and $\tilde{\eta}(\tilde{t}) := L\,\eta(\tau_D\tilde{t})/(k_\mathrm{B}T)$. Using Eq. (C.2), it follows that the autocorrelation of the dimensionless random force is given by

$$\left\langle\tilde{\eta}(\tilde{t})\tilde{\eta}(\tilde{t}')\right\rangle = \sum_{i=1}^{N}\frac{\gamma_i}{\gamma}\frac{\tau_D}{\tau_i}\exp\left[-\frac{\tau_D}{\tau_i}|\tilde{t}-\tilde{t}'|\right]. \tag{C.5}$$

For $N = 1$ we recover the case of single-exponential memory that was discussed in Chapter 3, for $N = 2$ and $\gamma_1 = \gamma_2$ we obtain the bi-exponential system studied in Chapter 4.

C.2 Transforming the GLE into a coupled system of Markovian equations

We now show that the dimensionless GLE with multiexponential memory, Eqs. (C.4), (C.5), is equivalent to the coupled system of equations

$$\frac{\tau_m}{\tau_D}\ddot{\tilde{x}}(\tilde{t}\,) = \sum_{i=1}^{N} R_i(\tilde{t}\,) + \tilde{F}\left(\tilde{x}(\tilde{t}\,)\right), \tag{C.6}$$

$$-\frac{\tau_i}{\tau_D}\dot{R}_i(\tilde{t}\,) = R_i(\tilde{t}\,) + \frac{\gamma_i}{\gamma}\dot{\tilde{x}}(\tilde{t}\,) + \sqrt{\frac{\gamma_i}{\gamma}}\xi_i(\tilde{t}\,) \qquad 1 \le i \le N, \tag{C.7}$$

where the ξ_i are Gaussian stochastic processes with zero mean and variance

$$\left\langle \xi_i(\tilde{t}\,)\xi_j(\tilde{t}'\,)\right\rangle = 2\delta_{i,j}\delta(\tilde{t}-\tilde{t}'). \tag{C.8}$$

To show the equivalence of Eqs. (C.6), (C.7), (C.8) to the GLE, we first note that the solution to Eq. (C.7) is given by

$$\begin{aligned} R_i(\tilde{t}) = R_i(0)\exp\left(-\frac{\tau_D}{\tau_i}\tilde{t}\right) - \frac{\gamma_i}{\gamma}\frac{\tau_D}{\tau_i}\int_0^{\tilde{t}} \mathrm{d}\tilde{t}'\exp\left[-\frac{\tau_D}{\tau_i}(\tilde{t}-\tilde{t}')\right]\dot{\tilde{x}}(\tilde{t}') \\ - \sqrt{\frac{\gamma_i}{\gamma}}\frac{\tau_D}{\tau_i}\int_0^{\tilde{t}} \mathrm{d}\tilde{t}'\exp\left[-\frac{\tau_D}{\tau_i}(\tilde{t}-\tilde{t}')\right]\xi(\tilde{t}'). \end{aligned} \tag{C.9}$$

Inserting this into Eq. (C.6), we obtain

$$\frac{\tau_m}{\tau_D}\ddot{\tilde{x}}(\tilde{t}) = -\sum_{i=1}^{N}\frac{\gamma_i}{\gamma}\frac{\tau_D}{\tau_i}\int_0^{\tilde{t}} \mathrm{d}\tilde{t}'\exp\left[-\frac{\tau_D}{\tau_i}\left(\tilde{t}-\tilde{t}'\right)\right]\dot{\tilde{x}}(\tilde{t}') + \tilde{F}(\tilde{x}(\tilde{t})) + \tilde{\eta}_R(\tilde{t}), \tag{C.10}$$

where we define

$$\tilde{\eta}_R(\tilde{t}) = \sum_{i=1}^{N}\left\{R_i(0)\exp\left(-\frac{\tau_D}{\tau_i}\tilde{t}\right) - \sqrt{\frac{\gamma_i}{\gamma}}\frac{\tau_D}{\tau_i}\int_0^{\tilde{t}} \mathrm{d}\tilde{t}'\exp\left[-\frac{\tau_D}{\tau_i}(\tilde{t}-\tilde{t}')\right]\xi(\tilde{t}')\right\}. \tag{C.11}$$

To obtain the equivalence of Eqs. (C.6), (C.7) to Eqs. (C.4), (C.5), $\tilde{\eta}_R$ should be a stochastic processes identical to $\tilde{\eta}$. For this, we assume that the initial conditions $R_i(0)$ are Gaussian random variables with mean zero and variance

$$\langle R_i(0)R_j(0)\rangle = \delta_{i,j}\frac{\gamma_i}{\gamma}\frac{\tau_D}{\tau_i}, \tag{C.12}$$

and furthermore that $\langle R_i(0)\xi_j(\tilde{t})\rangle = 0$. Then, the mean of $\tilde{\eta}_R$ is easily seen to be zero, and the variance is given by

$$\begin{aligned}
\left\langle \tilde{\eta}_R(\tilde{t})\tilde{\eta}_R(\tilde{t}')\right\rangle &= \sum_{i=1}^{N} \exp\left[-\frac{\tau_D}{\tau_i}(\tilde{t}+\tilde{t}')\right]\langle R_i(0)^2\rangle && \text{(C.13)}\\
&\quad + \sum_{i=1}^{N}\frac{\gamma_i}{\gamma}\left(\frac{\tau_D}{\tau_i}\right)^2\int_0^{\tilde{t}}\mathrm{d}u\int_0^{\tilde{t}'}\mathrm{d}u'\,\exp\left[-\frac{\tau_D}{\tau_i}(\tilde{t}+\tilde{t}'-u-u')\right]\langle\xi_i(u)\xi_i(u')\rangle\\
&= \sum_{i=1}^{N}\exp\left[-\frac{\tau_D}{\tau_i}(\tilde{t}+\tilde{t}')\right]\frac{\gamma_i}{\gamma}\frac{\tau_D}{\tau_i}\\
&\quad + \sum_{i=1}^{N}2\frac{\gamma_i}{\gamma}\left(\frac{\tau_D}{\tau_i}\right)^2\int_0^{\min\{\tilde{t},\tilde{t}'\}}\mathrm{d}u\,\exp\left[-\frac{\tau_D}{\tau_i}(\tilde{t}+\tilde{t}'-2u)\right] && \text{(C.14)}\\
&= \sum_{i=1}^{N}\exp\left[-\frac{\tau_D}{\tau_i}(\tilde{t}+\tilde{t}')\right]\frac{\gamma_i}{\gamma}\frac{\tau_D}{\tau_i}\\
&\quad + \sum_{i=1}^{N}\frac{\gamma_i}{\gamma}\frac{\tau_D}{\tau_i}\left\{\exp\left[-\frac{\tau_D}{\tau_i}\left(\tilde{t}+\tilde{t}'-2\min\{\tilde{t},\tilde{t}'\}\right)\right]-\exp\left[-\frac{\tau_D}{\tau_i}\left(\tilde{t}+\tilde{t}'\right)\right]\right\} && \text{(C.15)}\\
&= \sum_{i=1}^{N}\frac{\gamma_i}{\gamma}\frac{\tau_D}{\tau_i}\exp\left[-\frac{\tau_D}{\tau_i}|\tilde{t}-\tilde{t}'|\right], && \text{(C.16)}
\end{aligned}$$

where we use that $\tilde{t}+\tilde{t}'-2\min\{\tilde{t},\tilde{t}'\} = |\tilde{t}-\tilde{t}'|$. Thus, $\tilde{\eta}_R$ is a Gaussian stochastic process with the first two moments identical to those of the Gaussian stochastic process $\tilde{\eta}$, so that $\tilde{\eta}_R \equiv \tilde{\eta}$. For $N = 2$ and $\gamma_1 = \gamma_2$, we obtain the formulas used in Chapter 4.

To simulate Eqs. (C.6), (C.7) using a Runge-Kutta scheme, we introduce an auxiliary variable z to rewrite the equations as a system of first-order equations

$$\dot{\tilde{x}}(\tilde{t}\,) = z(\tilde{t}\,), \tag{C.17}$$

$$\frac{\tau_m}{\tau_D}\dot{z}(\tilde{t}\,) = \sum_{i=1}^{N} R_i(\tilde{t}\,) + \tilde{F}\left(\tilde{x}(\tilde{t}\,)\right), \tag{C.18}$$

$$-\frac{\tau_i}{\tau_D}\dot{R}_i(\tilde{t}\,) = R_i(\tilde{t}\,) + \frac{\gamma_i}{\gamma}z(\tilde{t}\,) + \sqrt{\frac{\gamma_i}{\gamma}}\xi_i(\tilde{t}\,) \qquad 1 \le i \le N, \tag{C.19}$$

C.3 Mean squared displacements for unequal memory times

In this appendix we illustrate that even in the asymmetric scenario $\tau_1 \ll \tau_2$, both terms in the bi-exponential memory kernel contribute equally to the long-time diffusion. In Fig. C.1 we show mean squared displacements (MSDs)

$$\langle \Delta x^2(t)\rangle = \left\langle \left(x(t)-x(0)\right)^2\right\rangle \tag{C.20}$$

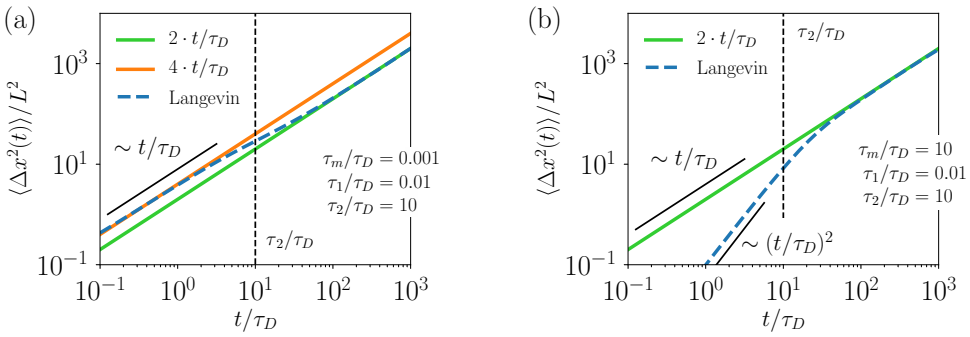

Figure C.1: Numerical MSDs together with theoretical predictions. (a) The blue dashed line shows the MSD for a bi-exponential system without external potential, $U = 0$, and $\tau_m/\tau_D = 0.001$, $\tau_1/\tau_D = 0.01$, $\tau_2/\tau_D = 10$, corresponding to Fig. 4.2 (c). The colored lines denote the expected MSD for diffusion with friction coefficients $\gamma/2$ (orange line) and γ (green line). The black solid line indicates the power law $\langle \Delta x^2(t) \rangle \sim t$ expected for diffusion, the black vertical dashed line denotes the value of τ_2. (b) The blue dashed line shows the MSD for a bi-exponential system without external potential, $U = 0$, and $\tau_m/\tau_D = 10$, $\tau_1/\tau_D = 0.01$, $\tau_2/\tau_D = 10$, corresponding to Fig. 4.2 (f). The green line denotes the expected MSD for diffusion with friction coefficients γ. The black solid lines indicate the power law $\langle \Delta x^2(t) \rangle \sim t$ expected for diffusion and the power law $\langle \Delta x^2(t) \rangle \sim t^2$ expected for ballistic motion, the black vertical dashed line denotes the value of τ_2.

obtained from simulations without a potential and unequal memory times $\tau_1/\tau_D = 0.01$, $\tau_2/\tau_D = 10$. The parameters used are the same as in Figs. 4.2 (c), (f).

Figure C.1 (a) shows the high-friction scenario $\tau_m/\tau_D = 0.001$. For times $t \gg \tau_1, \tau_2$ the MSD is given by $\langle \Delta x^2(t) \rangle / L^2 = 2t/\tau_D$. As we show now, this corresponds to diffusion with a friction coefficient γ. The MSD of a Brownian particle with friction coefficient γ is given by

$$\langle \Delta x^2(t) \rangle = 2Dt = 2\frac{k_\mathrm{B}T}{\gamma}t, \tag{C.21}$$

where the first equality sign is the definition of the diffusion coefficient D and at the second equality sign we use the Einstein relation $D = k_\mathrm{B}T/\gamma$. Upon dividing Eq. (C.21) by L^2 and using the definition of τ_D, Eq. (4.6), we obtain the observed MSD $\langle \Delta x^2(t) \rangle / L^2 = 2t/\tau_D$. For times $t < \tau_2$, only τ_1 contributes to the diffusion and the numerical MSD is given by $\langle \Delta x^2(t) \rangle / L^2 = 4t/\tau_D$. Using the same argument as in Eq. (C.21), it follows that this corresponds to diffusion with a friction coefficient $\gamma/2$.

For the low-friction scenario $\tau_m/\tau_D = 10$ depicted in Fig. C.1 (b), we see the inertial regime $\langle \Delta x^2(t) \rangle / L^2 \sim (t/\tau_D)^2$ for $t \ll \tau_m$, and as $t \gtrsim \tau_m$ the MSD crosses over to diffusive behavior, determined by the full friction coefficient γ. This is expected since for the parameters we use, once $t \gg \tau_m$ holds we also have $t \gg \tau_1, \tau_2$.

In summary, Fig. C.1 shows that even though the trajectories from Figs. 4.2 (c), (f) look as if the dynamics is completely dominated by the shorter memory time, and even though in Chapter

4 we find that for $\tau_i \ll \tau_j$, the barrier crossing time is independent of τ_j, the long time diffusion of the bi-exponential GLE is always determined the full bi-exponential memory kernel which contains both τ_1, τ_2.

C.4 Comparison of numerical MFPTs to GH theory

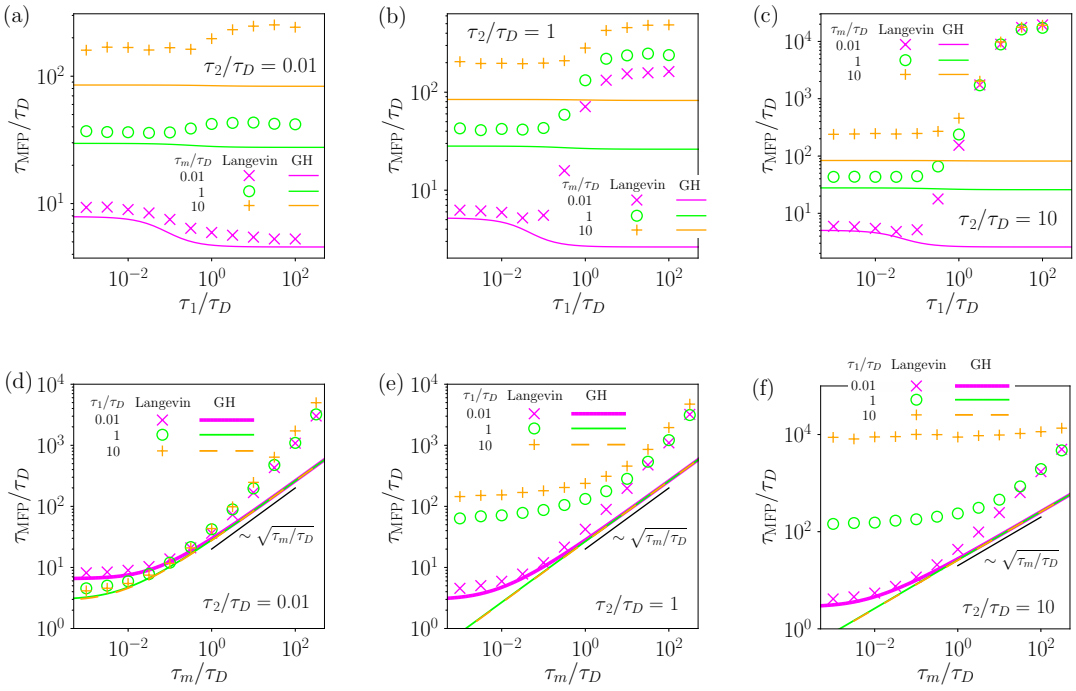

Figure C.2: Comparison of numerical MFPTs to Grote-Hynes (GH) theory. (a)-(c) Colored symbols denote the rescaled MFPT $\tau_{\mathrm{MFP}}/\tau_D$ as function of τ_1/τ_D for several values of τ_2/τ_D and fixed τ_m/τ_D, given by (a) $\tau_m/\tau_D = 0.01$, (b) $\tau_m/\tau_D = 1$, (c) $\tau_m/\tau_D = 10$. The numerical data is a replot of the data shown in Fig. 4.6 (a)-(c). The colored lines represent GH theory, evaluated for a bi-exponential memory kernel using the given parameters. (d)-(f) Colored symbols denote the rescaled MFPT $\tau_{\mathrm{MFP}}/\tau_D$ as function of τ_m/τ_D for several values of τ_2/τ_D and fixed τ_1/τ_D, given by (a) $\tau_1/\tau_D = 0.01$, (b) $\tau_1/\tau_D = 1$, (c) $\tau_1/\tau_D = 10$. The numerical data is a replot of the data shown in Fig. 4.8 (a)-(c). The colored lines represent GH theory, evaluated for a bi-exponential memory kernel using the given parameters. The black lines indicate the transition-state-theory (TST) scaling $\tau_{\mathrm{MFP}}/\tau_D \sim \sqrt{\tau_m/\tau_D}$ which GH theory attains in the energy-diffusion regime [87]. All data is obtained using $U_0 = 3\,k_{\mathrm{B}}T$.

In Fig. C.2 we compare numerical MFPTs to Grote-Hynes (GH) theory [87]. Consistent with our results from Chapter 3, we find that GH theory only describes the numerical MFPTs in the high-friction regime $\tau_m/\tau_D \ll 1$ and if both memory times are small, $\tau_1/\tau_D, \tau_2/\tau_D \ll 1$. If either $\tau_m/\tau_D \gg 1$ or $\min\{\tau_1/\tau_D, \tau_2/\tau_D\} \gg 1$, then GH theory reduces to the transition

state theory (TST) limit where $\tau_{\mathrm{MFP}}/\tau_D \sim \sqrt{\tau_m/\tau_D}$, as can be seen in Figs. C.2 (d)-(f). Thus, also for bi-exponential memory GH theory only yields accurate results in the high-friction short-memory regime.

Appendix D

Supplemental Material for Chapter 5

In this appendix we first derive the implicit dispersion relation, Eq. (5.8). Then we show how the dispersion relations of Rayleigh, capillary-gravity and Lucassen waves follow, and derive the CGV wave dispersion relation, Eq. (5.19). Finally, we supply a wave existence state diagram for surface tension $\sigma_{2\mathrm{D}} = 10\ \mathrm{mN/m}$, and show an example for the frequency dependent crossover from capillary-gravity and Lucassen waves to Rayleigh waves.

D.1 Derivation of the conditional equation

D.1.1 Linear viscoelasticity

For the bulk medium at $z < 0$, the linearized continuum mechanical momentum conservation equations are given as [168]

$$\rho(\vec{r},t)\partial_t^2 u_j(\vec{r},t) = \partial_k \sigma_{jk}(\vec{r},t) + F_j(\vec{r},t) \qquad j \in \{x,y,z\}, \tag{D.1}$$

where $\rho(\vec{r},t)$ is the mass density, $\vec{u}(\vec{r},t)$ is the displacement field and $\vec{F}(\vec{r},t)$ an external force and we use Cartesian coordinates $\vec{r} = (x,y,z)$. We assume the bulk medium to be a linear, isotropic and homogeneous viscoelastic medium, so that the dependence of the stress tensor σ_{jk} on the displacement field is given by the viscoelastic stress strain relation [168]

$$\sigma_{jk}(\vec{r},t) = \int_{-\infty}^{\infty} g_{\mathrm{s}}(t-t')\partial_{t'}\epsilon_{jk}(\vec{r},t')\,\mathrm{d}t' + \frac{\delta_{j,k}}{3}\int_{-\infty}^{\infty}\left[g_{\mathrm{d}}(t-t') - g_{\mathrm{s}}(t-t')\right]\partial_{t'}\epsilon_{ll}(x,t')\,\mathrm{d}t', \tag{D.2}$$

where the components of the strain tensor are given by

$$\epsilon_{jk} = \frac{1}{2}\left(\partial_j u_k + \partial_k u_j\right), \tag{D.3}$$

and the shear and dilational relaxation functions $g_{\mathrm{s}}(t)$, $g_{\mathrm{d}}(t)$ are independent of position. We use the Einstein summation convention, so that $\epsilon_{ll} = \partial_l u_l = \vec{\nabla}\cdot\vec{u}$. Furthermore, for the temporal

Fourier transform $\tilde{f}(\omega)$ of a function $f(t)$, we use the convention

$$\tilde{f}(\omega) = \int_{-\infty}^{\infty} e^{i\omega t} f(t)\, \mathrm{d}t, \tag{D.4}$$

$$f(t) = \frac{1}{2\pi} \int_{-\infty}^{\infty} e^{-i\omega t} \tilde{f}(\omega)\, \mathrm{d}\omega. \tag{D.5}$$

The temporal Fourier transform of Eq. (D.2) then reads

$$\tilde{\sigma}_{jk}(\vec{r},\omega) = (-i\omega)\tilde{g}_{\mathrm{s}}(\omega)\tilde{\epsilon}_{jk}(\vec{r},\omega) + \delta_{jk}\frac{-i\omega}{3}\left[\tilde{g}_{\mathrm{d}}(\omega) - \tilde{g}_{\mathrm{s}}(\omega)\right]\tilde{\epsilon}_{ll}(\vec{r},\omega) \tag{D.6}$$

and the Fourier transformed relaxation functions $\tilde{g}_{\mathrm{s}}(\omega)$, $\tilde{g}_{\mathrm{d}}(\omega)$, are related to the, in general frequency dependent and complex, shear and bulk moduli μ, K [151] via

$$\mu(\omega) = \frac{-i\omega}{2}\tilde{g}_{\mathrm{s}}(\omega), \qquad K(\omega) = \frac{-i\omega}{3}\tilde{g}_{\mathrm{d}}(\omega). \tag{D.7}$$

In classical elasticity theory, $\mu(\omega)$ and $K(\omega)$ are purely real and independent of ω.

D.1.2 Compressible Newtonian fluid

Since we want to apply our theory to situations where water is the bulk medium, we need to explain how the stress strain relation (D.2) is related to the usual stress strain relation of a compressible Newtonian fluid,

$$\sigma_{jk} = -P\delta_{jk} + 2\eta\partial_t\epsilon_{jk} + \left(\eta' - \frac{2}{3}\eta\right)\delta_{jk}\partial_t\epsilon_{ll}, \tag{D.8}$$

where η, η' are the shear and volume viscosities and P is the pressure. We do this by employing a similar argumentation as is usually used out to derive sound waves in bulk media, see e.g. Refs. [149, 172], and include gravity and compressibility effects in the derivation. Gravitational acceleration is modeled as an external force $F_i = -\delta_{i,z}\rho g$, and we are looking for solutions to the linearized momentum conservation Eq. (D.1) with the stress tensor given by Eq. (D.8).

We first recall the standard stationary solution of Eq. (D.1) for an incompressible ($\vec{\nabla}\cdot\vec{u} = \epsilon_{ll} = 0$) fluid at rest,

$$\vec{u}^{(0)}(\vec{r},t) = \vec{0}, \tag{D.9}$$

$$\rho^{(0)}(\vec{r},t) = \rho_0, \tag{D.10}$$

$$P^{(0)}(\vec{r},t) = P_0 - \rho_0 g z, \tag{D.11}$$

where ρ_0 is the constant density of the fluid and P_0 is the pressure at $z = 0$. We consider small perturbations around this solution, and by using this incompressible stationary solution as reference state, we assume that for the depths where the small perturbations are not negligibly small, the compression of the Newtonian fluid due to gravity can be neglected. To quantify this

statement, we first recall the thermodynamic definition of the modulus of compression (bulk modulus),

$$\frac{1}{K} = -\frac{1}{V}\frac{\partial V}{\partial P}. \tag{D.12}$$

The value of K in general depends not only on the material, but also on the thermodynamics of the process one is interested in. For adiabatic compression, $K \equiv K_S = 1/\kappa_S$ with κ_S the adiabatic compressibility, while for isothermal compression, $K \equiv K_T = 1/\kappa_T$, with κ_T the isothermal compressibility. For the stationary solution Eqs. (D.9-D.11), the isothermal bulk modulus is appropriate, and for water at $20\,^{\circ}\mathrm{C}$ it has the value [173]

$$K_T \approx 2.2 \cdot 10^8\ \mathrm{kg/m^2}. \tag{D.13}$$

The assumption that gravitational compression in the stationary solution can be neglected reads

$$\frac{\rho_0 g L}{K_T} \ll 1, \tag{D.14}$$

where L is the depth where the perturbation is so small that it can be neglected. Thus, for $\rho_0 = 10^3\ \mathrm{kg/m^3}$, $g = 9.81\ \mathrm{m/s^2}$,

$$L \ll 2.3 \times 10^4\ \mathrm{m}. \tag{D.15}$$

With the exception of low frequency gravity waves, the waves we consider decay at depths in the range of meters or less, so that neglecting the compression of the equilibrium state due to gravity is justified. Nevertheless, the following derivation could also be carried out to first order in $\rho_0 g z/K_T$. It would, however, be more complicated and lead to the same boundary condition, so that we perturb around the incompressible steady state solution (D.9-D.11).

We now consider small perturbations around the steady state solution Eqs. (D.9-D.11). We assume the perturbations to be of the form

$$\vec{u}(\vec{r},t) = \vec{0} + \vec{u}^{\,(1)}(\vec{r},t), \tag{D.16}$$

$$\rho(\vec{r},t) = \rho_0 + \rho^{(1)}(\vec{r},t), \tag{D.17}$$

$$P(\vec{r},t) = P_0 - \rho_0 g\left(z + u_z^{(1)}(\vec{r},t)\right) + P^{(1)}(\vec{r},t), \tag{D.18}$$

where $u_z^{(1)}$ is the z-component of $\vec{u}^{\,(1)}$.

Momentum conservation, Eq. (D.1), constitutes only 3 equations for the 5 unknowns $\rho^{(1)}$, $P^{(1)}$, $\vec{u}^{\,(1)}$. To close the system of equations, we introduce linearized mass conservation,

$$0 = \frac{\partial \rho}{\partial t} + \vec{\nabla}\cdot\left(\rho \partial_t \vec{u}\right), \tag{D.19}$$

and the definition of the modulus of compression (bulk modulus),

$$\frac{1}{K} = -\frac{1}{V}\frac{\partial V}{\partial P^{(1)}}, \tag{D.20}$$

which gives a relation between local volume changes and local pressure changes. Technically, the bulk modulus we defined earlier and denoted by the same symbol, Eq. (D.12), is the physical bulk modulus, but because we neglect the compression due to gravity we use Eq. (D.20), where P has been replaced by $P^{(1)}$, so that the gravitational contribution (the second term in Eq. (D.18)) has been excluded.

Integrating Eq. (D.19) with respect to time leads to

$$\rho^{(1)} = -\rho_0 \vec{\nabla} \cdot \vec{u}^{\,(1)}, \tag{D.21}$$

where the constant of integration has been chosen so that for a volume preserving perturbation, $\vec{\nabla} \cdot \vec{u}^{\,(1)} = 0$, we obtain vanishing density change, $\rho^{(1)} = 0$. Furthermore, Eq. (D.20) can be integrated to yield, to first order in $\vec{u}^{\,(1)}$,

$$P^{(1)} = -K \vec{\nabla} \cdot \vec{u}^{\,(1)}, \tag{D.22}$$

where we used the relation $\Delta V/V \approx \vec{\nabla} \cdot \vec{u}^{\,(1)}$ [151] and chose the constant of integration so that for a volume preserving perturbation, $\vec{\nabla} \cdot \vec{u}^{\,(1)} = 0$, the pressure change vanishes, $P^{(1)} = 0$.

Inserting the perturbed solution, Eqs. (D.16-D.18), into momentum conservation, Eq. (D.1), and using Eq. (D.21), (D.22) to eliminate $P^{(1)}$, $\rho^{(1)}$, we obtain, to linear order in the perturbations,

$$\begin{aligned} \rho_0 \partial_t^2 u_j^{(1)} = {} & \partial_k \left[2\eta \partial_t \epsilon_{jk}^{(1)} + \left(\eta' - \frac{2}{3}\eta \right) \delta_{jk} \partial_t \epsilon_{ll}^{(1)} \right] \\ & + \partial_j \left[-\rho_0 g u_z^{(1)} + K \vec{\nabla} \cdot \vec{u}^{\,(1)} \right] + \delta_{j,z} g \rho_0 \vec{\nabla} \cdot \vec{u}^{\,(1)}, \end{aligned} \tag{D.23}$$

where $\epsilon_{jk}^{(1)}$ is the strain tensor, Eq. (D.3), with $\vec{u}$ replaced by $\vec{u}^{\,(1)}$. Gravitational acceleration enters this equation via two terms, namely the restoring gravitational force (first term in second line of Eq. (D.23)), and the buoyancy (last term of Eq. (D.23)). One standard way to deal with these terms is the surface gravity approximation, where gravitational force terms are neglected in the bulk, but the restoring gravitational force is kept in the boundary condition [234]. In that case, Eq. (D.23) is simplified in the bulk, to yield

$$\rho_0 \partial_t^2 u_j^{(1)} = \partial_k \left[2\eta \partial_t \epsilon_{jk}^{(1)} + \left(\eta' - \frac{2}{3}\eta \right) \delta_{jk} \partial_t \epsilon_{ll}^{(1)} + \delta_{jk} K \epsilon_{ll}^{(1)} \right]. \tag{D.24}$$

Comparing this to Eqs. (D.1), (D.6), we see that our description of a compressible Newtonian fluid in the presence of gravity has now been approximated by that of a viscoelastic medium without external forces and with relaxation functions

$$\tilde{g}_{\mathrm{s}}(\omega) = 2\eta, \tag{D.25}$$

$$\tilde{g}_{\mathrm{d}}(\omega) = 3\eta' + \frac{3K}{-i\omega}. \tag{D.26}$$

The use of the symbol K here is consistent with our earlier use of the symbol in Eq. (D.7). More explicitly, if the dilational response is purely elastic then $\eta' = 0$, and direct comparison shows that the two formulas for $\tilde{g}_{\mathrm{d}}$, Eqs. (D.7) and (D.26), coincide if $K(\omega)$ in Eq. (D.7) is real and

independent of ω. Formally, the relaxation function (D.26) models a Kelvin-Voigt material [168], where for low frequencies the bulk modulus K dominates while for high frequencies the volume viscosity η' dominates. Assuming that the compression due to the perturbation is adiabatic, we can use the relation

$$K \equiv K_S = \rho_0 c_{bulk}^2 \tag{D.27}$$

to calculate the adiabatic bulk modulus K_S from the long wavelength sound velocity c_{bulk} [172]. For water at 25 °C, the relevant parameters are given by [173]

$$\eta \approx 1 \cdot 10^{-3}\ \mathrm{Pa \cdot s}, \tag{D.28}$$

$$\eta' \approx 3 \cdot 10^{-3}\ \mathrm{Pa \cdot s}, \tag{D.29}$$

$$\rho_0 \approx 1 \cdot 10^{3}\ \mathrm{kg/m^3}, \tag{D.30}$$

$$c_{bulk} \approx 1.5 \cdot 10^{3}\ \mathrm{m/s}. \tag{D.31}$$

For these values and frequencies $\omega \ll 10^{12}\ \mathrm{s}^{-1}$, we have $|\eta'| \ll \left|\rho_0 c_{bulk}^2/(-i\omega)\right|$, so that the response of water can be thought of as purely viscous in shear and purely elastic in dilation. Note that at sufficiently high frequencies, bulk water also shows an elastic response to shear deformation [235, 236]. These effects, which start to become important for frequencies in the GHz regime, could be incorporated in our model by replacing the shear relaxation function $\tilde{g}_\mathrm{s}$ by the relaxation function of a Maxwell material,

$$\tilde{g}_\mathrm{s}(\omega) = \frac{2\eta}{1 - i\omega\tau}, \tag{D.32}$$

where $\tau = \eta/\mu$ is a time scale characteristic for the material and μ characterizes the shear elasticity. In the limit $\tau \to 0$, the elasticity is negligible and one recovers Eq. (D.25).

Comparing Eq. (D.23) in the surface gravity approximation with the momentum conservation Eq. (D.1), the temporal Fourier transform of the stress tensor at the interface $z = 0$ becomes

$$\tilde{\sigma}_{jk} = -\delta_{jk}\left[\delta(\omega)P_0 - g\rho_0\tilde{u}_3^{(1)}\right] + (-i\omega)\tilde{g}_\mathrm{s}\tilde{\epsilon}_{jk}^{(1)} + \delta_{j,k}\frac{-i\omega}{3}\left(\tilde{g}_\mathrm{d} - \tilde{g}_\mathrm{s}\right)\tilde{\epsilon}_{ll}^{(1)}, \tag{D.33}$$

where the displacement field $\tilde{u}_j^{(1)}$ and its derivatives are assumed to be evaluated at $z = 0$. Equation (D.33) differs from the viscoelastic stress strain relation, Eq. (D.6) by the first term, which includes a homogeneous background pressure and the restoring gravitational force at the surface. Although these terms do not appear in the approximate momentum conservation Eq. (D.24), they appear in stress boundary conditions. If gravity can be neglected, $g = 0$, and the steady state pressure at the interface is set to zero, $P_0 = 0$, Eq. (D.33) simplifies to Eq. (D.6).

D.1.3 The stress boundary conditions for a viscoelastic interface

A detailed derivation of the continuum mechanical boundary conditions of two bulk media divided by a viscoelastic surface was given by Kralchevsky et al. [169]. In plane, they assumed the surface to have a purely viscous shear response with viscosity η_2D, a viscoelastic response

under dilation with viscosity $\eta'_{2\mathrm{D}}$ and a position dependent surface tension $\sigma_{2\mathrm{D}}$. For out-of-plane deformations, they assumed a bending rigidity κ_{2D} and a transverse viscosity $\eta^{\perp}_{2\mathrm{D}}$. Furthermore, they considered the interface to have an excess mass density $\rho_{2\mathrm{D}}$ and included an external force per area $\vec{f}_s$ acting on the surface. To linear order, they obtained[1]

$$\begin{aligned}\rho_{2\mathrm{D}}\partial_t v_{2\mathrm{D},\alpha} &= (\sigma_{\mathrm{III},n\alpha} - \sigma_{n\alpha}) + \rho_{2\mathrm{D}} f_{s,\alpha} + \left(\vec{\nabla}_s\right)_\alpha \sigma_{2\mathrm{D}} \\ &\quad + \eta'_{2\mathrm{D}} \left(\vec{\nabla}_s\right)_\alpha \left(\vec{\nabla}_s \cdot \vec{v}_{2\mathrm{D}}\right) + \eta_{2\mathrm{D}} \vec{\nabla}_s^2 v_{2\mathrm{D},\alpha} \qquad \alpha \in \{x, y\}, \qquad \text{(D.34)} \\ \rho_{2\mathrm{D}}\partial_t v_{2\mathrm{D},n} &= (\sigma_{\mathrm{III},nn} - \sigma_{nn}) + \rho_{2\mathrm{D}} f_{s,n} + \sigma_{2\mathrm{D}} \vec{\nabla}_s^2 u_{2\mathrm{D},z} \\ &\quad - \kappa_{2D} \vec{\nabla}_s^2 \vec{\nabla}_s^2 u_{2\mathrm{D},z} + \eta^{\perp}_{2\mathrm{D}} \vec{\nabla}_s^2 \partial_t u_{2\mathrm{D},z}, \qquad \text{(D.35)}\end{aligned}$$

where $u_{2\mathrm{D},z}(x, y, t) \equiv u_z(x, y, z = 0, t)$ is the displacement of the surface point $(x, y, 0)$ in z-direction, $\vec{v}_{2\mathrm{D}}$ is the velocity at the surface, the stress tensors for the bulk media below and above the surface, σ, σ_{III}, are understood to be evaluated at $z = 0$ and $\vec{\nabla}_s := \vec{\nabla} - \hat{n}\left(\hat{n} \cdot \vec{\nabla}\right)$ is the projection of the gradient onto the surface, with $\hat{n}$ the unit normal vector pointing into the $z > 0$ half-space. The indices α, n label tensor components parallel and perpendicular to the surface, respectively. More generally, we use the convention that greek indices run over $\{x, y\}$, while latin indices run over $\{x, y, z\}$. For the half-space $z > 0$, we do not consider any dynamics and assume that there is a constant pressure P_{III}, so that

$$\sigma_{\mathrm{III},jk} = -P_{\mathrm{III}}\delta_{j,k}. \qquad \text{(D.36)}$$

To rewrite the boundary conditions (D.34), (D.35), in a form more useful for the present context, we now relate the surface velocity to the surface displacement, explicitly evaluate $\vec{\nabla}_s$, relate the elastic in-surface dilational response $\sigma_{2\mathrm{D}}$ to the displacement and use gravitation as external force.

In the small displacement limit we approximate the velocity by the time derivative of the displacement,

$$\vec{v}_{2\mathrm{D}} \approx \partial_t \vec{u}_{2\mathrm{D}}, \qquad \text{(D.37)}$$

and the normal vector by the unit vector in z-direction, $\hat{n} \approx \hat{e}_z$. With the latter approximation, we get

$$\vec{\nabla}_s = \hat{e}_x\partial_x + \hat{e}_y\partial_y \equiv \hat{e}_\beta\partial_\beta. \qquad \text{(D.38)}$$

To express $\sigma_{2\mathrm{D}}$ in terms of the surface displacement, we use a two dimensional version of the argumentation used to derive Eq. (D.26). Assuming that the surface mass density and surface tension deviate only slightly from their (homogeneous in space and time) equilibrium values, we can write

$$\rho_{2\mathrm{D}}(x, y, t) = \rho^{(0)}_{2\mathrm{D}} + \rho^{(1)}_{2\mathrm{D}}(x, y, t), \qquad \text{(D.39)}$$

$$\sigma_{2\mathrm{D}}(x, y, t) = \sigma^{(0)}_{2\mathrm{D}} + \sigma^{(1)}_{2\mathrm{D}}(x, y, t), \qquad \text{(D.40)}$$

[1] This is ([169], 5.16), ([169], 5.17), but with interfacial inertia and body force kept. Also in Eq. ([169], 5.16), the stress tensor of the medium above the membrane was neglected, which we included.

with $\rho_{2\mathrm{D}}^{(1)}, \sigma_{2\mathrm{D}}^{(1)}$ small compared to $\rho_{2\mathrm{D}}^{(0)}, \sigma_{2\mathrm{D}}^{(0)}$. To express $\rho_{2\mathrm{D}}^{(1)}$ in terms of the surface displacement field, we integrate the linearized 2D mass conservation equation,

$$\partial_t \rho_{2\mathrm{D}}^{(1)} + \rho_{2\mathrm{D}}^{(0)} \partial_t \partial_\beta u_{2\mathrm{D},\beta} = 0, \tag{D.41}$$

with respect to time, to obtain

$$\rho_{2\mathrm{D}}^{(1)} = -\rho_{2\mathrm{D}}^{(0)} \partial_\beta u_{2\mathrm{D},\beta}. \tag{D.42}$$

The constant of integration has been chosen so that no area change, $\partial_\beta u_{2\mathrm{D},\beta} = 0$, implies no density change, $\rho_{2\mathrm{D}}^{(1)} = 0$. To express $\sigma_{2\mathrm{D}}^{(1)}$ in terms of the surface displacement field, we start with the definition of the 2D dimensional in-plane area elastic modulus $K_{2\mathrm{D}}$,

$$\frac{1}{K_{2\mathrm{D}}} = \frac{1}{A} \frac{\partial A}{\partial \sigma_{2\mathrm{D}}}, \tag{D.43}$$

which relates local changes in the area A of a surface element to the local surface tension $\sigma_{2\mathrm{D}}$. Note that because the surface tension can be thought of as a negative surface pressure, there is no minus sign here, contrary to Eq. (D.20). As in the three dimensional case, $K_{2\mathrm{D}}$ not only depends on the material the interface is made of but also on the thermodynamics of the process one wants to investigate (e.g. isothermal, adiabatic). Eq. (D.43) can be integrated to yield, to first order

$$\sigma_{2\mathrm{D}}^{(1)} = -K_{2\mathrm{D}} \partial_\beta u_{2\mathrm{D},\beta}, \tag{D.44}$$

where, analogous to the three dimensional situation, we use $\Delta A/A = \partial_\beta u_{2\mathrm{D},\beta}$, and assume that no compression implies no surface tension change. Eqs. (D.42), (D.44), can be used to eliminate $\rho_{2\mathrm{D}}^{(1)}$, $\sigma_{2\mathrm{D}}^{(1)}$ in Eqs. (D.39), (D.40), so that

$$\rho_{2\mathrm{D}} = \rho_{2\mathrm{D}}^{(0)} \left(1 - \partial_\beta u_{2\mathrm{D},\beta}\right), \tag{D.45}$$

$$\sigma_{2\mathrm{D}} = \sigma_{2\mathrm{D}}^{(0)} - K_{2\mathrm{D}} \partial_\beta u_{2\mathrm{D},\beta}. \tag{D.46}$$

The influence of gravity on the membrane yields an area force density

$$\rho_{2\mathrm{D}} \vec{f_s} = -\rho_{2\mathrm{D}} g \hat{e}_z = -\rho_{2\mathrm{D}}^{(0)} g \left(1 - \partial_\beta u_{2\mathrm{D},\beta}\right) \hat{e}_z, \tag{D.47}$$

where we use Eq. (D.45).

For the stationary solution Eqs. (D.9-D.11) around which we perturb, the surface should be at rest at $z = 0$. Therefore, the constant area force density acting on the interface, $-\rho_{2\mathrm{D}}^{(0)} g \hat{e}_z$, has to be counterbalanced by a pressure difference in the bulk media directly below and above the surface. This means that in the stationary solution, the constant background pressure P_0 in the lower bulk medium (c.f. Eq. (D.18)) and the constant pressure P_{III} in the upper bulk medium need to differ exactly by the pressure the surface exerts on the lower medium, $P_0 - P_{\mathrm{III}} = \rho_{2\mathrm{D}}^{(0)} g$, so that the surface remains at $z = 0$.

Inserting the expressions for $\vec{v}_{2\mathrm{D}}$, $\vec{\nabla}_s$, $\rho_{2\mathrm{D}}$, $\sigma_{2\mathrm{D}}$ and $\rho_{2\mathrm{D}}\vec{f}_s$, namely Eqs. (D.37), (D.38), (D.45), (D.46), (D.47), into the boundary conditions (D.34), (D.35), these can be rewritten, to linear order, as

$$\begin{aligned}\rho_{2\mathrm{D}}^{(0)}\partial_t^2 u_{2\mathrm{D},\alpha} &= (\sigma_{\mathrm{III},z\alpha} - \sigma_{z\alpha}) + \left(K_{2\mathrm{D}} + \eta'_{2\mathrm{D}}\partial_t\right)\partial_\alpha\partial_\beta u_{2\mathrm{D},\beta} \\ &\quad + \eta_{2\mathrm{D}}\partial_t\partial_\beta^2 u_{2\mathrm{D},\alpha} \qquad \alpha \in \{x, y\}, \end{aligned} \tag{D.48}$$

$$\begin{aligned}\rho_{2\mathrm{D}}^{(0)}\partial_t^2 u_{2\mathrm{D},z} &= (\sigma_{\mathrm{III},zz} - \sigma_{zz}) - \rho_{2\mathrm{D}}^{(0)} g\left(1 - \partial_\beta u_{2\mathrm{D},\beta}\right) \\ &\quad + \left(\sigma_{2\mathrm{D}}^{(0)} + \eta_{2\mathrm{D}}^{\perp}\partial_t - \kappa_{2D}\partial_\beta^2\right)\partial_\beta^2 u_{2\mathrm{D},z}. \end{aligned} \tag{D.49}$$

Kralchevksy et. al. [169] remark that in their Eqs. (5.16), (5.17), where body forces are neglected, the variables $u_{2\mathrm{D},x}$, $u_{2\mathrm{D},y}$ and the variable $u_{2\mathrm{D},z}$ decouple. In our equations this is not the case. Gravitation causes a downwards force if the membrane is locally compressed, reflected in the term $\rho_{2\mathrm{D}}^{(0)}\partial_\beta u_{2\mathrm{D},\beta}$ in Eq. (D.49).

D.1.4 The harmonic wave ansatz

We assume a displacement field $\vec{u}(\vec{r}, t)$ in the bulk medium which is given by displacement potentials $\varphi(\vec{r}, t)$, $\vec{\psi}(\vec{r}, t)$ as

$$\vec{u} = \vec{\nabla}\varphi + \vec{\nabla} \times \vec{\psi}. \tag{D.50}$$

Direct substitution shows that if the temporal Fourier transforms of the displacement potentials satisfy the Helmholtz equations

$$\rho_0(-i\omega)\tilde{\varphi} = \frac{1}{3}\left[2\tilde{g}_{\mathrm{s}}(\omega) + \tilde{g}_{\mathrm{d}}(\omega)\right]\Delta\tilde{\varphi}, \tag{D.51}$$

$$\rho_0(-i\omega)\tilde{\psi}_j = \frac{1}{2}\tilde{g}_{\mathrm{s}}(\omega)\Delta\tilde{\psi}_j, \qquad j \in \{x, y, z\}, \tag{D.52}$$

where Δ is the Laplace operator and the tilde signifies temporal Fourier transform, then the displacement field (D.50) fulfills the linearized momentum conservation Eq. (D.1) for a linear, isotropic, homogeneous viscoelastic material with stress strain relation (D.2) and without external forces, as is appropriate for the surface gravity approximation discussed following Eq. (D.23).

The harmonic wave ansatz [153] then consists of choosing the displacement potentials

$$\varphi(x, z, t) = \Phi \exp\left(z/\lambda_l\right)\exp\left[i\left(kx - \omega t\right)\right], \tag{D.53}$$

$$\vec{\psi}(x, z, t) = \Psi \exp\left(z/\lambda_t\right)\exp\left[i\left(kx - \omega t\right)\right]\hat{e}_y, \tag{D.54}$$

where we assume $\omega \in \mathbb{R}$ is a given parameter, while k, λ_l, λ_t, Φ, $\Psi \in \mathbb{C}$ are to be obtained. The requirement that the waves be damped as $z \to -\infty$ implies $\mathrm{Re}\left(\lambda_l^{-1}\right)$, $\mathrm{Re}\left(\lambda_t^{-1}\right) > 0$. Our choice $\omega \in \mathbb{R}$, $k \in \mathbb{C}$ means we consider plane wave solutions with frequency ω, which are damped as they propagate along the $\hat{e}_x$-axis, and that we later solve for $k(\omega)$.

Inserting the harmonic wave ansatz into Eqs. (D.51), (D.52), yields

$$\lambda_l^{-2}(k,\omega) = k^2 + \gamma^2(\omega), \tag{D.55}$$

$$\lambda_t^{-2}(k,\omega) = k^2 + \alpha^2(\omega), \tag{D.56}$$

where we define

$$\gamma^2(\omega) := \frac{3(-i\omega)\rho_0}{2\tilde{g}_\mathrm{s}(\omega) + \tilde{g}_\mathrm{d}(\omega)}, \tag{D.57}$$

$$\alpha^2(\omega) := \frac{2(-i\omega)\rho_0}{\tilde{g}_\mathrm{s}(\omega)}. \tag{D.58}$$

Equations (D.55), (D.56) and the requirements $\mathrm{Re}(\lambda_l^{-1})$, $\mathrm{Re}(\lambda_t^{-1}) > 0$ then determine λ_l, λ_t uniquely[2]. More generally, for a complex number $Z = |Z|e^{i\theta}$ with complex phase $arg(Z) = \theta \in (-\pi, \pi)$, we define the symbol $\sqrt{Z} := \sqrt{|Z|}e^{i\theta/2}$ to denote the complex square root with positive real part.

D.1.5 The implicit dispersion relation

Our ansatz for the lower half-space contains 6 parameters, namely k, ω, Φ, Ψ, λ_l, λ_t. We assume ω is constant and given. Equations (D.55), (D.56) determine λ_l, λ_t as functions of k, ω. The stress boundary conditions (D.48), (D.49) at $z = 0$ yield a homogeneous linear system of two equations for the two coefficients Φ, Ψ. This system can be obtained explicitly by calculating $\tilde{\sigma}_{ij}$, $\tilde{u}_{2\mathrm{D},i} = \tilde{u}_i|_{z=0}$, for the displacement field (D.50) and then inserting this into Eqs. (D.48), (D.49) (for (D.48), only the $\alpha = x$ case is needed, since for $\alpha = y$ the equation is fulfilled trivially, as a short calculation shows). For the stress tensor of the bulk medium, we use the generalized form (D.33), to include effects of compressibility and gravity as discussed in the derivation of Eq. (D.33). The result is

$$0 = ik\left[\, i\omega\rho_{2\mathrm{D}}^{(0)} - k^2\tilde{g}_{2\mathrm{D}} - \lambda_l^{-1}\tilde{g}_\mathrm{s} \,\right]\Phi + \left[\, \lambda_t^{-1}(k^2\tilde{g}_{2\mathrm{D}} - i\omega\rho_{2\mathrm{D}}^{(0)}) + \frac{1}{2}\tilde{g}_\mathrm{s}(k^2 + \lambda_t^{-2}) \,\right]\Psi \tag{D.59}$$

$$\begin{aligned} 0 = &\left[\, \lambda_l^{-1}(\omega^2\rho_{2\mathrm{D}}^{(0)} - k^2\tilde{\Pi}_{2\mathrm{D}} - \rho_0 g) - k^2\rho_{2\mathrm{D}}^{(0)}g + \frac{i\omega}{2}\tilde{g}_\mathrm{s}(k^2 + \lambda_t^{-2}) \,\right]\Phi \\ &+ \left[\, ik(\omega^2\rho_{2\mathrm{D}}^{(0)} - k^2\tilde{\Pi}_{2\mathrm{D}} - \lambda_t^{-1}\rho_{2\mathrm{D}}^{(0)}g) - ik\rho_0 g - \omega k\lambda_t^{-1}\tilde{g}_\mathrm{s} \,\right]\Psi, \end{aligned} \tag{D.60}$$

where again λ_l, λ_t are given by Eqs. (D.55), (D.56), and the response functions $\tilde{g}_{2\mathrm{D}}$, $\tilde{\Pi}_{2\mathrm{D}}$ are defined as

$$\tilde{g}_{2\mathrm{D}}(\omega) := \eta_{2\mathrm{D}} + \eta'_{2\mathrm{D}} + K_{2\mathrm{D}}/(-i\omega), \tag{D.61}$$

$$\tilde{\Pi}_{2\mathrm{D}}(k,\omega) := \sigma_{2\mathrm{D}}^{(0)} + (-i\omega)\eta_{2\mathrm{D}}^{\perp} + k^2\kappa_{2D}. \tag{D.62}$$

[2] If either λ_l^{-2} or λ_t^{-2} is purely real and negative, both square roots have vanishing real part. However, we do not accept such solutions, since the wave would not be damped away from the interface.

The symbol $\tilde{g}_{2\mathrm{D}}$ was chosen because of the structural similarity of Eqs. (D.26), (D.61). Since the perturbations $\rho^{(1)}$, $\rho_{2\mathrm{D}}^{(1)}$, $\sigma_{2\mathrm{D}}^{(1)}$ do not appear explicitly in Eqs. (D.59-D.62) anymore, we drop the subscripts 0 and superscripts (0) of the corresponding equilibrium values ρ_0, $\rho_{2\mathrm{D}}^{(0)}$, $\sigma_{2\mathrm{D}}^{(0)}$ in the following, and also have dropped the sub- and superscripts in Chapter 5. In order to have a propagating wave with nonzero amplitude, the system (D.59), (D.60) needs to have a nontrivial solution. Consequently, the implicit dispersion relation is obtained by setting the determinant of the 2×2 coefficient matrix for Φ, Ψ, obtained from (D.59), (D.60), equal to zero. This yields

$$\begin{aligned} 0 = {} & 4\left(k^2\tilde{\Pi}_{2\mathrm{D}} + \rho g - \omega^2\rho_{2\mathrm{D}}\right)\left[\left(k^2\tilde{g}_{2\mathrm{D}} - i\omega\rho_{2\mathrm{D}}\right)\left(k^2 - \lambda_l^{-1}\lambda_t^{-1}\right) + i\omega\rho\lambda_l^{-1}\right] \\ & + 4\left(k^2\tilde{g}_{2\mathrm{D}} - i\omega\rho_{2\mathrm{D}}\right)\omega^2\rho\lambda_t^{-1} \\ & + \tilde{g}_{\mathrm{s}}\left[\, i\omega\tilde{g}_{\mathrm{s}}\left(-4k^2\lambda_l^{-1}\lambda_t^{-1} + (k^2 + \lambda_t^{-2})^2\right) + 2\rho_{2\mathrm{D}}gk^2\left(2\lambda_l^{-1}\lambda_t^{-1} - (k^2 + \lambda_t^{-2})\right)\,\right], \end{aligned} \tag{D.63}$$

and thus completes our derivation of Eq. (5.8).

Finding a solution $k(\omega)$ to Eq. (D.63) yields the dispersion relation of a surface wave, for which phase velocity and propagation distance can then be calculated via

$$c_{\parallel}(\omega) = \frac{\omega}{\mathrm{Re}(k(\omega))}, \tag{D.64}$$

$$\lambda_{\parallel}(\omega) = \frac{1}{\mathrm{Im}(k(\omega))}. \tag{D.65}$$

D.2 Limiting cases

In the following subsections, we first discuss how the known dispersion relations for Rayleigh waves, capillary-gravity-flexural and Lucassen waves emerge from Eq. (D.63). Then we derive the dispersion relation for the capillary-gravity-viscosity (CGV) surface wave, Eq. (5.19).

D.2.1 Rayleigh waves

Upon removing the effects related to the surface ($\rho_{2\mathrm{D}} = 0$, $\tilde{g}_{2\mathrm{D}} = 0$, $\tilde{\Pi}_{2\mathrm{D}} = 0$) and also gravity ($g = 0$), Eq. (D.63) becomes

$$4k^2\lambda_l^{-1}\lambda_t^{-1} = \left(k^2 + \lambda_t^{-2}\right)^2, \tag{D.66}$$

where λ_l, λ_t are given by Eqs. (D.55), (D.56). This is the classical Rayleigh conditional equation whose solutions lead to the known (viscoelastic) Rayleigh waves [153–155]. Analytic solutions for Eq. (D.66) can be found as follows [153]. Squaring Eq. (D.66), one obtains

$$0 = 8\left(\frac{k}{\alpha(\omega)}\right)^6 + 8(2 - \nu(\omega))\left(\frac{k}{\alpha(\omega)}\right)^4 + 8(1 - \nu(\omega))\left(\frac{k}{\alpha(\omega)}\right)^2 + (1 - \nu(\omega)), \tag{D.67}$$

where

$$\nu(\omega) = \frac{\tilde{g}_\mathrm{d}(\omega) - \tilde{g}_\mathrm{s}(\omega)}{\tilde{g}_\mathrm{s}(\omega) + 2\tilde{g}_\mathrm{d}(\omega)} \tag{D.68}$$

is Poisson's ratio and α is defined in Eq. (D.58). Equation (D.67) is a cubic polynomial in $(k/\alpha(\omega))^2$, so that Cardano's formula [237] can be used to obtain its three roots

$$-\left(\frac{k(\omega)}{\alpha(\omega)}\right)_n^2 = \frac{2-\nu(\omega)}{3} + \frac{1}{3}\sqrt[3]{h_1(\nu(\omega))}e^{-i\pi(1-2n)/3} + \frac{1-\nu(\omega)+\nu(\omega)^2}{3\sqrt[3]{h_1(\nu(\omega))}}e^{i\pi(1-2n)/3}, \tag{D.69}$$

where

$$h_1(\nu) = \frac{1}{16}\left(-11+3\nu-24\nu^2+16\nu^3 \; +3\sqrt{3}\sqrt{-5+26\nu-37\nu^2+48\nu^3-32\nu^4}\right) \tag{D.70}$$

and $n \in \{1,2,3\}$ labels the distinct solutions. While Rayleigh originally derived this formula for isotropic homogeneous elastic media, his derivation is also valid for isotropic homogeneous viscoelastic media [154, 155, 180]. Since Eq. (D.69) is a solution to the squared Rayleigh conditional Eq. (D.67), it is not clear whether it also solves the original Rayleigh conditional Eq. (D.66). In the elastic case, only one of the solutions of the squared equation also solves the original equation, while in the viscoelastic case, there are situations where two of the solutions of Eq. (D.67) also solve the original Eq. (D.66), see Refs. [154, 155]. Recently, there has been a report on three solutions [170]. However, in that work a real wave number k was assumed and $\omega(k)$ was obtained, which amounts to solving (D.66) for ω or, equivalently, finding the inverse function of $k(\omega)$. As $k(\omega)$ need not be monotonic, the inverse can be non-unique so that this finding does not answer the still open question whether viscoelastic materials exist where all three solutions $k(\omega)$ of the squared conditional Eq. (D.67) also solve the original Rayleigh conditional Eq. (D.66). For the water-like viscoelastic material, which we discuss as an example in Chapter 5, we find that only two solutions of the squared conditional equation also solve the original conditional equation.

In the incompressible limit, $\tilde{g}_\mathrm{d} \to \infty$, Poisson's ratio reduces to $\nu(\omega) \equiv 1/2$, so that the right hand side of Eq. (D.69) becomes independent of ω. Consequently, we get

$$k(\omega) \sim \alpha(\omega), \tag{D.71}$$

and using the definition of α, Eq. (D.58), we see that for a Newtonian fluid with shear relaxation function given by Eq. (D.25),

$$k(\omega) \sim \omega^{1/2}. \tag{D.72}$$

According to Eqs. (D.64), (D.65), this implies that $c_\parallel(\omega) \sim \omega^{1/2}$, $\lambda_\parallel(\omega) \sim \omega^{-1/2}$. This is indeed what is observed in Figs. 5.2 (a), (d) and Figs. D.1 (a), (d), indicating that compressibility effects are not relevant for Rayleigh waves at the shown frequencies.

D.2.2 Factorization, capillary-gravity and longitudinal capillary waves

As we show now, there are situations where the conditional Eq. (D.63) factorizes. Assuming that the gravitational force on the surface can be neglected, i.e., that

$$\rho_{2\mathrm{D}} g \ll \omega|\tilde{g}_\mathrm{s}|, \qquad \rho_{2\mathrm{D}} g|k|^4 \ll \omega|\tilde{g}_\mathrm{s}||\lambda_t^{-1}|^4, \tag{D.73}$$

Eq. (D.63) first simplifies to

$$\begin{aligned} 0 = 4\left(k^2\tilde{\Pi}_{2\mathrm{D}} + \rho g - \omega^2\rho_{2\mathrm{D}}\right)\left[(k^2\tilde{g}_{2\mathrm{D}} - i\omega\rho_{2\mathrm{D}})\left(-k^2 + \lambda_l^{-1}\lambda_t^{-1}\right) - i\omega\rho\lambda_l^{-1}\right] \\ + (-i\omega)\tilde{g}_\mathrm{s}\left[2\left(k^2\tilde{g}_{2\mathrm{D}} - i\omega\rho_{2\mathrm{D}}\right)\lambda_t^{-1}\alpha^2 + \tilde{g}_\mathrm{s}\left(-4k^2\lambda_l^{-1}\lambda_t^{-1} + (k^2 + \lambda_t^{-2})^2\right)\right]. \end{aligned} \tag{D.74}$$

Furthermore assuming that

$$1 - k^2\lambda_l\lambda_t \approx 1, \tag{D.75}$$

$$\frac{1}{\alpha^4}\left[-4k^2\lambda_l^{-1}\lambda_t^{-1} + \left(k^2 + \lambda_t^{-2}\right)^2\right] \approx 1, \tag{D.76}$$

Eq. (D.74) factorizes to

$$0 = \left[(k^2\tilde{\Pi}_{2\mathrm{D}} + \rho g - \omega^2\rho_{2\mathrm{D}})\lambda_l^{-1} - \omega^2\rho\right]\left[\lambda_t^{-1}(k^2\tilde{g}_{2\mathrm{D}} - i\omega\rho_{2\mathrm{D}}) - i\omega\rho\right] \tag{D.77}$$

If the approximations (D.73), (D.75), (D.76) are justified can only be checked once a solution to Eq. (D.63) or Eq. (D.77) has been found, since $k(\omega)$ appears in the conditions. We want to point out an example where the rather complicated-looking conditions (D.75), (D.76) are met and give a physical interpretation for compressible Newtonian fluids, namely if

$$|k(\omega)|^2 \ll |\alpha(\omega)^2| = \frac{2|\omega|\rho}{|\tilde{g}_\mathrm{s}(\omega)|}, \tag{D.78}$$

$$|k(\omega)|^2 \gtrsim |\gamma(\omega)^2| = \frac{3|\omega|\rho}{|2\tilde{g}_\mathrm{s}(\omega) + \tilde{g}_\mathrm{d}(\omega)|}, \tag{D.79}$$

then $\lambda_t^{-1} \approx \alpha$ and $|\lambda_l^{-1}|$ is of the order of $|k|$. It is then clear that (D.75) holds, while the dominant term in the bracket on the left hand side of Eq. (D.76) can be seen to be $\lambda_t^{-4} \approx \alpha^4$, so that the condition (D.76) is also fulfilled. From Eq. (D.78) it furthermore follows that the left inequality in Eq. (D.73) implies the right one.

In the context of a Newtonian viscous fluid, where $\tilde{g}_\mathrm{s}$ is given by Eq. (D.25), Eq. (D.78) is equivalent to

$$\frac{\rho|\omega|}{\eta|k|^2} \gg 1, \tag{D.80}$$

which is the high Reynolds number condition, with typical velocity $|\omega|/|k|$ and typical length scale $|k|^{-1}$. Since k is in general complex and the phase velocity of a surface wave is not the local velocity of the motion of the bulk medium, this interpretation can of course not be taken too

literally. As for the interpretation of Eq. (D.79), assuming the dominant term in the denominator on the right hand side of Eq. (D.79) to be the imaginary part of $\tilde{g}_{\mathrm{d}}$, i.e.,

$$2\tilde{g}_{\mathrm{s}} + \tilde{g}_{\mathrm{d}} \approx \mathrm{Im}\left(\tilde{g}_{\mathrm{d}}\right), \tag{D.81}$$

which for $\tilde{g}_{\mathrm{s}}$, $\tilde{g}_{\mathrm{d}}$ given by Eqs. (D.25-D.27), with the parameters for water (D.28-D.31), is appropriate for $\omega \ll 10^{12}\ \mathrm{s}^{-1}$, Eq. (D.79) can be rewritten as

$$\frac{|\omega|^2}{|k|^2} \lesssim c_{bulk}^2. \tag{D.82}$$

Since the phase velocity is

$$c_{\parallel}(\omega) = \frac{\omega}{\mathrm{Re}(k(\omega))} \geq \frac{\omega}{|k(\omega)|}, \tag{D.83}$$

we see that a sufficient condition for condition (D.79) to hold is that the phase velocity of the wave solution should be smaller than the bulk sound velocity. In the limit of incompressibility, $c_{bulk} \to \infty$, we have $|\gamma| \to 0$, so that condition (D.79) is always fulfilled and $\lambda_l^{-1} = k$. On the other hand, if the phase velocity of a surface wave solution is much less than the sound velocity of the bulk medium, then $|k|^2 \gg |\gamma|^2$, so that Eq. (D.79) is fulfilled, we have $\lambda_l^{-1} \approx k$ and compressibility effects of the bulk medium can be neglected when considering surface waves.

The factorization (D.77) yields two independent equations which lead to wave solutions, obtained by setting the first or second factor equal to zero. The first one yields a generalization of the capillary-gravity-flexural surface waves, the second a generalization of Lucassen's longitudinal capillary waves. We remark that λ_l and the bending properties $\kappa_{2D}, \eta_{2\mathrm{D}}^{\perp}$ (which are contained in $\tilde{\Pi}_{2\mathrm{D}}$, Eq. (D.62)), only enter the former equation, while λ_t and the in-plane viscoelastic response of the surface, $\tilde{g}_{2\mathrm{D}}$, only enter the latter. As can be seen from this factorization, the Rayleigh solutions do not appear in this limit of a theory that includes bulk viscoelasticity, gravity, surface viscoelasticity and surface pressure. This factorization is a generalization of previous factorizations [165, 171]. That the factorization does not always hold was already predicted by Lucassen and is an established experimental result [160, 161].

D.2.3 Capillary-gravity-viscosity (CGV) surface wave

A sufficient condition to obtain the factorized conditional Eq. (D.77) was given by the inequalities (D.73), (D.78), (D.79). According to the definition of λ_t, Eq. (D.56), the second of these inequalities is equivalent to

$$\lambda_t^{-1} = \sqrt{k^2 + \alpha^2} \approx \alpha. \tag{D.84}$$

We now explore what happens if we assume the other term in the square root to be dominant,

$$|k| \gg |\alpha|, \tag{D.85}$$

so that

$$\lambda_t^{-1} = \sqrt{k^2\left(1+\left(\frac{\alpha}{k}\right)^2\right)} = \pm k\sqrt{1+\left(\frac{\alpha}{k}\right)^2} \pm k\left(1-\frac{\alpha^2}{2k^2}\right), \tag{D.86}$$

where the sign depends on the complex phases of the two complex numbers k^2, $1+(\alpha/k)^2$ and is due to our definition of the square root as the complex root with positive real part, c.f. the discussion after Eq. (D.58). Since we find numerically that the minus sign is the correct choice to obtain the CGV wave solution on water, we use it in the following.

To present a minimal model where the CGV wave appears, we assume the only non-negligible surface property to be the surface pressure $\sigma_{2\mathrm{D}}$, i.e., we set $\rho_{2\mathrm{D}}$, $\tilde{g}_{2\mathrm{D}}$, κ_{2D} equal to zero. Also, we limit ourselves here to the incompressible case, where $\lambda_l^{-1} = k$. Note that since the real part of λ_l^{-1} has to be positive for the wave to decay away from the interface, $\lambda_l^{-1} = k$ implies that we assume the real part of k to be positive, i.e., that we consider waves traveling into the positive x-direction. With these assumptions, and using the approximation (D.86), the conditional Eq. (D.63) simplifies to a polynomial of degree four in k,

$$0 = 2\tilde{g}_{\mathrm{s}}^2 k^4 + \rho\sigma_{2\mathrm{D}}k^3 - 3i\omega\rho\tilde{g}_{\mathrm{s}}k^2 + \rho^2 gk - \omega^2\rho^2. \tag{D.87}$$

There exists a general formula for the roots of fourth order polynomials, so that the four complex roots $k(\omega)$ could be written down explicitly. However, we content ourselves here with deriving a simple approximate solution to Eq. (D.87) for the physically relevant special case of a water-like viscoelastic bulk medium, as shown in Fig. 5.3.

We thus use the water density given by Eq. (D.30) and the shear relaxation function of water introduced in Eq. (D.25), with viscosity given by Eq. (D.28). We furthermore assume standard gravitational acceleration, $g = 9.81\,\mathrm{m/s^2}$, and surface tension, $\sigma_{2\mathrm{D}} = 72\,\mathrm{mN/m}$. The other surface parameters, namely $\rho_{2\mathrm{D}}$, $\eta_{2\mathrm{D}}$, $\eta'_{2\mathrm{D}}$, $\eta^{\perp}_{2\mathrm{D}}$, $K_{2\mathrm{D}}$, κ_{2D}, we set to zero.

Although the numerical solution for the CGV wave in Figs. 5.3 (b), (e) is calculated for a compressible water-like viscoelastic medium as described by Eqs. (D.26), (D.27), assuming incompressibility in the following derivation is appropriate, because compressibility effects at the frequencies considered ($\omega \lesssim 1$ Hz) are numerically found to be negligibly small (see also the discussion following Eq. (D.81)).

To begin our derivation, we denote the real- and imaginary parts of k by p, q,

$$k(\omega) = p(\omega) + iq(\omega), \tag{D.88}$$

with $p(\omega)$, $q(\omega)$ real and positive. From Figs. 5.3 (b), (e) we observe that the viscous surface wave solution should fulfill

$$|p(\omega)| \ll |q(\omega)|. \tag{D.89}$$

Suppressing the frequency dependence in the notation from now on, we approximate the powers

of k by keeping only terms up to linear order in p,

$$k = p + iq, \tag{D.90}$$
$$k^2 = \left[p^2 - q^2\right] + i\left[2pq\right] \approx -q^2 + i2pq, \tag{D.91}$$
$$k^3 = \left[p(p^2 - 3q^2)\right] + i\left[q(-q^2 + 3p^2)\right] \approx -3pq^2 - iq^3, \tag{D.92}$$
$$k^4 = \left[\left(p^2 - q^2\right)^2 - 4p^2q^2\right] + i\left[4pq\left(p^2 - q^2\right)\right] \approx q^4 - i4pq^3. \tag{D.93}$$

Next, we insert these powers into the polynomial Eq. (D.87) and, using that $\sigma_{2\mathrm{D}}$, ρ, g, $\tilde{g}_{\mathrm{s}} = 2\eta$ are all real numbers, decompose (D.87) into two seperate equations for real- and imaginary part, leading to

$$0 = \left(8\eta^2q^4 - \omega^2\rho^2\right) + p\left(-3\sigma_{2\mathrm{D}}\rho q^2 + 12\omega\eta\rho q + \rho^2 g\right), \tag{D.94}$$
$$0 = (-32\eta^2 p - \rho\sigma_{2\mathrm{D}})q^3 + 6\omega\rho\eta q^2 + \rho^2 gq. \tag{D.95}$$

In both equations, we make further simplifications by estimating the various sizes of the terms relative to each other based on the parameters for water and the expected sizes for p, q. We start with Eq. (D.95), which represents the imaginary part of the polynomial Eq. (D.87). Since $\eta^2 \approx 10^{-6}\ \mathrm{Pa}^2 \cdot \mathrm{s}^2$, while $\rho\sigma_{2\mathrm{D}} \approx 10^1\ \mathrm{Pa}^2 \cdot \mathrm{s}^2/\mathrm{m}$, and in view of the numerical solution, which indicates that $|p| \ll 10^6\ \mathrm{m}^{-1}$, we have

$$\eta^2 p/(\rho\sigma_{2\mathrm{D}}) \ll 1, \tag{D.96}$$

so that we approximate the bracket in the first term as

$$-32\eta^2 p - \rho\sigma_{2\mathrm{D}} \approx -\rho\sigma_{2\mathrm{D}}. \tag{D.97}$$

The second term of Eq. (D.95) is of the order $6\omega\rho\eta q^2 \approx 6\omega q^2\ \mathrm{kg}^2\mathrm{m}^{-4}\mathrm{s}^{-1}$, while the third term is of the order $\rho^2 gq \approx q10^7\ \mathrm{kg}^2\mathrm{m}^{-5}\mathrm{s}^{-2}$. In view of the numerical solution we expect $q \approx 10^3\ \mathrm{m}^{-1}$, $\omega \lesssim 10\ \mathrm{s}^{-1}$, so that

$$(6\omega\rho\eta q^2)/(\rho^2 gq) \ll 1, \tag{D.98}$$

and the second term can be neglected compared to the third term in Eq. (D.95).

Using Eqs. (D.97), (D.98), we simplify the bracket and neglect the second term in Eq. (D.95). Then, the equation does not depend on p anymore and can be solved directly for the imaginary part of $k(\omega)$, to give

$$q(\omega) = \sqrt{\frac{\rho g}{\sigma_{2\mathrm{D}}}}. \tag{D.99}$$

This result for q can now be inserted into Eq. (D.94), which can then be solved for the real part of $k(\omega)$ immediately, to yield

$$p(\omega) = \frac{4\eta^2 g}{\sigma_{2\mathrm{D}}^2} - \frac{\omega^2}{2g}, \tag{D.100}$$

where we have used the approximation

$$2g - 12\omega\eta\sqrt{g/(\rho\sigma_{2\mathrm{D}})} \approx 2g, \tag{D.101}$$

which is appropriate for $\omega \lesssim 10\ \mathrm{s}^{-1}$, since $\eta\sqrt{g/(\rho\sigma_{2\mathrm{D}})} \approx 10^{-2}\ \mathrm{m/s}$, so that

$$\omega\eta/\sqrt{g\rho\sigma_{2\mathrm{D}}} \ll 1. \tag{D.102}$$

Combining Eqs. (D.99), (D.100), we thus obtain the approximate dispersion relation

$$k(\omega) = \left[\frac{4\eta^2 g}{\sigma_{2\mathrm{D}}^2} - \frac{\omega^2}{2g}\right] + i\sqrt{\frac{\rho g}{\sigma_{2\mathrm{D}}}}. \tag{D.103}$$

This is Eq. (5.19), and as can be seen in Figs. 5.3 (b), (e) and Figs. D.1 (b), (e), it describes the the numerical solution accurately.

The solution (D.103) can be inserted back into the approximations (D.85), (D.89), (D.96), (D.98), (D.102), to see for which parameters it is self-consistent. After short calculation it follows that if

$$\frac{g\eta^4}{\rho\sigma_{2\mathrm{D}}^3} \ll 1, \qquad \frac{\omega\sigma_{2\mathrm{D}}}{\eta g} \ll 1, \tag{D.104}$$

then the result (D.103) is consistent with the assumptions made in deriving it. In that sense Eq. (D.103) can, for fixed g, ρ, $\sigma_{2\mathrm{D}}$, be interpreted as a low η, low ω/η asymptotic solution to the dispersion relation Eq. (D.63).

D.3 Existence regions for diminished surface tension

To facilitate comparison between different parameter regimes, the value $\sigma_{2\mathrm{D}} = 72\ \mathrm{mN/m}$ for the surface tension is used for all numerical calculations presented in Chapter 5. While this value is appropriate for pure water [173], in the presence of a monolayer the surface tension $\sigma_{2\mathrm{D}}$ is typically smaller, but of the same order of magnitude as for pure water [92, 93, 174]. To show that a smaller value of $\sigma_{2\mathrm{D}}$ leads to qualitatively similar results as those presented in Chapter 5, we recalculate Figs. 5.3, 5.4 for surface tension $\sigma_{2\mathrm{D}} = 10\ \mathrm{mN/m}$, and with otherwise identical parameters (namely $g = 9.81\ \mathrm{m/s^2}$, $\rho_{2\mathrm{D}}$, $\eta_{2\mathrm{D}}$, $\eta'_{2\mathrm{D}}$, $\eta^{\perp}_{2\mathrm{D}}$, κ_{2D} equal to zero, a water-like viscoelastic medium as given by Eqs. (D.25-D.31)). Figure D.1, which is the low-$\sigma_{2\mathrm{D}}$ analogue of Fig. 5.3, shows phase velocities and propagation distances for different surface configurations, while Fig. D.2, the low-$\sigma_{2\mathrm{D}}$ analogue of Fig. 5.4, shows the existence state diagram for the different wave solutions in the $(\omega, K_{2\mathrm{D}})$-plane.

Comparing Figs. 5.3, D.1, we see that the dispersion relations for the two values of $\sigma_{2\mathrm{D}}$ are qualitatively similar. More specifically, subplots (b), (e) of Fig. D.1 show that for vanishing area elastic modulus, $K_{2\mathrm{D}} = 0$, capillary-gravity and CGV wave exist, and that the wave number $k(\omega)$ of the CGV wave is very well approximated by Eq. (D.103). Comparing Figs. 5.3, D.1 (b), (e), we furthermore observe that the maximal frequency up to which the CGV wave exists, which we denote by $\omega_{\mathrm{max}}^{\mathrm{CGV}}$ in the following, is larger for the smaller value of $\sigma_{2\mathrm{D}}$. In view of our

analytical dispersion relation Eq. (D.103), this is expected. From Figs. 5.3 (b), D.1 (b), we see that the phase velocity of the CGV wave diverges as ω approaches $\omega_{\max}^{\mathrm{CGV}}$ from below. According to the definition of the phase velocity, Eq. (D.64), a divergence in phase velocity means that the real part of $k(\omega)$ is equal to zero. Equating the real part of $k(\omega)$, as defined by Eq. (D.103), with zero, and solving for ω, we obtain

$$\omega_{\max}^{\mathrm{CGV}} = \sqrt{2}\frac{2\eta g}{\sigma_{2\mathrm{D}}}. \tag{D.105}$$

From this equation we see that $\omega_{\max}^{\mathrm{CGV}} \sim 1/\sigma_{2\mathrm{D}}$, and using the parameters $\eta = 1\ \mathrm{mPa}\cdot\mathrm{s}$, $g = 9.81\ \mathrm{m/s^2}$, we get for $\sigma_{2\mathrm{D}} = 10\ \mathrm{mN/m}$ that $\omega_{\max}^{\mathrm{CGV}} \approx 2.8\ \mathrm{s}^{-1}$, while for $\sigma_{2\mathrm{D}} = 72\ \mathrm{mN/m}$ we obtain $\omega_{\max}^{\mathrm{CGV}} \approx 0.39\ \mathrm{s}^{-1}$. Both values are in good agreement with the numerical results shown in Figs. 5.3, D.1 (b) (e). Since the frequency range accessible in an experiment is usually limited, the fact that a lower surface tension leads to higher $\omega_{\max}^{\mathrm{CGV}}$ may be useful when designing an experiment to measure the CGV wave.

The inset of Fig. D.2 (a) shows that also for $\sigma_{2\mathrm{D}} = 10\ \mathrm{mN/m}$, there is a parameter range where three solutions $k(\omega)$ coexist. Comparing Figs. 5.4, D.2 (a), it can be inferred that for the smaller value of $\sigma_{2\mathrm{D}}$, this coexistence region is shifted towards higher angular frequencies ω and higher values of the area elastic modulus $K_{2\mathrm{D}}$.

D.4 Crossover from capillary-gravity and Lucassen wave to Rayleigh wave

As can be seen in Fig. 5.3 (a) and Fig. D.2 (a), the Lucassen wave transforms into the Rayleigh wave at high frequencies. In Fig. D.3, we illustrate this for $\sigma_{2\mathrm{D}} = 72\ \mathrm{mN/m}$, $K_{2\mathrm{D}} = 10\ \mathrm{mN/m}$. The figure shows the crossover of both capillary-gravity and Lucassen waves into the two Rayleigh waves that exist on a water-like viscoelastic half-space, i.e., the Rayleigh waves shown in Figs. 5.2 (a), (d). It can be seen that the capillary-gravity wave transforms into the $n = 3$ Rayleigh wave at $\omega \approx 10^{10}\ \mathrm{s}^{-1}$, while the Lucassen wave solutions transforms into the $n = 2$ Rayleigh wave at $\omega \approx 10^{9}\ \mathrm{s}^{-1}$.

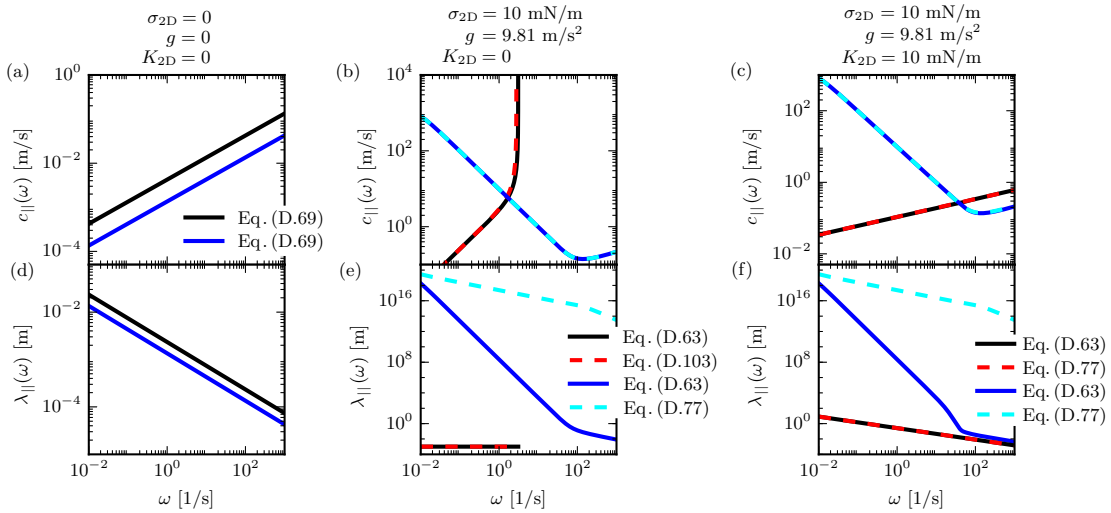

Figure D.1: Phase velocities and propagation distances on a water-like viscoelastic half-space for different surface parameters. (a), (d) The two Rayleigh waves that exist on a water-like viscoelastic half-space. (b), (e) The capillary-gravity wave and the viscous surface wave on a water-like viscoelastic half-space with surface tension $\sigma_{2D} = 10\ \mathrm{mN/m}$ and gravitational acceleration $g = 9.81\ \mathrm{m/s^2}$. (c), (f) The capillary-gravity wave and the Lucassen wave on a water-like viscoelastic half-space with an interface (surface tension $\sigma_{2D} = 10\ \mathrm{mN/m}$, area elastic modulus $K_{2D} = 10\ \mathrm{mN/m}$) and gravitational acceleration $g = 9.81\ \mathrm{m/s^2}$. The curves in subplots (a), (d) are calculated using the analytical solution of Eq. (D.66). The analytic formula for the CGV wave, Eq. (D.103), is shown as dashed red lines in subplots (b), (e). All other curves are obtained from numerically solving either the full dispersion relation, Eq. (D.63), or one of the two factors from the factorization, Eq. (D.77), with the interfacial parameters ρ_{2D}, η_{2D}, η'_{2D}, $\eta^{\perp}_{2D}$, κ_{2D} set to zero. In all cases, phase velocities and propagation distances are calculated from $k(\omega)$ via Eqs. (D.64), (D.65).

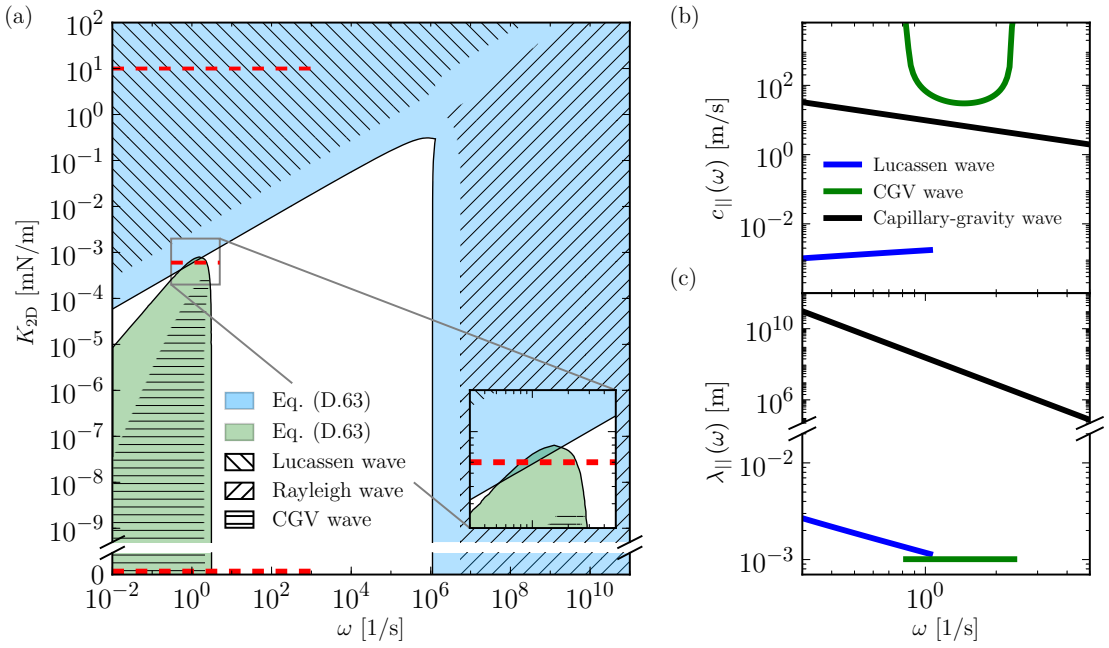

Figure D.2: Existence state diagram for surface waves. (a) Existence state diagram for surface waves for fixed $\sigma_{2D} = 10\ \mathrm{mN/m}$, $g = 9.81\ \mathrm{m/s^2}$, as a function of interface elastic modulus K_{2D} and frequency ω. The capillary-gravity wave exists throughout the plane, its existence region is therefore not plotted. The hatched regions indicate where both the phase velocities and propagation distances of the numerical solutions of Eq. (D.63) have less than 30% relative deviation from the phase velocities and propagation distances of the numerical solutions of the limiting Eqs. (D.66), (D.77), or the analytical formula (D.103), respectively. Upper and lower red dashed lines indicate the positions of the dispersion relations from Figs. D.1 (b), (e) (lower red line) and (c), (f) (upper red line) in the phase diagram. The inset shows that there is a region where three waves coexist. (b), (d) Phase velocities and propagation distances of Lucassen, CGV and capillary-gravity wave as a function of ω for $K_{2D} = 6 \cdot 10^{-4}\ \mathrm{mN/m}$, with this value for K_{2D} indicated by the short red dashed line in subplot (a). The shaded regions and the curves in subplots (b), (d) are obtained by numerically solving Eq. (D.63). For all calculations, a water-like viscoelastic half-space is used as bulk medium and ρ_{2D}, η_{2D}, η'_{2D}, $\eta^{\perp}_{2D}$, κ_{2D} are set to zero. Phase velocities and propagation distances are calculated from $k(\omega)$ using Eqs. (D.64), (D.65).

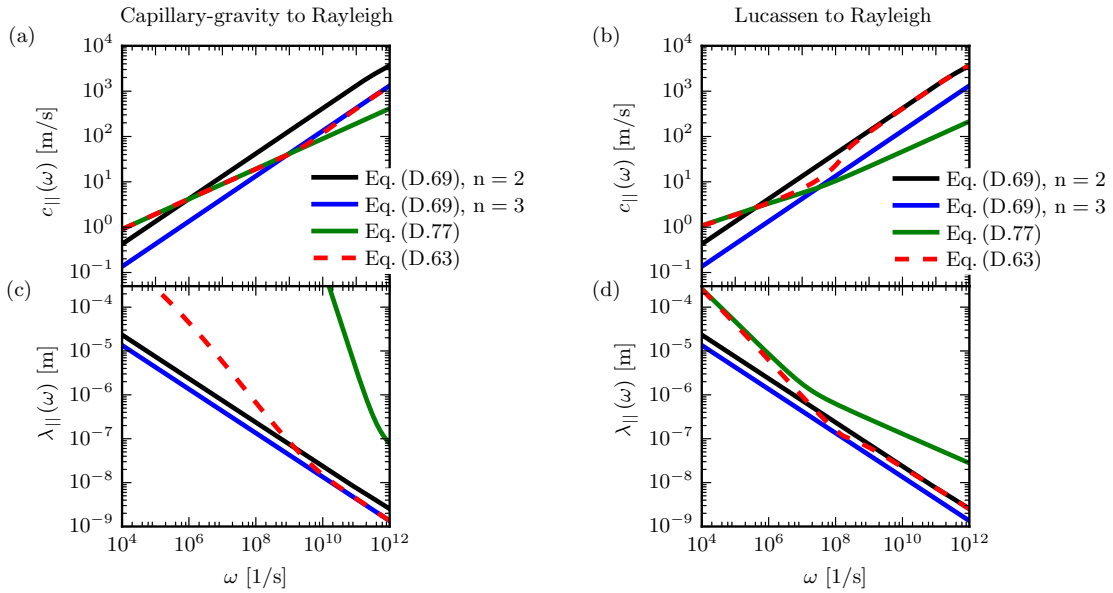

Figure D.3: Frequency dependent crossover of capillary-gravity and Lucassen wave to Rayleigh wave on a water-like viscoelastic half-space. (a), (c) Phase velocities and decay lengths of the Rayleigh waves (black and blue lines), together with the factorized capillary-gravity wave dispersion relation (green line) and the corresponding solution of the exact dispersion relation (red dashed line). Note that the factorized capillary-gravity wave dispersion relation predicts a much larger decay length and is therefore only visible for frequencies $\omega \gtrsim 10^{10}\ \mathrm{s}^{-1}$ in subplot (c), c.f. Fig. 5.2 (e). (b), (d) Phase velocities and decay lengths of the Rayleigh wave (black and blue lines), but together with the factorized Lucassen wave dispersion relation (green line) and the corresponding solution of the exact dispersion relation (red dashed line). For the Rayleigh waves, Eq. (D.69) is used. For the other curves, Eqs. (D.63), (D.77) are solved numerically using the parameters $\sigma_{2\mathrm{D}} = 72\ \mathrm{mN/m}$, $g = 9.81\ \mathrm{m/s^2}$, $K_{2\mathrm{D}} = 10\ \mathrm{mN/m}$, with all other surface parameters set to zero. For all curves, the bulk medium is a water-like viscoelastic material as described by Eqs. (D.25), (D.26) with parameters given by Eqs. (D.28-D.31). Phase velocities and decay lengths are calculated from $k(\omega)$ according to Eqs. (D.64), (D.65).

Appendix E

Supplemental Material for Chapter 6

In the present appendix, which supplements Chapter 6, we present detailed analytical derivations, the numerical algorithm we use, and show the robustness of our nonlinear theory with respect to varying both elastic modulus and boundary condition.

In Appendix E.1, we start by reviewing the derivation of the Lucassen dispersion relation and showing that for the Lucassen wave, the displacement is mainly parallel to the interface. In Appendix E.2, we provide an alternative derivation of the fractional wave equation, directly from momentum conservation and the stress boundary conditions at the interface. After having established the linear fractional wave equation, we discuss the elastic modulus $K_{2\mathrm{D}}$ in more detail. In Appendix E.3, we explain how we obtain $K_{2\mathrm{D}}$ from an experimentally measured Langmuir isotherm, and in Appendix E.5 discuss the assumption that the elastic modulus relevant for the Lucassen wave is isothermal. In Appendix E.4 we discuss the assumption that nonlinear effects due to local changes in the elastic modulus $K_{2\mathrm{D}}$ become relevant at smaller wave amplitudes than the convective nonlinear term in the Navier-Stokes equation. In Appendix E.6, we review the well-known analytical solution of the linear fractional wave equation. In the following Appendix E.7, we explain the algorithm we use for numerically solving the nonlinear fractional wave equation. In Appendix E.8, we validate this numerical algorithm by comparing results of numerical solutions of the linear fractional wave equation to the corresponding analytical solutions. In Appendix E.9, we explain how we obtain a boundary condition for our numerical calculations from experimental data. Finally, in Appendix E.10 we show that the numerical results presented in Chapter 6 are robust with respect to varying both the elastic modulus and the boundary condition.

E.1 Standard derivation of Lucassen's dispersion relation

In this appendix, we give a short derivation of the Lucassen dispersion relation. Most of the material presented here is a summary of the calculations given in Appendix D.1, but for the special case of an incompressible viscous fluid as bulk medium. Throughout this appendix, we use Cartesian coordinates $\vec{r} = (x, y, z)$.

We consider a viscous incompressible fluid in the lower half-space $z \leq 0$ of $\mathbb{R}^3$, bounded by a viscoelastic interface at $z = 0$. Gravitational acceleration acts in the negative z-direction and

couples to both the half-space and the interface, c.f. Fig. E.1.

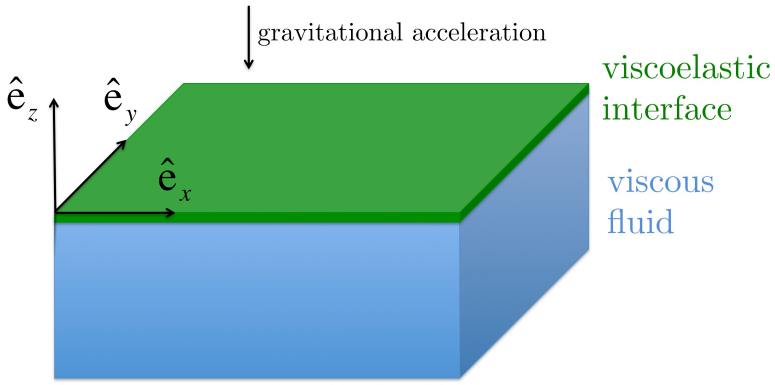

Figure E.1: Setup. We consider an incompressible viscous fluid with mass density ρ and shear viscosity η in the lower half-space $z \leq 0$, bounded by a viscoelastic interface at $z = 0$ with two-dimensional excess mass density $\rho_{2\mathrm{D}}$ and elastic modulus $K_{2\mathrm{D}}$. Gravitational acceleration g points in the negative z-direction and couples to both the fluid and the interface.

E.1.1 Linearized Navier-Stokes equation

For the bulk medium at $z < 0$, the linearized Navier-Stokes equation is given as [172]

$$\rho\, \partial_t v_i(\vec{r}, t) = \partial_j \sigma_{ij} + F_i(\vec{r}, t) \qquad i \in \{x, y, z\}, \tag{E.1}$$

where $\vec{v}(\vec{r}, t)$ is the velocity field, $\vec{F}(\vec{r}, t)$ is an external force, ρ is the mass density, which is assumed to be constant, ∂_t denotes the time derivative, the gradient operator is denoted by $\vec{\nabla} = (\partial_x, \partial_y, \partial_z)$, we use the Einstein sum convention to sum over repeated indices, and the stress tensor σ_{ij} is given by

$$\sigma_{ij} = -P\delta_{i,j} + \eta(\partial_i v_j + \partial_j v_i), \tag{E.2}$$

with η the shear viscosity, P the pressure and $\delta_{i,j}$ the Kronecker delta. We assume the medium to be incompressible,

$$\vec{\nabla} \cdot \vec{v} \equiv 0, \tag{E.3}$$

and consider gravitational acceleration $F_j = -\delta_{j,z} g\rho$ as external force.

Equations (E.1), (E.3) constitute four equations for the four unknowns $(\vec{v}, P)$. Direct substitution shows that a stationary solution is given by the fluid at rest,

$$\vec{v}^{(0)}(\vec{r}) = 0, \tag{E.4}$$

$$P^{(0)}(\vec{r}) = P_0 - \rho g z, \tag{E.5}$$

where P_0 is the pressure at $z = 0$. We consider perturbations $\vec{v}^{(1)}$, $P^{(1)}$ around this stationary solution, i.e., we consider velocity and pressure fields

$$\vec{v}(\vec{r}, t) = \vec{v}^{(0)} + \vec{v}^{(1)}(\vec{r}, t), \tag{E.6}$$

$$P(\vec{r}, t) = P^{(0)}(\vec{r}) + P^{(1)}(\vec{r}, t). \tag{E.7}$$

Substitution of Eqs. (E.6), (E.7) into Eqs. (E.1), (E.3) yields

$$\rho\, \partial_t \vec{v}^{(1)} = -\vec{\nabla} P^{(1)} + \eta \Delta \vec{v}^{(1)}, \tag{E.8}$$

$$\vec{\nabla} \cdot \vec{v}^{(1)} = 0, \tag{E.9}$$

where $\Delta = \partial_x^2 + \partial_y^2 + \partial_z^2$ denotes the Laplace operator. Since $\vec{v}^{(0)} = 0$, we have $\vec{v} \equiv \vec{v}^{(1)}$ and therefore will omit the superscript "(1)" for the velocity field perturbation in the following.

If the fluid only undergoes small displacements, the velocity field can be written as time derivative of the displacement field $\vec{u}(\vec{r}, t)$ as [172]

$$\vec{v} = \partial_t \vec{u}. \tag{E.10}$$

In line with the ansatz we will use in Appendix E.1.3 for the displacement field, we assume $\vec{u}$ to be of the form

$$\vec{u} = \vec{\nabla}\Phi + \vec{\nabla} \times \vec{\Psi}, \tag{E.11}$$

where Φ, Ψ are potentials for the longitudinal (curl free) and transversal (divergence free) part of the displacement field. Equations (E.8), (E.9) are then fulfilled if the potentials fulfill

$$\eta \Delta \vec{\Psi} = \rho \partial_t \vec{\Psi}, \tag{E.12}$$

$$\Delta \Phi = 0, \tag{E.13}$$

and the pressure perturbation is given in terms of the potentials by

$$P^{(1)} = -\rho \partial_t^2 \Phi. \tag{E.14}$$

E.1.2 Stress boundary conditions for a viscoelastic interface

A detailed derivation of the continuum mechanical boundary conditions for two bulk media separated by a viscoelastic interface was given by Kralchevsky et al. [169]. In plane, they assumed the interface to have a purely viscous shear response with viscosity $\eta_{2\mathrm{D}}$, a viscoelastic response to dilation with viscosity $\eta'_{2\mathrm{D}}$ and a position dependent surface tension $\sigma_{2\mathrm{D}}$. For out-of-plane deformations, they assumed a bending rigidity κ_{2D} and a transverse viscosity $\eta^{\perp}_{2\mathrm{D}}$. Furthermore, they considered the interface to have a two-dimensional excess mass density $\rho_{2\mathrm{D}}$ and included an external force per area $\vec{f}_s$ acting on the surface. To linear order in the surface velocity $\vec{v}_{2\mathrm{D}}$,

they obtained[1]

$$\rho_{2\mathrm{D}}\partial_t v_{2\mathrm{D},\alpha} = (\sigma_{\mathrm{III},n\alpha} - \sigma_{n\alpha}) + \rho_{2\mathrm{D}} f_{s,\alpha} + \left(\vec{\nabla}_s\right)_\alpha \sigma_{2\mathrm{D}} + \eta'_{2\mathrm{D}} \left(\vec{\nabla}_s\right)_\alpha \left(\vec{\nabla}_s \cdot \vec{v}_{2\mathrm{D}}\right) + \eta_{2\mathrm{D}} \vec{\nabla}_s^2 v_{2\mathrm{D},\alpha} \qquad \alpha \in \{x, y\}, \tag{E.15}$$

$$\rho_{2\mathrm{D}}\partial_t v_{2\mathrm{D},n} = (\sigma_{\mathrm{III},nn} - \sigma_{nn}) + \rho_{2\mathrm{D}} f_{s,n} + \sigma_{2\mathrm{D}} \vec{\nabla}_s^2 u_{2\mathrm{D},z} - \kappa_{2D} \vec{\nabla}_s^2 \vec{\nabla}_s^2 u_{2\mathrm{D},z} + \eta_{2\mathrm{D}}^{\perp} \vec{\nabla}_s^2 \partial_t u_{2\mathrm{D},z}, \tag{E.16}$$

where $u_{2\mathrm{D},z}(x, y, t) \equiv u_z(x, y, z = 0, t)$ is the displacement of the surface point $(x, y, 0)$ in z-direction, the stress tensors σ, σ_{III} for the bulk media below and above the surface are understood to be evaluated at $z = 0$, and $\vec{\nabla}_s := \vec{\nabla} - \hat{n}(\hat{n} \cdot \vec{\nabla})$ is the projection of the gradient onto the surface, with $\hat{n}$ the unit normal vector pointing into the $z > 0$ half-space. The indices α, n label tensor components parallel and perpendicular to the surface, respectively. More generally, we will use the convention that greek indices run over $\{x, y\}$, while latin indices run over $\{x, y, z\}$. For the half-space $z > 0$, we will not consider any dynamics and assume that there is a constant pressure P_{III}, so that

$$\sigma_{\mathrm{III},jk} = -P_{\mathrm{III}} \delta_{j,k}. \tag{E.17}$$

To rewrite the boundary conditions (E.15), (E.16), in a form more useful for the present context, we will now relate the surface velocity to the surface displacement, explicitly evaluate $\vec{\nabla}_s$ and use gravitation as external force. This will lead to the expressions Eqs. (E.25), (E.26) for the boundary conditions. To derive an explicit form for the boundary conditions in the linear regime, we will then further rewrite Eqs. (E.25), (E.26) by relating the elastic in-surface dilational response $\sigma_{2\mathrm{D}}$ to the displacement field, leading to Eqs. (E.31), (E.32).

As we did for the bulk medium, we assume small displacements and approximate the velocity by the time derivative of the displacement,

$$\vec{v}_{2\mathrm{D}} \approx \partial_t \vec{u}_{2\mathrm{D}}, \tag{E.18}$$

and furthermore the unit normal vector by the unit vector in $\hat{e}_z$-direction, $\hat{n} \approx \hat{e}_z$. Using the latter approximation, we get

$$\vec{\nabla}_s = \hat{e}_x \partial_x + \hat{e}_y \partial_y \equiv \hat{e}_\beta \partial_\beta. \tag{E.19}$$

To express $\rho_{2\mathrm{D}}$ in terms of the surface displacement field, we assume that the two-dimensional excess mass density deviates only slightly from its constant equilibrium value, and write

$$\rho_{2\mathrm{D}}(x, y, t) = \rho_{2\mathrm{D}}^{(0)} + \rho_{2\mathrm{D}}^{(1)}(x, y, t), \tag{E.20}$$

with $\rho_{2\mathrm{D}}^{(1)}$ small compared to $\rho_{2\mathrm{D}}^{(0)}$. To express $\rho_{2\mathrm{D}}^{(1)}$ in terms of the interfacial displacement field, we integrate the linearized 2D mass conservation equation,

$$\partial_t \rho_{2\mathrm{D}}^{(1)} + \rho_{2\mathrm{D}}^{(0)} \partial_t \partial_\beta u_{2\mathrm{D},\beta} = 0, \tag{E.21}$$

[1] This is ([169],5.16), ([169],5.17), but with the membrane inertia and body force kept. Also in Eq. ([169],5.16), the stress tensor of the medium above the membrane was neglected, which we include.

with respect to time, to obtain

$$\rho_{2\mathrm{D}}^{(1)} = -\rho_{2\mathrm{D}}^{(0)} \partial_\beta u_{2\mathrm{D},\beta}. \tag{E.22}$$

The constant of integration is chosen so that an area preserving deformation, $\partial_\beta u_{2\mathrm{D},\beta} = 0$, implies no area density change, $\rho_{2\mathrm{D}}^{(1)} = 0$. Using Eq. (E.22) to eliminate $\rho_{2\mathrm{D}}^{(1)}$ in Eq. (E.20), we obtain

$$\rho_{2\mathrm{D}} = \rho_{2\mathrm{D}}^{(0)} \left(1 - \partial_\beta u_{2\mathrm{D},\beta}\right). \tag{E.23}$$

Using this equation, the area force density due to gravitational acceleration is given by

$$\rho_{2\mathrm{D}} \vec{f_s} = -\rho_{2\mathrm{D}} g \vec{e}_z = -\rho_{2\mathrm{D}}^{(0)} g \left(1 - \partial_\beta u_{2\mathrm{D},\beta}\right) \vec{e}_z. \tag{E.24}$$

Equation (E.24) shows that even if there is no local compression or expansion, $\partial_\beta u_{2\mathrm{D},\beta} = 0$, gravity causes a constant area force density $-\rho_{2\mathrm{D}}^{(0)} g \vec{e}_z$ on the interface. For the stationary solution around which we perturb, the surface should be at rest at $z = 0$. Thus, for the stationary solution the constant background pressure P_0 in the lower bulk medium (c.f. Eq. (E.5)) and the constant pressure P_{III} in the upper bulk medium need to differ exactly by the pressure gravitational forces acting on the interface exert on the lower medium in equilibrium, i.e. $P_0 - P_{\mathrm{III}} = \rho_{2\mathrm{D}}^{(0)} g$, so that the interface remains at $z = 0$.

Inserting the expressions for $\vec{v}_{2\mathrm{D}}$, $\vec{\nabla}_s$, $\rho_{2\mathrm{D}}$ and $\rho_{2\mathrm{D}} \vec{f_s}$, namely Eqs. (E.18), (E.19), (E.23), (E.24), into the boundary conditions (E.15), (E.16), we obtain

$$\begin{aligned}
\rho_{2\mathrm{D}}^{(0)} \partial_t^2 u_{2\mathrm{D},\alpha} &= \left(\sigma_{\mathrm{III},z\alpha} - \sigma_{z\alpha}\right) + \partial_\alpha \sigma_{2\mathrm{D}} \\
&\quad + \eta'_{2\mathrm{D}} \partial_t \partial_\alpha \partial_\beta u_{2\mathrm{D},\beta} + \eta_{2\mathrm{D}} \partial_t \partial_\beta^2 u_{2\mathrm{D},\alpha} \qquad \alpha \in \{x, y\}, \qquad \text{(E.25)} \\
\rho_{2\mathrm{D}}^{(0)} \partial_t^2 u_{2\mathrm{D},z} &= \left(\sigma_{\mathrm{III},zz} - \sigma_{zz}\right) - \rho_{2\mathrm{D}}^{(0)} g \left(1 - \partial_\beta u_{2\mathrm{D},\beta}\right) \\
&\quad + \left(\sigma_{2\mathrm{D}} + \eta_{2\mathrm{D}}^{\perp} \partial_t - \kappa_{2D} \partial_\beta^2\right) \partial_\beta^2 u_{2\mathrm{D},z}. \qquad \text{(E.26)}
\end{aligned}$$

To express $\sigma_{2\mathrm{D}}$ in terms of the surface displacement, we assume that the surface tension deviates only slightly from its constant equilibrium value, and write

$$\sigma_{2\mathrm{D}}(x, y, t) = \sigma_{2\mathrm{D}}^{(0)} + \sigma_{2\mathrm{D}}^{(1)}(x, y, t), \tag{E.27}$$

with $\sigma_{2\mathrm{D}}^{(1)}$ small compared to $\sigma_{2\mathrm{D}}^{(0)}$. To express $\sigma_{2\mathrm{D}}^{(1)}$ in terms of the surface displacement field, we use the definition of the 2D in-plane elastic modulus $K_{2\mathrm{D}}$,

$$K_{2\mathrm{D}} = a \frac{\partial \sigma_{2\mathrm{D}}}{\partial a}, \tag{E.28}$$

which relates local changes in the area per lipid a of a surface element to the local surface tension $\sigma_{2\mathrm{D}}$. Note that, unlike in the analogous equation for the three dimensional bulk modulus, there is no minus sign in Eq. (E.28) because surface tension can be thought of as negative surface pressure.

$K_{2\mathrm{D}}$ not only depends on the material the interface is made of, but also on the thermodynamics of the deformation (e.g. isothermal, adiabatic). Equation (E.28) can be integrated to yield

$$\sigma_{2\mathrm{D}}^{(1)} = -K_{2\mathrm{D}}\partial_\beta u_{2\mathrm{D},\beta}, \tag{E.29}$$

where we used $\Delta a/\bar{a} \equiv (a-\bar{a})/\bar{a} = \partial_\beta u_{2\mathrm{D},\beta}$ [151], with $\bar{a}$ the equilibrium area per lipid, and fixed the constant of integration by demanding that no area change implies no surface tension change. Using Eq. (E.29) to eliminate $\sigma_{2\mathrm{D}}^{(1)}$ in Eq. (E.27), we get

$$\sigma_{2\mathrm{D}} = \sigma_{2\mathrm{D}}^{(0)} - K_{2\mathrm{D}}\partial_\beta u_{2\mathrm{D},\beta}, \tag{E.30}$$

so that the boundary conditions (E.25), (E.26) finally become, to linear order in the interfacial displacement field,

$$\begin{aligned}\rho_{2\mathrm{D}}^{(0)}\partial_t^2 u_{2\mathrm{D},\alpha} &= (\sigma_{\mathrm{III},z\alpha} - \sigma_{z\alpha}) + \partial_\alpha\left(K_{2\mathrm{D}} + \eta'_{2\mathrm{D}}\partial_t\right)\partial_\beta u_{2\mathrm{D},\beta} \\ &\quad + \eta_{2\mathrm{D}}\partial_t\partial_\beta^2 u_{2\mathrm{D},\alpha} \qquad \alpha \in \{x,y\}, \end{aligned} \tag{E.31}$$

$$\begin{aligned}\rho_{2\mathrm{D}}^{(0)}\partial_t^2 u_{2\mathrm{D},z} &= (\sigma_{\mathrm{III},zz} - \sigma_{zz}) - \rho_{2\mathrm{D}}^{(0)} g\left(1 - \partial_\beta u_{2\mathrm{D},\beta}\right) \\ &\quad + \left(\sigma_{2\mathrm{D}}^{(0)} + \eta_{2\mathrm{D}}^{\perp}\partial_t - \kappa_{2D}\partial_\beta^2\right)\partial_\beta^2 u_{2\mathrm{D},z}. \end{aligned} \tag{E.32}$$

Since the perturbations $\rho_{2\mathrm{D}}^{(1)}$, $\sigma_{2\mathrm{D}}^{(1)}$ do not appear explicitly in Eqs. (E.31), (E.32) anymore, we drop the superscripts (0) of the corresponding equilibrium values $\rho_{2\mathrm{D}}^{(0)}$, $\sigma_{2\mathrm{D}}^{(0)}$ in the following, and have dropped them in Chapter 6.

E.1.3 Harmonic wave ansatz and implicit dispersion relation

To solve Eqs. (E.8), (E.9) with boundary conditions (E.31), (E.32), we use a harmonic wave ansatz [158] for the displacement potentials that were introduced in Eq. (E.11),

$$\Phi(\vec{r},t) = \phi e^{z/\lambda_l} e^{i(kx-\omega t)}, \tag{E.33}$$

$$\vec{\Psi}(\vec{r},t) = \psi e^{z/\lambda_t} e^{i(kx-\omega t)}\hat{e}_y, \tag{E.34}$$

where we assume $\mathrm{Re}(k) > 0$, so that the wave propagates in the positive x-direction. According to Eq. (E.11), the resulting displacement field is given by

$$\vec{u}(\vec{r},t) = \left[\begin{pmatrix} ik \\ 0 \\ \lambda_l^{-1}\end{pmatrix}\phi e^{z/\lambda_l} + \begin{pmatrix} -\lambda_t^{-1} \\ 0 \\ ik\end{pmatrix}\psi e^{z/\lambda_t}\right] e^{i(kx-\omega t)}, \tag{E.35}$$

so that according to Eq. (E.10), we obtain the velocity field

$$\vec{v}(\vec{r},t) = (-i\omega)\left[\begin{pmatrix} ik \\ 0 \\ \lambda_l^{-1}\end{pmatrix}\phi e^{z/\lambda_l} + \begin{pmatrix} -\lambda_t^{-1} \\ 0 \\ ik\end{pmatrix}\psi e^{z/\lambda_t}\right] e^{i(kx-\omega t)}. \tag{E.36}$$

The harmonic wave ansatz contains 6 parameters, namely k, ω, ϕ, ψ, λ_l, λ_t. We assume $\omega \in \mathbb{R}$, $\omega > 0$, is a given constant, i.e., we consider waves of frequency ω and want to obtain the corresponding wave number $k(\omega)$. The decay lengths away from the interface λ_l, λ_t are determined by substituting (E.33), (E.34), into Eqs. (E.12), (E.13), which yields

$$\lambda_t^{-2} = k^2 + \frac{-i\omega\rho}{\eta}, \tag{E.37}$$

$$\lambda_l^{-2} = k^2. \tag{E.38}$$

The physical requirement that the surface wave decays as $z \to -\infty$ implies $\mathrm{Re}(\lambda_l^{-1}), \mathrm{Re}(\lambda_t^{-1}) > 0$, so that Eqs. (E.37), (E.38) determine λ_l, λ_t uniquely as a function of k, ω, because the complex square root with positive real part has to be chosen when solving for λ_l, λ_t. The stress boundary conditions (E.31), (E.32) at $z = 0$ yield a homogeneous linear system of two equations for the two coefficients ϕ, ψ. This system can be obtained explicitly by calculating σ_{ij}, $u_{2\mathrm{D},i} \equiv u_i|_{z=0}$, for the displacement field Eq. (E.35) and the stress strain relation Eq. (E.2), and then substituting these into the boundary conditions (E.31), (E.32) (for (E.31), only the $\alpha = 1$ case is needed, since for $\alpha = 2$ the equation is fulfilled trivially, as a short calculation shows). The stress boundary conditions then become

$$\begin{aligned} 0 = {} & ik \left[i\omega\rho_{2\mathrm{D}} - k^2\tilde{g}_{2\mathrm{D}} - 2\eta k \right] \phi \\ & + \left[\lambda_t^{-1}(k^2\tilde{g}_{2\mathrm{D}} - i\omega\rho_{2\mathrm{D}}) + \eta(k^2 + \lambda_t^{-2}) \right] \psi, \end{aligned} \tag{E.39}$$

$$\begin{aligned} 0 = {} & \left[k(\omega^2\rho_{2\mathrm{D}} - k^2\tilde{\Pi}_{2\mathrm{D}} - \rho_0 g) - k^2\rho_{2\mathrm{D}} g + i\omega\eta(k^2 + \lambda_t^{-2}) \right] \phi \\ & + ik \left[\omega^2\rho_{2\mathrm{D}} - k^2\tilde{\Pi}_{2\mathrm{D}} - \lambda_t^{-1}\rho_{2\mathrm{D}} g - \rho_0 g + i\omega 2\eta\lambda_t^{-1} \right] \psi, \end{aligned} \tag{E.40}$$

where again λ_t is given by Eq. (E.37), and the response functions $\tilde{g}_{2\mathrm{D}}$, $\tilde{\Pi}_{2\mathrm{D}}$ are defined as

$$\tilde{g}_{2\mathrm{D}}(\omega) := \eta_{2\mathrm{D}} + \eta'_{2\mathrm{D}} + K_{2\mathrm{D}}/(-i\omega), \tag{E.41}$$

$$\tilde{\Pi}_{2\mathrm{D}}(k,\omega) := \sigma_{2\mathrm{D}} + (-i\omega)\eta^{\perp}_{2\mathrm{D}} + k^2\kappa_{2D}. \tag{E.42}$$

In order to have a propagating wave with nonzero amplitude, Eqs. (E.39), (E.40) need to have a nontrivial solution for ϕ, ψ. Consequently, the implicit dispersion relation is obtained by setting the determinant of the 2×2 coefficient matrix for ϕ, ψ, obtained from Eqs. (E.39), (E.40), equal to zero. This leads to

$$\begin{aligned} 0 = {} & k\left(k^2\tilde{\Pi}_{2\mathrm{D}} + \rho g - \omega^2\rho_{2\mathrm{D}}\right)\left[(k^2\tilde{g}_{2\mathrm{D}} - i\omega\rho_{2\mathrm{D}})\left(k - \lambda_t^{-1}\right) + i\omega\rho\right] \\ & + \left(k^2\tilde{g}_{2\mathrm{D}} - i\omega\rho_{2\mathrm{D}}\right)\omega^2\rho\lambda_t^{-1} \\ & + \eta\left[i\omega\eta\left(-4k^2\lambda_l^{-1}\lambda_t^{-1} + (k^2 + \lambda_t^{-2})^2\right) - \rho_{2\mathrm{D}} g k^2\left(k - \lambda_t^{-1}\right)^2\right]. \end{aligned} \tag{E.43}$$

A solution $k(\omega)$ to Eq. (E.43) yields the dispersion relation of a surface wave, for which phase velocity $c_\parallel$ and propagation distance $\lambda_\parallel$ can then be calculated via

$$c_\parallel(\omega) = \frac{\omega}{\mathrm{Re}(k(\omega))}, \tag{E.44}$$

$$\lambda_\parallel(\omega) = \frac{1}{\mathrm{Im}(k(\omega))}. \tag{E.45}$$

E.1.4 Factorization of the implicit dispersion relation and Lucassen dispersion relation

As it stands, Eq. (E.43) is too complicated to be solved analytically. However, under certain conditions, which as we will see in Appendix E.1.5 are appropriate for the surface waves we are interested in, approximate analytical solutions can be obtained.

Assuming

$$\frac{\rho|\omega|}{\eta|k|^2} \gg 1, \tag{E.46}$$

we have

$$\lambda_t^{-2} \approx -i\omega\rho/\eta, \tag{E.47}$$

c.f. Eq. (E.37), and $|\lambda_t^{-1}| \gg |k|$, so that Eq. (E.43) simplifies to

$$\begin{aligned} 0 = {} & k\left(k^2\tilde{\Pi}_{2\mathrm{D}} + \rho g - \omega^2\rho_{2\mathrm{D}}\right)\left[\left(k^2\tilde{g}_{2\mathrm{D}} - i\omega\rho_{2\mathrm{D}}\right)\left(k - \lambda_t^{-1}\right) + i\omega\rho\right] \\ & + \left(k^2\tilde{g}_{2\mathrm{D}} - i\omega\rho_{2\mathrm{D}}\right)\omega^2\rho\lambda_t^{-1} - i\omega\rho\left(\omega^2\rho - \rho_{2\mathrm{D}}gk^2\right). \end{aligned} \tag{E.48}$$

Furthermore assuming that the gravitational force on the interface can be neglected,

$$\rho_{2\mathrm{D}}g \ll \frac{\rho|\omega|^2}{|k|^2}, \tag{E.49}$$

Eq. (E.48) factorizes to yield

$$0 = \left[k\left(k^2\tilde{\Pi}_{2\mathrm{D}} + \rho g - \omega^2\rho_{2\mathrm{D}}\right) - \rho\omega^2\right]\left[\left(k^2\tilde{g}_{2\mathrm{D}} - i\omega\rho_{2\mathrm{D}}\right)\lambda_t^{-1} - i\omega\rho\right], \tag{E.50}$$

and one obtains the two independent dispersion relations

$$0 = k\left(k^2\tilde{\Pi}_{2\mathrm{D}} + \rho g - \omega^2\rho_{2\mathrm{D}}\right) - \rho\omega^2, \tag{E.51}$$

$$0 = \left(k^2\tilde{g}_{2\mathrm{D}} - i\omega\rho_{2\mathrm{D}}\right)\sqrt{(-i\omega\rho)/\eta} - i\omega\rho, \tag{E.52}$$

where we used Eq. (E.47) and the square root in (E.52) is the complex root with positive real part. Whether a solution $k(\omega)$ of Eqs. (E.51), (E.52) fulfills the factorization conditions (E.46),

(E.49), can of course only be checked a posteriori, i.e. once a solution $k(\omega)$ has been obtained, because k appears in both inequalities.

Equation (E.51) is a generalization of the standard capillary-gravity wave dispersion relation [152, 172], and additionally includes the inertia of the interface, as well as surface viscosity and bending rigidity of the interface via $\tilde{\Pi}_{2\mathrm{D}}$, c.f. Eq. (E.42). Equation (E.52) is a generalization of the Lucassen dispersion relation [158, 159], and additionally includes the inertia of the interface. To obtain the classic Lucassen dispersion relation, we first note that Eq. (E.52) can immediately be solved for k^2, to yield

$$k^2 = \frac{i\omega}{\tilde{g}_{2\mathrm{D}}}\left(\sqrt{\frac{\rho\eta}{-i\omega}} + \rho_{2\mathrm{D}}\right). \tag{E.53}$$

If the inertia of the interface can be neglected,

$$|\rho_{2\mathrm{D}}| \ll \left|\sqrt{\frac{\rho\eta}{-i\omega}}\right|, \tag{E.54}$$

Eq. (E.53) simplies to

$$k^2 = \frac{i\omega}{\tilde{g}_{2\mathrm{D}}}\sqrt{\frac{\rho\eta}{-i\omega}}. \tag{E.55}$$

If furthermore the interfacial response is purely elastic,

$$\tilde{g}_{2\mathrm{D}}(\omega) = \eta_{2\mathrm{D}} + \frac{K_{2\mathrm{D}}}{-i\omega} \approx \frac{K_{2\mathrm{D}}}{-i\omega}, \tag{E.56}$$

Eq. (E.55) further simplifies to

$$k^2 = \frac{\omega^2}{K_{2\mathrm{D}}}\sqrt{\frac{\rho\eta}{-i\omega}}, \tag{E.57}$$

which finally leads to

$$k(\omega) = e^{i\pi/8}\sqrt{\frac{\sqrt{\rho\eta\omega^3}}{K_{2\mathrm{D}}}}, \tag{E.58}$$

where we choose the complex square root that leads to a positive real part for k, so that the resulting wave propagates in the positive $\hat{e}_x$-direction. This approximate solution of Eq. (E.52), valid as long as Eqs. (E.54), (E.56) are fulfilled, is the classical Lucassen dispersion relation [158].

E.1.5 Discussion of the factorization conditions for Lucassen waves in a lipid monolayer on water

In Appendix E.1.4 we showed that the derivation of the classical Lucassen dispersion relation, Eq. (E.58), from the full implicit dispersion relation, Eq. (E.43), rests on four inequalities, namely (E.46), (E.49), (E.54), (E.56). We now show that for a DPPC monolayer on water, there is a

frequency range spanning 10 orders of magnitude and including the frequency range relevant to us, where these inequalities are fulfilled.

More explicitly, we consider the parameters

$$\eta = 10^{-3}\,\mathrm{Pa}\cdot\mathrm{s}, \tag{E.59}$$
$$\rho = 10^{3}\,\mathrm{kg/m^3}, \tag{E.60}$$
$$g = 9.81\,\mathrm{m/s^2}, \tag{E.61}$$

appropriate for water as bulk medium [173] and standard gravitational acceleration, and the interface parameters

$$\rho_{2\mathrm{D}} = 1\cdot 10^{-6}\,\mathrm{kg/m^2}, \tag{E.62}$$
$$\eta_{2\mathrm{D}} = 1\cdot 10^{-9}\,\mathrm{Pa}\cdot\mathrm{s}\cdot\mathrm{m}, \tag{E.63}$$
$$\eta'_{2\mathrm{D}} = 0, \tag{E.64}$$
$$\eta^{\perp}_{2\mathrm{D}} = 1\cdot 10^{-9}\,\mathrm{Pa}\cdot\mathrm{s}\cdot\mathrm{m}, \tag{E.65}$$
$$K_{2\mathrm{D}} = 1\cdot 10^{-2}\,\mathrm{N/m}, \tag{E.66}$$
$$\sigma_{2\mathrm{D}} = 7\cdot 10^{-2}\,\mathrm{N/m}, \tag{E.67}$$
$$\kappa_{2D} = 3\cdot 10^{-19}\,\mathrm{N}\cdot\mathrm{m}, \tag{E.68}$$

appropriate for a DPPC monolayer. The values for $\sigma_{2\mathrm{D}}$, $K_{2\mathrm{D}}$ can be obtained via measuring Langmuir isotherms [92, 174], the shear viscosity $\eta_{2\mathrm{D}}$ for a DPPC bilayer can be measured by observing diffusion in lipid membranes [217, 218], while the bending rigidity κ_{2D} can be measured via weakly deforming bilayer vesicles [219, 220].

Using these parameters and the solution Eq. (E.58), the inequalities (E.46), (E.49), (E.54), (E.56) become, respectively,

$$\text{(E.46)} \quad\Longleftrightarrow\quad \omega \ll \frac{K_{2\mathrm{D}}^2\rho}{\eta^3} = 10^{10}\frac{1}{\mathrm{s}}, \tag{E.69}$$
$$\text{(E.49)} \quad\Longleftrightarrow\quad \omega \gg \frac{\eta\rho_{2\mathrm{D}}^2 g^2}{\rho K_{2\mathrm{D}}} \approx 10^{-3}\frac{1}{\mathrm{s}}, \tag{E.70}$$
$$\text{(E.54)} \quad\Longleftrightarrow\quad \omega \ll \frac{\rho\eta}{\rho_{2\mathrm{D}}^2} = 10^{12}\frac{1}{\mathrm{s}}, \tag{E.71}$$
$$\text{(E.56)} \quad\Longleftrightarrow\quad \omega \ll \frac{K_{2\mathrm{D}}}{\eta_{2\mathrm{D}}} = 10^{7}\frac{1}{\mathrm{s}}. \tag{E.72}$$

Thus, for frequencies

$$10^{-3}\frac{1}{\mathrm{s}} \ll \omega \ll 10^{7}\frac{1}{\mathrm{s}}, \tag{E.73}$$

Eq. (E.58), an approximate solution to the implicit dispersion relation Eq. (E.43), is self-consistent with the approximations used to derive it. In particular, since we are interested in dynamics on

the millisecond time scale, $\omega \approx 10^3\ 1/\mathrm{s}$, this frequency range includes the regime of interest to us.

In Fig. E.2, we supplement our analytical estimates by a plot of the phase velocities and propagation distances for both the approximate solution Eq. (E.58) and the corresponding numerical solution of the full implicit dispersion relation, Eq. (E.43). Consistent with Eq. (E.73), the two solutions $k(\omega)$ lead to basically identical wave properties for frequencies up to $\omega \approx 10^6\ 1/\mathrm{s}$.

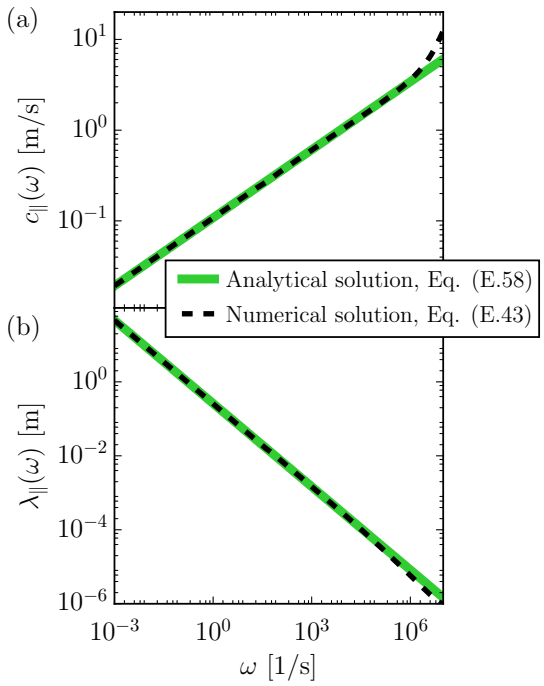

Figure E.2: Comparison of analytical Lucassen relation to numerical solution of full implicit dispersion relation. The black dashed line shows the numerical solution of Eq. (E.43) corresponding to the Lucassen wave, while the green solid line depicts the analytical Lucassen dispersion relation, Eq. (E.58). Phase velocities and propagation distances are calculated using Eqs. (E.44), (E.45).

E.1.6 Identification of the dominating term in the displacement field of the Lucassen wave

As discussed in Appendix E.1.3, the displacement field of the Lucassen wave has components in the $\hat{e}_x$ and $\hat{e}_z$ direction. More explicitly, it is given by Eq. (E.35) as

$$\vec{u}(\vec{r},t) = (\vec{\nabla}\Phi)(\vec{r},t) + (\vec{\nabla}\times\vec{\Psi})(\vec{r},t) = \tag{E.74}$$

$$= \left[\phi\begin{pmatrix} ik \\ 0 \\ k \end{pmatrix} e^{kz} + \psi\begin{pmatrix} -\lambda_t^{-1} \\ 0 \\ ik \end{pmatrix} e^{z/\lambda_t}\right] e^{i(kx-\omega t)}, \tag{E.75}$$

where $\lambda_l^{-1} = k$, $\lambda_t^{-1} = \sqrt{(-i\omega\rho)/\eta}$, c.f. Eqs. (E.38), (E.47), and with k given by Eq. (E.58).

To determine which component of the displacement field (E.75) is dominant, we compare the magnitudes of all components of both the longitudinal and transversal parts, i.e. we compare $|\hat{e}_x\cdot(\vec{\nabla}\Phi)|$, $|\hat{e}_z\cdot(\vec{\nabla}\Phi)|$, $|\hat{e}_x\cdot(\vec{\nabla}\times\vec{\Psi})|$, $|\hat{e}_z\cdot(\vec{\nabla}\times\vec{\Psi})|$. For this, we consider the displacement field at the interface ($z=0$) using the parameters from Appendix E.1.5, Eqs. (E.59)-(E.68).

From Eq. (E.75) it can immediately be read off that $|\hat{e}_x\cdot(\vec{\nabla}\Phi)|$, $|\hat{e}_z\cdot(\vec{\nabla}\Phi)|$ have the same order of magnitude, namely $|\phi k|$. On the other hand, as shown in Appendix E.1.4, for $\omega \ll 10^7$ 1/s it holds that $|\lambda_t^{-1}| \gg |k|$, so that $|\hat{e}_x\cdot(\vec{\nabla}\times\vec{\Psi})| \gg |\hat{e}_z\cdot(\vec{\nabla}\times\vec{\Psi})|$.

To compare $|\hat{e}_i\cdot(\vec{\nabla}\Phi)|$, $|\hat{e}_x\cdot(\vec{\nabla}\times\vec{\Psi})|$, we need an order-of-magnitude estimate for $|\phi/\psi|$. This relative amplitude can be obtained by solving any of the boundary condition (E.39), (E.40) for ϕ/ψ. We solve Eq. (E.39) for ϕ/ψ and calculate the fraction $|\phi/\psi|$ as a function of frequency ω, using the numerical solution of Eq. (E.43) corresponding to the Lucassen wave for $k(\omega)$. The result is shown in Fig. E.3 (a). As can be seen there, for frequencies 10^{-3} 1/s $< \omega < 10^7$ 1/s, it holds that

$$0.1 < \left|\frac{\phi}{\psi}\right| < 10, \tag{E.76}$$

so that $|\phi|$, $|\psi|$ are of the same order of magnitude. Thus, since according to Eq. (E.46) we have $|\lambda_t^{-1}| \gg |k|$, it follows that $|\phi k| \ll |\psi\lambda_t^{-1}|$, and therefore $|\hat{e}_x\cdot(\vec{\nabla}\times\vec{\Psi})| \gg |\hat{e}_i\cdot(\vec{\nabla}\Phi)|$, $i\in\{x,z\}$.

In summary, for angular frequencies 10^{-3} 1/s $< \omega < 10^7$ 1/s, the displacement field for the Lucassen wave at the interface $z=0$ is dominated by the $\hat{e}_x$ component of $\vec{\nabla}\times\vec{\Psi}$, and thus approximately given by

$$\vec{u}(x,z=0,t) \approx -\hat{e}_x\psi\lambda_t^{-1}e^{i(kx-\omega t)}. \tag{E.77}$$

In accordance with these estimates, we show in Fig. E.3 (b) plots of $|k\phi|$, $|k\psi|$, $|\lambda_t^{-1}\psi|$, representing the components of Eq. (E.75) we just compared. To obtain the curves shown in the figure, we use the numerical solution of Eq. (E.43) corresponding to the Lucassen wave for $k(\omega)$, $\phi = 1$ m^2 and ψ as calculated from Eq. (E.39). The term $|\lambda_t^{-1}\psi|$, which according to Eq. (E.75) gives the order of magnitude of the $\hat{e}_x$ component of $\vec{\nabla}\times\vec{\Psi}$, is indeed the largest term.

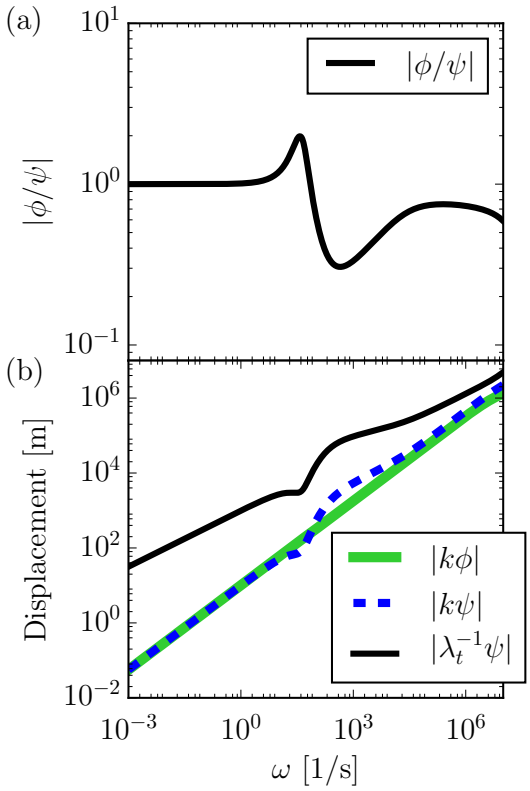

Figure E.3: (a) Relative magnitude of the coefficients ϕ, ψ of longitudinal and transversal parts of the harmonic wave ansatz. The boundary condition (E.39) is solved for ϕ/ψ, and using for $k(\omega)$ the numerical solution of Eq. (E.43) corresponding to the Lucassen wave with the parameters from Appendix E.1.5, $|\phi/\psi|$ is calculated as a function of ω. (b) Absolute values of the individual vector components of longitudinal and transversal parts of the harmonic wave ansatz. Using for $k(\omega)$ the numerical solution of Eq. (E.43) corresponding to the Lucassen wave, λ_t as given by Eq. (E.37), ϕ/ψ as obtained by solving Eq. (E.39) for ϕ/ψ, and setting $\phi = 1$ m^2, the quantities $|k\psi|$, $|k\psi|$, $|\lambda_t^{-1}\psi|$ are calculated as a function of ω. According to Eq. (E.75), the plotted curves correspond to the magnitudes of the individual terms appearing in the surface wave displacement field. Note that in the context of linear theory, the choice $\phi = 1$ m^2 simply sets a scale, and only the relative sizes of the terms plotted here are of relevance for determining the dominant component of the displacement field.

E.2 Direct derivation of the fractional wave equation from momentum conservation and stress boundary conditions

In Chapter 6, we introduce the fractional wave equation based on the Lucassen dispersion relation and the fact that the corresponding interfacial displacement is dominated by the $\hat{e}_x$-component, c.f. Appendix E.1. In the present appendix, we give a derivation of the fractional wave equation

directly from momentum conservation in the bulk medium $z < 0$ and the stress boundary condition at the interface $z = 0$.

As already stated in Appendix E.1, a stationary solution of the linearized Navier-Stokes equation (E.1) for an incompressible medium under the influence of gravity, $\vec{F} = -\hat{e}_z \rho g$, is given by the fluid at rest, with velocity and pressure fields

$$\vec{v}^{(0)}(\vec{r}) = 0, \tag{E.78}$$

$$P^{(0)}(\vec{r}) = P_0 - \rho g z, \tag{E.79}$$

with P_0 the pressure at $z = 0$. As in the derivation of the Lucassen dispersion relation, we consider perturbations $\vec{v}^{(1)}$, $P^{(1)}$ around this solution, i.e., we consider velocity and pressure fields

$$\vec{v}(\vec{r}, t) = \vec{v}^{(0)} + \vec{v}^{(1)}(\vec{r}, t), \tag{E.80}$$

$$P(\vec{r}, t) = P^{(0)}(\vec{r}) + P^{(1)}(\vec{r}, t). \tag{E.81}$$

Substitution of these into momentum conservation, Eq. (E.1), and the incompressibility condition, Eq. (E.3), yields

$$\rho \partial_t \vec{v}^{(1)} = -\vec{\nabla} P^{(1)} + \eta \Delta \vec{v}^{(1)}, \tag{E.82}$$

$$\vec{\nabla} \cdot \vec{v}^{(1)} = 0, \tag{E.83}$$

which are the linearized equations for incompressible Newtonian fluids with constant density and without external forces. Since $\vec{v}^{(0)} = 0$, we have $\vec{v} \equiv \vec{v}^{(1)}$ and will therefore omit the superscript "(1)" for the velocity field perturbation in the following.

Assuming a displacement field of the form

$$\vec{u}(\vec{r}, t) = \begin{pmatrix} u_x(x, z, t) \\ 0 \\ u_z(x, z, t) \end{pmatrix}, \tag{E.84}$$

appropriate for a wavefront traveling in the $\hat{e}_x$-direction, and assuming that the pressure only depends on the distance from the interface, $P^{(1)}(\vec{r}, t) \equiv P^{(1)}(z, t)$, momentum conservation in the $\hat{e}_x$ direction, Eq. (E.82) with $i = x$, becomes

$$\rho \partial_t^2 u_x = \eta \Delta \partial_t u_x, \tag{E.85}$$

where we used that for small displacements $\partial_t \vec{u} \approx \vec{v}$. Assuming that the right-hand side of this equation is dominated by the velocity gradient away from the interface,

$$\Delta \partial_t u_x = \left(\partial_x^2 + \partial_z^2\right) \partial_t u_x \approx \partial_z^2 \partial_t u_x \tag{E.86}$$

which physically means the velocity of the surface wave varies on a much shorter length scale away from the interface than in the direction of propagation, Eq. (E.85) becomes

$$\rho \partial_t^2 u_x = \eta \partial_t \partial_z^2 u_x. \tag{E.87}$$

Integrating this equation with respect to time and dividing by η leads to

$$\frac{\rho}{\eta}\partial_t u_x = \partial_z^2 u_x, \tag{E.88}$$

where we chose the constant of integration such that no spatial change in stress implies no temporal change in displacement. Formally taking the square root of the differential operators on both sides of Eq. (E.88) introduces a fractional derivative and yields

$$\sqrt{\frac{\rho}{\eta}}\partial_t^{1/2} u_x = \partial_z u_x. \tag{E.89}$$

Now as for the stress boundary condition at $z = 0$, the $\alpha = x$ component of the stress boundary condition (E.25) for an interface with negligible interfacial viscosities is

$$\rho_{2\mathrm{D}}\partial_t^2 U = \left(\sigma_{\mathrm{III},z\alpha} - \sigma_{z\alpha}\right)\big|_{z=0} + \partial_x \sigma_{2\mathrm{D}}, \tag{E.90}$$

where $\rho_{2\mathrm{D}}$ is the equilibrium two-dimensional excess mass density of the interface, $U(x,t) \equiv u_x(x, z = 0, t)$ is the interfacial displacement in the $\hat{e}_x$-direction, σ_{III}, σ are the stress tensors of the bulk medium above and below the interface, and $\sigma_{2\mathrm{D}}$ is the surface tension of the interface. [Note that in Eq. (E.90) we have dropped the superscript "(0)" of the equilibrium two-dimensional excess mass density $\rho_{2\mathrm{D}}^{(0)}$, as opposed to Eq. (E.25).]

We now rewrite the term $\partial_x \sigma_{2\mathrm{D}}$ on the right-hand side of Eq. (E.90). For this, first note that the surface tension $\sigma_{2\mathrm{D}}$ is just the negative interfacial pressure π, so that

$$\sigma_{2\mathrm{D}}(a) = -\pi(a), \tag{E.91}$$

with a the area per lipid (or more generally area per molecule). For a given equilibrium area per lipid $\bar{a}$, the actual area per lipid can be written in terms of the relative area change

$$\Delta a/\bar{a} := \frac{a - \bar{a}}{\bar{a}} \tag{E.92}$$

as

$$a = \bar{a}\,(1 + \Delta a/\bar{a})\,, \tag{E.93}$$

which follows immediately from solving Eq. (E.92) for a. Using Eqs. (E.91), (E.93) and the chain rule, we calculate

$$\partial_x \sigma_{2\mathrm{D}} = -\partial_x \pi = -(\partial_a \pi)\partial_x a = -(\partial_a \pi)\,\bar{a}\,\partial_x(\Delta a/\bar{a}). \tag{E.94}$$

To simplify this expression, we note that the elastic modulus $K_{2\mathrm{D}}$ (the inverse of the compressibility) of the interface is defined by

$$K_{2\mathrm{D}} = -a\partial_a \pi, \tag{E.95}$$

and that the local relative area change is given in terms of the interfacial displacement field as [151]

$$\Delta a/\bar{a} = \partial_\beta u_{2\mathrm{D},\beta}|_{z=0} = \partial_x U, \tag{E.96}$$

where at the last equality sign we used that there is no displacement in the $\hat{e}_y$-direction, c.f. Eq. (E.84). Equations (E.95), (E.96) can then be used to rewrite Eq. (E.94) as

$$\partial_x \sigma_{2\mathrm{D}} = -(\partial_a \pi)\, \bar{a}\, \partial_x(\Delta a/\bar{a}) = -a\, (\partial_a \pi)\, \bar{a}/a\, \partial_x^2 U = \frac{K_{2\mathrm{D}}}{1+\partial_x U}\, \partial_x^2 U, \tag{E.97}$$

where at the last equality sign we used $\bar{a}/a = 1/(1+\Delta a/\bar{a}) = 1/(1+\partial_x U)$, c.f. Eqs. (E.92), (E.96).

As we will justify in Appendix E.4, we neglect nonlinear effects caused by the factor $1/(1+\partial_x U)$, so that Eq. (E.97) allows us to rewrite the boundary condition (E.90) as

$$\rho_{2\mathrm{D}} \partial_t^2 U = \left(\sigma_{\mathrm{III},z\alpha} - \sigma_{z\alpha}\right)\big|_{z=0} + K_{2\mathrm{D}} \partial_x^2 U. \tag{E.98}$$

If we now assume again that the velocities change on a smaller length scale away from the interface than in the direction of propagation, which we already assumed to obtain Eq. (E.86), and that dynamical stresses from the upper half-space $z > 0$ can be neglected, we can approximate the bulk media stress difference as

$$\begin{aligned}\left(\sigma_{\mathrm{III},zx} - \sigma_{zx}\right)\big|_{z=0} &= -\eta\, \left(\partial_x v_z + \partial_z v_x\right)\big|_{z=0} \approx -\eta \partial_z\, v_x\big|_{z=0} \\ &= -\eta \partial_t \partial_z\, u_x\big|_{z=0}\,. \end{aligned} \tag{E.99}$$

Inserting this into Eq. (E.98) and replacing $\partial_z u_x|_{z=0}$ using Eq. (E.89), the boundary condition Eq. (E.98) finally becomes

$$\rho_{2\mathrm{D}} \partial_t^2 U = -\sqrt{\eta\rho}\, \partial_t^{3/2} U + K_{2\mathrm{D}}\, \partial_x^2 U, \tag{E.100}$$

which is the fractional wave equation we use in Chapter 6. It is derived here as an approximate stress boundary condition at the interface, and momentum conservation in the bulk medium $z < 0$ has been used to eliminate the derivative ∂_z, so that the equation could be expressed solely in terms of the displacement field $\vec{u}$ at $z = 0$ and its spatial derivatives in the $\hat{e}_x$-direction, i.e. along the interface. The two approximations used here, Eqs. (E.86), (E.99), are of course motivated by the properties of the Lucassen wave discussed in Appendix E.1.

We note that with the present derivation, it is immediately clear how one could include the membrane shear viscosity in the derivation. One would simply not neglect the corresponding terms in the boundary condition, Eq. (E.31).

As a final remark, we note that the interfacial displacement in the $\hat{e}_z$-direction, $u_{2\mathrm{D},z}(x, z = 0, t)$, can be calculated from a solution of Eq. (E.100). After solving Eq. (E.100), the resulting $U(x,t) \equiv u_{2\mathrm{D},x}(x, z = 0, t)$ can be considered as inhomogeneity in the remaining boundary condition, Eq. (E.32), which can then be solved to obtain the displacement of the surface in the $\hat{e}_z$-direction.

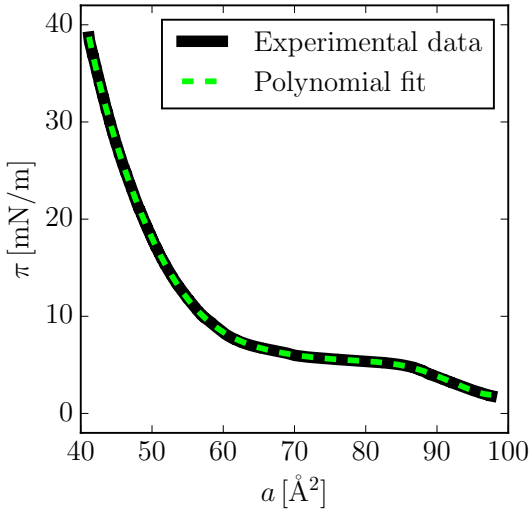

Figure E.4: Experimentally measured pressure-area isotherm together with polynomial fit. To calculate the elastic modulus K_{2D} for a DPPC monolayer on water, a polynomial (green dashed line) is fitted to the experimental isotherm (black solid line), c.f. Appendix E.3.

E.3 Numerical details for the calculation of the elastic modulus K_{2D}

In the present appendix, we give details for the calculation of the experimental isothermal elastic modulus K_{2D} from experimental data. Experimentally, a Langmuir isotherm $\pi(a)$, with π the surface pressure and a the area per lipid, is measured for a DPPC monolayer on water. The isothermal elastic modulus is then given by

$$K_{2D} = -a \left(\frac{\partial \pi}{\partial a} \right)_T . \tag{E.101}$$

To stably calculate the derivative on the right-hand side of this equation from the experimental data, we fit a polynomial of order 9 to the measured isotherm, see Fig. E.4, and use the analytical derivative of the fitted polynomial.

E.4 Discussion of the linearization assumption for momentum conservation

The nonlinear fractional wave equation we consider in Chapter 6 and derive in Appendix E.2 is motivated by the dispersion relation of the Lucassen wave, which in turn is derived using the linearized Navier-Stokes equation, c.f. Appendix E.1. We therefore rely on the assumption that the nonlinearity due to local changes in the elastic modulus K_{2D} is relevant, while the convective derivative term $(\vec{v} \cdot \vec{\nabla})\vec{v}$ of the velocity field, which appears in the full Navier-Stokes equation, is negligible. In this appendix, we want to underpin this assumption.

For this, we assume that the displacement field in the $\hat{e}_x$-direction at the interface, $u_x(x, z = 0, t) \equiv U(x, t)$, varies on a characteristic length scale L, and on a characteristic time scale T.

We first estimate the linearization condition for the Navier-Stokes equation,

$$|\partial_t^2 U| \gg |(\partial_t U)\partial_x(\partial_t U)|, \tag{E.102}$$

to be

$$\frac{|U|}{T^2} \gg \frac{|U|^2}{T^2 L}, \qquad \Longleftrightarrow \qquad 1 \gg \frac{|U|}{L}. \tag{E.103}$$

To estimate when nonlinear effects due to local changes in the elastic modulus become important, we consider Eq. (6.22),

$$K_{2\mathrm{D}} = K_{2\mathrm{D}}^{(0)} + K_{2\mathrm{D}}^{(2)} \left(\bar{a} + \bar{a}\partial_x U(x,t) - a_0\right)^2, \tag{E.104}$$

which gives the local elastic modulus as a function of the surface displacement field U. According to Eq. (6.23), nonlinear effects are negligible as long as the term linear in U in Eq. (E.104) is small compared to the term independent of U in Eq. (E.104), i.e., as long as

$$\left|2\bar{a}^2 K_{2\mathrm{D}}^{(2)}(1 - a_0/\bar{a})\partial_x U\right| \ll \left|K_{2\mathrm{D}}^{(0)} + \bar{a}^2 K_{2\mathrm{D}}^{(2)}(1 - a_0/\bar{a})^2\right|, \tag{E.105}$$

which leads to the estimate

$$\frac{|U|}{L} \ll \left|\frac{K_{2\mathrm{D}}^{(0)} + \bar{a}^2 K_{2\mathrm{D}}^{(2)}(1 - a_0/\bar{a})^2}{2\bar{a}^2 K_{2\mathrm{D}}^{(2)}(1 - a_0/\bar{a})}\right|. \tag{E.106}$$

Comparing this inequality to Eq. (E.103), we see that which nonlinearity becomes important first as the displacement U increases depends on the value of

$$f(\bar{a}) := \left|\frac{K_{2\mathrm{D}}^{(0)} + \bar{a}^2 K_{2\mathrm{D}}^{(2)}(1 - a_0/\bar{a})^2}{2\bar{a}^2 K_{2\mathrm{D}}^{(2)}(1 - a_0/\bar{a})}\right|. \tag{E.107}$$

if $f(\bar{a}) < 1$, the nonlinearity due to local variations in the elastic modulus is dominant, while for $f(\bar{a}) > 1$ the convective term appearing in the full Navier-Stokes equation is the dominant nonlinearity.

We plot f in Fig. E.5, and as can be seen, except for equilibrium areas $\bar{a}$ close to the minimum of the elastic modulus, f is of the order of 0.1, so that inequality (E.106) will be violated at amplitudes much lower than inequality (E.103). We therefore expect the nonlinearity arising from changes in the elastic modulus to become relevant approximately one order of magnitude below the convective nonlinearity in the Navier-Stokes equation. Thus, our premise of including one nonlinearity but not the other, is reasonable.

Note furthermore that inequality (E.103) is also the basis for neglecting the term $1/(1 + \partial_x U)$ in going from Eq. (E.97) to Eq. (E.98) in Appendix E.2, the justification for neglecting quadratic terms in the strain tensor [224], and is furthermore used in the derivation of Eq. (E.29) from Eq. (E.28).

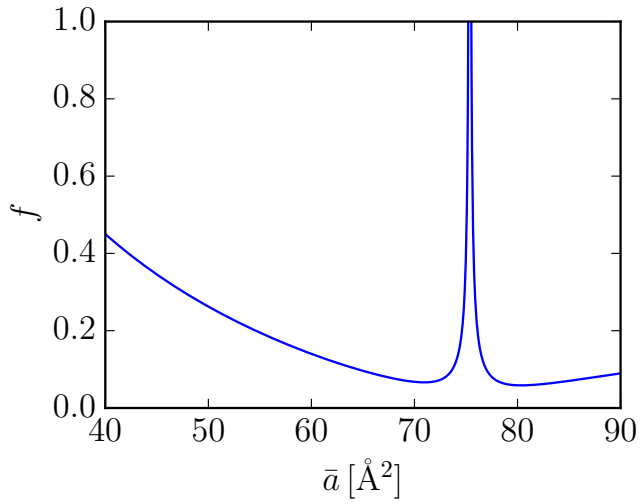

Figure E.5: Comparison of nonlinear effects from convective derivative in the Navier-Stokes equation and area per lipid dependence of the elastic modulus K_{2D}. The function f as defined by Eq. (E.107) is plotted as a function of equilibrium area per lipid $\bar{a}$. For the parameters appearing in f, the values from Chapter 6 are used, namely $K_{2D}^{(0)} = 2.55$ mN/m, $a_0 = 75.4\,\text{Å}^2$ and $K_{2D}^{(2)} = 0.12$ mN/(mÅ^2).

E.5 Isothermal vs. adiabatic elastic modulus

Throughout Chapter 6, we use the isothermal elastic modulus for the elastic modulus K_{2D} in the Lucassen dispersion relation and the fractional wave equation. Whether this is appropriate is a question of time scales. The isothermal elastic modulus is only appropriate if the compression and expansion of the interface during wave propagation is slow compared to the time scale of heat exchange with the bulk medium below, so that the temperature within the interface can be assumed to be constant. In the opposite limit, i.e., if the compression and expansion of the interface is so fast that there is no heat exchange during one oscillation, the adiabatic elastic modulus is the appropriate choice [229].

In the present appendix we discuss whether the thermodynamics of the interface during wave propagation is isothermal or adiabatic. We do this by comparing the time scale of heat conduction within the bulk medium below the membrane to the time scale of wave oscillations.

To estimate the time scale for heat conduction in the bulk medium, we consider the standard balance equation for the internal energy in the medium below the interface ($z < 0$), which in the absence of external forces reads

$$\rho \frac{\mathrm{d}e}{\mathrm{d}t} = \sigma_{ij} \partial_j v_i + \partial_i \left(\kappa \, \partial_i T \right), \tag{E.108}$$

where ρ is the density, e is the internal energy per unit mass, σ is the stress tensor and κ is the heat conduction coefficient. The first term on the right hand side of Eq. (E.108) models changes

in internal energy due to viscous dissipation, while the second term on the right hand side models changes in the internal energy due to heat conduction.

Neglecting the first term (c.f. Appendix E.4 and note that the first term is quadratic in the velocity) and using $\mathrm{d}e/\mathrm{d}t \approx \partial e/\partial t = c_p \partial T/\partial t$ with c_p the isobaric specific heat capacity (note that this is an approximation, as the pressure in the bulk medium is not strictly constant), we get

$$\rho c_p \frac{\partial T}{\partial t} = \partial_i \left(\kappa \, \partial_i T\right), \tag{E.109}$$

so that we obtain the relation

$$\tau_T \sim \frac{\rho c_p L^2}{\kappa}, \tag{E.110}$$

for the time scale τ_T in which temperature equilibrates over a length scale L. For water, the parameters are $c_p = 4\ \mathrm{kJ/(kg \cdot K)}$, $\rho = 10^3\ \mathrm{kg/m^3}$, $\kappa = 0.6\ \mathrm{J/(m \cdot s \cdot K)}$ [173]. We now use the relation (E.110) to compare the time scale of heat conduction in the fluid below the surface to the time scale of the Lucassen wave that propagates along the surface. For this, we use the dispersion relation

$$k(\omega) = e^{i\pi/8} \sqrt{\frac{\sqrt{\rho\eta\omega^3}}{K_{\mathrm{2D}}}} \tag{E.111}$$

of the Lucassen wave derived in Appendix E.1, see Eq. (E.58).

- First, we consider heat conduction parallel to the interface. The frequency dependent wave length of the Lucassen wave sets the length scale, and is given by

$$L = \frac{1}{\mathrm{Re}\left[k(\omega)\right]} = \frac{\sqrt{K_{\mathrm{2D}}}}{\cos(\pi/8)(\rho\eta\omega^3)^{1/4}}. \tag{E.112}$$

  Thus, the time scale for "parallel" thermal equilibration of the water below the surface is given by

$$\tau_T \sim \frac{\rho c_p K_{\mathrm{2D}}}{\kappa \cos^2(\pi/8)} \sqrt{\frac{\rho}{\eta\omega^3}}. \tag{E.113}$$

  This time scale is of the order of the time scale of oscillations, $\tau = 1/\omega$, if

$$\tau \sim \tau_T \tag{E.114}$$

$$\iff \qquad \omega \sim \frac{c_p^2 K_{\mathrm{2D}}^2 \rho}{\kappa^2 \eta \cos^4(\pi/8)} \approx 6 \cdot 10^9 \ \frac{1}{\mathrm{s}}, \tag{E.115}$$

  where we use $K_{\mathrm{2D}} \approx 10^{-2}\ \mathrm{N/m}$ as an order-of-magnitude estimate for the elastic modulus. For smaller frequencies, the time scale of thermal diffusion parallel to the surface is larger than the time scale of oscillations ($\tau < \tau_T$, adiabatic), while for larger frequencies, the time scale of thermal diffusion parallel to the surface is smaller than the time scale of oscillations ($\tau > \tau_T$, isothermal).

- Second, we consider heat conduction perpendicular to the interface. The relevant length scale is the decay length of the wave away from the interface (i.e., the distance of the oscillating surface to the "bulk water reservoir"), which for the Lucassen wave is given by

$$L = \frac{1}{\mathrm{Re}(\lambda_t^{-1})} = \sqrt{\frac{2\eta}{\rho\omega}}, \tag{E.116}$$

c.f. Eq. (E.47) (and note that the factorization condition (E.46) holds for a Lucassen wave on water, as discussed in Appendix E.1.5). Comparing the resulting time scale for heat conduction with the time scale of oscillations, $\tau = 1/\omega$, we obtain

$$\tau \sim \tau_T \tag{E.117}$$

$$\iff \qquad 1 \sim \frac{c_p \eta}{\kappa} \approx 13. \tag{E.118}$$

Since both time scales have the same frequency dependence, the crossover is independent of ω, and only depends on the system parameters. Because Eq. (E.110) is only a rough estimate, we conclude from Eq. (E.118) that there is no clear separation of the time scales τ, τ_T.

From these order-of-magnitude estimates, we conclude that for water, heat conduction parallel to the surface can be ignored, while heat conduction away from the surface happens on a time scale comparable to the wave oscillations. Thus, the elastic modulus $K_{2\mathrm{D}}$ appropriate for the Lucassen wave is neither isothermal nor adiabatic, but somewhere in between.

For simplicity and because it is experimentally readily accessible, we use the isothermal elastic modulus in Chapter 6, but in view of the estimates performed in the present appendix, this is clearly an approximation.

E.6 Analytical solution of linear theory

In the present appendix we consider the linearized fractional wave equation, Eq. (6.17) with $\rho_{2\mathrm{D}} = 0$,

$$K_{2\mathrm{D}} \frac{\partial^2 U}{\partial x^2} = \sqrt{\rho\eta}\, \frac{\partial^{3/2} U}{\partial t^{3/2}}. \tag{E.119}$$

This is a fractional wave equation, i.e., a wave equation where the second order time derivative has been replaced by a fractional derivative $\alpha \in (1, 2]$, which in our case is $\alpha = 3/2$. The fundamental solution (also called propagator or Green function) to the fractional wave equation was first derived by Schneider and Wyss in the 80s [222], the derivation was later simplified by Mainardi [203, 223].

We follow Ref. [203] to discuss the signaling problem for Eq. (E.119), which is the appropriate boundary value problem for the experimental setup we want to model. In Ref. [203], the signaling

problem is defined as the boundary value problem

$$\frac{\partial^{2\nu} U}{\partial t^{2\nu}} = D_0 \frac{\partial^2 U}{\partial x^2} \qquad \forall (x,t) \in [0,\infty) \times [0,\infty), \tag{E.120}$$

$$U(x,0) = 0 \qquad \forall x \in (0,\infty), \tag{E.121}$$

$$U(0,t) = U_0(t) \qquad \forall t \in (0,\infty), \tag{E.122}$$

$$U(\infty,t) = 0 \qquad \forall t \in (0,\infty), \tag{E.123}$$

where $U_0(t)$ is a given function that models a time dependent excitation at the boundary $x = 0$. In view of Eq. (E.119), we will later set $D_0 = K_{2\mathrm{D}}/\sqrt{\rho\eta}$ and will be interested in the case $\nu = 3/4$. For the sake of generality, we quote here the results for arbitrary $\nu \in (0,1)$. For the particular choice $U_0(t) = \delta(t)$, the solution is called the fundamental solution and written $\mathcal{G}_s(x,t;\nu)$. Given any other function $U_0(t)$, the respective solution to the signaling problem is then given as linear superposition of fundamental solutions, as

$$U(x,t;\nu) = \int_{0^-}^{t^+} \mathcal{G}_s(x, t-\tau;\nu) U_0(\tau)\, \mathrm{d}\tau, \tag{E.124}$$

see Eq. (6.9b) of Ref. [203]. According to Chapter 6 of Ref. [203], $\mathcal{G}_s$ is given by

$$\mathcal{G}_s(x,t;\nu) = \frac{\nu x}{t^{1+\nu}\sqrt{D_0}} M_\nu\left(\frac{x}{t^\nu \sqrt{D_0}}\right), \tag{E.125}$$

where $M_\nu(z)$ is given by the power series

$$M_\nu(z) = \frac{1}{\pi} \sum_{n=1}^{\infty} \frac{(-z)^{n-1}}{(n-1)!} \Gamma(\nu n) \sin(\pi \nu n), \tag{E.126}$$

with Γ the Gamma function.

Although the power series (E.126) converges for all $z \in \mathbb{C}$, convergence is slowing down as $|z|$ increases. For that reason, Ref. [203] gives the asymptotic formula

$$M_\nu(\xi/\nu) \sim A_\nu(\xi/\nu) := \frac{\xi^{(\nu-1/2)/(1-\nu)}}{\sqrt{2\pi(1-\nu)}} \exp\left[-\frac{1-\nu}{\nu}\xi^{1/(1-\nu)}\right], \tag{E.127}$$

valid for $|\xi/\nu|$ large. Since for us, the case $\nu = 3/4$ with real z is most relevant, in Fig. E.6 we plot the function $M_{3/4}(x)$ as calculated from the power series Eq. (E.126), together with the asymptotic formula $A_{3/4}(x)$, Eq. (E.127). As stopping criterion for the numerical summation of the power series (E.126), we use that the relative change of the absolute value of the partial sum should be smaller than 10^{-8}, i.e., we sum in Eq. (E.126) until term number

$$N := \inf\left\{ K \in \mathbb{N} \;\middle|\; \frac{|z|^K \Gamma(3/4 \cdot (K+1))/K!}{\pi |M_{3/4}^K(z)|} < 10^{-8} \right\} + 1, \tag{E.128}$$

where $M_{3/4}^K(z)$ is the partial sum of the power series in Eq. (E.126) (for $\nu = 3/4$) up to the K-th term. The calculations are performed at 500 digit floating point precision using the python module mpmath [226]. From Fig. E.6 we conclude that the asymptotic formula approximates $M_{3/4}(x)$ well for $x > 4$, meaning that the relative error $|A_{3/4}(x) - M_{3/4}(x)|/|M_{3/4}(x)| < 0.1\%$ for $x > 4$. For all subsequent numerical evaluations of $M_{3/4}(x)$ we therefore proceed as follows. Using Eq. (E.126), we pre-calculate a table of values for $M_{3/4}$ on the grid

$$\left\{ i \cdot \Delta x \mid \Delta x = 0.001,\ i \in \{0, 1, ..., 4 \cdot 10^3\} \right\}, \tag{E.129}$$

and then use linear interpolation on that dataset to evaluate $M_{3/4}(x)$ for $0 \leq x \leq 4$. For $x > 4$, we use the asymptotic formula (E.127).

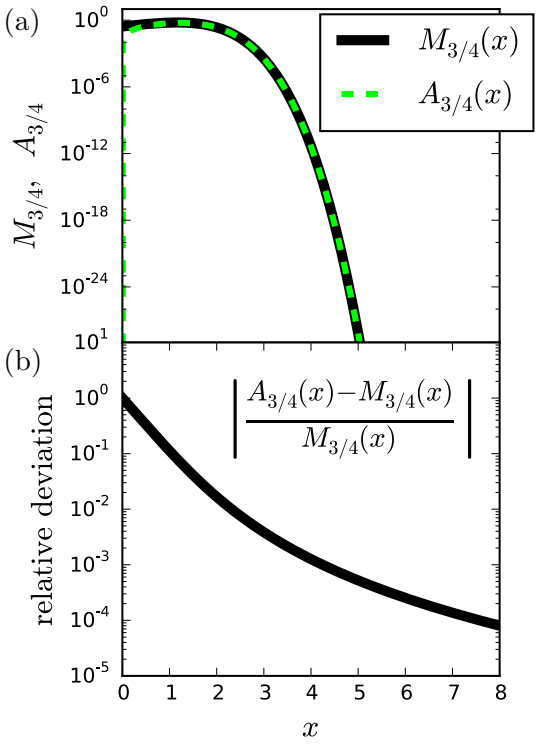

Figure E.6: (a) The functions $M_{3/4}$, $A_{3/4}$ as defined in Eqs. (E.126), (E.127); (b) The relative deviation $|A_{3/4} - M_{3/4}|/|M_{3/4}|$ of the asymptotic expansion $A_{3/4}$ to $M_{3/4}$.

E.7 Numerical algorithm for solving the nonlinear fractional wave equation

E.7.1 Introduction

In the present appendix, we present and validate a numerical scheme for solving the nonlinear fractional wave equation Eq. (6.23). More specifically, we discuss a nonlinear version of the signaling problem from Appendix E.6, i.e., we consider the boundary value problem

$$\frac{\partial^{2\nu} U}{\partial t^{2\nu}} = D(\partial_x U)\frac{\partial^2 U}{\partial x^2} \qquad \forall (x,t) \in [0,L]\times[0,\infty), \tag{E.130}$$

$$U(x,0) = (\partial_t U)(x,0) = 0 \qquad \forall x \in (0,L), \tag{E.131}$$

$$U(0,t) = U_0(t) \qquad \forall t \in (0,\infty), \tag{E.132}$$

$$U(L,t) = U_L(t) \qquad \forall t \in (0,\infty), \tag{E.133}$$

where U_0, U_L are given functions that model imposed displacements at the boundaries of a system of length L. While U_0 will model a mechanical excitation at $x = 0$, U_L will be set to zero later to model a rigid wall at $x = L$. D is a function that depends on $\partial_x U$ locally, i.e., $D(\partial_x U)(x) = D(\partial_x U(x))$, and if it is not constant, then Eq. (E.130) is nonlinear. While we state the algorithm for an arbitrary function D, in view of Eq. (6.23) we will later be interested in the case where D is of the form

$$D(\partial_x U) = \frac{K_{\mathrm{2D}}^{(0)} + K_{\mathrm{2D}}^{(2)}\left(\bar{a} + \bar{a}\partial_x U - a_0\right)^2}{\sqrt{\rho\eta}}. \tag{E.134}$$

For the sake of generality, we furthermore state the algorithm for arbitrary fractional derivative $\nu \in (1/2, 1)$, although we will later be interested in the case $\nu = 3/4$.

Before starting, we remark that, apart from the nonlinearity, the only difference between Eqs. (E.120)-(E.123) and Eqs. (E.130)-(E.133) is that, while in the former the spatial domain is $[0,\infty)$, in the present section we assume a bounded domain $[0, L]$. The reason for this is that a numerical solution can only be calculated on a finite domain, and that there seems to be no satisfactory way to implement free boundary conditions numerically. Our approach therefore is to calculate the numerical solution on a finite domain $[0, L]$ with boundary condition $U_L(t) \equiv 0$, and to choose L large enough so that for a subinterval $[0, l]$ with $l \ll L$ we can effectively speak of free boundary conditions at $x = l$. We discuss an appropriate choice for L for our system in Appendix E.8.5, by comparing numerical solutions for the linear theory to the analytical solution from Appendix E.6.

E.7.2 Methods

To solve the boundary value problem given by Eqs. (E.130)-(E.133) numerically, we discretize the equation in time and space and use the backward Euler-method to calculate the time evolution of the displacement field.

For the temporal discretization we follow Li et al. [225], where a numerical scheme for a class of nonlinear fractional wave equations (which does not include Eq. (E.130)) is presented. In the reference, the authors discretize time with a timestep Δt, and only consider $U(x,t)$ at times

$$t_j := j \cdot \Delta t \qquad j \in \mathbb{N}. \tag{E.135}$$

To discretize the fractional derivative [203],

$$\frac{\partial^{2\nu} U}{\partial t^{2\nu}}(x,t) = \frac{1}{\Gamma(1-2\nu)} \int_0^t \left[\frac{\partial^2}{\partial \tau^2} U(x,\tau)\right] \frac{1}{(t-\tau)^{2\nu-1}}\, \mathrm{d}\tau, \tag{E.136}$$

with Γ the Gamma function, they approximate the second derivative of $U(x,t)$ using the center difference scheme, and take this second derivative to be constant in each interval (t_j, t_{j+1}). Then, after writing the integral on the right-hand side of Eq. (E.136) as a sum over integrals over all the subintervals (t_j, t_{j+1}), these can be evaluated to obtain the approximate formula

$$\frac{\partial^{2\nu} U}{\partial t^{2\nu}}(x,t_{m+1}) = \frac{(\Delta t)^{-\alpha}}{\Gamma(3-\alpha)} \left(-\omega_0 U(x,t_{m+1}) - \sum_{j=-1}^{m} b_j^m U(x,t_m) \right), \tag{E.137}$$

where the scalars b_j^m are defined as

$$b_j^m := \begin{cases} -\omega_m & j = -1, \\ 2\omega_m - \omega_{m-1} & j = 0, \\ -\omega_{m-j+1} + 2\omega_{m-j} - \omega_{m-j-1} & 1 \le j \le m-1, \\ -\omega_1 + 2\omega_0 & j = m, \end{cases} \tag{E.138}$$

with

$$\omega_j := (j+1)^{2(1-\nu)} - j^{2(1-\nu)}. \tag{E.139}$$

The initial conditions enter Eq. (E.137) via $U(x,0)$ and

$$U(x,t_{-1}) := U(x,0) - \Delta t (\partial_t U)(x,0). \tag{E.140}$$

In our particular situation, both $U(x,t)$ and $U(x,t_{-1})$ are zero, c.f. Eq. (E.131).

To discretize space, we divide the interval $[0,L]$ into $N+1$ subintervals of equal length $\Delta x := L/(N+1)$. The $N+2$ boundary points of these subintervals are then given by the positions

$$x_j := j \cdot \Delta x \qquad j \in \{0, ..., N+1\}. \tag{E.141}$$

We discretize the second order spatial derivative in Eq. (E.130) using the center difference scheme, i.e. we approximate

$$\frac{\partial^2 U}{\partial x^2}(x_n,t) = \frac{U(x_{n+1},t) - 2U(x_n,t) + U(x_{n-1},t)}{\Delta x^2}. \tag{E.142}$$

Note that $U(x_0, t)$, $U(x_{N+1}, t)$ are given by the spatial boundary conditions,

$$U(x_0, t) \equiv U_0(t), \tag{E.143}$$
$$U(x_{N+1}, t) \equiv U_L(t). \tag{E.144}$$

Since we want to calculate $U(x, t)$ on the grid (x_n, t_m), we introduce the notation

$$U_n^m := U(x_n, t_m). \tag{E.145}$$

With this notation, and using Eqs. (E.137), (E.142), we obtain a discretized version of Eq. (E.130), given by

$$\left(\omega_0 \mathbb{I}_{N,N+2} + \lambda W\left(\vec{U}^{m+1}\right)\right)\vec{U}^{m+1} = \sum_{j=-1}^{n} b_j^n \vec{U}^m, \tag{E.146}$$

where

$$\lambda = \frac{\Gamma(3-2\nu)(\Delta t)^{2\nu}}{\Delta x^2}, \tag{E.147}$$

the $N+1$ dimensional vector $\vec{U}^k$ describing the discretized displacement field at time t_k is given by

$$\vec{U}^k := \begin{pmatrix} U_0^k \\ U_1^k \\ \vdots \\ U_N^k \\ U_{N+1}^k \end{pmatrix} \qquad k \in \mathbb{N}, \tag{E.148}$$

and the two $N \times (N+2)$ matrices $\mathbb{I}_{N,N+2}$, W are given by

$$\mathbb{I}_{N,N+2} := \begin{pmatrix} 0 & 1 & 0 & 0 & & \cdots & 0 & 0 \\ 0 & 0 & 1 & 0 & 0 & & \vdots & 0 \\ \vdots & 0 & 0 & 1 & 0 & \ddots & \vdots & \vdots \\ \vdots & & \ddots & 0 & \ddots & \ddots & 0 & \vdots \\ \vdots & & & \ddots & \ddots & \ddots & 0 & 0 \\ 0 & \cdots & \cdots & \cdots & 0 & 0 & 1 & 0 \end{pmatrix} \in \mathbb{R}^{N\times(N+2)}, \tag{E.149}$$

$$W(\vec{U}^m) := \begin{pmatrix} -W_1(\vec{U}^m) & 2W_1(\vec{U}^m) & -W_1(\vec{U}^m) & 0 & & \cdots & 0 & 0 \\ 0 & -W_2(\vec{U}^m) & 2W_2(\vec{U}^m) & -W_2(\vec{U}^m) & 0 & & \vdots & 0 \\ \vdots & 0 & -W_3(\vec{U}^m) & 2W_3(\vec{U}^m) & -W_3(\vec{U}^m) & \ddots & \vdots & \vdots \\ \vdots & & \ddots & -W_4 & \ddots & \ddots & 0 & \vdots \\ \vdots & & & \ddots & \ddots & \ddots & -W_{N-1}(\vec{U}^m) & 0 \\ 0 & \cdots & \cdots & \cdots & 0 & W_N(\vec{U}^m) & 2W_N(\vec{U}^m) & W_N(\vec{U}^m) \end{pmatrix} \in \mathbb{R}^{N\times(N+2)}, \tag{E.150}$$

with

$$W_i(\vec{U}^m) = D\left(\frac{U^m_{i+1} - U^m_{i-1}}{2\Delta x}\right), \tag{E.151}$$

where we use the symmetric approximation $\partial_x U(x_i, t_m) = (U^m_{i+1} - U^m_{i-1})/(2\Delta x)$ for the derivative in the argument of D.

Note that while the vector $\vec{U}^k$ defined in Eq. (E.148) has $N+2$ elements, at every timestep only N of them are unknown because U^k_0, U^k_{N+1} are fixed by the spatial boundary conditions according to (E.143), (E.144). The discretized equation (E.146) is an equation for the N remaining components of $\vec{U}^k$ at every timestep.

E.7.3 Special case: Linear theory

If we assume D to be constant,

$$D(\partial_x U) \equiv D_0 \equiv const. \in (0, \infty), \tag{E.152}$$

the matrix $W\left(\vec{U}^{m+1}\right)$ as defined in Eqs. (E.150), (E.151), is independent of $\vec{U}^{m+1}$ and given by

$$W = D_0 \begin{pmatrix} -1 & 2 & -1 & 0 & & \cdots & & 0 & 0 \\ 0 & -1 & 2 & -1 & 0 & & & & \\ & 0 & -1 & 2 & -1 & \ddots & & \vdots & \vdots \\ \vdots & & \ddots & -1 & \ddots & \ddots & \ddots & & \vdots \\ \vdots & \vdots & & \ddots & \ddots & \ddots & -1 & 0 & \\ & & & & 0 & -1 & 2 & -1 & 0 \\ 0 & 0 & & \cdots & & 0 & -1 & 2 & -1 \end{pmatrix}, \tag{E.153}$$

as can easily be verified from the definition of the matrix elements, Eq. (E.151). Thus, Eq. (E.146) becomes linear and is given by

$$\left(\omega_0 \mathbb{I}_{N,N+2} + \lambda W\right) \vec{U}^{m+1} = \sum_{j=-1}^{n} b_j^n \vec{U}^m. \tag{E.154}$$

E.8 Linear theory: Comparison of analytical and numerical results

E.8.1 Introduction

To validate the numerical algorithm from Appendix E.7, we consider the linearized fractional wave equation, i.e., the situation where $\nu = 3/4$ and

$$D_0 \equiv \frac{K_{2\mathrm{D}}}{\sqrt{\rho\eta}} \equiv const., \tag{E.155}$$

with $K_{2\mathrm{D}}$ constant, c.f. Eqs. (E.134), (E.152). For water, $\rho = 10^3\ \mathrm{kg/m^3}$, $\eta = 10^{-3}\ \mathrm{Pa \cdot s}$. In this appendix, we compare the analytical solution of the signaling problem, defined by Eqs. (E.120)-(E.123), to the numerical solution of Eqs. (E.130)-(E.133).

Note that in the linear case, the only difference between the two boundary value problems is the right boundary. In the analytical solution, the spatial domain is $[0, \infty)$ with spatial boundary conditions $U(0,t) = U_0(t)$, $U(\infty, t) = 0$, with U_0 a given function, c.f. Eqs. (E.122), (E.123). In the numerical scheme, the spatial domain is the bounded interval $[0, L]$ with spatial boundary conditions $U(0,t) = U_0(t)$, $U(L,t) = U_L(t)$, with U_0, U_L given functions, c.f. Eqs. (E.132), (E.133).

Although every experimental system is of finite size, it is usually chosen large enough so that boundary effects from the walls are not relevant, meaning we are actually interested in the solution on an infinite spatial domain, as in the analytical solution. We expect that if we choose the right boundary condition in the numerical approach to be zero identically, $U_L(t) \equiv 0$, and we use an interval $[0, L]$ so large that, during the simulation time T, a field U excited at the left boundary does not reach the right boundary (so that there is no reflection), and only consider the values of $U(x,t)$ for $x \in (0, l)$ with $l \ll L$ (sufficiently far away from the rigid wall at $x = L$), then we expect the numerical scheme to yield a solution comparable to the analytical one from Appendix E.6.

E.8.2 Parameters

Throughout this work, we use the parameters

$$L = 30\ \mathrm{mm}, \tag{E.156}$$

$$\Delta x = 0.1\ \mathrm{mm}, \tag{E.157}$$

$$\Delta t = 0.01\ \mathrm{ms} \tag{E.158}$$

for numerical solution of the fractional wave equation, while analytical solutions are directly evaluated on a lattice with the same spacings Δx, Δt.

The right boundary condition is set to zero in all numerical calculations, $U_L(t) \equiv 0$, for the left boundary condition we use a normalized discretized delta peak, i.e.

$$U_0^j \overset{(E.143)}{=} U_0(j \cdot \Delta t) := \delta_{j,1} \frac{1}{\Delta t}. \tag{E.159}$$

Accordingly, the analytical solution is always calculated using a delta peak initial condition at $x = 0$, i.e. using the propagator $\mathcal{G}_s(x, t; \nu)$ from Appendix E.6.

We only consider the numerical solution for $x \leq 10\ \mathrm{mm} =: l$, so that $l/L = 1/3$, and up to times $T = 100$ ms.

In the following subsections, we validate our choices for L, l, T, as well as for the discretization parameters Δx, Δt, by comparing numerical and analytical solutions.

E.8.3 Position and time dependence of solutions at fixed $K_{2\mathrm{D}}$

Using the parameters from Appendix E.8.2, we first compare numerical and analytical solutions for

$$K_{2\mathrm{D}} \in \{1,\ 10,\ 100\}\ \mathrm{mN/m}. \tag{E.160}$$

Figure E.7 shows the displacement fields at $x = 5$ mm and $x = 10$ mm as a function of time. Although there are deviations when the displacement field has almost decayed (subplot (d) at $t = 150$-200 ms and subplot (f) around $t = 40$ ms), overall the displacement fields of numerical and analytical solutions agree very well.

Figure E.8 shows both the maximal displacement,

$$U^{\max}(x) := \max_t \{\ U(x,t)\ \}, \tag{E.161}$$

and the time elapsed until this maximal displacement occurs,

$$t^{\max}(x) := \min_t \{\ U(x,t) = U^{\max}(x)\ \}, \tag{E.162}$$

as a function of x, the distance from the left boundary. There are some deviations between numerical and analytical results close to the delta peak initial condition, namely for $x \lesssim 0.3$ mm, but for $x \gtrsim 1\ \mathrm{mm}$ the solutions agree very well.

Figure E.9 shows the compression fields, defined as

$$-U_x(x,t) = -\frac{\partial U}{\partial x}(x,t), \tag{E.163}$$

calculated from the numerical solutions shown in Fig. E.7. Agreement between numerical and analytical solutions is excellent here. Note that the times t at which deviations occurred in Fig. E.7 are not shown here for better visibility of the main peaks (at $t = 20$ ms in subplot (d) and $t = 4$ ms in subplot (f)). However, since the numerical and analytical curves in Fig. E.7 have

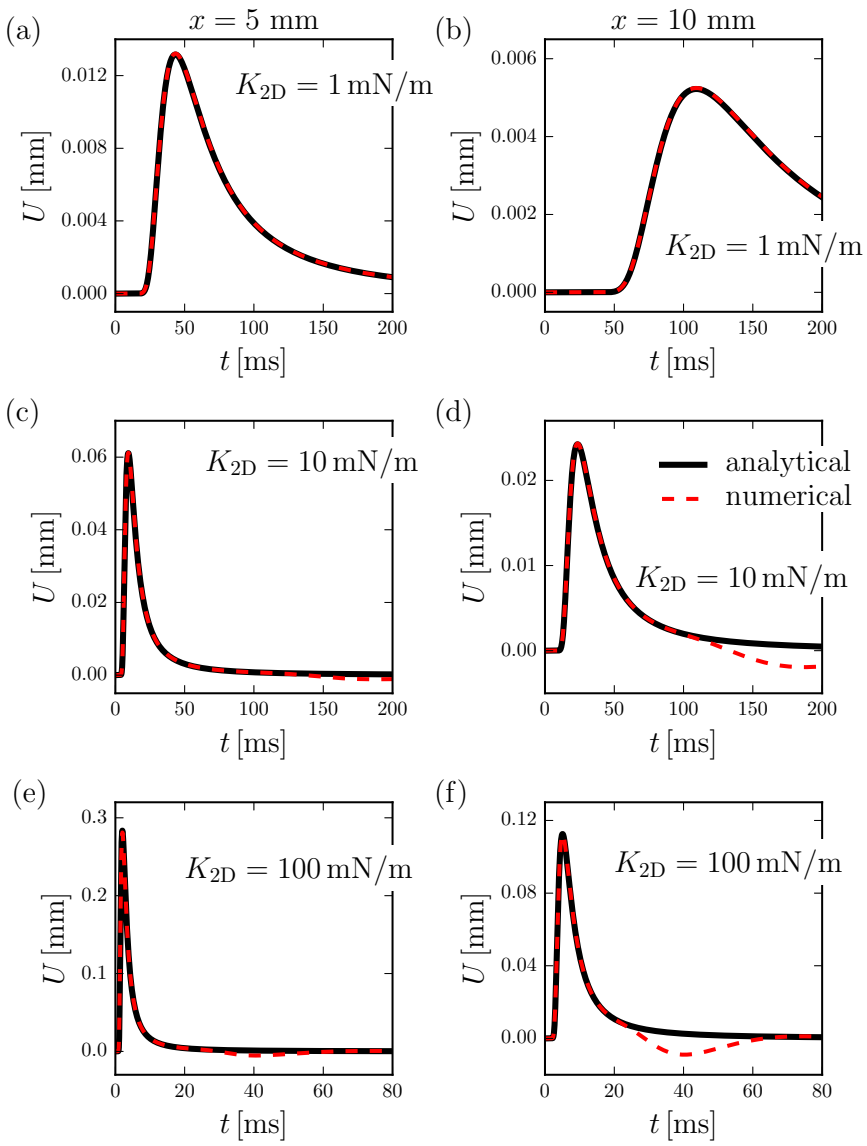

Figure E.7: Displacement fields as calculated from the analytical and numerical solution to the linear fractional wave equation. The parameters given in Appendix E.8.2 are used to calculate both the analytical and the numerical solution for elastic moduli $K_{2D} = 1, 10, 100$ mN/m. The respective solutions $U(x,t)$ are shown here as a function of time for $x = 5$ mm (left column) and $x = 10$ mm (right column).

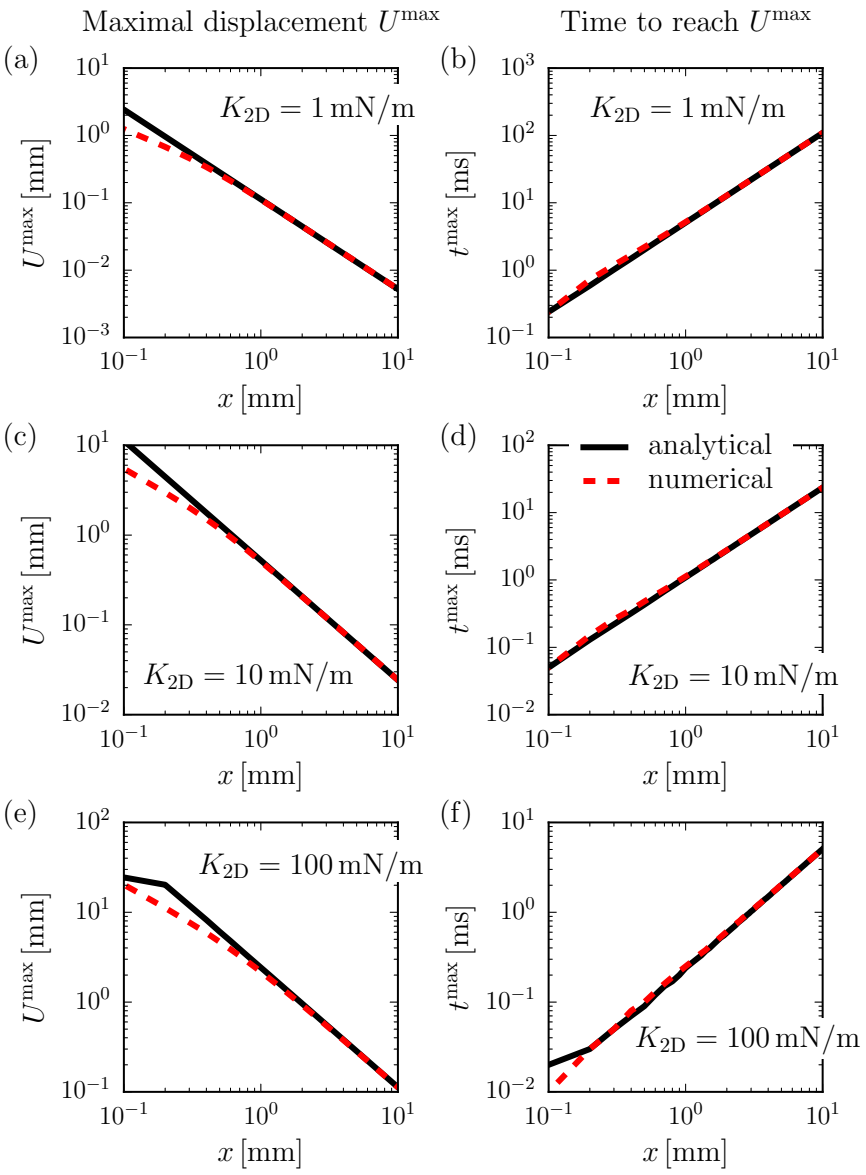

Figure E.8: Maximal displacement and time needed until maximal displacement occurs as calculated from analytical and numerical solution of the linear fractional wave equation. The parameters given in Appendix E.8.2 are used to calculate both the analytical and the numerical solution for elastic moduli $K_{2D} = 1$, 10, 100 mN/m. Using the respective solutions and Eqs. (E.162), (E.162), the maximal displacement as a function of position and the time elapsed until this displacement occurs are calculated and shown here as functions of position x.

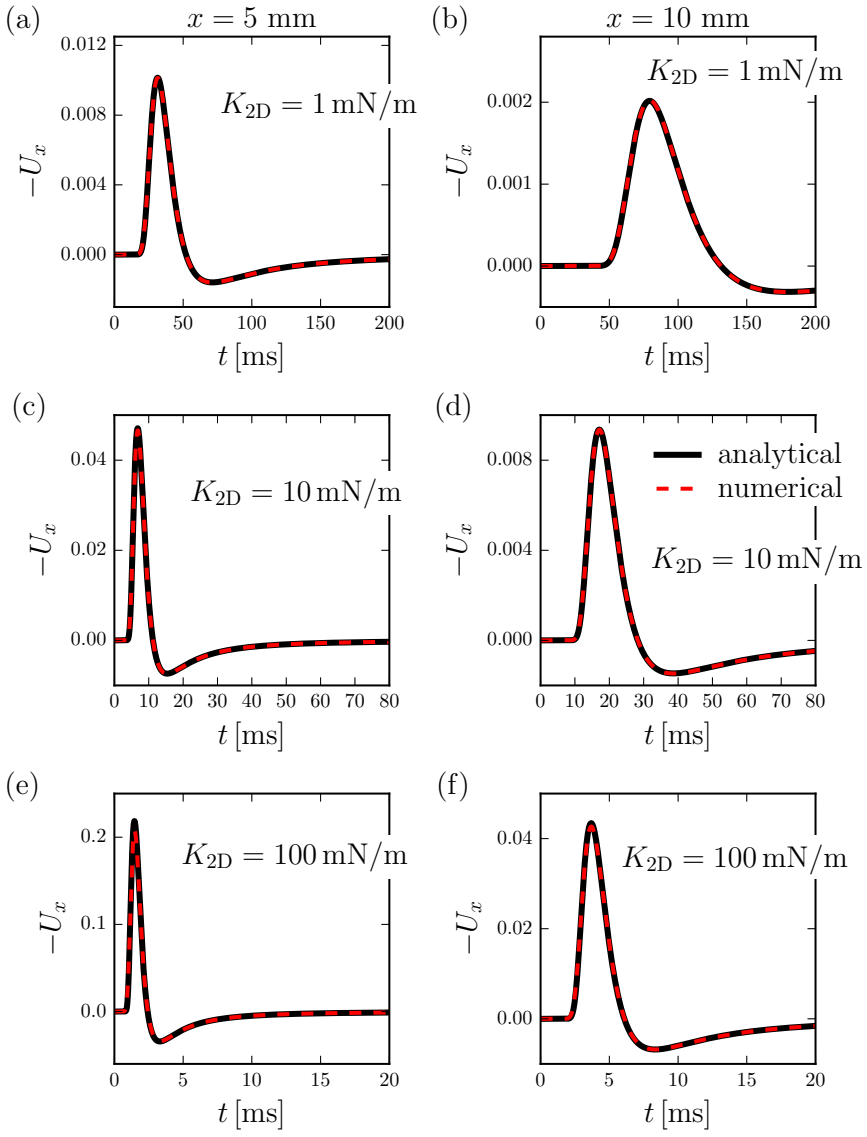

Figure E.9: Compression fields as function of time as calculated from analytical and numerical solution of the linear fractional wave equation. The parameters given in Appendix E.8.2 are used to calculate both the analytical and the numerical solution for elastic moduli $K_{2D} = 1$, 10, 100 mN/m. Using the respective solutions and Eq. (E.163), the compression field $-\partial_x U$ is calculated and shown here as a function of time for $x = 5$ mm (left column) and $x = 10$ mm (right column).

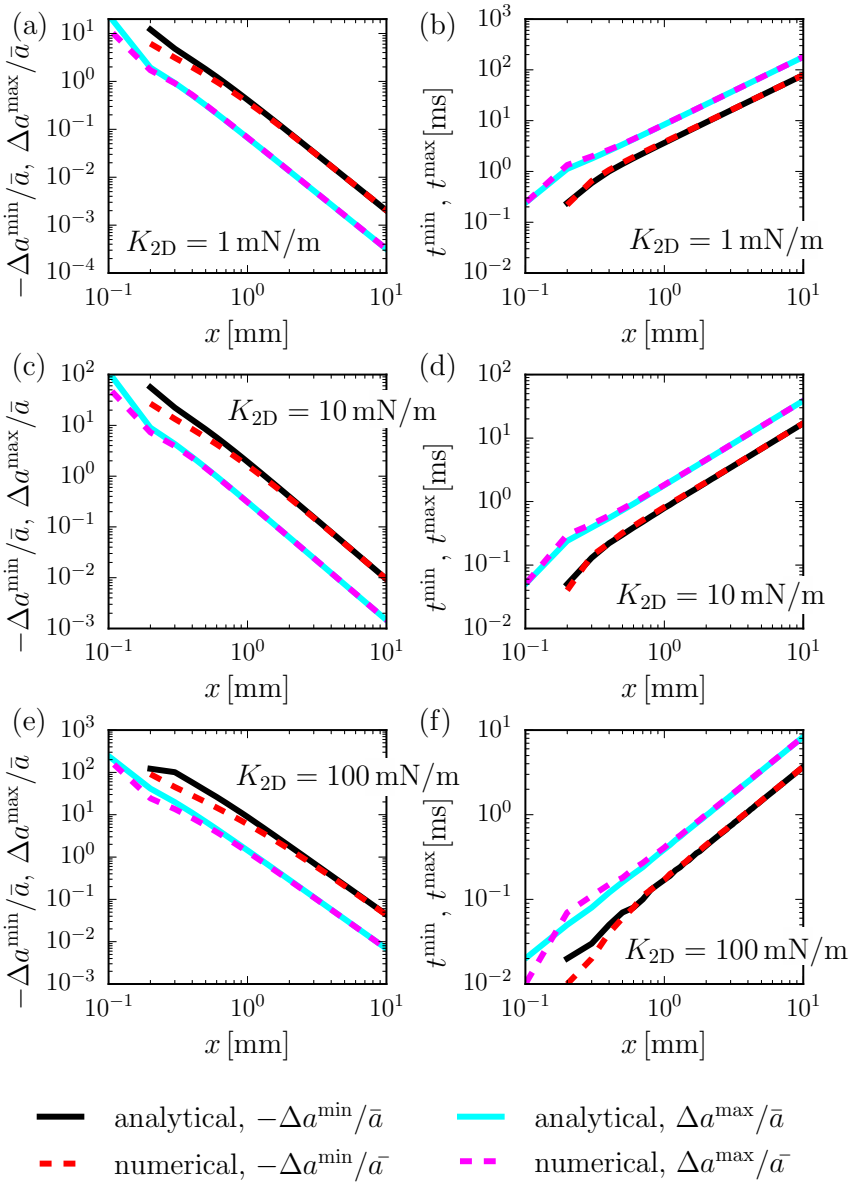

Figure E.10: Maximal compression and expansion as well as time elapsed until these extremal values occur, as calculated from analytical and numerical solutions of the linear fractional wave equation. The parameters given in Appendix E.8.2 are used to calculate both the analytical and the numerical solution for elastic moduli $K_{2D} = 1$, 10, 100 mN/m. Using the respective solutions and Eqs. (E.164)-(E.167), maximal compression $-\Delta a^{\min}/\bar{a}$ and maximal expansion $\Delta a^{\max}/\bar{a}$, as well as the time elapsed until these occur are calculated and shown here as functions of position x.

comparable slopes in the region where they deviate, the compression fields look quite similar even for the times where the displacement fields deviate.

Figure E.10 shows both the extremal values of compression and expansion,

$$(-\Delta a^{\min}/\bar{a})(x) := \min_t \{\, \partial_x U(x,t) \,\}, \tag{E.164}$$

$$(\Delta a^{\max}/\bar{a})(x) := \max_t \{\, \partial_x U(x,t) \,\}, \tag{E.165}$$

and the time until these extremal values occur,

$$t^{\min}(x) := \min_t \left\{\, -\partial_x U(x,t) = (-\Delta a^{\min}/\bar{a})(x) \,\right\}, \tag{E.166}$$

$$t^{\max}(x) := \min_t \{\, \partial_x U(x,t) = (\Delta a^{\max}/\bar{a})(x) \,\}, \tag{E.167}$$

as a function of x. Close to the left boundary, there are deviations between numerical and analytical predictions, but for $x \gtrsim 1$ mm agreement is perfect.

In summary, except for small distances $x \lesssim 1$ mm from the left boundary condition that are comparable to the spatial discretization $\Delta x = 0.1$ mm, the numerical and analytical results agree very well, validating both our numerical algorithm and our parameter choices for L, Δx, Δt.

E.8.4 Elastic modulus dependence of maximal compression and wave velocity at fixed position x

As a further check of consistency between numerical and analytical solution, we calculate the solutions for elastic moduli in the range

$$10^{-1} \leq \frac{K_{2\mathrm{D}}}{\mathrm{mN/m}} \leq 10^3, \tag{E.168}$$

and subsequenctly calculate both the maximal compression/expansion, as defined in Eqs. (E.164), (E.165), at distances $x = 1, 5, 9$ mm, as well as the compression wave velocities, defined as

$$c^{\min}(x) = \frac{x}{t^{\min}(x)}, \tag{E.169}$$

$$c^{\max}(x) = \frac{x}{t^{\max}(x)}, \tag{E.170}$$

where $t^{\min}$, $t^{\max}$ are the times elapsed until the extremal compression occurs, c.f. Eqs. (E.166), (E.167). The results are shown in Fig. E.11. Except for the smallest distance $x = 1$ mm at small elastic moduli $K_{2\mathrm{D}} \lesssim 1\,\mathrm{mN/m}$, numerical and analytical results agree very well.

E.8.5 Conclusion

Based on the comparison between numerical and analytical solution carried out in Appendices E.8.3, E.8.4, we conclude that our numerical algorithm works reliably and that our choice

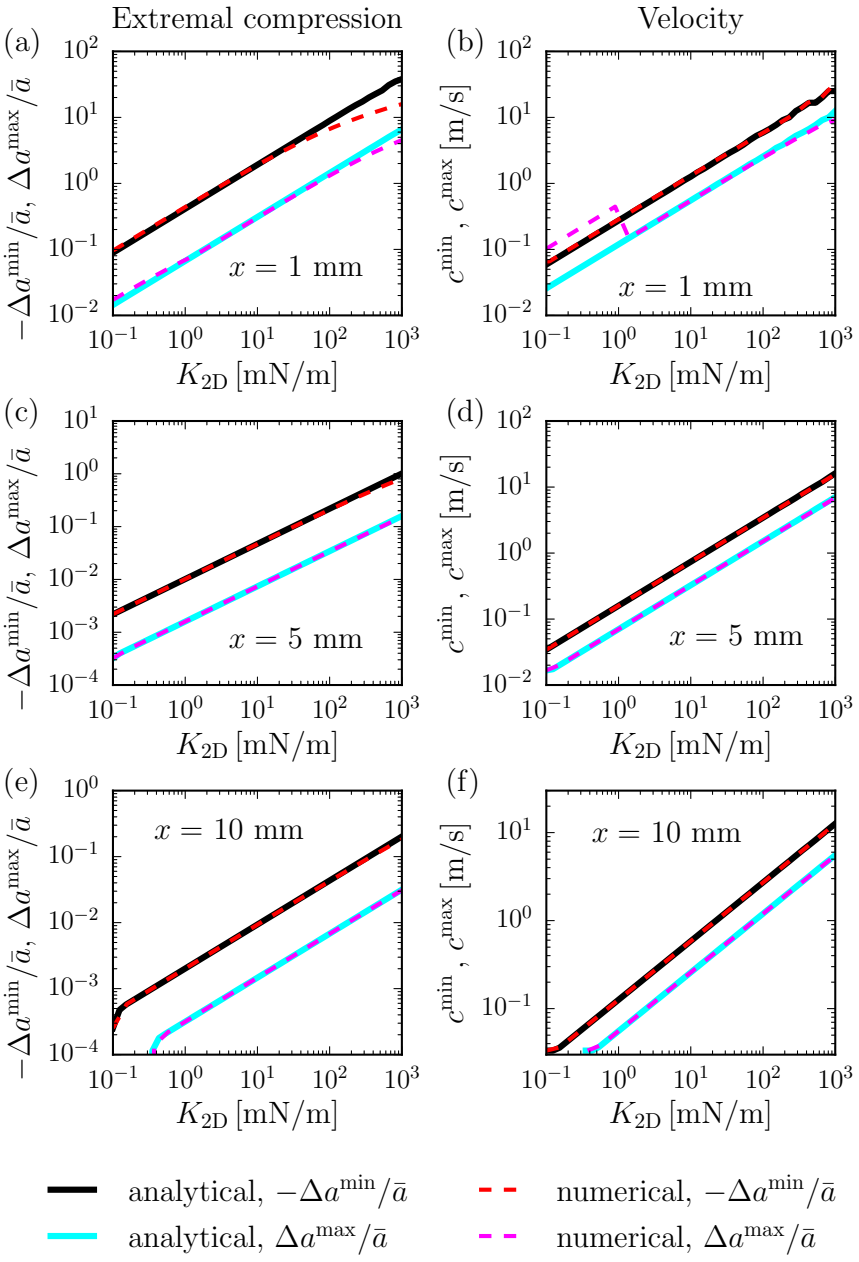

Figure E.11: Dependence of analytical and numerical solution of the linear fractional wave equation on the elastic modulus. The parameters given in Appendix E.8.2 are used to calculate both the analytical and the numerical solution for elastic moduli between $K_{2D} = 0.1$ mN/m and $K = 1000$ mN/m. Using these solutions and Eq. (E.163), first the compression field $-U_x$ is calculated. From the compression field, extremal values and propagation velocities for positions $x = 1, 5, 10$ mm are subsequently calculated using Eqs. (E.164), (E.165), (E.169), (E.170). These extremal values and velocities are shown here as a function of the elastic modulus K_{2D}.

of parameters, $L = 30$ mm, $\Delta x = 0.1$ mm, $\Delta t = 0.01$ ms, is appropriate if we are interested the displacement field at positions

$$1 \text{ mm} \leq x \leq 10 \text{ mm}, \tag{E.171}$$

for times

$$1 \text{ ms} \leq t \leq 100 \text{ ms}, \tag{E.172}$$

and area moduli

$$0.1 \text{ mN/m} \leq K \leq 100 \text{ mN/m}. \tag{E.173}$$

Thus, the value $l/L = 1/3$ is appropriate to emulate free boundary conditions at $x = 1$ cm for times $t \leq 100$ ms.

E.9 Obtaining the numerical boundary condition from experimental data

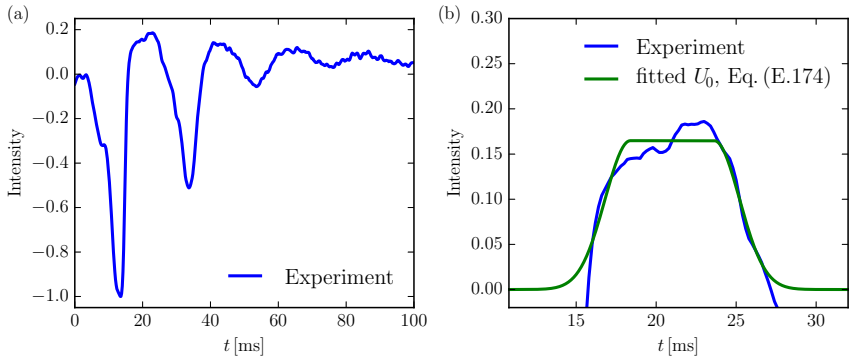

Figure E.12: (a) Experimentally determined intensity as a function of time, as recorded by a camera focusing on the razor blade during excitation; (b) Zoom in on the region around the first positive peak in subplot (a), together with fitted function Eq. (E.174).

To model the experimental excitation mechanism as a boundary condition in our simulation, a DPPC monolayer (without FRET marker) on water at a surface pressure around 5 mN/m is considered. Details of the experimental setup are given in Refs. [93, 94, 176]. The camera is focused on the razor blade, and the intensity as a function of time is recorded during an excitation. The result is shown in Fig. E.12 (a).

To model the excitation theoretically, a function of the form

$$U_0(t) = U_0^{\max} \cdot \begin{cases} \exp\left[-(t-t_1)^2/\tau^2\right] & t < t_1, \\ 1 & t_1 \leq t \leq t_2, \\ \exp\left[-(t-t_2)^2/\tau^2\right] & t_2 < t, \end{cases} \tag{E.174}$$

is fitted to the first positive peak, see Fig. E.12 (b). The resulting fit parameters are $\tau^2 = 5.01\,\mathrm{ms}^2$, $t_1 = 18.39$ ms, $t_2 = 23.63$ ms. To save simulation time, in Chapter 6 we subtract 10 ms from both t_1 and t_2.

E.10 Robustness of nonlinear numerical results with respect to varying elastic modulus and boundary condition

To solve Eq. (6.17) numerically, we need two input functions.

i) A function $K_{2\mathrm{D}}(a)$ that describes how the elastic modulus changes as a function of area per lipid. In Chapter 6 we use a quadratic fit to the experimentally obtained isothermal elastic modulus, c.f. Appendix E.3. The green dashed line in Fig. E.13 (a) shows a replot of this quadratic elastic modulus $K_{2\mathrm{D}}$, together with the elastic modulus obtained from experiment as described in Appendix E.3, and denoted in the following by $K_{2\mathrm{D}}^{\mathrm{exp}}$.

ii) A function $U_0(t)$ for the boundary condition at $x = 0$. We discussed the boundary condition we use in Chapter 6 in Appendix E.9.

In the present appendix we show the robustness of our nonlinear results with respect to varying both the elastic modulus function $K_{2\mathrm{D}}$ and the boundary condition U_0. We do this by evaluating Eq. (6.17) with $\rho_{2\mathrm{D}} = 0$ for several different elastic modulus functions and boundary conditions, and calculating the maximal compression at $x = 8.4\,\mathrm{mm}$ as well as the corresponding wave velocity, as defined by Eqs. (6.29), (6.30).

The main result from the following discussion is that the qualitative features of our nonlinear theory, a steep increase in observed compression accompanied by an increase in wave velocity, are roboust with respect to varying both the elastic modulus function $K_{2\mathrm{D}}$ and the boundary condition U_0. However, the details, namely at which driving amplitude $U_0^{\max}$ the steep increase happens, how steep it is, and the wave velocity, depend on the exact form of both nonlinearity and boundary condition.

E.10.1 Varying the elastic modulus

First, we consider three different elastic moduli:

i) We consider a quadratic elastic modulus $K_{2\mathrm{D}}^{\mathrm{I}}$ that is fitted to $K_{2\mathrm{D}}^{\mathrm{exp}}$ (the experimentally obtained elastic modulus as discussed in Appendix E.3) in the region $a > a_{\min}$, where $a_{\min} \approx 80\,\text{Å}^2$ is the position of the minimum of $K_{2\mathrm{D}}^{\mathrm{exp}}$, with the additional constraint that the minimum of $K_{2\mathrm{D}}^{\mathrm{I}}$ be at the same point as the minimum of $K_{2\mathrm{D}}^{\mathrm{exp}}$, $(a_{\min}, K_{2\mathrm{D}}^{\mathrm{I}}(a_{\min})) = (a_{\min}, K_{2\mathrm{D}}^{\mathrm{exp}}(a_{\min}))$. $K_{2\mathrm{D}}^{\mathrm{I}}$ is shown in Fig. E.13 (b).

ii) For $K_{2\mathrm{D}}^{\mathrm{II}}$, we use the experimental $K_{2\mathrm{D}}^{\mathrm{exp}}$ directly and extend the elastic modulus as constant

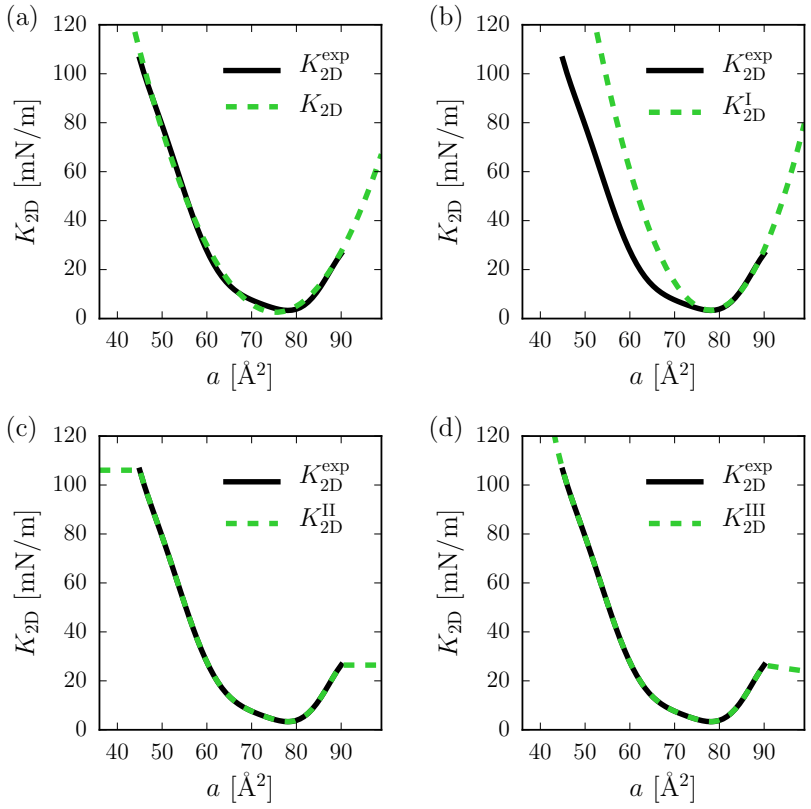

Figure E.13: Elastic modulus functions considered in Appendix E.10.1. In all subplots, black lines depict the experimentally obtained isothermal elastic modulus K_{2D}^{exp} introduced in Appendix E.3, green dashed lines denote various choices for the elastic modulus, defined as follows. (a) K_{2D}: The quadratic elastic modulus used in Chapter 6, obtained from fitting a quadratic polynomial to K_{2D}^{exp}. (b) K_{2D}^{I}: A quadratic polynomial, fitted to the right of the minimum of K_{2D}^{exp} at around $a_{min} \approx 80\,\text{Å}^2$, with the additional constraint that $K_{2D}^{exp}(a_{min}) = K_{2D}^{I}(a_{min})$. (c) K_{2D}^{II}: The elastic modulus K_{2D}^{exp}, extended as constant for $a < 45\,\text{Å}^2$ and $a > 90\,\text{Å}^2$. (d) K_{2D}^{III}: The elastic modulus K_{2D}^{exp} from Appendix E.3, extrapolated by a second order polynomial for $a < 45\,\text{Å}^2$, and a second oder polynomial in a^{-1} without constant term for $a > 90\,\text{Å}^2$, c.f. Eq. (E.176). The extensions are chosen such that K_{2D}^{III} and its first derivative are continuous.

outside of the region where experimental data is available,

$$K_{2D}^{II}(a) := \begin{cases} K_{2D}^{exp}(a_L) & a < a_L, \\ K_{2D}^{exp}(a) & a_L < a < a_R, \\ K_{2D}^{exp}(a_R) & a_R < a, \end{cases} \tag{E.175}$$

where K_{2D}^{exp} is the experimental isothermal elastic modulus as discussed in Appendix E.3,

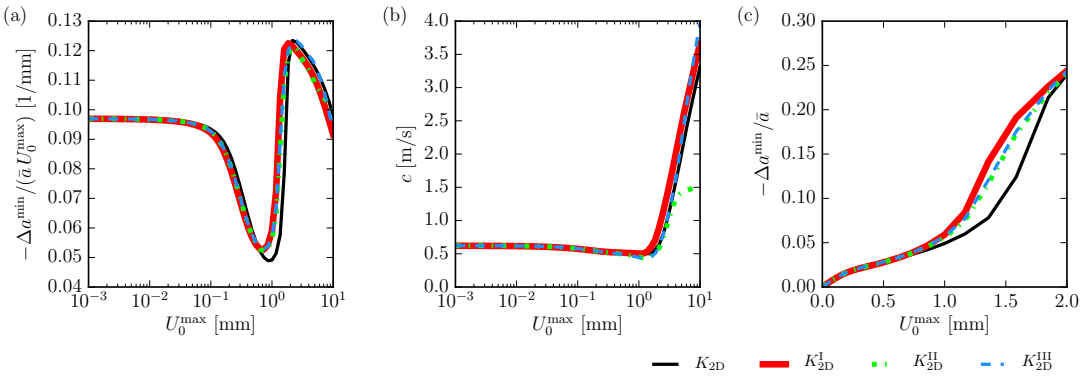

Figure E.14: Numerical results for area moduli considered in Appendix E.10.1. Numerical solutions of Eq. (6.17) with $\rho_{2D} = 0$, using the same boundary condition as in Chapter 6, are calculated using as nonlinearity the four elastic moduli K_{2D}, K_{2D}^{I}, K_{2D}^{II}, K_{2D}^{III} introduced in Appendix E.10.1 and plotted in Fig. E.13. Calculations are carried out for $\bar{a} = 88.4\,\text{Å}^2$. Using Eqs. (6.28)-(6.30), maximal compression $-\Delta a^{\min}/\bar{a}$ and wave velocity c are calculated at $x = 8.4$ mm and shown in subplots (a)-(c) as function of the driving amplitude $U_0^{\max}$.

$a_L = 45\,\text{Å}^2$ and $a_R = 90\,\text{Å}^2$. K_{2D}^{II} is shown in Fig. E.13 (c).

iii) While K_{2D}^{II} extrapolates beyond the experimental data in a very simple way, it is clearly unphysical. The elastic modulus is expected to diverge as the area per lipid a decreases (at some point, of course the monolayer is expected to disintegrate if it gets more and more compressed), while it is expected to approach zero as the area per lipid increases. Therefore, we also consider

$$K_{2D}^{III}(a) := \begin{cases} K_{2D}^{III,L}(a) & a < a_L, \\ K_{2D}^{exp}(a) & a_L < a < a_R, \\ K_{2D}^{III,R}(a) & a_R < a, \end{cases} \tag{E.176}$$

where again $K_{2D}^{exp}(a)$ is the experimental isothermal elastic modulus introduced in Appendix E.3, $K_{2D}^{III,L}$ is a second order polynomial and $K_{2D}^{III,R}(a) = a_1^R a^{-1} + a_2^R a^{-2}$. The polynomial $K_{2D}^{III,L}$ and the coefficients a_1^R, a_2^R are chosen such that K_{2D}^{III} and its first derivative are continuous at $a_L = 45\,\text{Å}^2$, $a_R = 90\,\text{Å}^2$. K_{2D}^{III} is shown in Fig. E.13 (d).

Using the same boundary condition as we use in Chapter 6, c.f. Appendix E.9, and the initial area per lipid $\bar{a} = 88.4\,\text{Å}^2$, we evaluate Eq. (6.17) for $\rho_{2D} = 0$, using the area moduli K_{2D}^{I}, K_{2D}^{II}, K_{2D}^{III} as nonlinearities. Using Eqs. (6.28)-(6.30), we calculate maximal compression $-\Delta a^{\min}/\bar{a}$ and wave speed c at a distance $x = 8.4$ mm from the excitation source (which is at $x = 0$). Figure E.14 shows the results, together with the corresponding results obtained from using the quadratic K_{2D} as in Chapter 6. As the figure shows, all elastic modulus functions yield qualitatively similar

results. The most notable difference is that the threshold amplitude, i.e., the value of $U_0^{\max}$ at which $-\Delta a^{\min}/\bar{a}$ increases steeply, is sensitive to the detailed form of the elastic modulus function, see Fig. E.14 (c). Overall, we can conclude that the main features of our nonlinear results (a steep increase in observed compression accompanied by an increase in wave velocity) are robust with respect to varying the elastic modulus.

E.10.2 Different boundary conditions

In Appendix E.9, we fitted a function of the form

$$U(t) = U_0^{\max} \cdot \begin{cases} \exp\left[-\left(t-t_1\right)^2/\tau^2\right] & t < t_1, \\ 1 & t_1 \le t \le t_2, \\ \exp\left[-\left(t-2_1\right)^2/\tau^2\right] & t_2 < t \end{cases} \tag{E.177}$$

to parts of the intensity time series recorded by a camera during excitation of the razor blade, to obtain the boundary condition we use in Chapter 6. To better gauge the influence of the boundary condition on the results of the nonlinear theory, in the present appendix we consider several other boundary conditions, namely:

i) The full recorded intensity time series, c.f. Appendix E.9, rescaled such that the maximal positive displacement is $U_0^{\max}$.

ii) Smoothed rectangular functions Eq. (E.177) of different plateau width $\tau_p := t_2 - t_1$ and steepness τ.

iii) Smoothed step functions, obtained by setting $t_2 = \infty$ in Eq. (E.177), for several values of τ.

These boundary conditions are shown in Figs. E.15 (a) and E.16, the corresponding parameter values are given in Table E.1. For all these boundary conditions, we evaluate Eq. (6.23) at the equilibrium area per lipid $\bar{a} = 88.4\,\text{Å}^2$. Using Eqs. (6.28)-(6.30), we subsequently calculate maximal compression $-\Delta a^{\min}/\bar{a}$ and wave speed c at a distance $x = 8.4$ mm from the excitation source (which is at $x = 0$).

In Fig. E.15 we show the numerical results for using the full recorded intensity profile as boundary condition. As subplots (c), (d) show, using the recorded intensity profile also yields a steep increase in compression accompanied by an increase in wave speed. However, as subplot (b) shows, the driving amplitude $U_0^{\max}$ at which the steep increase occurs is decreased by factor of about 3.

In Fig. E.16 we show the smoothed rectangular functions and step functions considered, and in Fig. E.17 we show the corresponding results. Both Figures show that all boundary conditions produce qualitatively similar results, and in particular produce a steep increase in $-\Delta a^{\min}/\bar{a}$ at a threshold driving amplitude, which is accompanied by an increase in wave speed c. The exact position of this increase, however, depends on the details of the boundary condition.

In summary, we conclude that the main features of our nonlinear results (a steep increase in observed compression accompanied by an increase in wave velocity) are also robust with respect to varying the boundary condition.

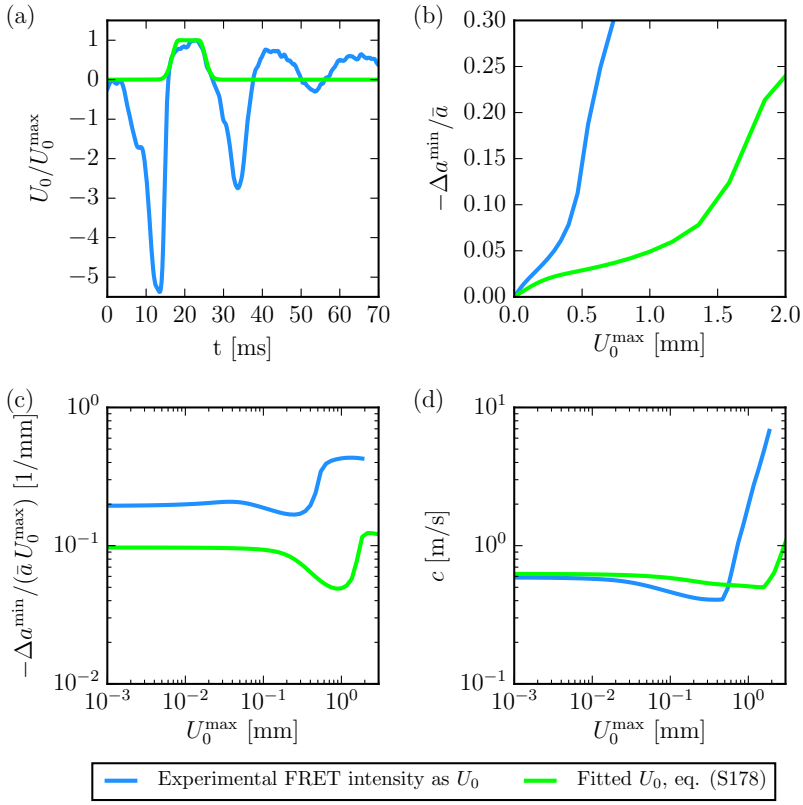

Figure E.15: Numerical results for recorded intensity profile as boundary condition, as discussed in Appendix E.10.2. (a) Recorded intensity profile together with the fit from Appendix E.9; (b) The corresponding maximal compression $-\Delta a^{\min}/\bar{a}$ at a distance $x = 8.4$ mm, as a function of driving amplitude $U_0^{\max}$. As elastic modulus, the quadratic polynomial from Chapter 6 is used with $\bar{a} = 88.4\,\text{Å}^2$. (c), (d) The corresponding relative maximal compression $(-\Delta a^{\min}/\bar{a})/U_0^{\max}$ and the wave speed c, obtained using Eqs. (6.28)-(6.30).

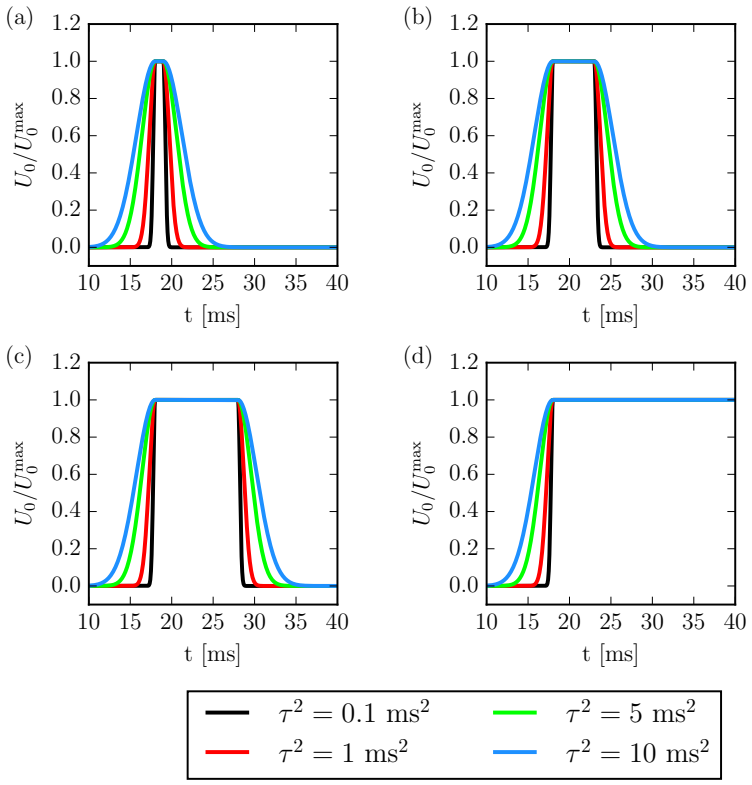

Figure E.16: Different boundary conditions considered in Appendix E.10. All boundary conditions shown here are given by Eq. (E.177), the corresponding parameters can be found in Table E.1. Plateau widths $\tau_p := t_2 - t_1$ are (a) $\tau_p = 1$ ms, (b) $\tau_p = 5$ ms, (c) $\tau_p = 10$ ms, (d) $\tau_p = \infty$. Results from numerical solutions of the nonlinear fractional wave equation Eq. (6.23) with these boundary conditions are shown in Fig. E.17.

Subplot of Fig. E.16	t_1 [ms]	t_2 [ms]	τ^2 [ms^2]
(c)	18	19	0.1
	18	19	1
	18	19	5
	18	19	10
(d)	18	23	0.1
	18	23	1
	18	23	5
	18	23	10
(e)	18	28	0.1
	18	28	1
	18	28	5
	18	28	10
(f)	18	∞	0.1
	18	∞	1
	18	∞	5
	18	∞	10

Table E.1: Parameters for the boundary conditions considered in Appendix E.10.2, c.f. Eq. (E.177) and Figs. E.16, E.17.

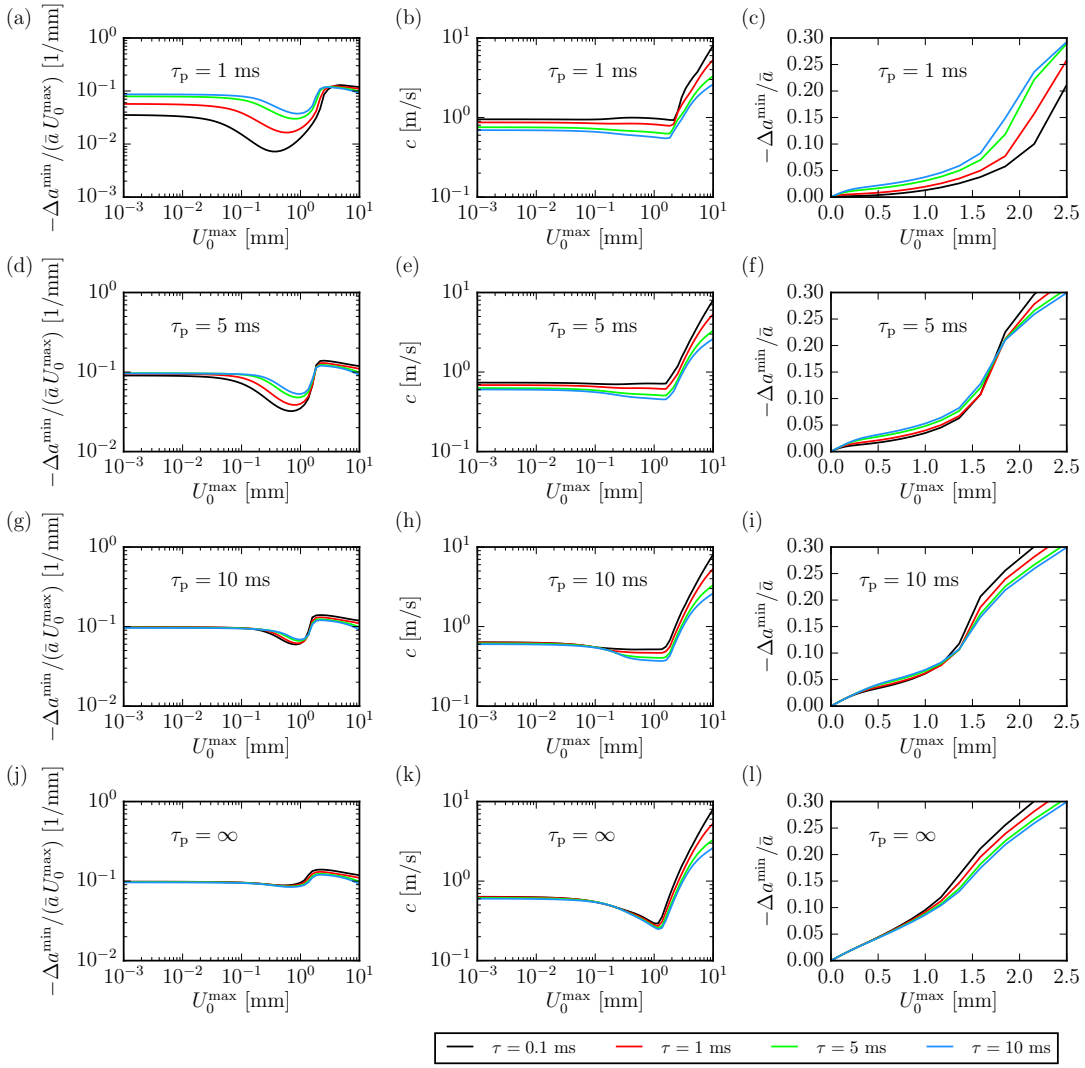

Figure E.17: Numerical results for different boundary conditions considered in Appendix E.10. Equation (6.23) is evaluated for each of the boundary conditions shown in Fig. E.16, with elastic modulus $K_{2\mathrm{D}}$ the quadratic polynomial from the main text at $\bar{a} = 88.4\,\text{Å}^2$. From each solution, maximal compression $-\Delta a^{\min}/\bar{a}$ and wave speed c at $x = 8.4$ mm away from the excitation source are obtained using Eqs. (6.28)-(6.30). The first row (subplots (a-c)) shows the results for the boundary conditions shown in Fig. E.16 (a). The second row (subplots (d-f)) shows the results for the boundary conditions shown in Fig. E.16 (b). The third row (subplots (g-i)) shows the results for the boundary conditions shown in Fig. E.16 (c). The fourth row (subplots (j-l)) shows the results for the boundary conditions shown in Fig. E.16 (d).

List of Publications

The present thesis is based on the following manuscripts, which have been published or are in preparation for publication in peer-reviewed journals:

[i] Julian Kappler, Frank Noé, and Roland R. Netz, "Cyclization dynamics of ideal and self-avoiding collapsed polymers", *in preparation*

[ii] Julian Kappler, Jan O. Daldrop, Florian N. Brünig, Moritz D. Boehle, and Roland R. Netz, "Memory-induced acceleration and slowdown of barrier crossing", *The Journal of Chemical Physics*, vol. 148, p. 014903, **2018**
DOI: 10.1063/1.4998239

[iii] Julian Kappler, Victor B. R. Hinrichsen, and Roland R. Netz, "Barrier crossing in the presence of bi-exponential memory is dominated by the shorter memory time", *in preparation*

[iv] Julian Kappler and Roland R. Netz, "Multiple surface wave solutions on linear viscoelastic media", *Europhysics Letters*, vol. 112, p. 19002, **2015**
DOI: 10.1209/0295-5075/112/19002

[v] Julian Kappler, Shamit Shrivastava, Matthias F. Schneider, and Roland R. Netz, "Nonlinear fractional waves at elastic interfaces", *Physical Review Fluids*, vol. 2, p. 114804, **2017**
DOI: 10.1103/PhysRevFluids.2.114804

Publications not considered in this thesis

[vi] Alexander Schlaich, Julian Kappler, and Roland R. Netz, "Hydration Friction in Nanoconfinement: From Bulk via Interfacial to Dry Friction", *Nano Letters*, vol. 17, pp. 5969-5976, **2017**
DOI: 10.1021/acs.nanolett.7b02000

Bibliography

[1] R. Balian. *From microphysics to macrophysics: methods and applications of statistical physics*. Theoretical and mathematical physics. Springer, Berlin (2007). ISBN 978-3-540-45469-4 978-3-540-45478-6

[2] M. Kardar. *Statistical physics of particles*. Cambridge University Press, Cambridge (2007). ISBN 978-0-521-87342-0. OCLC: ocn148639922

[3] K. Huang. *Introduction to statistical physics*. Taylor & Francis, London, New York (2001). ISBN 978-0-7484-0942-6 978-0-7484-0941-9

[4] P. Langevin. Sur la théorie du mouvement brownien. *C. R. Acad. Sci. (Paris)*, **146**:530–533 (1908)

[5] D. S. Lemons and A. Gythiel. Paul Langevin's 1908 paper "On the Theory of Brownian Motion" ["Sur la théorie du mouvement brownien," C. R. Acad. Sci. (Paris) **146** , 530–533 (1908)]. *American Journal of Physics*, **65 (11)**:1079–1081 (1997). ISSN 0002-9505, 1943-2909. doi:10.1119/1.18725

[6] H. Risken. *The Fokker-Planck equation*. Number 18) in (Springer-series in synergetics. Springer, Berlin, Heidelberg [usw.] (1984). ISBN 978-3-540-13098-7 978-0-387-13098-9. OCLC: 230639136

[7] N. G. v. Kampen. *Stochastic processes in physics and chemistry*. North-Holland personal library. Elsevier, Amsterdam, 3rd edition (2007). ISBN 978-0-444-52965-7. OCLC: ocm81453662

[8] R. Zwanzig. *Nonequilibrium Statistical Mechanics*. Oxford University Press, USA (2001). ISBN 978-0-19-803215-1

[9] K. Huang. *Lectures on statistical physics and protein folding*. World Scientific, Hackensack, N.J (2005). ISBN 978-981-256-143-5 978-981-256-150-3. OCLC: ocm61171377

[10] R. Brown. *The Miscellaneous Botanical Works of Robert Brown*. Cambridge University Press, Cambridge (2015). ISBN 978-1-107-77547-3. DOI: 10.1017/CBO9781107775473

[11] A. Einstein. Über die von der molekularkinetischen Theorie der Wärme geforderte Bewegung von in ruhenden Flüssigkeiten suspendierten Teilchen. *Annalen der Physik*, **322 (8)**:549–560 (1905). ISSN 0003-3804, 1521-3889. doi:10.1002/andp.19053220806

[12] M. von Smoluchowski. Zur kinetischen Theorie der Brownschen Molekularbewegung und der Suspensionen. *Annalen der Physik*, **326 (14)**:756–780 (1906). ISSN 0003-3804, 1521-3889. doi:10.1002/andp.19063261405

[13] J. B. Perrin. Mouvement brownien et réalité moléculaire. *Ann. Chim. Phys.*, **18**:5–114 (1909)

[14] H. Mori. Transport, Collective Motion, and Brownian Motion. *Progress of Theoretical Physics*, **33 (3)**:423–455 (1965). ISSN 0033-068X. doi:10.1143/PTP.33.423

[15] R. Zwanzig. Memory Effects in Irreversible Thermodynamics. *Physical Review*, **124 (4)**:983–992 (1961). ISSN 0031-899X. doi:10.1103/PhysRev.124.983

[16] R. Zwanzig. Nonlinear generalized Langevin equations. *Journal of Statistical Physics*, **9 (3)**:215–220 (1973). ISSN 0022-4715, 1572-9613. doi:10.1007/BF01008729

[17] J. Ashcroft, M. Besnard, V. Aquada, and J. Jonas. High-pressure NMR study of dynamical solvent effects on the conformational isomerization of 1,1-difluorocyclohexane. *Chemical Physics Letters*, **110 (4)**:420–424 (1984). ISSN 0009-2614. doi:10.1016/0009-2614(84)85456-1

[18] R. B. Best and G. Hummer. Reaction coordinates and rates from transition paths. *Proceedings of the National Academy of Sciences*, **102 (19)**:6732–6737 (2005). ISSN 0027-8424, 1091-6490. doi:10.1073/pnas.0408098102

[19] O. K. Dudko, T. G. W. Graham, and R. B. Best. Locating the Barrier for Folding of Single Molecules under an External Force. *Physical Review Letters*, **107 (20)** (2011). ISSN 0031-9007, 1079-7114. doi:10.1103/PhysRevLett.107.208301

[20] B. Peters and B. L. Trout. Obtaining reaction coordinates by likelihood maximization. *The Journal of Chemical Physics*, **125 (5)**:054108 (2006). ISSN 0021-9606. doi:10.1063/1.2234477

[21] M. A. Rohrdanz, W. Zheng, M. Maggioni, and C. Clementi. Determination of reaction coordinates via locally scaled diffusion map. *The Journal of Chemical Physics*, **134 (12)**:124116 (2011). ISSN 0021-9606. doi:10.1063/1.3569857

[22] A. V. Mokshin, R. M. Yulmetyev, and P. Hänggi. Simple Measure of Memory for Dynamical Processes Described by a Generalized Langevin Equation. *Physical Review Letters*, **95 (20)** (2005). ISSN 0031-9007, 1079-7114. doi:10.1103/PhysRevLett.95.200601

[23] G. Hummer. From transition paths to transition states and rate coefficients. *The Journal of Chemical Physics*, **120 (2)**:516 (2004). ISSN 0021-9606. doi:10.1063/1.1630572

[24] B. Peters. Reaction Coordinates and Mechanistic Hypothesis Tests. *Annual Review of Physical Chemistry*, **67 (1)**:669–690 (2016). ISSN 0066-426X, 1545-1593. doi:10.1146/annurev-physchem-040215-112215

[25] R. G. Mullen, J.-E. Shea, and B. Peters. Transmission Coefficients, Committors, and Solvent Coordinates in Ion-Pair Dissociation. *Journal of Chemical Theory and Computation*, **10 (2)**:659–667 (2014). ISSN 1549-9618, 1549-9626. doi:10.1021/ct4009798

[26] P. G. Bolhuis, D. Chandler, C. Dellago, and P. L. Geissler. TRANSITION PATH SAMPLING: Throwing Ropes Over Rough Mountain Passes, in the Dark. *Annual Review of Physical Chemistry*, **53 (1)**:291–318 (2002). ISSN 0066-426X, 1545-1593. doi:10.1146/annurev.physchem.53.082301.113146

[27] F. Höfling and T. Franosch. Anomalous transport in the crowded world of biological cells. *Reports on Progress in Physics*, **76 (4)**:046602 (2013). ISSN 0034-4885, 1361-6633. doi:10.1088/0034-4885/76/4/046602

[28] D. M. Zuckerman and T. B. Woolf. Transition events in butane simulations: Similarities across models. *The Journal of Chemical Physics*, **116 (6)**:2586 (2002). ISSN 0021-9606. doi:10.1063/1.1433501

[29] D. de Sancho, A. Sirur, and R. B. Best. Molecular origins of internal friction effects on protein-folding rates. *Nature Communications*, **5** (2014). ISSN 2041-1723. doi:10.1038/ncomms5307

[30] R. Metzler, J.-H. Jeon, and A. Cherstvy. Non-Brownian diffusion in lipid membranes: Experiments and simulations. *Biochimica et Biophysica Acta (BBA) - Biomembranes*, **1858 (10)**:2451–2467 (2016). ISSN 0005-2736. doi:10.1016/j.bbamem.2016.01.022

[31] J.-H. Jeon, M. Javanainen, H. Martinez-Seara, R. Metzler, and I. Vattulainen. Protein Crowding in Lipid Bilayers Gives Rise to Non-Gaussian Anomalous Lateral Diffusion of Phospholipids and Proteins. *Physical Review X*, **6 (2)** (2016). ISSN 2160-3308. doi:10.1103/PhysRevX.6.021006

[32] D. Panja. Generalized Langevin equation formulation for anomalous polymer dynamics. *Journal of Statistical Mechanics: Theory and Experiment*, **2010 (02)**:L02001 (2010). ISSN 1742-5468. doi:10.1088/1742-5468/2010/02/L02001

[33] C. Maes and S. R. Thomas. From Langevin to generalized Langevin equations for the nonequilibrium Rouse model. *Physical Review E*, **87 (2)** (2013). ISSN 1539-3755, 1550-2376. doi:10.1103/PhysRevE.87.022145

[34] H. Vandebroek and C. Vanderzande. On the Generalized Langevin Equation for a Rouse Bead in a Nonequilibrium Bath. *Journal of Statistical Physics*, **167 (1)**:14–28 (2017). ISSN 0022-4715, 1572-9613. doi:10.1007/s10955-017-1734-x

[35] P. Nelson, M. Radosavljević, S. Bromberg, and D. S. Goodsell. *Biological physics: energy, information, life*. Freeman, New York, NY (2014). ISBN 978-0-7167-9897-2. OCLC: 931490066

[36] B. Alberts, editor. *Molecular biology of the cell*. Garland Science, New York, 5th edition (2008). ISBN 978-0-8153-4105-5 978-0-8153-4106-2. OCLC: ocm82473851

[37] G. Bao and S. Suresh. Cell and molecular mechanics of biological materials. *Nature Materials*, **2 (11)**:715–725 (2003). ISSN 1476-1122, 1476-4660. doi:10.1038/nmat1001

[38] M. Gruebele. Protein Dynamics: From Molecules, to Interactions, to Biology. *International Journal of Molecular Sciences*, **10 (3)**:1360–1368 (2009). ISSN 1422-0067. doi:10.3390/ijms10031360

[39] W. S. Bialek. *Biophysics: searching for principles*. Princeton University Press, Princeton, NJ (2012). ISBN 978-0-691-13891-6

[40] R. Phillips. *Physical biology of the cell*. Garland Science, London, New York, 2nd edition (2013). ISBN 978-0-8153-4450-6

[41] N. T. Southall, K. A. Dill, and A. D. J. Haymet. A View of the Hydrophobic Effect. *The Journal of Physical Chemistry B*, **106 (3)**:521–533 (2002). ISSN 1520-6106, 1520-5207. doi:10.1021/jp015514e

[42] F. Ulrich Hartl and J. Martin. Molecular chaperones in cellular protein folding. *Current Opinion in Structural Biology*, **5 (1)**:92–102 (1995). ISSN 0959440X. doi:10.1016/0959-440X(95)80014-R

[43] K. A. Dill. Polymer principles and protein folding. *Protein Science*, **8 (6)**:1166–1180 (1999). ISSN 0961-8368, 1469-896X. doi:10.1110/ps.8.6.1166

[44] C. M. Dobson. Protein folding and misfolding. *Nature*, **426 (6968)**:884–890 (2003). ISSN 0028-0836, 1476-4687. doi:10.1038/nature02261

[45] D. Thirumalai and G. H. Lorimer. Chaperonin-Mediated Protein Folding. *Annual Review of Biophysics and Biomolecular Structure*, **30 (1)**:245–269 (2001). ISSN 1056-8700, 1545-4266. doi:10.1146/annurev.biophys.30.1.245

[46] D. Thirumalai, D. K. Klimov, and G. H. Lorimer. Caging helps proteins fold. *Proceedings of the National Academy of Sciences*, **100 (20)**:11195–11197 (2003). ISSN 0027-8424, 1091-6490. doi:10.1073/pnas.2035072100

[47] A. B. Mamonov, M. G. Kurnikova, and R. D. Coalson. Diffusion constant of K+ inside Gramicidin A: A comparative study of four computational methods. *Biophysical Chemistry*, **124 (3)**:268–278 (2006). ISSN 0301-4622. doi:10.1016/j.bpc.2006.03.019

[48] D. Bemporad, J. W. Essex, and C. Luttmann. Permeation of Small Molecules through a Lipid Bilayer: A Computer Simulation Study. *The Journal of Physical Chemistry B*, **108 (15)**:4875–4884 (2004). ISSN 1520-6106, 1520-5207. doi:10.1021/jp035260s

[49] S.-J. Marrink and H. J. C. Berendsen. Simulation of water transport through a lipid membrane. *The Journal of Physical Chemistry*, **98 (15)**:4155–4168 (1994). ISSN 0022-3654, 1541-5740. doi:10.1021/j100066a040

[50] H. A. Kramers. Brownian motion in a field of force and the diffusion model of chemical reactions. *Physica*, **7 (4)**:284–304 (1940)

[51] V. Mel'nikov. The Kramers problem: Fifty years of development. *Physics Reports*, **209 (1-2)**:1–71 (1991). ISSN 0370-1573. doi:10.1016/0370-1573(91)90108-X

[52] P. Hänggi, P. Talkner, and M. Borkovec. Reaction-rate theory: fifty years after Kramers. *Reviews of Modern Physics*, **62 (2)**:251–341 (1990). ISSN 0034-6861, 1539-0756. doi:10.1103/RevModPhys.62.251

[53] B. Schuler, E. A. Lipman, and W. A. Eaton. Probing the free-energy surface for protein folding with single-molecule fluorescence spectroscopy. *Nature*, **419 (6908)**:743–747 (2002). ISSN 0028-0836, 1476-4687. doi:10.1038/nature01060

[54] H. S. Chung, K. McHale, J. M. Louis, and W. A. Eaton. Single-Molecule Fluorescence Experiments Determine Protein Folding Transition Path Times. *Science*, **335 (6071)**:981–984 (2012). ISSN 0036-8075, 1095-9203. doi:10.1126/science.1215768

[55] I. König, A. Zarrine-Afsar, M. Aznauryan, A. Soranno, B. Wunderlich, F. Dingfelder, J. C. Stüber, A. Plückthun, D. Nettels, and B. Schuler. Single-molecule spectroscopy of protein conformational dynamics in live eukaryotic cells. *Nature Methods*, **12 (8)**:773–779 (2015). ISSN 1548-7091, 1548-7105. doi:10.1038/nmeth.3475

[56] J. C. M. Gebhardt, T. Bornschlogl, and M. Rief. Full distance-resolved folding energy landscape of one single protein molecule. *Proceedings of the National Academy of Sciences*, **107 (5)**:2013–2018 (2010). ISSN 0027-8424, 1091-6490. doi:10.1073/pnas.0909854107

[57] M. J. Abraham, T. Murtola, R. Schulz, S. Páll, J. C. Smith, B. Hess, and E. Lindahl. GROMACS: High performance molecular simulations through multi-level parallelism from laptops to supercomputers. *SoftwareX*, **1-2**:19–25 (2015). ISSN 2352-7110. doi:10.1016/j.softx.2015.06.001

[58] B. R. Brooks, C. L. Brooks, A. D. Mackerell, L. Nilsson, R. J. Petrella, B. Roux, Y. Won, G. Archontis, C. Bartels, S. Boresch, A. Caflisch, L. Caves, Q. Cui, A. R. Dinner, M. Feig, S. Fischer, J. Gao, M. Hodoscek, W. Im, K. Kuczera, T. Lazaridis, J. Ma, V. Ovchinnikov, E. Paci, R. W. Pastor, C. B. Post, J. Z. Pu, M. Schaefer, B. Tidor, R. M. Venable, H. L. Woodcock, X. Wu, W. Yang, D. M. York, and M. Karplus. CHARMM: The biomolecular simulation program. *Journal of Computational Chemistry*, **30 (10)**:1545–1614 (2009). ISSN 0192-8651, 1096-987X. doi:10.1002/jcc.21287

[59] A. C. Pan, T. M. Weinreich, S. Piana, and D. E. Shaw. Demonstrating an Order-of-Magnitude Sampling Enhancement in Molecular Dynamics Simulations of Complex Protein Systems. *Journal of Chemical Theory and Computation*, **12 (3)**:1360–1367 (2016). ISSN 1549-9618, 1549-9626. doi:10.1021/acs.jctc.5b00913

[60] K. Lindorff-Larsen, P. Maragakis, S. Piana, and D. E. Shaw. Picosecond to Millisecond Structural Dynamics in Human Ubiquitin. *The Journal of Physical Chemistry B*, **120 (33)**:8313–8320 (2016). ISSN 1520-6106, 1520-5207. doi:10.1021/acs.jpcb.6b02024

[61] F. Amblard, A. C. Maggs, B. Yurke, A. N. Pargellis, and S. Leibler. Subdiffusion and Anomalous Local Viscoelasticity in Actin Networks. *Physical Review Letters*, **77 (21)**:4470–4473 (1996). ISSN 0031-9007, 1079-7114. doi:10.1103/PhysRevLett.77.4470

[62] T. Guérin, O. Bénichou, and R. Voituriez. Non-Markovian polymer reaction kinetics. *Nature Chemistry*, **4 (7)**:568–573 (2012). ISSN 1755-4330, 1755-4349. doi:10.1038/nchem.1378

[63] T. Guérin, M. Dolgushev, O. Bénichou, R. Voituriez, and A. Blumen. Cyclization kinetics of Gaussian semiflexible polymer chains. *Physical Review E*, **90 (5)** (2014). ISSN 1539-3755, 1550-2376. doi:10.1103/PhysRevE.90.052601

[64] W. Min, G. Luo, B. J. Cherayil, S. C. Kou, and X. S. Xie. Observation of a Power-Law Memory Kernel for Fluctuations within a Single Protein Molecule. *Physical Review Letters*, **94 (19)** (2005). ISSN 0031-9007, 1079-7114. doi:10.1103/PhysRevLett.94.198302

[65] L. Milanesi, J. P. Waltho, C. A. Hunter, D. J. Shaw, G. S. Beddard, G. D. Reid, S. Dev, and M. Volk. Measurement of energy landscape roughness of folded and unfolded proteins. *Proceedings of the National Academy of Sciences*, **109 (48)**:19563–19568 (2012). ISSN 0027-8424, 1091-6490. doi:10.1073/pnas.1211764109

[66] L. J. Lapidus, W. A. Eaton, and J. Hofrichter. Measuring the rate of intramolecular contact formation in polypeptides. *Proceedings of the National Academy of Sciences*, **97 (13)**:7220–7225 (2000). ISSN 0027-8424, 1091-6490. doi:10.1073/pnas.97.13.7220

[67] O. Bieri, J. Wirz, B. Hellrung, M. Schutkowski, M. Drewello, and T. Kiefhaber. The speed limit for protein folding measured by triplet-triplet energy transfer. *Proceedings of the National Academy of Sciences*, **96 (17)**:9597–9601 (1999). ISSN 0027-8424, 1091-6490. doi:10.1073/pnas.96.17.9597

[68] A. Amitai and D. Holcman. Polymer physics of nuclear organization and function. *Physics Reports*, **678**:1–83 (2017). ISSN 0370-1573. doi:10.1016/j.physrep.2017.02.002

[69] H. Krämer, M. Niemöller, M. Amouyal, B. Revet, B. von Wilcken-Bergmann, and B. Müller-Hill. lac repressor forms loops with linear DNA carrying two suitably spaced lac operators. *The EMBO Journal*, **6 (5)**:1481–1491 (1987). ISSN 0261-4189. doi:10.1002/j.1460-2075.1987.tb02390.x

[70] S. Kadauke and G. A. Blobel. Chromatin loops in gene regulation. *Biochimica et Biophysica Acta (BBA) - Gene Regulatory Mechanisms*, **1789 (1)**:17–25 (2009). ISSN 1874-9399. doi:10.1016/j.bbagrm.2008.07.002

[71] S. Holwerda and W. d. Laat. Chromatin loops, gene positioning, and gene expression. *Frontiers in Genetics*, **3** (2012). ISSN 1664-8021. doi:10.3389/fgene.2012.00217

[72] G. Wilemski and M. Fixman. General theory of diffusion-controlled reactions. *The Journal of Chemical Physics*, **58 (9)**:4009–4019 (1973). ISSN 0021-9606, 1089-7690. doi:10.1063/1.1679757

[73] G. Wilemski and M. Fixman. Diffusion-controlled intrachain reactions of polymers. II Results for a pair of terminal reactive groups. *The Journal of Chemical Physics*, **60 (3)**:878–890 (1974). ISSN 0021-9606, 1089-7690. doi:10.1063/1.1681163

[74] A. Szabo, K. Schulten, and Z. Schulten. First passage time approach to diffusion controlled reactions. *The Journal of Chemical Physics*, **72 (8)**:4350–4357 (1980). ISSN 0021-9606, 1089-7690. doi:10.1063/1.439715

[75] A. Berezhkovskii and A. Szabo. One-dimensional reaction coordinates for diffusive activated rate processes in many dimensions. *The Journal of Chemical Physics*, **122 (1)**:014503 (2005). ISSN 0021-9606. doi:10.1063/1.1818091

[76] J. D. Bryngelson, J. N. Onuchic, N. D. Socci, and P. G. Wolynes. Funnels, pathways, and the energy landscape of protein folding: A synthesis. *Proteins: Structure, Function, and Genetics*, **21 (3)**:167–195 (1995). ISSN 0887-3585, 1097-0134. doi:10.1002/prot.340210302

[77] J. D. Bryngelson and P. G. Wolynes. Intermediates and barrier crossing in a random energy model (with applications to protein folding). *The Journal of Physical Chemistry*, **93 (19)**:6902–6915 (1989). ISSN 0022-3654, 1541-5740. doi:10.1021/j100356a007

[78] O. Dudko, G. Hummer, and A. Szabo. Intrinsic Rates and Activation Free Energies from Single-Molecule Pulling Experiments. *Physical Review Letters*, **96 (10)** (2006). ISSN 0031-9007, 1079-7114. doi:10.1103/PhysRevLett.96.108101

[79] N. D. Socci, J. N. Onuchic, and P. G. Wolynes. Diffusive dynamics of the reaction coordinate for protein folding funnels. *The Journal of Chemical Physics*, **104 (15)**:5860 (1996). ISSN 0021-9606. doi:10.1063/1.471317

[80] H. Orland. Generating transition paths by Langevin bridges. *The Journal of Chemical Physics*, **134 (17)**:174114 (2011). ISSN 0021-9606. doi:10.1063/1.3586036

[81] H. S. Chung, S. Piana-Agostinetti, D. E. Shaw, and W. A. Eaton. Structural origin of slow diffusion in protein folding. *Science*, **349 (6255)**:1504–1510 (2015). ISSN 0036-8075, 1095-9203. doi:10.1126/science.aab1369

[82] K. Truex, H. S. Chung, J. M. Louis, and W. A. Eaton. Testing Landscape Theory for Biomolecular Processes with Single Molecule Fluorescence Spectroscopy. *Physical Review Letters*, **115 (1)** (2015). ISSN 0031-9007, 1079-7114. doi:10.1103/PhysRevLett.115.018101

[83] K. Neupane, A. P. Manuel, and M. T. Woodside. Protein folding trajectories can be described quantitatively by one-dimensional diffusion over measured energy landscapes. *Nature Physics*, **12 (7)**:700–703 (2016). ISSN 1745-2473, 1745-2481. doi:10.1038/nphys3677

[84] R. Best and G. Hummer. Diffusive Model of Protein Folding Dynamics with Kramers Turnover in Rate. *Physical Review Letters*, **96 (22)** (2006). ISSN 0031-9007, 1079-7114. doi:10.1103/PhysRevLett.96.228104

[85] W. Zheng and R. B. Best. Reduction of All-Atom Protein Folding Dynamics to One-Dimensional Diffusion. *The Journal of Physical Chemistry B*, **119 (49)**:15247–15255 (2015). ISSN 1520-6106, 1520-5207. doi:10.1021/acs.jpcb.5b09741

[86] R. Rey and E. Guardia. Dynamical aspects of the sodium(1+)-chloride ion pair association in water. *The Journal of Physical Chemistry*, **96 (11)**:4712–4718 (1992). ISSN 0022-3654, 1541-5740. doi:10.1021/j100190a104

[87] R. F. Grote and J. T. Hynes. The stable states picture of chemical reactions. II. Rate constants for condensed and gas phase reaction models. *The Journal of Chemical Physics*, **73 (6)**:2715 (1980). ISSN 0021-9606. doi:10.1063/1.440485

[88] E. Pollak, H. Grabert, and P. Hänggi. Theory of activated rate processes for arbitrary frequency dependent friction: Solution of the turnover problem. *The Journal of Chemical Physics*, **91 (7)**:4073 (1989). ISSN 0021-9606. doi:10.1063/1.456837

[89] I. Tasaki, A. Watanabe, R. Sandlin, and L. Carnay. Changes in fluorescence, turbidity, and birefringence associated with nerve excitation. *Proceedings of the National Academy of Sciences of the United States of America*, **61 (3)**:883–8 (1968)

[90] I. Tasaki. Mechanical and thermal changes in the Torpedo electric organ associated with its postsynaptic potentials. *Biochemical and biophysical research communications*, **215 (2)**:654–8 (1995). doi:10.1006/bbrc.1995.2514

[91] J. Griesbauer, A. Wixforth, and M. F. Schneider. Wave propagation in lipid monolayers. *Biophysical journal*, **97 (10)**:2710–6 (2009). doi:10.1016/j.bpj.2009.07.049

[92] J. Griesbauer, S. Bössinger, A. Wixforth, and M. F. Schneider. Propagation of 2d Pressure Pulses in Lipid Monolayers and Its Possible Implications for Biology. *Phys. Rev. Lett.*, **108 (19)**:198103–198103 (2012). doi:10.1103/PhysRevLett.108.198103

[93] S. Shrivastava and M. F. Schneider. Evidence for two-dimensional solitary sound waves in a lipid controlled interface and its implications for biological signalling. *Journal of*

The Royal Society Interface, **11 (97)**:20140098–20140098 (2014). ISSN 1742-5689, 1742-5662. doi:10.1098/rsif.2014.0098

[94] S. Shrivastava, K. H. Kang, and M. F. Schneider. Solitary shock waves and adiabatic phase transition in lipid interfaces and nerves. *Physical Review E*, **91 (1)** (2015). ISSN 1539-3755, 1550-2376. doi:10.1103/PhysRevE.91.012715

[95] L. J. Lapidus, P. J. Steinbach, W. A. Eaton, A. Szabo, and J. Hofrichter. Effects of Chain Stiffness on the Dynamics of Loop Formation in Polypeptides. Appendix: Testing a 1-Dimensional Diffusion Model for Peptide Dynamics. *The Journal of Physical Chemistry B*, **106 (44)**:11628–11640 (2002). ISSN 1520-6106, 1520-5207. doi:10.1021/jp020829v

[96] H. Sahoo, D. Roccatano, M. Zacharias, and W. M. Nau. Distance Distributions of Short Polypeptides Recovered by Fluorescence Resonance Energy Transfer in the 10 å Domain. *Journal of the American Chemical Society*, **128 (25)**:8118–8119 (2006). ISSN 0002-7863, 1520-5126. doi:10.1021/ja062293n

[97] T. Guérin, O. Bénichou, and R. Voituriez. Reactive conformations and non-Markovian cyclization kinetics of a Rouse polymer. *The Journal of Chemical Physics*, **138 (9)**:094908 (2013). ISSN 0021-9606, 1089-7690. doi:10.1063/1.4792437

[98] D. J. Bicout and A. Szabo. First passage times, correlation functions, and reaction rates. *The Journal of Chemical Physics*, **106 (24)**:10292–10298 (1997). ISSN 0021-9606, 1089-7690. doi:10.1063/1.474066

[99] C. Yeung and B. A. Friedman. Relation between cyclization of polymers with different initial conditions. *Europhysics Letters (EPL)*, **73 (4)**:621–627 (2006). ISSN 0295-5075, 1286-4854. doi:10.1209/epl/i2005-10440-4

[100] P. Debnath and B. J. Cherayil. Dynamics of chain closure: Approximate treatment of nonlocal interactions. *The Journal of Chemical Physics*, **120 (5)**:2482–2489 (2004). ISSN 0021-9606, 1089-7690. doi:10.1063/1.1637574

[101] P. Debnath, W. Min, X. S. Xie, and B. J. Cherayil. Multiple time scale dynamics of distance fluctuations in a semiflexible polymer: A one-dimensional generalized Langevin equation treatment. *The Journal of Chemical Physics*, **123 (20)**:204903 (2005). ISSN 0021-9606, 1089-7690. doi:10.1063/1.2109809

[102] J. Gowdy, M. Batchelor, I. Neelov, and E. Paci. Nonexponential Kinetics of Loop Formation in Proteins and Peptides: A Signature of Rugged Free Energy Landscapes? *The Journal of Physical Chemistry B*, **121 (41)**:9518–9525 (2017). ISSN 1520-6106, 1520-5207. doi:10.1021/acs.jpcb.7b07075

[103] M. Volk, Y. Kholodenko, H. S. M. Lu, E. A. Gooding, W. F. DeGrado, and R. M. Hochstrasser. Peptide Conformational Dynamics and Vibrational Stark Effects Following Photoinitiated Disulfide Cleavage. *The Journal of Physical Chemistry B*, **101 (42)**:8607–8616 (1997). ISSN 1520-6106, 1520-5207. doi:10.1021/jp971951a

[104] D. Panja and G. T. Barkema. Rouse modes of self-avoiding flexible polymers. *The Journal of Chemical Physics*, **131 (15)**:154903 (2009). ISSN 0021-9606, 1089-7690. doi:10.1063/1.3244678

[105] N. M. Toan, G. Morrison, C. Hyeon, and D. Thirumalai. Kinetics of Loop Formation in Polymer Chains. *The Journal of Physical Chemistry B*, **112 (19)**:6094–6106 (2008). ISSN 1520-6106, 1520-5207. doi:10.1021/jp076510y

[106] C. Oostenbrink, A. Villa, A. E. Mark, and W. F. Van Gunsteren. A biomolecular force field based on the free enthalpy of hydration and solvation: The GROMOS force-field parameter sets 53a5 and 53a6. *Journal of Computational Chemistry*, **25 (13)**:1656–1676 (2004). doi:10.1002/jcc.20090

[107] B. J. Berne and G. D. Harp. On the Calculation of Time Correlation Functions. In *Advances in Chemical Physics*, volume 17, pp. 63–227. John Wiley & Sons, Inc., Hoboken, NJ, USA (1970). ISBN 978-0-470-14363-6 978-0-471-69922-4. DOI: 10.1002/9780470143636.ch3

[108] J. O. Daldrop, J. Kappler, F. N. Brünig, and R. R. Netz. Butane dihedral angle dynamics in water is dominated by internal friction. *submitted* (2018)

[109] M. Doi and S. F. Edwards. *The theory of polymer dynamics*. Number 73 in International series of monographs on physics. Clarendon Press, Oxford (2007). ISBN 978-0-19-852033-7. OCLC: 845169495

[110] A. N. Rissanou, S. H. Anastasiadis, and I. A. Bitsanis. Monte Carlo study of the coil-to-globule transition of a model polymeric system. *Journal of Polymer Science Part B: Polymer Physics*, **44 (24)**:3651–3666 (2006). ISSN 08876266, 10990488. doi:10.1002/polb.21024

[111] J. C. F. Schulz, L. Schmidt, R. B. Best, J. Dzubiella, and R. R. Netz. Peptide Chain Dynamics in Light and Heavy Water: Zooming in on Internal Friction. *Journal of the American Chemical Society*, **134 (14)**:6273–6279 (2012). ISSN 0002-7863, 1520-5126. doi:10.1021/ja211494h

[112] K. Kremer and K. Binder. Dynamics of polymer chains confined into tubes: Scaling theory and Monte Carlo simulations. *The Journal of Chemical Physics*, **81 (12)**:6381–6394 (1984). ISSN 0021-9606, 1089-7690. doi:10.1063/1.447549

[113] G. S. Grest and K. Kremer. Molecular dynamics simulation for polymers in the presence of a heat bath. *Physical Review A*, **33 (5)**:3628–3631 (1986). ISSN 0556-2791. doi:10.1103/PhysRevA.33.3628

[114] R. Morgado, F. A. Oliveira, G. G. Batrouni, and A. Hansen. Relation between Anomalous and Normal Diffusion in Systems with Memory. *Physical Review Letters*, **89 (10)** (2002). ISSN 0031-9007, 1079-7114. doi:10.1103/PhysRevLett.89.100601

[115] D. Ceperley, M. H. Kalos, and J. L. Lebowitz. Computer Simulation of the Dynamics of a Single Polymer Chain. *Physical Review Letters*, **41 (5)**:313–316 (1978). ISSN 0031-9007. doi:10.1103/PhysRevLett.41.313

[116] P. G. De Gennes. Dynamics of Entangled Polymer Solutions. II. Inclusion of Hydrodynamic Interactions. *Macromolecules*, **9 (4)**:594–598 (1976). ISSN 0024-9297, 1520-5835. doi:10.1021/ma60052a012

[117] S. C. Kou and X. S. Xie. Generalized Langevin Equation with Fractional Gaussian Noise: Subdiffusion within a Single Protein Molecule. *Physical Review Letters*, **93 (18)** (2004). ISSN 0031-9007, 1079-7114. doi:10.1103/PhysRevLett.93.180603

[118] O. F. Lange and H. Grubmüller. Collective Langevin dynamics of conformational motions in proteins. *The Journal of Chemical Physics*, **124 (21)**:214903 (2006). ISSN 0021-9606. doi:10.1063/1.2199530

[119] R. O. Rosenberg, B. J. Berne, and D. Chandler. Isomerization dynamics in liquids by molecular dynamics. *Chemical Physics Letters*, **75 (1)**:162–168 (1980). ISSN 0009-2614. doi:10.1016/0009-2614(80)80487-8

[120] J. M. Sancho, A. H. Romero, and K. Lindenberg. The Kramers problem in the energy-diffusion limited regime. *The Journal of Chemical Physics*, **109 (22)**:9888 (1998). ISSN 0021-9606. doi:10.1063/1.477657

[121] Z. Li, X. Bian, X. Li, and G. E. Karniadakis. Incorporation of memory effects in coarse-grained modeling via the Mori-Zwanzig formalism. *The Journal of Chemical Physics*, **143 (24)**:243128 (2015). ISSN 0021-9606, 1089-7690. doi:10.1063/1.4935490

[122] J. E. Straub, M. Borkovec, and B. J. Berne. Non-Markovian activated rate processes: Comparison of current theories with numerical simulation data. *The Journal of Chemical Physics*, **84 (3)**:1788 (1986). ISSN 0021-9606. doi:10.1063/1.450425

[123] P. Reimann, G. J. Schmid, and P. Hänggi. Universal equivalence of mean first-passage time and Kramers rate. *Physical Review E*, **60 (1)**:R1–R4 (1999). ISSN 1063-651X, 1095-3787. doi:10.1103/PhysRevE.60.R1

[124] S. Arrhenius. Über die Dissociationswärme und den Einfluss der Temperatur auf den Dissociationsgrad der Elektrolyte. *Z. Phys. Chem.*, **4**:96–116 (1889). doi:10.1515/zpch-1889-0408

[125] H. Eyring. The Activated Complex in Chemical Reactions. *The Journal of Chemical Physics*, **3 (2)**:107 (1935). ISSN 0021-9606. doi:10.1063/1.1749604

[126] V. I. Mel'nikov and S. V. Meshkov. Theory of activated rate processes: Exact solution of the Kramers problem. *The Journal of Chemical Physics*, **85 (2)**:1018 (1986). ISSN 0021-9606. doi:10.1063/1.451844

[127] B. Carmeli and A. Nitzan. Non-Markoffian Theory of Activated Rate Processes. *Physical Review Letters*, **49 (7)**:423–426 (1982). ISSN 0031-9007. doi:10.1103/PhysRevLett.49.423

[128] P. Hänggi. Escape from a metastable state. *Journal of Statistical Physics*, **42 (1-2)**:105–148 (1986). ISSN 0022-4715, 1572-9613. doi:10.1007/BF01010843

[129] P. Talkner and H.-B. Braun. Transition rates of a non-Markovian Brownian particle in a double well potential. *The Journal of Chemical Physics*, **88 (12)**:7537 (1988). ISSN 0021-9606. doi:10.1063/1.454318

[130] E. Pollak and R. Ianconescu. Finite barrier corrections to the PGH solution of Kramers' turnover theory. *The Journal of Chemical Physics*, **140 (15)**:154108 (2014). ISSN 0021-9606, 1089-7690. doi:10.1063/1.4871281

[131] E. Pollak and R. Ianconescu. Kramers' Turnover Theory: Improvement and Extension to Low Barriers. *The Journal of Physical Chemistry A*, **120 (19)**:3155–3164 (2016). ISSN 1089-5639, 1520-5215. doi:10.1021/acs.jpca.5b11502

[132] R. Ianconescu and E. Pollak. A study of Kramers' turnover theory in the presence of exponential memory friction. *The Journal of Chemical Physics*, **143 (10)**:104104 (2015). ISSN 0021-9606, 1089-7690. doi:10.1063/1.4929709

[133] E. Pollak. Classical and Quantum Rate Theory for Condensed Phases. In S. D. Schwartz, editor, *Theoretical Methods in Condensed Phase Chemistry*, volume 5, pp. 1–46. Kluwer Academic Publishers, Dordrecht (2002). ISBN 978-0-7923-6687-4. DOI: 10.1007/0-306-46949-9_1

[134] D. A. Rose and I. Benjamin. Molecular dynamics of adiabatic and nonadiabatic electron transfer at the metal–water interface. *The Journal of Chemical Physics*, **100 (5)**:3545 (1994). ISSN 0021-9606. doi:10.1063/1.466397

[135] D. E. Smith and L. X. Dang. Computer simulations of NaCl association in polarizable water. *The Journal of Chemical Physics*, **100 (5)**:3757 (1994). ISSN 0021-9606. doi:10.1063/1.466363

[136] M. Roca, V. Moliner, I. Tuñón, and J. T. Hynes. Coupling between Protein and Reaction Dynamics in Enzymatic Processes: Application of Grote-Hynes Theory to Catechol *O* -Methyltransferase. *Journal of the American Chemical Society*, **128 (18)**:6186–6193 (2006). ISSN 0002-7863, 1520-5126. doi:10.1021/ja058826u

[137] L. X. Dang and G. K. Schenter. Solvent exchange in liquid methanol and rate theory. *Chemical Physics Letters*, **643**:142–148 (2016). ISSN 0009-2614. doi:10.1016/j.cplett.2015.10.045

[138] H. V. R. Annapureddy and L. X. Dang. Understanding the Rates and Molecular Mechanism of Water-Exchange around Aqueous Ions Using Molecular Simulations. *The Journal*

of Physical Chemistry B, **118 (30)**:8917–8927 (2014). ISSN 1520-6106, 1520-5207. doi:10.1021/jp502922c

[139] B. Carmeli and A. Nitzan. Theory of Activated Rate Processes: Bridging between the Kramers Limits. *Physical Review Letters*, **51 (4)**:233–236 (1983). ISSN 0031-9007. doi:10.1103/PhysRevLett.51.233

[140] D. Chandler. Statistical mechanics of isomerization dynamics in liquids and the transition state approximation. *The Journal of Chemical Physics*, **68 (6)**:2959 (1978). ISSN 0021-9606. doi:10.1063/1.436049

[141] S. S. Plotkin and P. G. Wolynes. Non-Markovian Configurational Diffusion and Reaction Coordinates for Protein Folding. *Physical Review Letters*, **80 (22)**:5015–5018 (1998). ISSN 0031-9007, 1079-7114. doi:10.1103/PhysRevLett.80.5015

[142] I. S. Tolokh, G. W. N. White, S. Goldman, and C. G. Gray. Prediction of ion channel transport from Grote-Hynes and Kramers theories. *Molecular Physics*, **100 (14)**:2351–2359 (2002). ISSN 0026-8976, 1362-3028. doi:10.1080/00268970210124828

[143] D. Lesnicki, R. Vuilleumier, A. Carof, and B. Rotenberg. Molecular Hydrodynamics from Memory Kernels. *Physical Review Letters*, **116 (14)** (2016). ISSN 0031-9007, 1079-7114. doi:10.1103/PhysRevLett.116.147804

[144] F. Gottwald, S. Karsten, S. D. Ivanov, and O. Kühn. Parametrizing linear generalized Langevin dynamics from explicit molecular dynamics simulations. *The Journal of Chemical Physics*, **142 (24)**:244110 (2015). ISSN 0021-9606, 1089-7690. doi:10.1063/1.4922941

[145] J. O. Daldrop, B. G. Kowalik, and R. R. Netz. External Potential Modifies Friction of Molecular Solutes in Water. *Physical Review X*, **7 (4)** (2017). ISSN 2160-3308. doi:10.1103/PhysRevX.7.041065

[146] S. C. Tucker, M. E. Tuckerman, B. J. Berne, and E. Pollak. Comparison of rate theories for generalized Langevin dynamics. *The Journal of Chemical Physics*, **95 (8)**:5809 (1991). ISSN 0021-9606. doi:10.1063/1.461603

[147] J. Kappler, J. O. Daldrop, F. N. Brünig, M. D. Boehle, and R. R. Netz. Memory-induced acceleration and slowdown of barrier crossing. *The Journal of Chemical Physics*, **148 (1)**:014903 (2018). ISSN 0021-9606, 1089-7690. doi:10.1063/1.4998239

[148] W. Thomson. Ripples and Waves. *Nature*, **5**:1–2 (1871). doi:10.1038/005001a0

[149] L. D. Landau and E. M. Lifshitz. *Fluid Mechanics*. Bd. 6. Elsevier Science (1959). ISBN 978-1-4831-4050-6

[150] F. Behroozi, J. Smith, and W. Even. Stokes' dream: Measurement of fluid viscosity from the attenuation of capillary waves. *American Journal of Physics*, **78 (11)**:1165–1169 (2010). ISSN 0002-9505, 1943-2909. doi:10.1119/1.3467887

[151] L. D. Landau, E. M. Lifshitz, A. M. Kosevitch, and L. P. Pitaevskii. *Theory of Elasticity*. Course of theoretical physics. Butterworth-Heinemann (1986). ISBN 978-0-7506-2633-0

[152] T. Chou. Band structure of surface flexural-gravity waves along periodic interfaces. *Journal of Fluid Mechanics*, **369**:333–350 (1998). ISSN 1469-7645

[153] L. Rayleigh. On Waves Propagated along the Plane Surface of an Elastic Solid. *Proceedings of the London Mathematical Society*, **s1-17 (1)**:4–11 (1885). doi:10.1112/plms/s1-17.1.4

[154] P. K. Currie, M. A. Hayes, and P. O'Leary. Viscoelastic Rayleigh waves. *Q. Appl. Math.*, **35**:35–53 (1977). doi:10.1090/qam/99648

[155] P. K. Currie and P. O'Leary. Viscoelastic Rayleigh waves II. *Q. Appl. Math.*, **36**:445–454 (1978). doi:10.1090/qam/99642

[156] M. V. D. Tempel and R. P. V. D. Riet. Damping of Waves by Surface-Active Materials. *The Journal of Chemical Physics*, **42 (8)**:2769–2777 (1965). doi:10.1063/1.1703235

[157] J. Lucassen. Longitudinal capillary waves. Part 2.-Experiments. *Trans. Faraday Soc.*, **64 (0)**:2230–2235 (1968). doi:10.1039/TF9686402230

[158] J. Lucassen. Longitudinal capillary waves. Part 1.-Theory. *Trans. Faraday Soc.*, **64 (0)**:2221–2229 (1968). doi:10.1039/TF9686402221

[159] J. Lucassen and M. V. D. Tempel. Longitudinal waves on visco-elastic surfaces. *Journal of Colloid and Interface Science*, **41 (3)**:491–498 (1972). ISSN 0021-9797. doi:http://dx.doi.org/10.1016/0021-9797(72)90373-6

[160] J. Earnshaw and E. McCoo. Mode mixing of liquid surface waves. *Physical Review Letters*, **72 (1)**:84–87 (1994). ISSN 0031-9007. doi:10.1103/PhysRevLett.72.84

[161] F. Monroy and D. Langevin. Direct Experimental Observation of the Crossover from Capillary to Elastic Surface Waves on Soft Gels. *Physical Review Letters*, **81 (15)**:3167–3170 (1998). doi:10.1103/PhysRevLett.81.3167

[162] L. Kramer. Theory of Light Scattering from Fluctuations of Membranes and Monolayers. *Journal of Chemical Physics*, **55**:2097–2105 (1971). doi:10.1063/1.1676380

[163] H. Pleiner, J. L. Harden, and P. Pincus. Surface Modes on a Viscoelastic Medium. *EPL (Europhysics Letters)*, **7 (5)**:383 (1988). doi:10.1209/0295-5075/7/5/001

[164] J. L. Harden, H. Pleiner, and P. A. Pincus. Hydrodynamic surface modes on concentrated polymer solutions and gels. *The Journal of Chemical Physics*, **94 (7)**:5208–5208 (1991). doi:10.1063/1.460525

[165] J. L. Harden and H. Pleiner. Hydrodynamic modes of viscoelastic polymer films. *Physical Review E*, **49 (2)**:1411–1423 (1994). ISSN 1063-651X. doi:10.1103/PhysRevE.49.1411

[166] C. Tejero and M. Baus. Viscoelastic surface waves and the surface structure of liquids. *Molecular Physics*, **54 (6)**:1307–1324 (1985). doi:10.1080/00268978500101021

[167] K. Falk and K. Mecke. Capillary waves of compressible fluids. *Journal of Physics: Condensed Matter*, **23 (18)**:184103 (2011). doi:10.1088/0953-8984/23/18/184103

[168] R. M. Christensen. *Theory of Viscoelasticity*. Civil, Mechanical and Other Engineering Series. Dover Publications (2003). ISBN 978-0-486-42880-2

[169] P. A. Kralchevsky, J. C. Eriksson, and S. Ljunggren. Theory of curved interfaces and membranes: Mechanical and thermodynamical approaches. *Advances in Colloid and Interface Science*, **48**:19–59 (1994). ISSN 00018686. doi:10.1016/0001-8686(94)80004-9

[170] S. Chiriţă, M. Ciarletta, and V. Tibullo. Rayleigh Surface Waves on a Kelvin-Voigt Viscoelastic Half-Space. *Journal of Elasticity*, **115 (1)**:61–76 (2013). ISSN 0374-3535. doi:10.1007/s10659-013-9447-0

[171] E. Lucassen-Reynders and J. Lucassen. Properties of capillary waves. *Advances in Colloid and Interface Science*, **2 (4)**:347–395 (1970). doi:10.1016/0001-8686(70)80001-X

[172] D. J. Acheson. *Elementary fluid dynamics*. Oxford applied mathematics and computing science series. Oxford University Press, Oxford (1990). ISBN 978-0-19-859660-8 978-0-19-859679-0

[173] W. M. Haynes. *CRC Handbook of Chemistry and Physics, 95th Edition*. CRC Press (2014). ISBN 978-1-4822-0868-9

[174] J. Krägel, J. B. Li, R. Miller, M. Bree, G. Kretzschmar, and H. Möhwald. Surface viscoelasticity of phospholipid monolayers at the air/water interface. *Colloid and Polymer Science*, **274 (12)**:1183–1187 (1996). doi:10.1007/bf00655690

[175] M. F. Schneider, K. Lim, G. G. Fuller, and M. Tanaka. Rheology of glycocalix model at air/water interface. *Physical Chemistry Chemical Physics*, **4 (10)**:1949–1952 (2002). doi:10.1039/b110631g

[176] S. Shrivastava and M. F. Schneider. Opto-Mechanical Coupling in Interfaces under Static and Propagative Conditions and Its Biological Implications. *PLoS ONE*, **8 (7)**:1–7 (2013). doi:10.1371/journal.pone.0067524

[177] T. Hoshino, Y. Ohmasa, R. Osada, and M. Yao. Dispersion relation of capillary waves on ionic liquids: Observation of the fast overdamped mode. *Phys. Rev. E*, **78 (6)**:061604 (2008). doi:10.1103/PhysRevE.78.061604

[178] M. Rabaud and F. Moisy. Ship Wakes: Kelvin or Mach Angle? *Physical Review Letters*, **110 (21)** (2013). ISSN 0031-9007, 1079-7114. doi:10.1103/PhysRevLett.110.214503

[179] A. Likar and N. Razpet. Towards the Kelvin wake and beyond. *American Journal of Physics*, **81 (4)**:245–252 (2013). ISSN 0002-9505, 1943-2909. doi:10.1119/1.4793510

[180] J. J. M. Carcione. *Wave Fields in Real Media: Wave Propagation in Anisotropic, Anelastic, Porous and Electromagnetic Media*. Handbook of Geophysical Exploration: Seismic Exploration. Elsevier Science (2007). ISBN 978-0-08-046890-7

[181] N. M. Shapiro. High-Resolution Surface-Wave Tomography from Ambient Seismic Noise. *Science*, **307 (5715)**:1615–1618 (2005). ISSN 0036-8075, 1095-9203. doi: 10.1126/science.1108339

[182] P. Hess. Surface Acoustic Waves in Materials Science. *Physics Today*, **55 (3)**:42–47 (2002). ISSN 0031-9228, 1945-0699. doi:10.1063/1.1472393

[183] A. Ben-Menahem and S. J. Singh. *Seismic Waves and Sources*. Springer New York, New York, NY (1981). ISBN 978-1-4612-5856-8

[184] A. D. D. Craik. The origins of water wave theory. *Annual Review of Fluid Mechanics*, **36 (1)**:1–28 (2004). doi:10.1146/annurev.fluid.36.050802.122118

[185] G. B. Airy. Tides and waves. *Encyclopedia Metropolitana*, **3** (1841)

[186] R. D. Borcherdt. *Viscoelastic Waves Layered Media*. Cambridge University Press (2009). ISBN 978-0-521-89853-9

[187] F. Behroozi, B. Lambert, and B. Buhrow. Noninvasive measurement of viscosity from damping of capillary waves. *ISA Transactions*, **42 (1)**:3–8 (2003). ISSN 00190578. doi:10.1016/S0019-0578(07)60108-6

[188] C. Cinbis and B. T. Khuri-Yakub. A noncontacting technique for measuring surface tension of liquids. *Review of Scientific Instruments*, **63 (3)**:2048–2050 (1992). ISSN 0034-6748, 1089-7623. doi:10.1063/1.1143164

[189] J. Kappler and R. R. Netz. Multiple surface wave solutions on linear viscoelastic media. *EPL (Europhysics Letters)*, **112 (1)**:19002 (2015). ISSN 0295-5075, 1286-4854. doi: 10.1209/0295-5075/112/19002

[190] J. Giermanska-Kahn, F. Monroy, and D. Langevin. Negative effective surface viscosities in insoluble fatty acid monolayers: Effect of phase transitions on dilational viscoelasticity. *Phys. Rev. E*, **60 (6)**:7163–7173 (1999). doi:10.1103/PhysRevE.60.7163

[191] A. El Hady and B. B. Machta. Mechanical surface waves accompany action potential propagation. *Nature Communications*, **6**:6697 (2015). ISSN 2041-1723. doi:10.1038/ncomms7697

[192] T. Heimburg and A. D. Jackson. On soliton propagation in biomembranes and nerves. *Proceedings of the National Academy of Sciences*, **102 (28)**:9790–9795 (2005). ISSN 0027-8424, 1091-6490. doi:10.1073/pnas.0503823102

[193] R. Appali, U. van Rienen, and T. Heimburg. A Comparison of the Hodgkin-Huxley Model and the Soliton Theory for the Action Potential in Nerves. In *Advances in Planar Lipid Bilayers and Liposomes*, volume 16, pp. 275–299. Elsevier (2012). ISBN 978-0-12-396534-9

[194] M. M. Rvachev. On axoplasmic pressure waves and their possible role in nerve impulse propagation. *Biophysical Reviews and Letters*, **05 (02)**:73–88 (2010). ISSN 1793-0480, 1793-7035. doi:10.1142/S1793048010001147

[195] L. D. Mosgaard, A. D. Jackson, and T. Heimburg. Low-Frequency Sound Propagation in Lipid Membranes. In *Advances in Planar Lipid Bilayers and Liposomes*, volume 16, pp. 51–74. Elsevier (2012). ISBN 978-0-12-396534-9

[196] B. Fichtl, S. Shrivastava, and M. F. Schneider. Protons at the speed of sound: Predicting specific biological signaling from physics. *Scientific Reports*, **6**:22874 (2016). ISSN 2045-2322. doi:10.1038/srep22874

[197] B. Martinac, M. Buechner, A. H. Delcour, J. Adler, and C. Kung. Pressure-sensitive ion channel in Escherichia coli. *Proceedings of the National Academy of Sciences*, **84 (8)**:2297–2301 (1987). ISSN 0027-8424, 1091-6490. doi:10.1073/pnas.84.8.2297

[198] B. Coste, J. Mathur, M. Schmidt, T. J. Earley, S. Ranade, M. J. Petrus, A. E. Dubin, and A. Patapoutian. Piezo1 and Piezo2 Are Essential Components of Distinct Mechanically Activated Cation Channels. *Science*, **330 (6000)**:55–60 (2010). ISSN 0036-8075, 1095-9203. doi:10.1126/science.1193270

[199] G. H. Kim, P. Kosterin, A. L. Obaid, and B. M. Salzberg. A mechanical spike accompanies the action potential in Mammalian nerve terminals. *Biophysical journal*, **92 (9)**:3122–9 (2007). doi:10.1529/biophysj.106.103754

[200] B. Coste, B. Xiao, J. S. Santos, R. Syeda, J. Grandl, K. S. Spencer, S. E. Kim, M. Schmidt, J. Mathur, A. E. Dubin, M. Montal, and A. Patapoutian. Piezo proteins are pore-forming subunits of mechanically activated channels. *Nature*, **483 (7388)**:176–181 (2012). ISSN 0028-0836, 1476-4687. doi:10.1038/nature10812

[201] S. Sukharev and F. Sachs. Molecular force transduction by ion channels - diversity and unifying principles. *Journal of Cell Science*, **125 (13)**:3075–3083 (2012). ISSN 0021-9533, 1477-9137. doi:10.1242/jcs.092353

[202] E. Villagran Vargas, A. Ludu, R. Hustert, P. Gumrich, A. D. Jackson, and T. Heimburg. Periodic solutions and refractory periods in the soliton theory for nerves and the locust femoral nerve. *Biophysical Chemistry*, **153 (2-3)**:159–167 (2011). ISSN 0301-4622. doi:10.1016/j.bpc.2010.11.001

[203] F. Mainardi. *Fractional Calculus and Waves in Linear Viscoelasticity: An Introduction to Mathematical Models*. World Scientific (2010). ISBN 1-84816-330-4

[204] S. Holm and S. P. Näsholm. Comparison of Fractional Wave Equations for Power Law Attenuation in Ultrasound and Elastography. *Ultrasound in Medicine and Biology*, **40 (4)**:695–703 (2014). ISSN 0301-5629. doi:10.1016/j.ultrasmedbio.2013.09.033

[205] M. Caputo. Linear models of dissipation whose Q is almost frequency independent. *Annals of Geophysics*, **19 (4)**:383–393 (1966). doi:10.4401/ag-5051

[206] M. G. Wismer. Finite element analysis of broadband acoustic pulses through inhomogenous media with power law attenuation. *The Journal of the Acoustical Society of America*, **120 (6)**:3493–3502 (2006). ISSN 0001-4966. doi:10.1121/1.2354032

[207] A. Jaishankar and G. H. McKinley. Power-law rheology in the bulk and at the interface: quasi-properties and fractional constitutive equations. *Proceedings of the Royal Society A: Mathematical, Physical and Engineering Sciences*, **469 (2149)**:20120284–20120284 (2012). ISSN 1364-5021, 1471-2946. doi:10.1098/rspa.2012.0284

[208] Y. Wang. Generalized viscoelastic wave equation. *Geophysical Journal International*, **204 (2)**:1216–1221 (2016). doi:10.1093/gji/ggv514

[209] S. Holm, S. P. Näsholm, F. Prieur, and R. Sinkus. Deriving fractional acoustic wave equations from mechanical and thermal constitutive equations. *Computers & Mathematics with Applications*, **66 (5)**:621–629 (2013). ISSN 0898-1221. doi:10.1016/j.camwa.2013.02.024

[210] R. C. MacDonald and S. A. Simon. Lipid monolayer states and their relationships to bilayers. *Proceedings of the National Academy of Sciences*, **84 (12)**:4089–4093 (1987). ISSN 0027-8424, 1091-6490. doi:10.1073/pnas.84.12.4089

[211] J. R. Hazel. Thermal Adaptation in Biological Membranes: Is Homeoviscous Adaptation the Explanation? *Annual Review of Physiology*, **57 (1)**:19–42 (1995). ISSN 0066-4278, 1545-1585. doi:10.1146/annurev.ph.57.030195.000315

[212] G. Matsumoto and I. Tasaki. A study of conduction velocity in nonmyelinated nerve fibers. *Biophysical Journal*, **20 (1)**:1–13 (1977). ISSN 0006-3495. doi:10.1016/S0006-3495(77)85532-X

[213] M. Ringkamp, L. M. Johanek, J. Borzan, T. V. Hartke, G. Wu, E. M. Pogatzki-Zahn, J. N. Campbell, B. Shim, R. J. Schepers, and R. A. Meyer. Conduction Properties Distinguish Unmyelinated Sympathetic Efferent Fibers and Unmyelinated Primary Afferent Fibers in the Monkey. *PLoS ONE*, **5 (2)**:e9076 (2010). ISSN 1932-6203. doi:10.1371/journal.pone.0009076

[214] F. K. Sanders and D. Whitteridge. Conduction velocity and myelin thickness in regenerating nerve fibres. *The Journal of Physiology*, **105 (2)**:152–174 (1946). ISSN 0022-3751. doi:10.1113/jphysiol.1946.sp004160

[215] D. N. Franz and A. Iggo. Conduction failure in myelinated and non-myelinated axons at low temperatures. *The Journal of Physiology*, **199 (2)**:319–345 (1968). ISSN 0022-3751. doi:10.1113/jphysiol.1968.sp008656

[216] A. L. Hodgkin and A. F. Huxley. A quantitative description of membrane current and its application to conduction and excitation in nerve. *The Journal of Physiology*, **117 (4)**:500–544 (1952). ISSN 0022-3751. doi:10.1113/jphysiol.1952.sp004764

[217] E. P. Petrov and P. Schwille. Translational Diffusion in Lipid Membranes beyond the Saffman-Delbrück Approximation. *Biophysical Journal*, **94 (5)**:L41 – L43 (2008). ISSN 0006-3495. doi:http://dx.doi.org/10.1529/biophysj.107.126565

[218] E. P. Petrov, R. Petrosyan, and P. Schwille. Translational and rotational diffusion of micrometer-sized solid domains in lipid membranes. *Soft Matter*, **8 (29)**:7552–7555 (2012). doi:10.1039/C2SM25796C

[219] C.-H. Lee, W.-C. Lin, and J. Wang. All-optical measurements of the bending rigidity of lipid-vesicle membranes across structural phase transitions. *Phys. Rev. E*, **64 (2)**:020901 (2001). doi:10.1103/PhysRevE.64.020901

[220] N. Delorme and A. Fery. Direct method to study membrane rigidity of small vesicles based on atomic force microscope force spectroscopy. *Physical Review E*, **74 (3)**:030901 (2006). ISSN 1539-3755. doi:10.1103/PhysRevE.74.030901

[221] M. Caputo. Linear Models of Dissipation whose Q is almost Frequency Independent–II. *Geophysical Journal International*, **13 (5)**:529–539 (1967). ISSN 0956-540X, 1365-246X. doi:10.1111/j.1365-246X.1967.tb02303.x

[222] W. R. Schneider and W. Wyss. Fractional diffusion and wave equations. *Journal of Mathematical Physics*, **30 (1)**:134 (1989). ISSN 0022-2488. doi:10.1063/1.528578

[223] F. Mainardi. The fundamental solutions for the fractional diffusion-wave equation. *Applied Mathematics Letters*, **9 (6)**:23–28 (1996). ISSN 0893-9659. doi:10.1016/0893-9659(96)00089-4

[224] J. Marsden and T. Hughes. *Mathematical Foundations of Elasticity*. Dover Civil and Mechanical Engineering Series. Dover (1994). ISBN 978-0-486-67865-8

[225] C. Li, Z. Zhao, and Y. Chen. Numerical Approximation of Nonlinear Fractional Differential Equations with Subdiffusion and Superdiffusion. *Comput. Math. Appl.*, **62 (3)**:855–875 (2011). ISSN 0898-1221. doi:10.1016/j.camwa.2011.02.045

[226] F. Johansson and others. mpmath: a Python library for arbitrary-precision floating-point arithmetic (version 0.14). http://mpmath.org/ (2010)

[227] K. Klopfer and T. Vanderlick. Isotherms of Dipalmitoylphosphatidylcholine (DPPC) Monolayers: Features Revealed and Features Obscured. *Journal of Colloid and Interface Science*, **182 (1)**:220–229 (1996). ISSN 0021-9797. doi:10.1006/jcis.1996.0454

[228] J. F. Holzwarth. Structure and Dynamics of Phospholipid Membranes from Nanoseconds to Seconds. In A. Cooper, J. L. Houben, and L. C. Chien, editors, *The Enzyme Catalysis Process: Energetics, Mechanism and Dynamics*, pp. 383–412. Springer US, Boston, MA (1989). ISBN 978-1-4757-1607-8. DOI: 10.1007/978-1-4757-1607-8_26

[229] W. W. Van Osdol, R. L. Biltonen, and M. L. Johnson. Measuring the kinetics of membrane phase transitions. *Journal of Biochemical and Biophysical Methods*, **20 (1)**:1–46 (1989). ISSN 0165-022X. doi:10.1016/0165-022X(89)90079-1

[230] I. Tasaki, K. Kusano, and P. M. Byrne. Rapid mechanical and thermal changes in the garfish olfactory nerve associated with a propagated impulse. *Biophys J*, **55 (6)**:1033–1040 (1989). ISSN 0006-3495. doi:10.1016/s0006-3495(89)82902-9

[231] E. P. Petrov, T. Ohrt, R. G. Winkler, and P. Schwille. Diffusion and Segmental Dynamics of Double-Stranded DNA. *Physical Review Letters*, **97 (25)** (2006). ISSN 0031-9007, 1079-7114. doi:10.1103/PhysRevLett.97.258101

[232] L. Y. Yeo and J. R. Friend. Ultrafast microfluidics using surface acoustic waves. *Biomicrofluidics*, **3 (1)**:012002 (2009). ISSN 1932-1058. doi:10.1063/1.3056040

[233] Y. Yang, M. H. Ritzwoller, A. L. Levshin, and N. M. Shapiro. Ambient noise Rayleigh wave tomography across Europe. *Geophysical Journal International*, **168 (1)**:259–274 (2007). ISSN 0956-540X, 1365-246X. doi:10.1111/j.1365-246X.2006.03203.x

[234] P. Segall. *Earthquake and Volcano Deformation*. Princeton University Press (2010). ISBN 978-1-4008-3385-6

[235] W. M. Slie, A. R. Donfor, and T. A. Litovitz. Ultrasonic Shear and Longitudinal Measurements in Aqueous Glycerol. *The Journal of Chemical Physics*, **44 (10)**:3712–3718 (1966). doi:http://dx.doi.org/10.1063/1.1726524

[236] M. Pelton, D. Chakraborty, E. Malachosky, P. Guyot-Sionnest, and J. Sader. Viscoelastic Flows in Simple Liquids Generated by Vibrating Nanostructures. *Physical Review Letters*, **111 (24)**:244502 (2013). ISSN 0031-9007. doi:10.1103/PhysRevLett.111.244502

[237] C. Karpfinger and K. Meyberg. *Algebra: Gruppen - Ringe - Körper*. Spektrum Akademischer Verlag (2009). ISBN 978-3-8274-2018-3

Abstract

In biological and other non-isolated systems, an environment is typically coupled to a collective variable that characterizes the physical process of interest. Therefore, effective models are necessary for the description of the collective variable, which is also called the reaction coordinate. If there is no separation of time scales between the dynamics of reaction coordinate and environment, memory effects are present. This thesis investigates several systems in the realm of biological physics where memory effects are relevant.

In the first part, we study cyclization kinetics of linear polymers via Langevin simulations of different backbone models, and phantom as well as self-avoiding collapsed chains. We find that while details of bonded interactions do not influence the end-to-end distance dynamics qualitatively, self-avoidance does. All memory kernels for the end-to-end distance and cyclization times extracted from our simulations are explained by scaling arguments based on Flory theory.

In the second part, we study the mean first-passage time τ_{MFP} for barrier crossing for non-Markovian dynamics using Langevin simulations. For single-exponential memory, we recover known asymptotic scalings and identify a new parameter regime where memory effects accelerate barrier crossing. These numerical results are supplemented by a theoretical analysis. We present a heuristic formula for calculating τ_{MFP} and use it to globally characterize the dependence of the barrier crossing time on the system parameters. For bi-exponential memory, we find that τ_{MFP} can be calculated using the single-exponential heuristic formula with effective parameters, which are dominated by the shorter of the two memory times. This dominance is corroborated by an analytical calculation.

In the third part, we consider surface waves. We study linear surface waves on a viscoelastic medium bounded by a viscoelastic interface, including the effects of gravitation. We investigate in which parameter regimes the classical Rayleigh, capillary-gravity and Lucassen surface waves exist and how they are related, and identify an additional wave solution which exists on a pure air-water interface. We subsequently derive the nonlinear fractional wave equation that governs compression waves at an elastic interface that is coupled to a viscous bulk medium. The fractional character of the equation constitutes a memory effect and comes from the frequency-dependent effective thickness of the bulk layer that is coupled to the interface. The nonlinearity arises from the dependence of the interface compressibility on the local compression. Numerical solutions of our theory reproduce experimental key features of surface waves in phospholipid monolayers at the air-water interface without freely adjustable fitting parameters.

Kurzfassung

In biologischen und anderen nicht isolierten Systemen besteht typischerweise eine Kopplung zwischen der Umgebung und der Reaktionskoordinate, welche die betrachtete physikalische Fragestellung charakterisiert. Um diese Kopplung bei der Beschreibung der Reaktionskoordinate zu berücksichtigen sind effektive Modelle notwendig. Falls die Zeitskalen der Dynamik von Reaktionskoordinate und Umgebung nicht entkoppeln, treten Memoryeffekte auf. In der vorliegenden Dissertation werden mehrere Systeme aus dem Bereich der biologischen Physik, für die Memoryeffekte relevant sind, untersucht.

Im ersten Teil untersuchen wir die Zyklisierung von Polymeren anhand von Langevinsimulationen verschiedener Modelle für die Hauptkette (Backbone). Dabei betrachten wir sowohl Phantomketten als auch selbstvermeidenende kollabierte Ketten. Wir finden, dass Details des Backbone-Modells das dynamische Verhalten des End-zu-End-Abstands nicht qualitativ beeinflussen, Selbstvermeidung jedoch schon. Sowohl die aus unseren Simulationen berechneten Memorykernels für den End-zu-End-Abstand als auch die aus unseren Simulationen berechneten Zyklisierungszeiten werden durch auf Flory-Theorie basierenden Skalenargumenten erklärt.

Der zweite Teil untersucht die mittlere für einen Barrierenübergang benötigte Zeit τ_{MFP} für nicht-Markovsche Dynamik mithilfe von Langevinsimulationen. Für exponentielles Memory bestätigen wir bekanntes asymptotisches Skalenverhalten und identifizieren einen neuen Parameterbereich in dem Memoryeffekte zu einer Beschleunigung des Barrierenübergangs führen, was wir durch eine analytische Herleitung ergänzen. Mithilfe einer heuristischen Formel charakterisieren wir das Verhalten von τ_{MFP} als Funktion der Systemparameter. Für bi-exponentielles Memory finden wir, dass sich τ_{MFP} durch die heuristische Formel für exponentielles Memory mit effektiven Parametern berechnen lässt. Die effektiven Parameter werden von der kürzeren der beiden Memoryzeiten dominiert, was wir durch ein analytisches Argument untermauern.

Im dritten Teil beschäftigen wir uns mit Oberflächenwellen. Wir leiten eine Gleichung für lineare Oberflächenwellen auf viskoelastischen Medien mit viskoelastischer Grenzfläche unter dem Einfluss der Gravitationskraft her. Wir veranschaulichen die Beziehungen zwischen den bekannten Rayleigh-, Kapillar-Gravitations-, und Lucassenwellen, und finden eine neue Wellenlösung, welche an einer reinen Luft-Wasser-Grenzfläche existiert. Weiterhin leiten wir eine nichtlineare Gleichung für Kompressionswellen in elastischen Grenzflächen auf viskosen Flüssigkeiten her. Die nichtlinearen Effekte entstammen der Abhängigkeit der Grenzflächenkompressibilität von der lokalen Kompression. Unsere Gleichung enthält Memoryeffekte, welche die frequenzabhängige Eindringtiefe der Oberflächenwelle in die Flüssigkeit widerspiegeln. Numerische Lösungen unserer Theorie reproduzieren die Hauptmerkmale von in Phospholipid-Monolayern an der Luft-Wasser Grenzfläche beobachteten Oberflächenwellen.

Erklärung

Hiermit erkläre ich, dass ich die vorliegende Dissertationsschrift mit dem Titel

Memory effects in soft matter

selbständig angefertigt und hierfür keine anderen als die angegebenen Hilfsmittel verwendet habe. Die Arbeit ist weder in einem früheren Promotionsverfahren angenommen noch als ungenügend beurteilt worden.

Berlin, den 1. Februar 2018

Curriculum vitae

For data privacy reasons, the curriculum vitae is not included in the online version of this thesis.

Danksagung

Ich möchte mich an dieser Stelle bei allen bedanken, die zum Gelingen dieser Dissertation beigetragen haben. Mein besonderer Dank gilt dabei Prof. Dr. Roland Netz für die vielfältigen und interessanten Aufgabenstellungen, die am Anfang dieser Arbeit standen, sowie für die stetige Diskussionsbereitschaft, und die mir überlassene Freiheit bei der Bearbeitung der Themen.

Für die erfolgreiche Zusammenarbeit bei den aus den Teilprojekten entstandenen und entstehenden Veröffentlichungen danke ich weiterhin meinen Co-Autoren Matthias Schneider, Shamit Shrivastava, Alexander Schlaich, Jan Daldrop, Moritz Böhle, Florian Brünig, Victor Hinrichsen, Julius Schulz, und Frank Noé. Der IT-Abteilung des Fachbereichs Physik der FU Berlin, und insbesondere Jens Dreger, danke ich für die bereitgestellten Ressourcen und die stets kompetente Unterstützung.

Auch bei allen nicht bereits genannten Arbeitskollegen möchte ich mich für die schöne Zeit und die vielen Diskussionen bedanken. Meinen (ehemaligen) Bürokollegen, insbesondere Won Kyu Kim, Tetsuya Hiraiwa, Yann von Hansen, und Florian Brünig, danke ich für die stets freundschaftliche Atmosphäre im Büro.

Für die vielen schönen Momente abseits der Wissenschaft danke ich meinen Freunden Heather Partner, Carlos Riofrío, Benni Böhm, Myriam Kammerlander, Claire Gauthier, und Aniruddha Bapat. Weiterhin möchte ich meinen Eltern Roswitha und Erich, sowie meinen Schwestern Vanessa, Marietta, und Korinna für ihre fortwährende Unterstützung danken.